UNIVERSIDADE TECNOLÓGICA FEDERAL DO PARANÁ

GUSTAVO GARBELINI DE MENEZES

DESIGN OPTIMIZATION OF PERMANENT MAGNET SYNCHRONOUS GENERATORS APPLIED TO A PILOT EXCITER

CURITIBA

2024

GUSTAVO GARBELINI DE MENEZES

DESIGN OPTIMIZATION OF PERMANENT MAGNET SYNCHRONOUS GENERATORS APPLIED TO A PILOT EXCITER

Projeto Ótimo de Geradores Síncronos de Ímãs Permanentes Aplicado a uma Excitatriz Auxiliar

Master's Dissertation presented as a requirement to obtain the title of Master in Programa de Pós-Graduação em Sistemas de Energia (PPGSE) from Universidade Tecnológica Federal do Paraná (UTFPR).
Advisor: Thiago de Paula Machado Bazzo.
Co-advisor: Elissa Soares de Carvalho.

CURITIBA

2024

4.0 Internacional

Esta licença permite remixe, adaptação e criação a partir do trabalho, para fins não comerciais, desde que sejam atribuídos créditos ao(s) autor(es). Conteúdos elaborados por terceiros, citados e referenciados nesta obra não são cobertos pela licença.

Ministério da Educação
Universidade Tecnológica Federal do Paraná
Campus Curitiba

GUSTAVO GARBELINI DE MENEZES

DESIGN OPTIMIZATION OF PERMANENT MAGNET SYNCHRONOUS GENERATORS APPLIED TO A PILOT EXCITER

Trabalho de pesquisa de mestrado apresentado como requisito para obtenção do título de Mestre Em Engenharia Elétrica da Universidade Tecnológica Federal do Paraná (UTFPR). Área de concentração: Automação E Sistemas De Energia.

Data de aprovação: 26 de Novembro de 2024

Dr. Thiago De Paula Machado Bazzo, Doutorado - Universidade Tecnológica Federal do Paraná

Dr. Aly Ferreira Flores Filho, Doutorado - Universidade Federal do Rio Grande do Sul (Ufrgs)

Dr. Bruno Akihiro Tanno Iamamura, Doutorado - Universidade Tecnológica Federal do Paraná

Me. Carlos Ogawa, Mestrado - Weg Equipamentos Elétricos S. A.

Dr. Joao Pedro Assumpcao Bastos, Doutorado - Universidade Tecnológica Federal do Paraná

Dr. Renato Carlson, Doutorado - Universidade Federal de Santa Catarina (Ufsc)

Documento gerado pelo Sistema Acadêmico da UTFPR a partir dos dados da Ata de Defesa em 05/12/2024.

ACKNOWLEDGEMENTS

Certainly, these paragraphs will not encompass everyone who played a part in this important phase of my life. I apologise in advance to those not mentioned here. Please know that you are present in my thoughts and in my gratitude.

First and foremost, I owe deep gratitude to my parents, Salvador and Giuliana, for their unconditional support throughout my life, especially during this part of my academic journey, and for their constant love and care. I also wish to thank the family members who have shared any encouragement or a few words of companionship.

I am also deeply grateful to my fiancée, Amanda, who has been by my side with unconditional love and understanding. She has been my steadfast cornerstone of support throughout this period and to whom I call upon in times of need.

I could not forget to express my gratitude to my advisor, Professor Thiago Bazzo, for his dedication and guidance throughout not only this work but also a significant part of my academic journey. Beyond his commitment to my development as a researcher, there were times when he also helped me grow as an individual. I am profoundly grateful for the knowledge he shared and for his constant support, which played a crucial role in the successful completion of this work.

I would also like to express my gratitude to my fellow research colleagues from PPGSE for their camaraderie and collaborative spirit throughout this journey. Also, I thank my long-time colleague João Kasper for his companionship, which has been invaluable even before this master's work.

Lastly, I extend my thanks to all those who have contributed to my journey in one way or another and to those unintentionally left out of this acknowledgement.

RESUMO

DE MENEZES, G. G. Design Optimization of Permanent Magnet Synchronous Generators Applied to a Pilot Exciter. 203f. Dissertação de mestrado – Programa de Pós-Graduação em Sistemas de Energia (PPGSE), Universidade Tecnológica Federal do Paraná (UTFPR). Curitiba, 2024.

Esta dissertação apresenta o desenvolvimento do projeto ótimo de geradores síncronos de ímãs permanentes aplicados a excitatrizes auxiliares. O constante crescimento do consumo de energia elétrica em todo o mundo tornou o mercado de geradores elétricos altamente competitivo, abrangendo desde pequenos conjuntos geradores-diesel até grandes turbogeradores e hidrogeradores síncronos. Atualmente, geradores síncronos de rotor bobinado são a maioria na geração de energia, devido às suas vantagens em relação aos geradores de ímãs permanentes e assíncronos. Essas máquinas requerem que seus enrolamentos de campo sejam excitados com corrente contínua para produzir o campo magnético principal, que por sua vez é regulada por um regulador automático de tensão. Entre os vários métodos para se alimentar o regulador, uma das soluções mais robustas e confiáveis é o uso de uma excitatriz auxiliar, que consiste em um pequeno gerador síncrono de ímãs permanentes acoplado ao mesmo eixo que o gerador principal. Possuindo uma máquina adicional, essa solução requer uma excitatriz auxiliar otimizada, para alcançar elevados valores de eficiência e densidade de torque, a fim de permanecer uma solução competitiva. Alta eficiência garante a entrega da potência necessária para o regulador com perdas mínimas de energia, enquanto uma maior densidade de torque assegura a máxima produção de potência em um tamanho compacto. Para alcançar uma máquina compacta e eficiente, inicialmente, um método semi-analítico para projetar geradores síncronos de ímãs permanentes montados na superfície é desenvolvido e validado por meio de simulações de elementos finitos. Em seguida, duas redes de relutâncias são desenvolvidas para obter o fluxo principal do gerador à vazio e a reação de armadura, que são essenciais para o projeto e para o cálculo preciso da tensão terminal. Após validação com elementos finitos, esses circuitos magnéticos são integrados ao procedimento de projeto, resultando em um modelo eletromagnético orientado à otimização que permite a otimização precisa em tempo reduzido de geradores síncronos com ímãs permanentes montados na superfície do rotor. Uma fronteira de Pareto é gerada para avaliar o compromisso entre eficiência e densidade de torque, orientando a seleção de uma solução ótima que equilibre ambos os objetivos. Finalmente, o gerador síncrono de ímãs permanentes otimizado é validado com simulações de elementos finitos, demonstrando a precisão do método proposto.

Palavras-chave: gerador síncrono; ímã permanente; excitatriz auxiliar; projeto ótimo.

ABSTRACT

DE MENEZES, G. G. Design Optimization of Permanent Magnet Synchronous Generators Applied to a Pilot Exciter. 203f. Master's Dissertation – Postgraduate Program in Energy Systems (PPGSE), Federal Technological University of Paraná (UTFPR). Curitiba, 2024.

This dissertation presents the development of a design optimisation for permanent magnet synchronous generators applied to pilot exciters. The constant growth of worldwide electrical energy consumption has made the electrical generator market highly competitive, from small-scaled generator-diesel sets to large turbogenerators and synchronous hydro-generators. The preferred choice for power generation nowadays are wound-rotor synchronous generators, given their many advantages over permanent magnet and asynchronous generators. These machines require DC excitation to be supplied to their field winding to establish the primary magnetic field, typically regulated by an automatic voltage regulator. Among the various methods to supply power to the regulator, one of the most robust and reliable solutions is the use of a pilot exciter, which consists of a small permanent magnet synchronous generator mounted on the same shaft as the main generator. Given the additional machine required, the pilot exciter must be optimised to achieve maximum efficiency and torque density to remain a competitive solution. High efficiency ensures the delivery of the required power for the regulator with minimal energy losses, whereas increased torque density ensures maximum power output in a compact size. To accomplish this goal of a compact and efficient machine, firstly, a semi-analytical method for designing surface-mounted permanent magnet synchronous generators is developed and validated through finite element simulations. Two reluctance networks are then developed to obtain the no-load linkage flux and the armature reaction, which are essential for the design and for accurately calculating the terminal voltage. After validating their results, these magnetic circuits are integrated into the design procedure, resulting in an optimisation-oriented electromagnetic model that enables the precise and time-efficient optimisation of surface-mounted permanent magnet synchronous generators. A Pareto front is generated to evaluate the trade-off between efficiency and torque density, guiding the selection of an optimal solution that balances both objectives. Finally, the optimised permanent magnet generator is validated with finite element simulations, demonstrating the accuracy of the proposed method.

Keywords: synchronous generator; permanent magnet; pilot exciter; optimal design.

LIST OF FIGURES

LIST OF TABLES

LIST OF ACRONYMS

AC	Alternating Current
AVR	Automatic Voltage Regulator
CADES	Component Architecture for Design of Engineering Systems
DC	Direct-Current
EPE	Empresa de Pesquisa Energética
FES	Finite Element Simulations
FFT	Fast Fourier Transformation
ME	Main Exciters
MMF	Magnetomotive Force
PC	Permeance Coefficient
PE	Pilot Exciters
PM	Permanent Magnets
PMSG	Permanent Magnet Synchronous Generators
RN	Reluctance Networks
SG	Synchronous Generators
SML	System Modeling Language
SQP	Sequential Quadratic Programming
THD	Total Harmonic Content
WRSG	Wound-Rotor Synchronous Generators

LIST OF SYMBOLS

H	Magnetic field intensity
C	Closed contour
S	Surface
J	Current density
B	Magnetic flux density
μ	Magnetic permeability
φ	Magnetic flux
e	Induced voltage
N	Number of turns
f	Electrical frequency
n	Mechanical speed
P	Number of poles
L	Inductance
$\Re$	Reluctance
λ	Flux linkage
I	Current
F_{mm}	Magnetomotive force
l	Length
μ_r	Relative magnetic permeability
μ_0	Vacuum magnetic permeability
$\vec{B}_R$	Rotor magnetic flux density phasor
$\vec{E}_{Af}$	Induced no-load voltage phasor
$\vec{I}_A$	Armature current phasor
$\vec{B}_{Ra}$	Armature reaction field phasor
$\vec{B}_N$	Net flux density phasor
$\vec{V}_\varphi$	Phase terminal voltage phasor
$\vec{V}_{Ra}$	Armature reaction voltage drop phasor
L_a	Leakage inductance
X_a	Leakage reactance
X_S	Synchronous reactance
$\vec{I}_d$	Direct axis component of the armature current phasor
$\vec{I}_q$	Quadrature axis component of the armature current phasor
$\vec{B}_d$	Direct axis component of the armature reaction field phasor
$\vec{B}_q$	Quadrature axis component of the armature reaction field phasor
X_d	Direct axis synchronous reactance
X_q	Quadrature axis synchronous reactance
I_d	Direct axis component of the armature current
ϕ	Displacement angle between terminal voltage and armature current
δ	Load angle
I_q	Quadrature axis component of the armature current
V_d	Direct axis component of the terminal voltage
R_A	Armature resistance
V_q	Quadrature axis component of the terminal voltage

E_{Af}	Induced full-load voltage
V_{φ}	Phase terminal voltage
V_{Td}	Desired terminal voltage
B_r	Remanent flux density
H_c	Coercivity
μ_{re}	Recoil permeability
PC	Permeance coefficient
H_{PM}	Permanent magnet magnetic field
h_{PM}	Permanent magnet height
H_{AG}	Air-gap magnetic field
L_{AG}	Air-gap length
μ_{rES}	Electric steel permeability
H_{ES}	Electric steel magnetic field
L_{ES}	Electric steel length
B_{PM}	Permanent magnet operative flux density
S_{PM}	Permanent magnet cross-section area
B_{AG}	Air-gap flux density
S_{AG}	Air-gap cross-section area
ω	Rotational speed
α_P	Pole pitch
α_{Pef}	Effective pole pitch
$k_{\alpha P}$	Pole pitch factor
D_{Ro}	Rotor outer diameter
k_{AG}	Air-gap factor
W_{PM}	Permanent magnet width
h_{Ry}	Rotor yoke height
B_{Ry}	Rotor yoke flux density
D_{PMt}	Diameter at the permanent magnet top
D_{Ri}	Rotor inner diameter
φ_{PM}	Permanent magnet flux
L_G	Machine stack length
k_{MS}	Machine shape factor
φ_{AG}	Air-gap flux
$\Delta\varphi_{PMAG}$	Permanent magnet to air-gap leakage flux factor
L_{AGa}	Length of the arc at the middle of the air-gap
B_{AG}	Air-gap flux density
D_{Si}	Stator inner diameter
W_{So}	Slot opening width
N_S	Number of slots
k_{Sow}	Slot opening width to outer diameter factor
h_{So}	Slot opening height
k_{Soh}	Slot opening height factor
h_{Sw}	Slot wedge height
k_{Sw}	Slot wedge height factor
D_{St}	Diameter at the slot top
D_{Si}	Stator inner diameter
α_S	Slot pitch
θ_{St}	Angle of the slot on the top
k_{TS}	Tooth-to-slot width factor

W_{St}	Width at the slot top
W_t	Tooth width
W_{Sw}	Slot wedge width
h_{Sy}	Stator yoke height
k_{PMSy}	Permanent magnet width to stator yoke factor
h_S	Slot height
k_{SyS}	Stator yoke to slot height factor
θ_{Sei}	Inclination angle of the slot edge
W_{Sb}	Width at the slot bottom
D_{So}	Stator outer diameter
α_{Ac}	Armature coil pitch
k_{Ac}	Armature coil-shortening factor
$\Delta\varphi_{Cs}$	Reduction factor due to coil shortening
q	Number of slots per pole per phase
N_{ph}	Number of phases
$\Delta\varphi_{Wd}$	Reduction factor due to winding distribution
T_A	Number of turns of armature winding per phase
E_{Af}	Estimated induced full-load voltage
$\Delta\varphi_{AGA}$	Air-gap-to-armature flux leakage factor
N_{Cs}	Number of coils in series per phase
N_{Cp}	Number of parallel coils
k_{Cop}	Consequent pole factor
N_{Cpp}	Number of coils per pole per phase
N_{Sl}	Number of slot layers
T_{Ac}	Number of turns of the armature winding per coil
S_S	Slot area
S_{Ac}	Armature conductor surface
k_{Sf}	Slot fill factor
I_A	Armature current
J_A	Armature current density
S_E	Generator electrical output power
P_E	Generator electrical output active power
PF	Power factor
L_C	Arc length between two slots
L_{Ce}	Coil end length
L_{At}	Armature coils length
R_{Aref}	Armature resistance at the reference temperature
R_{km}	Conductor resistance per kilometer
T_{op}	Operating temperature
T_{ref}	Reference temperature
L_{ag}	Air-gap inductance
M_{ag}	Air-gap mutual inductance
L_{Sl}	Slot-leakage inductance
L_S	Synchronous inductance
V_T	Phase-to-phase terminal voltage
P_{Ac}	Copper losses
V_{Sy}	Stator yoke volume
V_{St}	Stator teeth volume

B_{Sy}	Stator yoke flux density
B_{St}	Stator teeth flux density
P_{Syh}	Stator yoke hysteresis losses
k_{Syh}	Stator yoke hysteresis losses factor
ρ_{ee}	Electrical steel mass density
P_h	Hysteresis losses per kilogram
P_{Syf}	Stator yoke Foucault losses
k_{Syf}	Stator yoke Foucault losses factor
P_F	Foucault losses per kilogram
P_{Sth}	Stator teeth hysteresis losses
k_{Sth}	Stator teeth hysteresis loss factor
P_{Stf}	Stator teeth Foucault losses
k_{Stf}	Stator teeth Foucault losses factor
P_{PM}	Permanent magnet losses
k_{PM}	Permanent magnet specific losses
P_T	Total losses
k_{Sl}	Stray losses factor
η	Efficiency
θ_{Sw}	Slot wedge inclination angle
θ_{PM}	Angle between permanent magnets
W_{fbt}	Flux barrier width at the top
W_{fbb}	Flux barrier width at the bottom
L_{fb}	Flux barrier gap length
h_{fb}	Flux barrier height
L_{PMc}	Length of the gap between permanent magnets
L_{Ro}	Length of the gap between the PM tip and the rotor outer diameter
L_{PMe}	Length of the gap between permanent magnets edges
k_{PMRy}	Rotor yoke height to PM width factor
V_R	Rotor volume of the generator
θ_t	Angle occupied by a tooth at the top of the slot
θ_{WSo}	Angle occupied by the slot opening at the top of the slot
θ_{WSw}	Angle occupied by the slot wedge at the top of the slot
S_{Sef}	Effective slot area
V_S	Stator volume of the generator
V_G	Generator volume
ρ_τ	Torque density of the machine
k_M	Permanent magnet form factor
k_{fbt}	Flux barrier top width to permanent magnet height factor
k_{fbb}	Flux barrier bottom width to permanent magnet height factor
k_{fbh}	Flux barrier height factor
k_{fb}	Flux barrier gap to PM height factor
k_{Ro}	Gap between permanent magnet tip to rotor outer diameter factor
x_{fbe}	X coordinate on the top end of the flux barrier
y_{fbe}	Y coordinate on the top end of the flux barrier
R_{fbe}	Radius on the top end of the flux barrier
θ_{fbe}	Angle on the top end of the flux barrier
L_{fbe}	Length of the gap between the PM edges

L_d	Direct axis synchronous inductance
L_q	Quadrature axis synchronous inductance

TABLE OF CONTENTS

1 INTRODUCTION

The transformation industry represents a big share of the global economy, manufacturing goods by manipulating raw materials and adding value to the final product. Over the last two hundred years, this sector of the economy has been experiencing technological leaps, each one changing the current production paradigm. Today called industrial revolutions, these leaps were marked firstly by the mechanisation of the production process (1st revolution), followed by intense use of electrical energy (2nd revolution), and, lastly, by generalised digitisation (use of computers in the 3rd revolution). A new paradigm shift is considered to be occurring with the introduction of a combination of Internet and future-oriented technologies (4th revolution), further increasing automation and digitalisation while adding networking and miniaturisation (LASI et al., 2014).

Thereby, since the second industrial revolution, electricity became a big necessity for basically all industry sectors and, gradually, for the whole society. Thus, as expected, energy generation became a fundamental matter for countries all over the world due to the fact that energy consumption increases every year. In Brazil, energy consumption grew 1.74 % on average between 2016 and 2021, when it reached 570 TWh, as Figure 1 shows. Except for 2020 (due to the pandemic), energy consumption increased every year.

Figure 1 – Energy consumption in Brazil between 2016 and 2021

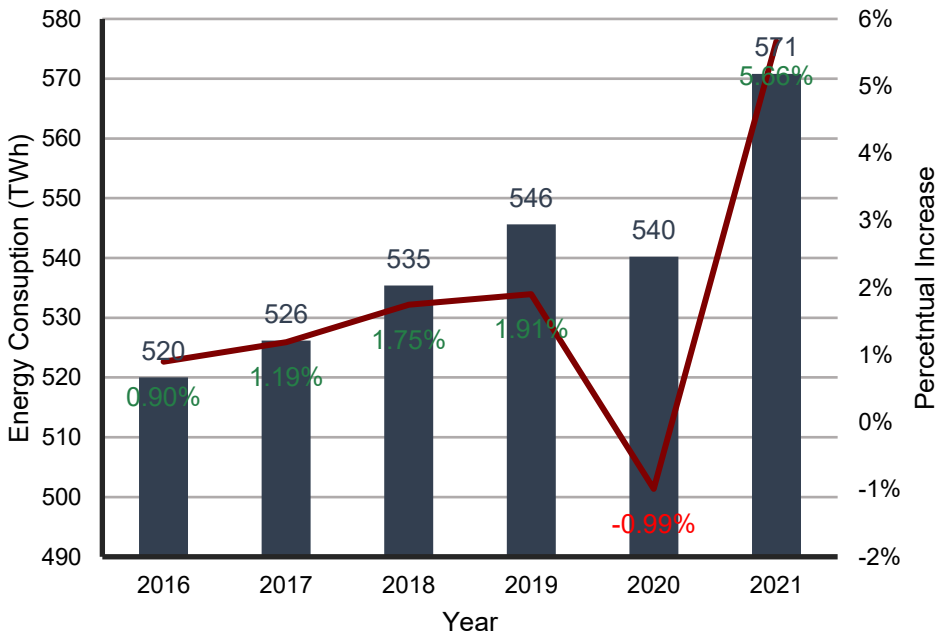

Source: Based on Empresa de Pesquisa Energética (2017; 2018; 2019; 2020; 2021)

Except for solar energy, all other significant primary energy sources, such as hydraulic, coal, nuclear, natural gas, wind, biomass, etc., need electric generators to convert the mechanical energy provided by the primary mover into electricity (BAZZO; MOURA; CARLSON, 2021). Synchronous generators are by far the most used electrical machines in electric energy production, regardless of the above-mentioned primary sources, with doubly-fed induction machines (asynchronous generators) being used in a significant part of wind-powered systems.

There are basically two types of synchronous generators, and their distinction is made from the creation of their main magnetic field, either from a permanent magnet or an electromagnet (BOLDEA, 2006). Permanent magnet synchronous generators (PMSG) have permanent magnets (PM) on their rotor, either placed on the rotor surface or buried, producing a constant magnetic field, which value depends on the material characteristics (BH curve) (GIERAS; WILL, 2002). On the other hand, wound-rotor synchronous generators (WRSG) have field windings in the rotor (either within their slots or winded around the pole bodies), which are powered by a DC source and produce a magnetic field whose magnitude is proportional to the supplied current. Therefore, whereas PMSG do not need an external system to supply field excitation, it is possible to regulate the terminal voltage of WRSG by adjusting its field current (BOLDEA, 2006).

The preferred choice for power generation in the order of kilowatts up to a few gigawatts are WRSG. This is due to the fact that this type of machine allows the control of reactive power flow, has reliability and resilience during short-circuit faults (without risks of demagnetisation), superior dynamics during electromechanical transients and, most importantly, intrinsic flux regulation capability, which allows terminal voltage regulation (a fundamental requirement of power quality in a power system) (NØLAND et al., 2019). However, PMSG and WRSG are not antagonists and can operate concurrently to create a reliable and independent generating solution.

It is very well established that brushless excitation is the most reliable and modern way to provide power to the field of WRSG (NUZZO et al., 2018). Among the several methods to power supply the automatic voltage regulator of the brushless excitation system, the most robust uses a pilot exciter (PE), which consists of a permanent-magnet synchronous generator mounted on the same shaft of the main generator. This configuration is more suited to medium-size generator sets (rated between 700 kVA and 4 MVA) and is the better solution for some specific applications, such as emergency generators and isolated generation, since it allows an entirely independent generation and several other advantages when compared with other brushless methods, at the cost of being more complex and expensive (NØLAND et al., 2019). Thus, to remain a competitive generating solution, the PE of the excitation system should have the smallest cost possible and deliver high efficiency, which can only be achieved by performing an optimisation.

1.1 Literature Review

Given the substantial importance of synchronous generators in nowadays society, their design also receives considerable attention. Extensive knowledge of electrical machine design can be found with ease in several bibliography materials. Even though an expressive number of papers address permanent magnet synchronous machine design, only a few have a detailed design methodology and present all the design equations and parameters, which is crucial to reproducing the method. Additionally, in most cases, essential details of the design are not discussed, and the focus is either on specific parts of the design, determining the machine's outer dimensions, presenting the highlights of the designed machine and its results, or in a new machine topology.

In Bazzo, Moura, and Carlson (2021), a thorough design methodology is presented to design salient-pole wound-rotor synchronous generators. Such design method is carried out using analytical equations to determine the machine geometry and magnetic and electrical quantities, except for the direct and quadrature axis inductances that are obtained with finite element simulations (FES). A machine is designed using the proposed method and validated with a final finite element simulation.

Hebala, Ghoneim, and Ashur (2019) developed a design procedure for permanent magnet synchronous generators with surface PM for direct-driven wind turbines. This type of generator has a non-salient pole construction that allows the armature reaction components to be calculated analytically, and thus, the machine terminal voltage can be found more effortlessly. However, the authors do not show how to perform adjustments during the design process to meet the calculated terminal voltage of the designed generator to the specified value. Furthermore, the design procedure starts with stator sizing rather than the rotor, in which the stator slots are dimensioned to fit a calculated conductor surface. This can lead to long and thin stator teeth, causing saturation problems and leading to excessive losses and vibration, especially with inexperienced designers.

Yazdanpanah, Afroozeh, and Eslami (2022) present the design of a synchronous generator with PM buried within the rotor, which is a salient-pole geometry that is more complex to model and design than surface PM machines. However, the authors do not show design procedure specifics concerning the PM and the design choices, which makes it challenging for others to replicate. Moreover, being a salient-pole machine, the method to obtain the direct and quadrature axis reactances used to calculate the generator's terminal voltage is not addressed.

Thus, this work intends to reduce the literature gap regarding PM synchronous generator design, presenting a thorough design procedure. Throughout this manuscript, all the design stages, along with their equations and parameters, are explained. Even though the procedure is composed of a considerable number of equations, it is not an overly complex method, fully considering PM generator fundamentals with a few simplifications. Differently from the work developed by Hebala, Ghoneim, and Ashur (2019), the proposed design method sizes the armature conductors based on the slot dimensions, which are imposed by the designer. This allows a feasible generator since a reasonable range of each imposed parameter is

provided. Furthermore, a significant amount of information concerning imposed values and procedure specifics are presented, as well as how needed adjustments in output power, terminal voltage, etc., can be made in the proposed design method.

The proposed design method is not intended to reach a competitive design in terms of efficiency, power density, or cost; but to present a framework for others to incorporate into their research or build upon for further development. Being a simplified procedure that accounts for the permanent magnet generator's main fundamentals, it becomes easy to be replicated and, thus, it can be used in a variety of applications. Building on this, the design procedure and its equations were adapted to develop a optimization-oriented electromagnetic model that is further used to find an optimised high-efficiency generator with elevated torque density.

Two magnetic submodels (reluctance networks) were developed and also incorporated into the optimization-oriented model to calculate the no-load magnetic flux and the synchronous inductance of the PM machine instead of calculating it analytically or using FES. The procedure for designing PM generators relies on finite element simulations to obtain a few parameters and maintain a good level of accuracy. However, this approach becomes less attractive in an optimisation procedure, as it is very time-consuming and would result in an even more time-consuming optimisation. Thus, the two nonlinear reluctance networks (RN) were incorporated into the optimization-oriented model to reduce optimisation time without compromising precision.

As maximising torque density and efficiency are conflicting objectives, prioritising one would require compromises in the other. Thus, a Pareto front is generated using the proposed electromagnetic model and optimisation procedure to guide the identification of an optimal solution that presents an optimal trade-off between torque density and efficiency. Lastly, the optimal surface-mounted PM synchronous generator chosen from the Pareto front is validated with finite element simulations, providing final confirmation of both the optimisation process and the electromagnetic model.

Therefore, in summary, this work can contribute to a range of applications:

- Beginners in designing PM synchronous machines can use the design procedure to replicate the results and gain experience;
- Experienced designers can easily improve the electromagnetic model by refining or eliminating the remaining simplifications, incorporating

complexity and new physics; and find an optimal design according to their objectives;

- Fellow researchers from other fields, such as power electronics, control, or mechanical engineering, may use either the procedure or the optimisation to quickly find the parameters of the generator for their studies.

1.2 Motivation

In modern wound-rotor synchronous generators, brushless excitation is more commonly used to supply DC power to the rotor windings (NUZZO et al., 2018). In this type of excitation, a special synchronous machine called main exciter (ME) is mounted on the same shaft of the main generator. This machine is supplied with DC voltage in the field winding and produces a constant and stationary magnetic field on the stator, inducing an AC voltage in the armature windings of the rotor. With a three-phase rectifier circuit (also mounted on its rotor) this AC voltage is converted to DC and connected to the field windings of the WRSG (BOLDEA, 2006).

In this excitation system, there is still an automatic voltage regulator (AVR) that acts upon the main exciter field circuit, which is stationary (hence the absence of brushes). By adjusting the field current applied to the ME, its output is also adjusted and, after being rectified, the field current value of the WRSG is changed. In an isolated generation scenario, this will determine the no-load voltage value and, ultimately, for a given load, the terminal voltage of the generator will be adjusted as required (TARTIBI; DOMIJAN, 1996). In a grid-connected operation, adjusting the field current applied to the ME, and consequently the field current of the WRSG, provides control over reactive power flow.

To accurately supply the DC power to the ME, the AVR clearly needs to be connected to a power source. One of the most well-known and robust forms to produce power to the AVR is by using a pilot exciter (PE). The PE consists of a small permanent synchronous magnet generator placed on the WRSG shaft. Since the permanent magnets of the PMSG produce a constant magnetic field, this excitation form provides a reliable isolated power input to the AVR as long as the shaft is rotating at synchronous speed. Although adding the PMSG ends up adding complexity to the WRSG system, there are many more advantages of using this type of excitation, such

as sustained short circuit fault conditions, powerful voltage build-up on starting, high overload capacity, and suitability for demanding applications (NØLAND et al., 2019).

Therefore, even though adding a PMSG may result in a costlier generating system (when compared to other brushless excited systems), it allows the WRSG to produce electrical energy completely independent of external electrical power sources. This feature, along with the above-mentioned characteristics, makes power supplying the AVR with a PE a very attractive solution to medium-size generator sets, emergency generators, isolated generation, and other cases. In these scenarios, the PE can be a vital component of the whole generating system. Thus, to deliver the most competitive generating solution possible, the PMSG should have an optimised design since a well-rounded optimisation can produce a PMSG with reduced cost while delivering high efficiency and respecting its specifications and restrictions.

1.3 Objectives

1.3.1 Main Objective

The main objective of this master's thesis is to develop a detailed design procedure for permanent magnet synchronous generators applied to a pilot exciter of the excitation system of wound-rotor generators.

1.3.2 Specific Objectives

The specific objectives of this thesis are:

- To examine the literature on: Synchronous Generators and their excitation systems, design of Permanent Magnet Machines, Reluctance Networks, Optimization Techniques, and Finite Element Simulations;
- To develop a design methodology for the design of permanent magnet synchronous generators, focusing on the pilot exciter application;
- To validate the proposed methodology of the designed machine with finite element simulations;
- To create reluctance networks that model the magnetic flux of permanent magnet generators to aid the design process;
- To optimise the designed machine for torque density and efficiency maximising purposes;
- To validate the optimised generator with finite element simulations;

2 THEORETICAL FRAMEWORK

This section is dedicated to the theoretical underpinnings and key concepts that form the basis of the research. It contains explanations about the construction, operating principles, and excitation systems of WRSG, as well as the principles of construction and operating principles of PMSG.

2.1 Wound-rotor Synchronous Generators

Electric generators are essentially rotating mechanical energy converters, converting the mechanical power delivered from the shaft of a primary mover into electrical power. Most electric energy nowadays is produced by synchronous generators that deliver energy with alternating current (AC) at constant voltage and frequency. The synchronous denomination is because, in the steady state, its main magnetic field produced on the rotor rotates at the same speed as the armature magnetic field produced in the stator (UMANS, 2014).

2.1.1 Principles of Construction

Synchronous generators are characterised by two electrically isolated components: the stator is the stationary part, a uniformly slotted laminated core, and the rotor is the rotating part that produces the main magnetic field of the machine. Synchronous generators (SG) have a uniformly slotted stator that changes slightly from generator to generator. Thus, the distinction between SG is made through the rotor configuration, mainly by the magnetic field excitation. SG can produce its main magnetic field either with direct current (DC) excited windings, in the case of wound-rotor SG, or with PM, being then called permanent magnet SG (BOLDEA, 2006). Figure 2 shows the cross-section of the active part of a salient-pole WRSG, with rotor, stator, and its windings indicated; ellipses with different colours illustrate field windings and the three-phase armature windings.

Figure 2 – Wound-rotor synchronous generator

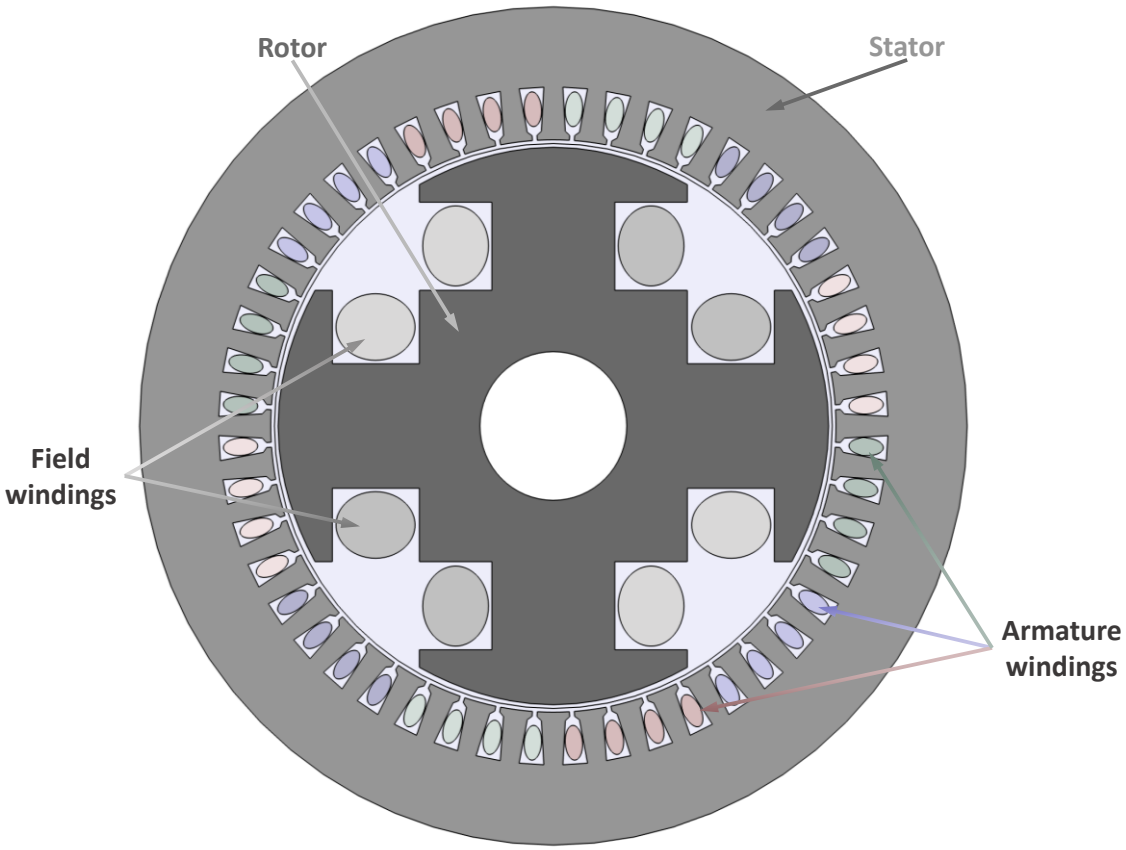

Source: Own authorship (2023)

2.1.1.1Stator

The stator is usually the external part of the machine, consisting of a frame, an electromagnetic core, and the armature windings. The frame encloses the entire machine, providing mechanical isolation from the external environment, structural support and exchanging heat. The stator core is made of insulated steel laminations of high magnetic permeability, providing low reluctance paths for the magnetic flux. With a lower reluctance value, more flux can be linked by the armature windings, which in turn will increase the power density of the machine. The thickness of the laminations and the type of steel are chosen to minimise eddy current and hysteresis losses while maintaining the required effective core length and minimising costs. Most machines are made of electrical steel, a high permeability iron alloy that still has a small hysteresis area, which reduces energy losses per cycle (FITZGERALD; KINGSLEY; UMANS, 2003).

The electromagnetic core of the stator is slotted to house the three-phase AC winding, called armature windings. The armature coils are arranged within the stator slots so that each phase winding is displaced 120 electrical degrees in space from each other. Respecting this, three balanced and sinusoidal voltages will be generated when the rotor produces constant magnetic flux and turns at constant speed (HENDERSHOT; MILLER, 1994).

A homogeneous and uniform distribution of these windings is a fundamental premise in the design of synchronous machines, ensuring a more effective utilisation of active conductors for energy production. Another important goal in arranging the armature coils is to have as little harmonic content as possible. Thus, the designer may vary the number of slots and the manner in which individual coils are connected, producing different winding patterns. Several winding arrangements are possible, such as concentric windings, split windings, lap windings, and a few others (KLEMPNER; KERSZENBAUMM, 2004).

The armature windings can be configured in two main ways, depending on the relationship between the number of stator slots, rotor poles, and phases. Integral-slot windings have an integer number of slots per pole per phase. In such cases, coils can be easily grouped, with each group containing the same number of coils per pole. Since the pole pitch corresponds to a whole number of slots, naturally, it results in a more regular and symmetrical winding. Integral-slot windings can be either concentrated, with only one coil per pole per phase, or distributed, with more than one coil per pole per phase (HENDERSHOT; MILLER, 1994).

Distributed windings can be arranged either concentrically or in a lap winding configuration. Concentric windings are more commonly used in three-phase induction machines, typically inserted by automated machinery, whereas lap windings are found in larger machines, manually inserted, achieving higher slot fill factors. This factor represents how much copper (armature conductors) can be packed in the total slot area, and with higher fillings, the armature resistance, losses and temperature rise are reduced (HENDERSHOT; MILLER, 2010).

On the other hand, when the number of slots per pole per phase is not an integer, the windings are referred to as fractional-slot windings. These, too, can be concentric or lap windings. Fractional-slot windings offer the advantage of improving the quality of the voltage waveform by reducing certain harmonics. However, their greatest disadvantage is the introduction of sub-harmonics (PYRHÖNEN, 2008).

2.1.1.2Rotor

The WRSG can have two rotor types, either non-salient-pole or salient-pole construction. The difference is that the first has a constant reluctance throughout the entire air-gap, whereas salient-pole rotors have different reluctance values depending on the rotor position (KRAUSE; WASYNCZUK; SUDHOFF, 2002). Moreover, because they are so different structurally, their application ends up being different. Non-salient rotors are used for higher-speed applications since the basic cylindrical structure has more structural integrity than salient-pole ones; this also implies in a smaller number of poles. Typically, they are made of forged solid steel (for more mechanical rigidity and better heat transmission) and slots are machined out of the rotor surface to host the distributed field winding. Since a large centrifugal force is upon those windings, usually metallic wedges made of aluminium or steel are used to retain them to the rotor (KLEMPNER; KERSZENBAUMM, 2004).

Therefore, for lower-speed applications, WRSG salient-pole rotors are more common, and since the peripheral speeds are lower, larger outer diameters can be applied. This type of rotor has a more prominent structure with concentrated windings evolving around each pole body, with pole shoes retaining these windings to the pole and modelling the air-gap magnetomotive force waveform. Depending on the machine size, rotor pole shoes and body can have different constructions. When connected to a load, the armature reaction magnetic field can have some harmonic content, which will penetrate mostly on the rotor surface, causing eddy current losses and generating excessive heat. In the case of larger machines, this effect can be significant, and to reduce it, the pole shoes are made of laminations, whereas the pole bodies and core are made of mild magnetic solid steel (BOLDEA, 2006).

Nevertheless, DC excitation is required to create the main magnetic field for both rotor structures. An excitation system is used to provide this DC power, and it is designed to control the supplied voltage and thus control the field current to ultimately control the generator terminal voltage in isolated generation, or provide reactive power control between the generator and the connected system (KLEMPNER; KERSZENBAUMM, 2004). Since the field windings rotate with the rotor at synchronous speed, transmitting power to it can be made in a contact-less way or not, with both methods having advantages and disadvantages regarding performance under different situations, maintenance, and cost.

2.1.2 Operating Principles

Despite the complex construction of real electric generators and motors, the operating principles of all AC synchronous machines can be explained by the same principles. These principles are obtained through the quasi-static magnetic form of Maxwell's equations that relate magnetic fields to the currents that produce them: Ampère, magnetic flux conservation, and Faraday's laws.

From Ampère's Law, magnetic field production can be understood since it states that the total current passing through a surface S produces a magnetic field intensity $\vec{H}$ tangential to the closed contour C (which is bounded to S) as (FITZGERALD; KINGSLEY; UMANS, 2003):

$$\oint_C \vec{H} \cdot \overrightarrow{dl} = \int_S \vec{J} \cdot \overrightarrow{da} \tag{1}$$

On the other hand, the flux conservation law states that no monopole charge produces a resulting magnetic field, i.e., the net magnetic flux on an enclosed surface S is always zero, and the magnetic induction $\vec{B}$ is conserved, as (CHAPMAN, 2013):

$$\oint_S \vec{B} \cdot \overrightarrow{da} = 0 \tag{2}$$

In other words, flux lines always form a closed path.

In a sense, the magnetic field intensity $\vec{H}$ corresponds to the effort a current makes to establish a magnetic field, which in turn corresponds to a magnetic flux density $\vec{B}$ on the surface of a given material. The relationship between these two quantities is dictated by the magnetic permeability μ of the material in which the field exists (UMANS, 2014):

$$\vec{B} = \mu\vec{H} \tag{3}$$

These presented principles are the basis for explaining how the main magnetic field of the WRSG is created. Applying a direct current to the field windings will produce

a time-constant magnetic field and, consequently, a constant magnetic flux that will circulate within the machine. Finally, Faraday's law states that the variation of magnetic flux φ linked by the coil conductor will induce a voltage e at the coil terminals. This voltage is directly proportional to the time rate of change of the magnetic flux ($\frac{d\varphi}{dt}$), as Eq. (4) shows (CHAPMAN, 2013):

$$e = -N\frac{d\varphi}{dt} \tag{4}$$

in which N is the number of turns of the coil. This equation assumes that the time-varying magnetic flux crosses all N turns of the coil.

As the WRSG rotor turns at a certain speed, the time-constant rotor magnetic flux will be time-varying for the windings housed in the stator, thus, generating a time-varying voltage at the machine terminals of each phase. The electrical frequency f of the induced voltage is strictly tied to the mechanical speed n transmitted from the prime mover to the generator rotor. Equation (5) shows this relationship (FITZGERALD; KINGSLEY; UMANS, 2003):

$$f = \frac{n \cdot P}{120} \tag{5}$$

in which P is the number of poles of the machine.

These concepts can resume WRSG working principle at no-load, but when the generator is connected to a load, the explanation goes a bit further. While feeding a load, current will flow in the armature windings, and a magnetic field will be created according to equation (1). Depending on the load characteristics (inductive or capacitive) the stator have magnetic field will weaken of contribute to the rotor magnetic field. This distortion of the main magnetic field intensity due to the interaction with the armature magnetic field is called armature reaction. The net magnetic flux density resulting from this interaction will correspond to the generator terminal voltage.

2.1.3 Excitation Systems

As SG increased in power, permanent magnet field excitation became unfeasible. So, the rotor of WRSG is an electromagnet consisting of field windings that

evolve the core and are powered by a DC excitation system. This system is designed to control the voltage for operation near steady-state stability limits, regulate the voltage under fault conditions, and provide reactive power and power factor control between the generator and the system (SAY, 1976). Excitation systems differ according to how the DC power is transmitted to the field windings, either with slip-rings and brushes or by a special DC source mounted on the generator's shaft.

In a brushed excitation system, as shown in Figure 3, the field windings have their ends connected to two slip-rings, which are metal rings, usually made of copper, mounted on the generator shaft. Whereas the inner part is connected to the rotor windings, the outer part of each slip-ring is in contact with a brush. This brush is a stationary block of carbon (similar to graphite) that can conduct electricity at low friction so that the slip-ring is not easily worn out with the continuous movement of the rotor. A stationary controllable DC source's positive and negative terminals are then connected to the brushes, continuously applying DC voltage to the field windings.

This static excitation is dominant in large synchronous generators (with power ratings in the order of several MVA) since they are required to satisfy standardised technical requirements in terms of dynamic performance, such as a fast dynamic response (NØLAND et al., 2019). However, it requires frequent monitoring and maintenance since brushes eventually wear out due to friction. Furthermore, it can cause safety issues (possible sparking of the brushes) and elevated power losses (once the voltage drop on the brushes is significant when carrying high currents) (CHAPMAN, 2013).

Figure 3 – Brushed excitation

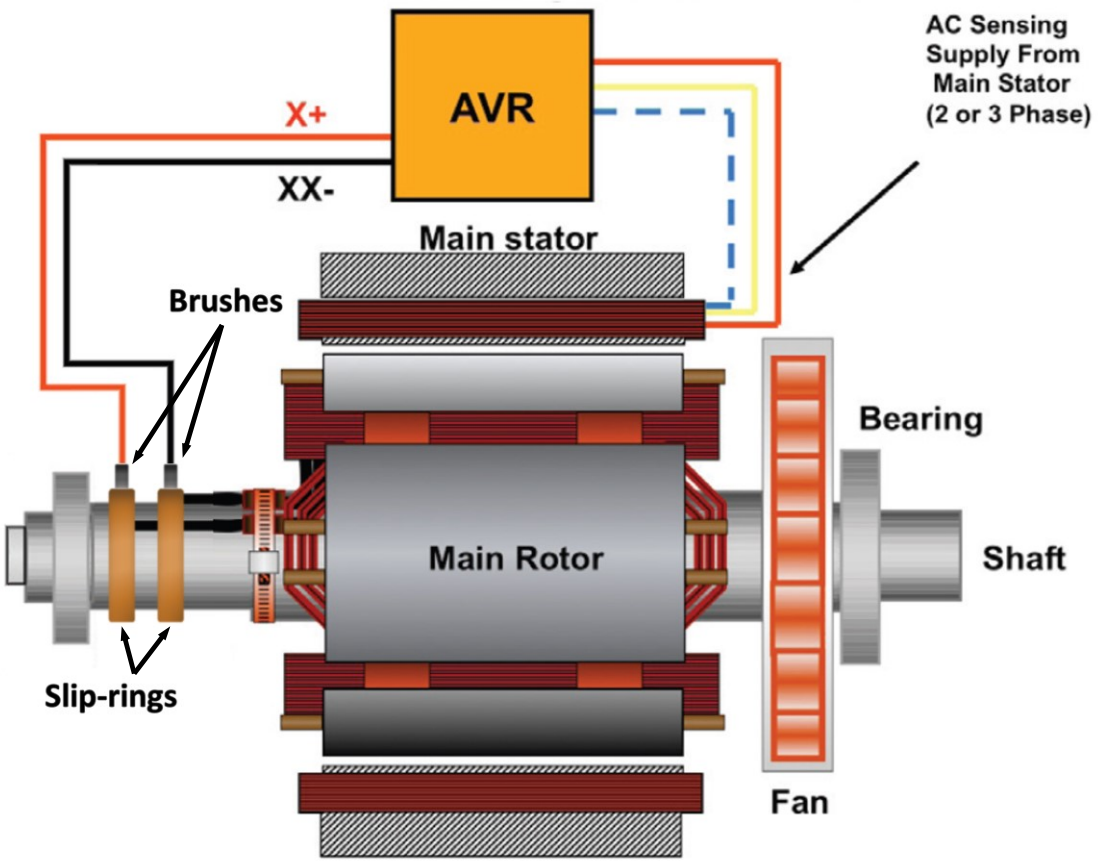

Source: Adaptation from Laliberte (2023)

Brushless excitation systems overcome these challenges. Figure 4 shows a basic schematic of this type of field excitation method. In brushless excitation, rotating and stationary parts do not have direct physical contact and consist of an automatic voltage regulator and a smaller AC generator. The latter is mounted on the same shaft as the main generator and has its armature windings connected to the field windings of the WRSG through a three-phase diode rectifier (attached to its armature). This machine is called main exciter (ME) and has the field windings housed in the stator, whereas the armature windings are in its rotor. The field windings of the main exciter are powered by the automatic voltage regulator with DC voltage, producing a time-constant and stationary magnetic field. This field will induce an AC voltage in the armature windings of the rotor, which is then converted back to DC by the three-phase rectifier circuit connected to the field windings of the WRSG (BOLDEA, 2006).

Figure 4 – Brushless Excitation

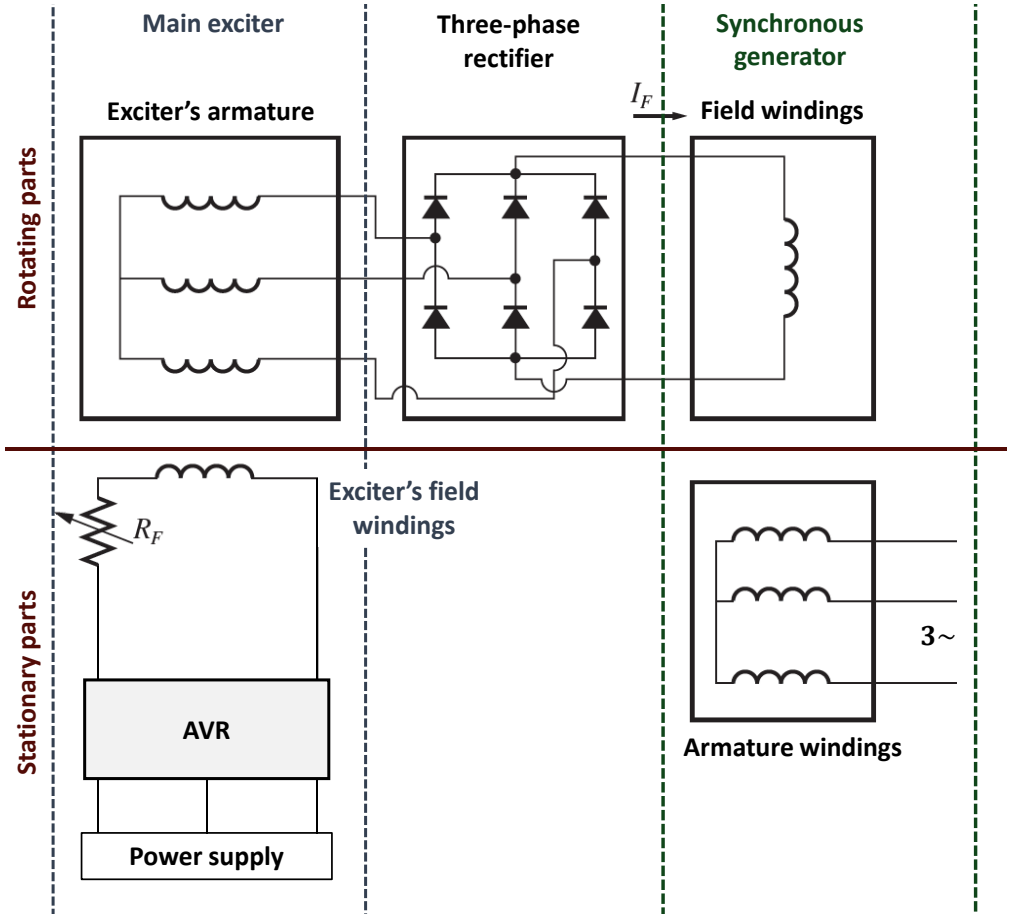

Source: Adaptation from Chapman (2013)

Brushless exciters represent a good solution for applications where the speed of response is not a stringent requirement and require flexible excitation control, limited maintenance, and operational costs, such as standby power, marine, oil and gas, etc. These are mainly passive ohmic-inductive loads, for which AVR response and de-excitation capabilities are not major concerns. As such, they nowadays represent the most common configuration applied by industry in small-to-medium generator sets (ranging from a few kVA to a few MVA) (NØLAND et al., 2019).

2.1.3.1 Automatic Voltage Regulator (AVR)

The AVR is a stationary electronic device that acts upon the DC power supplied to the main exciter to ultimately regulate the SG terminal voltage for a given load. Figure 5 shows a basic configuration of the AVR, the ME, and the WRSG. The control process consists of collecting information on SG current and voltage (I_g, V_g) through sense lines connected to the main machine stator. The AVR can then increase

or decrease the DC power to the field of the ME to, consequently, increase or decrease the AC voltage generated on the ME armature windings. After being rectified, this will result in a bigger or smaller field current (I_f) in the SG rotor (BOLDEA, 2006).

Figure 5 – Exciter with an automatic voltage regulator

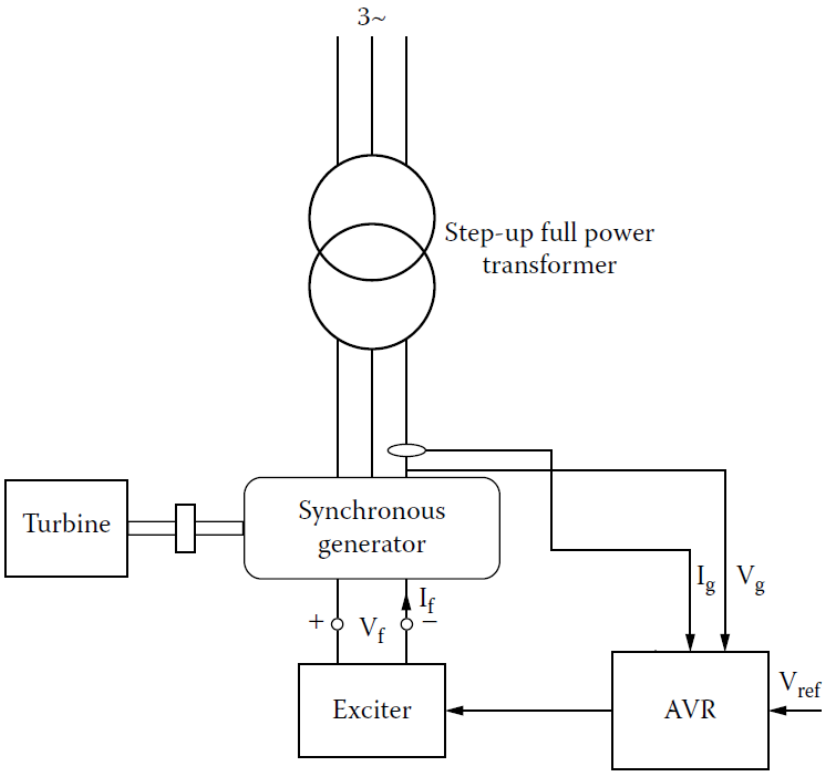

Source: Adaptation from Boldea (2006)

Therefore, the AVR must have a strong power source to be able to provide the appropriate amount of excitation current, especially in a transient situation. Generator set (generator connected to the internal combustion machine as a prime mover) and turbogenerator manufacturers offer different options for providing power to the AVR, each having their own unique features, advantages, and disadvantages that should be taken into consideration according to the application requirements. Without a proper power source, the system may be unable to recover voltage during a start or fault condition, potentially leading to damage or the shutdown of the system.

2.1.3.1.1 Shunt

Shunt is an indirect self-excitation method and the most simple and cost-effective solution, not requiring additional parts or wiring, as Figure 6 shows. It uses the output of the main generator armature to power supply the AVR. This configuration

is directly impacted by the loads the alternator is powering downstream. In isolated generation, when a load is connected/started, or a fault occurs downstream, both voltage and frequency will drop, and the AVR will try to increase the field excitation of the ME. However, with reduced input voltage and frequency, the AVR may not have the capability to support the voltage long enough to bear the transient. Furthermore, when powering a non-linear load, harmonics will cause a power input variation, which will limit the ability of the AVR to provide appropriate output power (MAHON, 1992).

Figure 6 – Indirect self-excited generator (Shunt)

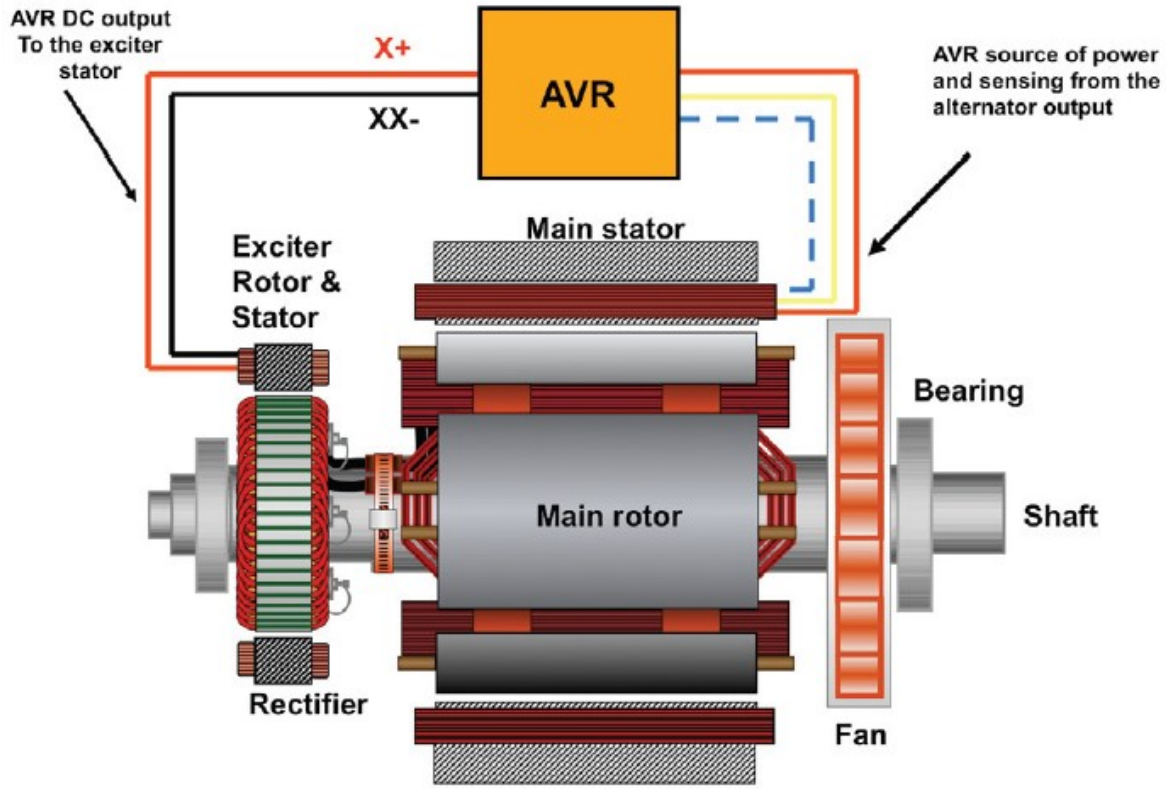

Source: Laliberte (2023)

Nonetheless, this is the cheapest and simplest brushless excitation system, typically used in generator sets rated up to 700 kVA and some in the order of MVA (NØLAND et al., 2019).

2.1.3.1.2 Auxiliary Winding

The auxiliary winding is another indirect self-excitation method, and it consists of a separate single-phase winding inserted into the main stator slots alongside the main output winding. Figure 7 illustrates this excitation configuration. This is a less common solution, suited to power ratings between 4MVA and 15MVA, and has been

used for many years on marine and industrial applications. By using the SG magnetic field to generate power for the AVR, it avoids some issues presented in shunt excitation, with a more sustainable power output less susceptible to harmonics due to non-linear loads, but that still depends on the main machine operating condition (NØLAND et al., 2019).

Additionally, a major limitation of the shunt configuration is that the only power supply comes from the output voltage of the main generator. If this voltage differs from the regulator's supply voltage, a transformer is required. In contrast, auxiliary windings can directly produce the voltage required by the AVR, which eliminates the need for transformers even in a high-voltage generator.

Figure 7 – Indirect self-excited generator (auxiliary winding)

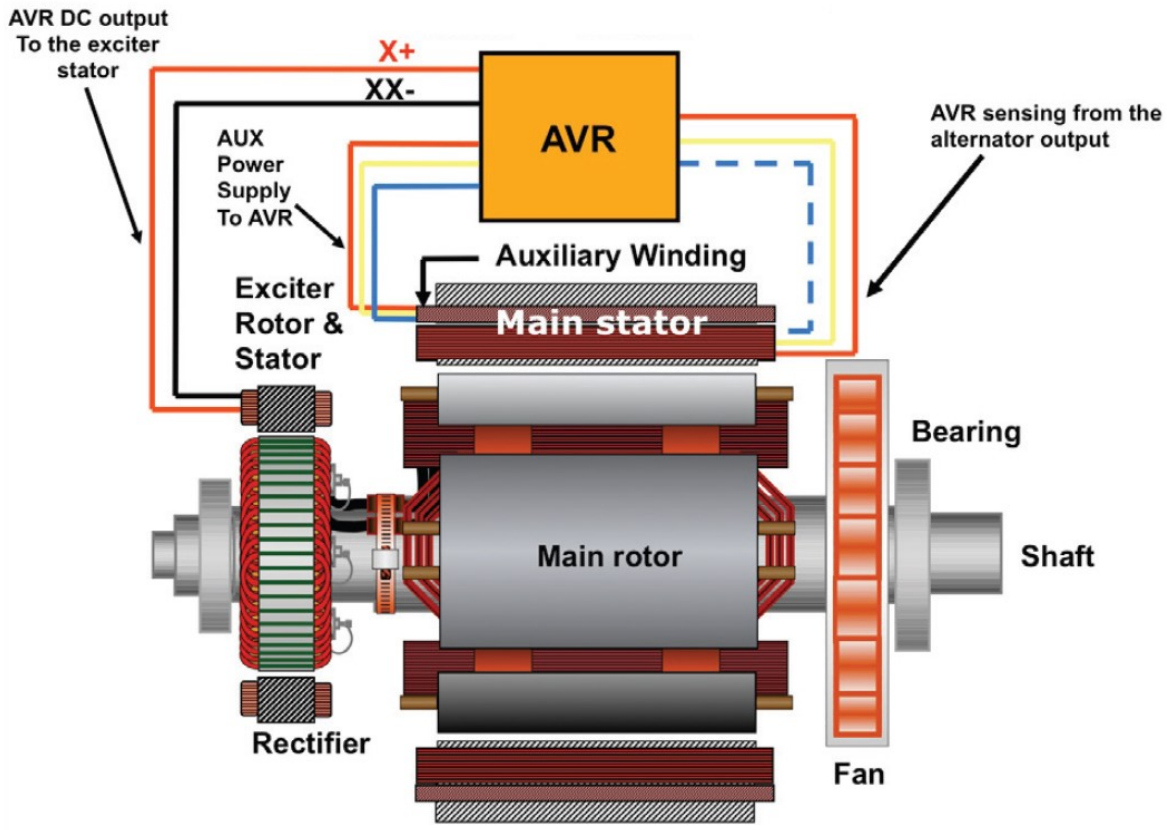

Source: Laliberte (2023)

This is considered a suitable option for demanding applications since the power generated has a certain effect on the voltage input to the AVR but a negligible impact on the performance of the set (MAHON, 1992).

2.1.3.1.3 Pilot Exciter

Using a PMSG to power supply the AVR is one of the most well-known forms of excitation and is also very suitable for demanding applications. This is a separately excited configuration, shown in Figure 8, with an additional small permanent magnet generator, called Pilot Exciter (PE), placed at the end of the WRSG shaft, providing extremely reliable independent power input. Due to its permanent magnets, the PE provides near-constant output voltage under all operating conditions (as long as the shaft is turning at rated speed), including considerable voltage build-up on start-up. Moreover, there are no disturbances in the AVR input power since a clean, uninterrupted 3-phase waveform is produced, and it does not affect the load connected to the main generator (MAHON, 1992).

Figure 8 – Separate excitation (Permanent Magnet Generator)

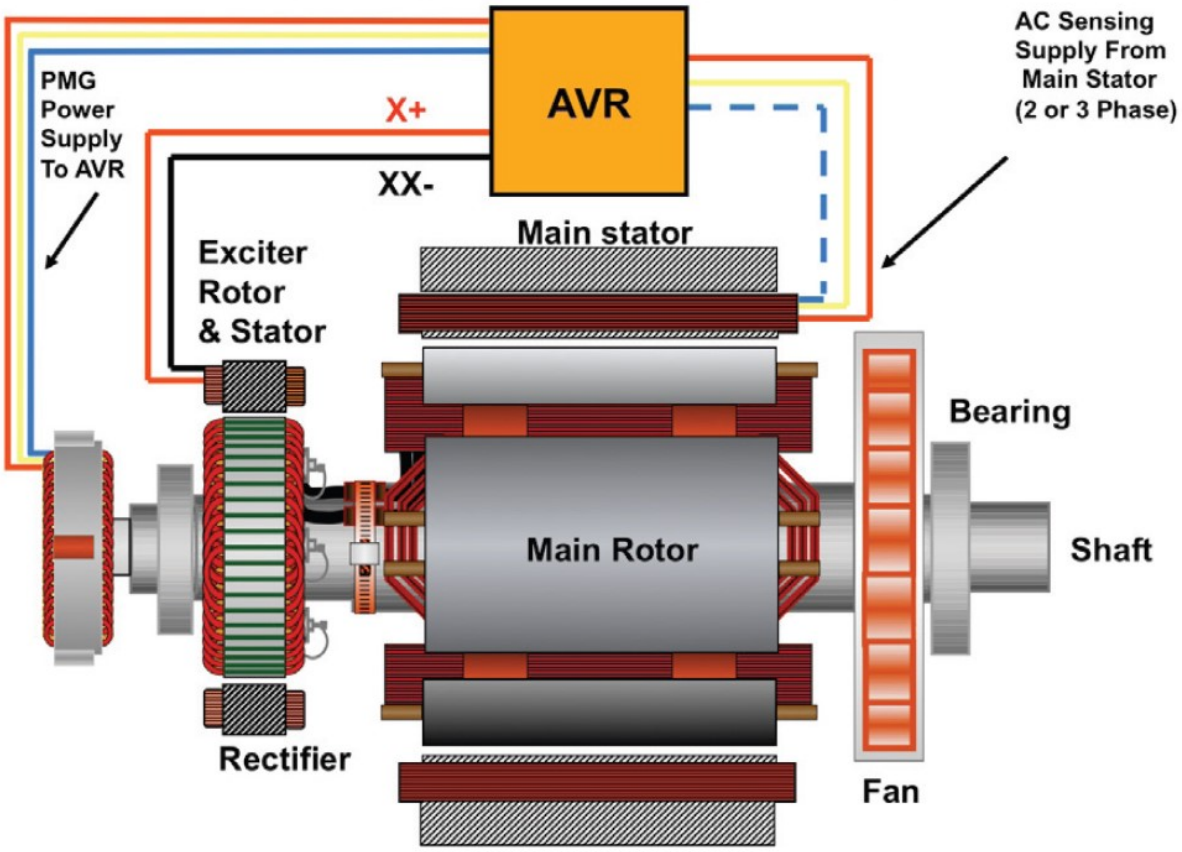

Source: Laliberte (2023)

Thus, with the counterpart of adding length, weight, and complexity to the generating system, performance in general (under starting, fault conditions, selective coordination, and non-linear loads) is superior to either of the self-excited systems.

Overall, it is mostly used in medium-size generator sets (rated between 700 kVA and 4 MVA) (NØLAND et al., 2019).

2.2 Permanent Magnet Synchronous Generators

Permanent magnet synchronous generators do not need DC excitation or even an excitation system to create the main magnetic flux of the machine. PM machines have a greater potential to increase efficiency and can be produced with less active material, which can result in a higher power density when compared to their wound rotor equivalents. All these advantages over the WRSG come with counterparts of elevated PM cost and not being able to adjust the machine terminal voltage for different operating conditions since it is not possible to adjust the intensity of the magnetic field of the permanent magnets (UMANS, 2014).

2.2.1 Principles of Construction

PMSG and WRSG have similar construction, both having the same uniformly slotted laminated stator. Another resemblance is that PMSG rotor can have either a non-salient-pole or a salient-pole construction, depending on how the PM are arranged within the rotor. Furthermore, how these PM are arranged gives the machine different operating characteristics (HENDERSHOT; MILLER, 2010). In general, the magnets are placed on the rotor surface or buried in it. Figure 9 shows the main rotor configurations of permanent magnet machines. In a) is the surface-magnet rotor, and b) is the inset-magnet rotor. Even though both have arc-shaped magnets attached to the rotor surface, the first is a non-salient pole, and the second a salient-pole rotor. Whereas c) and d) are both salient-pole rotors, but the PM are buried with tangential (Spoke) and radial magnetisation, respectively.

Figure 9 – Permanent magnet machine rotors

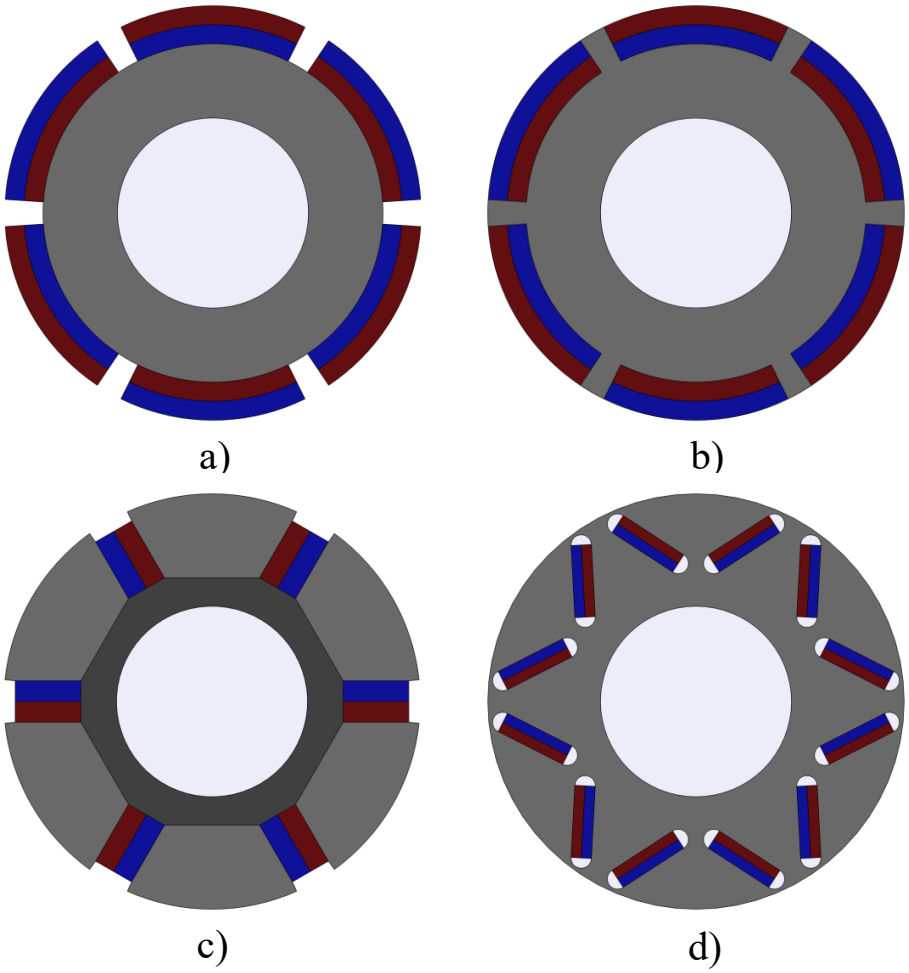

Source: Own authorship (2023)

Surface permanent magnet machines, as shown in Figure 10, are more conventional (HENDERSHOT; MILLER, 2010). In this configuration, the machine is a non-salient one because, despite the presence of magnets providing prominences, the reluctance of the air-gap is constant, regardless of the position of the rotor, as the magnetic permeability of the magnets is very close to that of air.

This type of construction has less mechanical robustness since the magnets attached to the rotor surface are exposed to centrifugal forces (BORISAVLJEVIC et al., 2010). Furthermore, this problem tends to be more significant at high speeds (GERADA et al., 2014). To address this issue, a non-magnetic sleeve to retain the PM on the rotor surface can be used (FANG et al., 2017).

Figure 10 – Surface permanent magnet machines

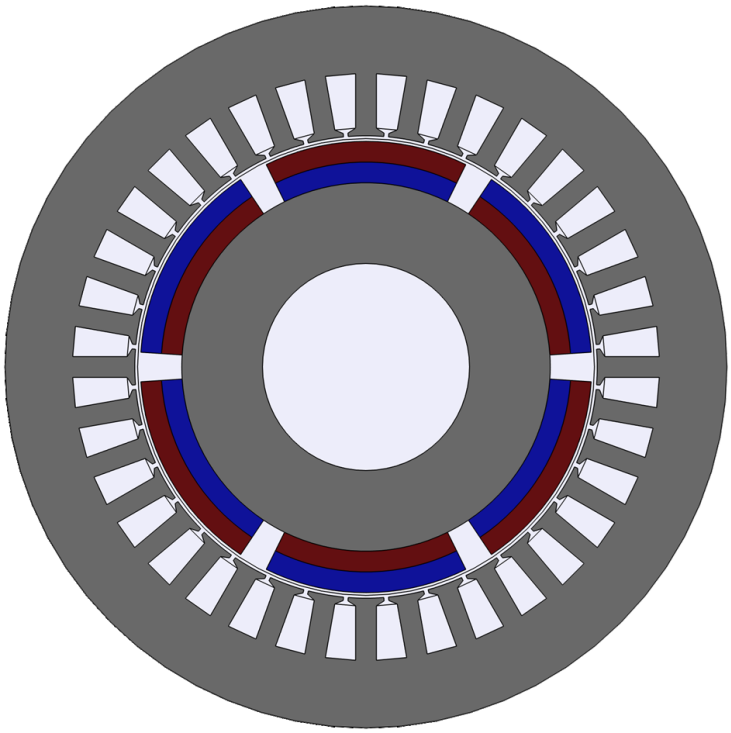

Source: Own authorship (2023)

Interior PM pole rotors are designed to mechanically protect the PM and produce reluctance torque. Even though the rotor surface gives the impression of a non-salient geometry, by placing the permanent magnets inside the rotor, as shown in Figure 11, the machine now has salient poles since the magnetic flux created by the stator experiences paths with different reluctance values in relation to the angular position of the rotor. This rotor configuration has a more complex manufacturing process but allows the use of rectangular magnets, which are simpler to manufacture (BOLDEA, 2006). Unlike surface magnets, buried permanent magnets are less exposed to centrifugal force, which gives the rotor more mechanical robustness.

Figure 11 – Interior permanent magnet machines

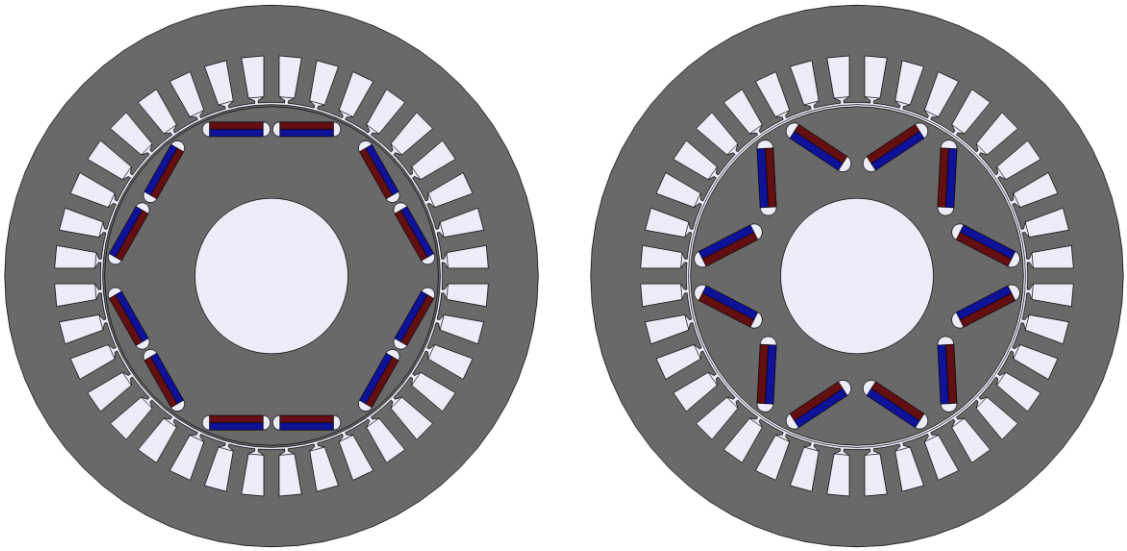

Source: Own authorship (2023)

Non-salient and salient-pole rotors end up producing different values of direct and quadrature axis inductances (MILLER, 2002). The direct axis is the magnetic axis of the rotor, through which the main magnetic flux of the magnets flows, and the quadrature axis is displaced ninety electrical degrees from the direct axis (KRAUSE; WASYNCZUK; SUDHOFF, 2002). Figure 12 shows the axes highlighted in four configurations of permanent magnet rotors. In the red PM, the magnetic flux's direction is towards the rotor's outside, whereas in the blue ones, it is towards the inside.

Figure 12 – Direct and quadrature axis in permanent magnet machine rotors

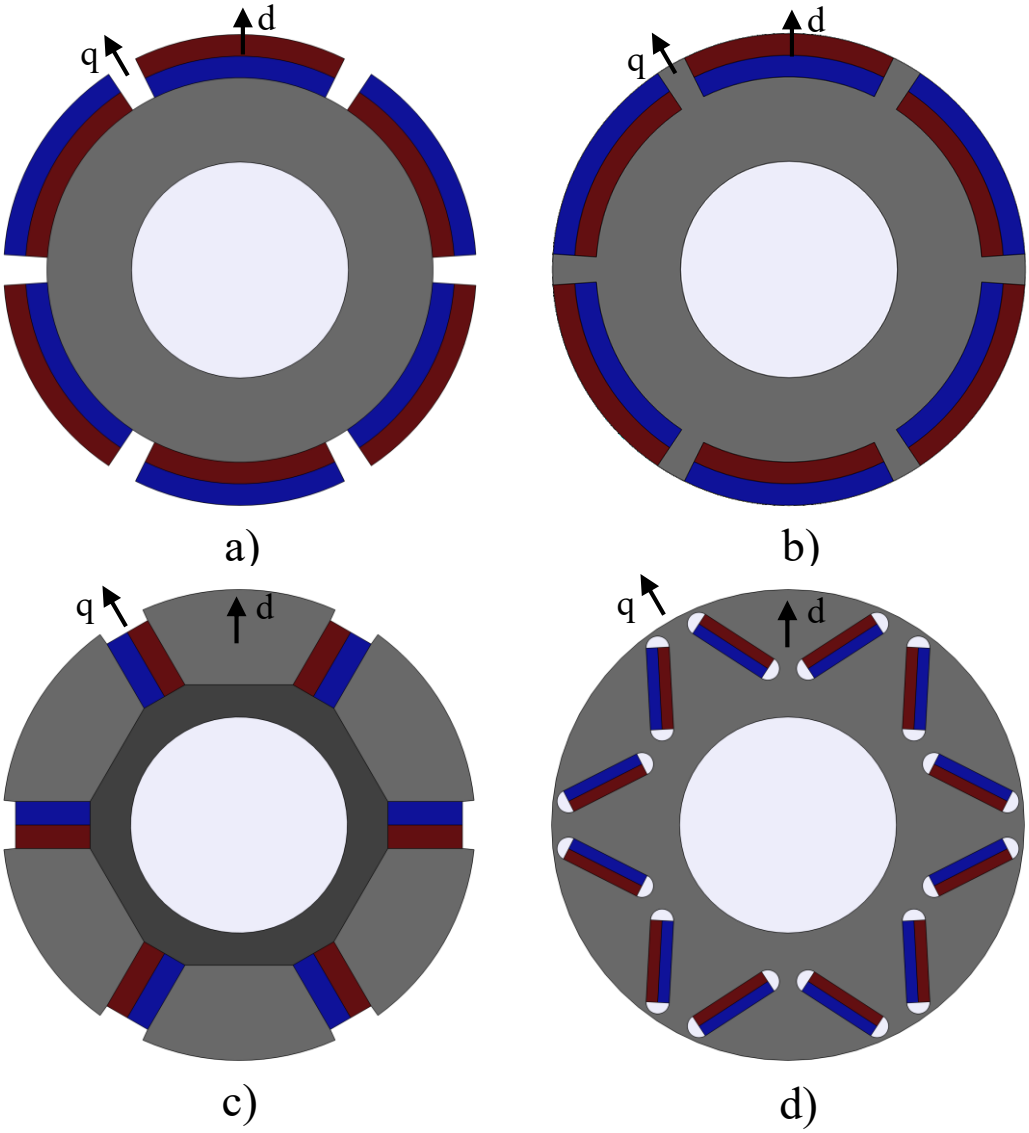

Source: Own authorship (2023)

Considering that the magnetic permeability of permanent magnets is equivalent to that of air, the arrangement of the magnets in the rotor can cause the direct and quadrature axis reluctances to be different. Consequently, the axis inductances may also differ (KRISHAN, 2010). The relationship between inductance L and reluctance $\Re$ is expressed as:

$$L = \frac{\lambda}{I} = \frac{N \cdot \varphi}{I} = \frac{N \cdot F_{mm}}{I \cdot \Re} = \frac{N \cdot N \cdot I}{I \cdot \Re} = \frac{N^2}{\Re} \tag{6}$$

Inductance is the flux linkage of a coil λ divided by the current I that circulates in it. The linkage flux is the magnetic flux of a coil φ multiplied by its number of turns N. The magnetic flux, in turn, is the magnetomotive force F_{mm} (the product of the current by the number of turns in a coil) divided by the reluctance of the magnetic circuit. Reluctance represents the opposition that a magnetic flux encounters when it tries to flow through the material. The reluctance value ($\Re$) of an element is found with:

$$\Re = \frac{l}{\mu_r \cdot \mu_o \cdot S} \tag{7}$$

The reluctance depends on the length l, the relative permeability μ_r and the cross-sectional area S of the element (KRISHAN, 2010). In non-salient pole PMSG, the direct-axis and quadrature inductances are equal, commonly called synchronous inductance, whereas, in salient-pole PMSG, the direct and quadrature reluctances vary depending on how the magnets are arranged, as shown in Figure 12. In V-shaped PM machines (shown in Figure 12d)), the direct axis is the path of greatest reluctance, as the magnetic flux created in the stator passes through the magnets. The reluctance path of the quadrature axis is mainly composed of ferromagnetic material, whose relative permeability is greater than that of air and, thus, is a path of lower reluctance. Therefore, the direct axis inductance is smaller than the quadrature axis since the inductance is inversely proportional to the reluctance (equations (6) and (7)).

2.2.2 Operating Principles

PM synchronous machines follow the same principles of WRSG, i.e., Ampère, magnetic flux conservation, and Faraday's laws. However, the way that the rotor's magnetic field is created with permanent magnets deserves some attention. In general terms, the PMSG performs electromagnetic energy conversion by creating a time-constant magnetic flux with its PM, which is time-varying for the armature windings perspective when the rotor is turning at synchronous speed.

During no-load operation, only the rotor produces magnetic flux. The radial component of the rotor magnetic flux flows through the machine's air-gap, reaching the stator. As stated by magnetic flux conservation's law, flux lines are always a closed path, and so the magnetic flux continues through the stator yoke and returns to the adjacent pole on the rotor. When the SG is connected to a load, current flows in the

armature windings; thus, an armature magnetic field is created (Ampère's law). This distortion and weakening of the main magnetic field due to the armature reaction corresponds to a voltage drop.

In order to explain this interaction and how the terminal voltage is affected, Figure 13 can be used for non-salient machines, in this case, a two-pole machine connected to an inductive load. The PM create the rotor magnetic flux density $\vec{B}_R$ that will induce the no-load voltage $\vec{E}_{Af}$ on the armature windings, 90 degrees behind (considering an anti-clock wise rotation). When a load is connected, the armature current $\vec{I}_A$ will then create an armature reaction field $\vec{B}_{Ra}$, whose magnitude will be proportional to the armature current. The armature reaction flux density is aligned with the armature current, whose angle depends on the load characteristics (inductive or capacitive). Adding $\vec{B}_R$ and $\vec{B}_{Ra}$ vectorially will result in the net magnetic flux density $\vec{B}_N$, from which derives the terminal voltage $\vec{V}_\varphi$, that is also 90 electrical degrees behind the magnetic flux density that originated it.

Figure 13 – Two-pole surface PMSG

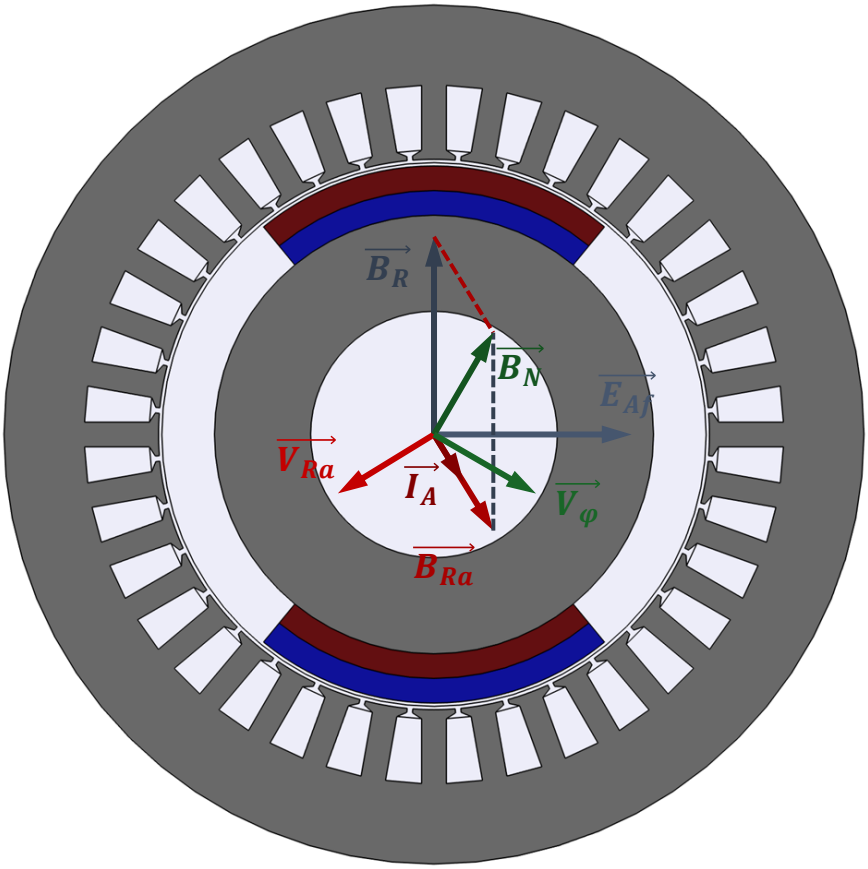

Source: Own authorship (2023)

Since the voltage drop $\vec{V}_{Ra}$ is proportional to the armature reaction field $\vec{B}_{Ra}$, it is also proportional to the armature current $\vec{I}_A$. The relationship between $\vec{V}_{Ra}$ and $\vec{I}_A$ can be expressed using a constant x and the complex operator $-\mathrm{j}$ since the latter is $90°$ lagged (SAY, 1976):

$$\vec{V}_{Ra} = -\mathrm{j}x\vec{I}_A \tag{8}$$

Thus, the terminal voltage could be found with:

$$\vec{V}_\varphi = \vec{E}_{Af} - \mathrm{j}x\vec{I}_A \tag{9}$$

However, in addition to the armature reaction, the armature winding also has a resistance R_A and a leakage inductance L_a, that becomes leakage reactance X_a when multiplied by the synchronous speed of the machine. For non-salient pole PM

machines, since the leakage inductance and the armature reaction field can be electrically represented by reactances, they are usually combined in a single reactance called synchronous reactance X_S (CHAPMAN, 2013):

$$X_S = \mathrm{x} + X_a \tag{10}$$

Finally, the machine's terminal voltage is:

$$\vec{V}_\varphi = \vec{E}_{Af} - \mathrm{R}_A\vec{I}_A - \mathrm{jX}_S\vec{I}_A \tag{11}$$

The same logic can also be applied to salient-pole machines. However, the difference is that for this type of machine, the armature reaction magnetic flux density $\vec{B}_{Ra}$ intensity is affected not only by the armature current value but also by the load characteristics since it can affect the angle of the armature current ($\vec{I}_A$). Considering the salient-pole machine of Figure 14, the machine direct axis has a larger reluctance path than the quadrature axis since the PM has a similar magnetic permeability of the air. Therefore, the magnetic flux density when the armature reaction is along the direct axis is less than if it were directed along the quadrature axis (for the same armature current). Thus, the same phasors that explain the armature reaction for non-salient pole machines should be decomposed in direct and quadrature axes.

Figure 14 – Two-pole interior PMSG phasors

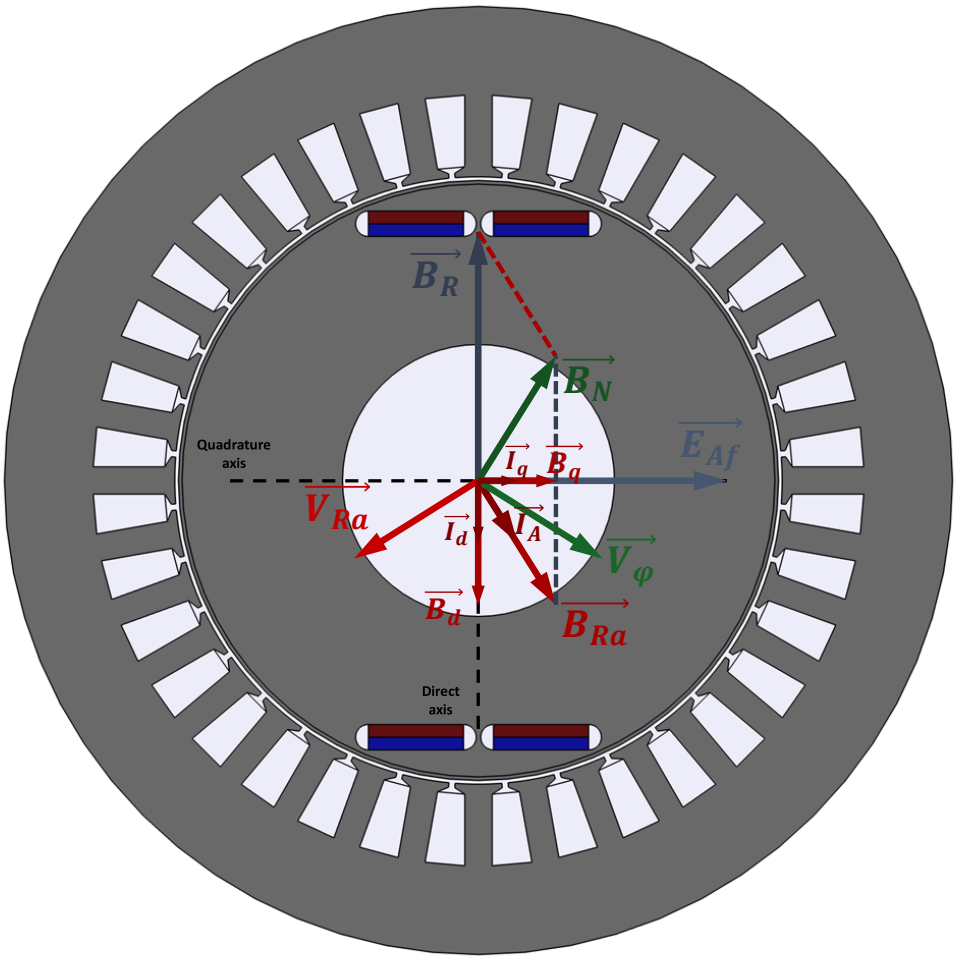

Source: Own authorship (2023)

Each component of the armature current ($\vec{I}_d$ and $\vec{I}_q$) produces a component of the armature reaction flux density ($\vec{B}_d$ and $\vec{B}_q$) which in turn corresponds to a voltage drop in the armature windings. Since the leakage reactance X_a is not affected by the load characteristics, its value can also be combined with the axis reactances, creating the direct axis synchronous reactance X_d and the quadrature axis synchronous reactance X_q:

$$X_d = x_d + X_a$$

$$X_q = x_q + X_a \tag{12}$$

With these and the phasors presented in Figure 14, the phasor diagram of Figure 15 is built, already considering the armature winding resistance R_a, where ϕ is

the displacement angle between the terminal voltage and the armature and δ is the load angle.

Figure 15 – Salient-pole machine's phasor diagram

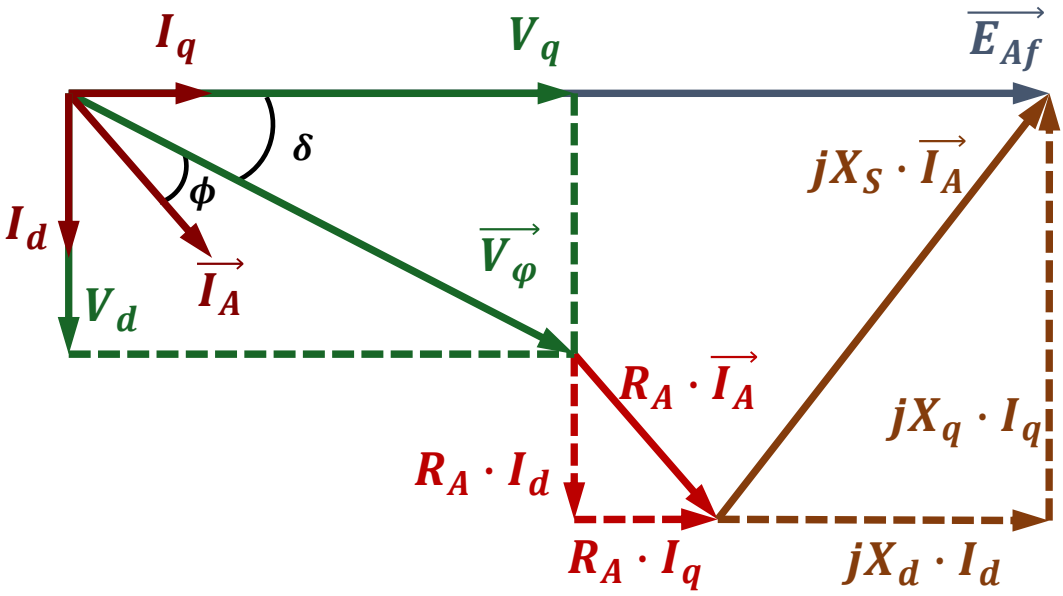

Source: Adaptation from Bazzo, Moura and Carlson (2021)

From Figure 15, the following relations can be established:

$$I_d = I_A \cdot \sin(\phi + \delta) \tag{13}$$

$$I_q = I_A \cdot \cos(\phi + \delta) \tag{14}$$

$$V_d = X_q \cdot I_q - R_A \cdot I_d \tag{15}$$

$$V_q = E_{Af} - X_d \cdot I_d - R_A \cdot I_q \tag{16}$$

$$V_{\varphi} = \sqrt{{V_d}^2 + {V_q}^2} \tag{17}$$

From these equations, it is clear that to obtain the terminal voltage $\vec{V}_{\varphi}$, the armature current components (I_d and I_q) should be known, and they depend on ϕ and δ. The displacement angle between the terminal voltage and the armature current can be easily found since it is the arc cosine of the machine power factor, which is a design specification (PYRHÖNEN; JOKINEN; HRABOVCOVÁ, 2008). The load angle, however, is not immediately seen through Figure 15 but can be found with (BAZZO; MOURA; CARLSON, 2021):

$$\delta = \tan^{-1} \frac{I_A \cdot X_q \cdot \cos\phi - I_A \cdot R_A \cdot \sin\phi}{I_A \cdot X_q \cdot \sin\phi + I_A \cdot R_A \cdot \cos\phi + {V_{Td}}/{\sqrt{3}}} \tag{18}$$

In equation (18) V_{Td} is the desired terminal voltage, a design specification. The above equations can be solved once the direct and quadrature axis synchronous reactances are known. Therefore, an essential step of a salient-pole synchronous generator design, either wound-rotor or permanent magnet, is obtaining these reactance values. In a reminder note, the developed analysis (from equation (8) to equation (18)) does not consider the harmonic content of a real operating condition, only the fundamental components.

2.2.2.1 Permanent Magnets

Permanent magnets produce a magnetic field in the PMSG air-gap and can be described through their B-H hysteresis loop, a magnetic flux density B curve as a function of the field strength H. The relationship between the field intensity and the magnetic flux density of the magnets is not linear, as Figure 16 shows. Permanent magnets have a wide hysteresis loop and, therefore, they are called hard magnetic materials (GIERAS; WILL, 2002).

Figure 16 – Permanent magnet BH characteristic curve

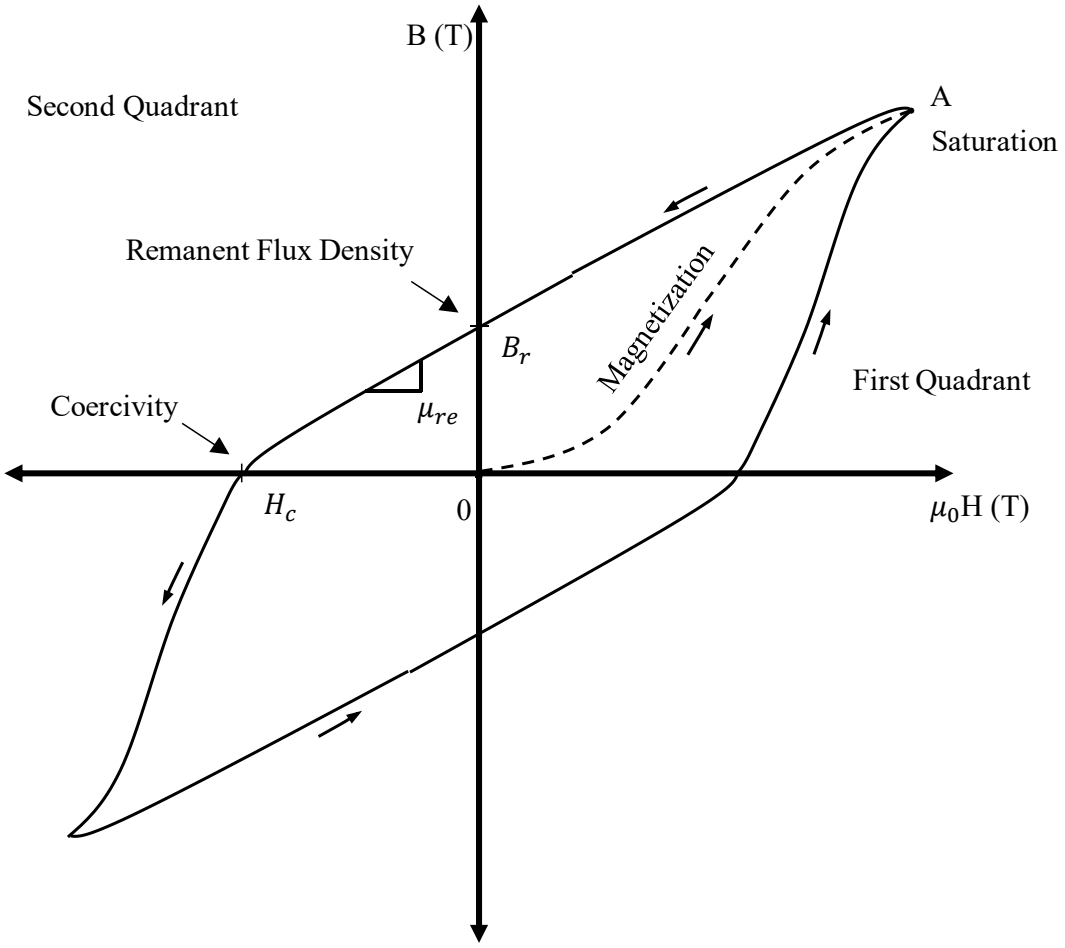

Source: Adaptation from Miller (2002)

When a sample of ferromagnetic material is completely demagnetised, its magnetic induction and magnetic field are zero (point 0 in Figure 16). When exposed to an external magnetic field whose intensity gradually increases, the first magnetisation curve is formed (curve 0A), the induction rises and goes up to the saturation point, when the intrinsic magnetisation reaches its maximum value (point A in Figure 16) (FRATILA, 2014). When the external field is extinguished, the ferromagnetic material of the permanent magnet "relaxes" and travels along the curve (in the direction of the arrows).

If the permanent magnet is surrounded by a highly permeable magnetic circuit (as if its poles were shorted together), then its magnetic flux density is the remanent magnetic induction (point B_r in Figure 16), which is the maximum flux density that the permanent magnet can retain. In a practical magnetic circuit, as in a permanent magnet machine, the PM operating point (H, B) is on the curve of the second quadrant and will depend on the PM shape and the permeance of the surrounding magnetic circuit

(KRISHAN, 2010). The operating point moves, up or down, in the straight part of the curve, always following the constant slope of the demagnetisation curve, called recoil permeability (μ_{re}). To bring the magnetic flux density from the remanent point to zero, an external magnetic field with an opposite magnetisation direction of the magnet is required to produce an opposing magnetic force (point H_c in Figure 16) called coercivity (MILLER, 2002).

The straight line that could be drawn from the operating point to the origin is known as the load line, and its slope is called the permeance coefficient (PC), shown in Figure 17 (HENDERSHOT; MILLER, 1994). The shape of the demagnetisation curve depends on the PM material and the operating temperature. For rare-earth magnets, the demagnetisation curve shrinks towards the origin for higher temperatures, creating a “knee” for low magnetic flux density values, as shown in Figure 17. For room temperatures, high-performance magnets such as Samarium-Cobalt and Neodymium-Iron-Boron have straight lines in the second quadrant, whereas ferrite magnets have a knee where the curve approaches coercivity (HANSELMAN, 2003).

Figure 17 – Demagnetisation curve and permeance coefficient and temperature influence

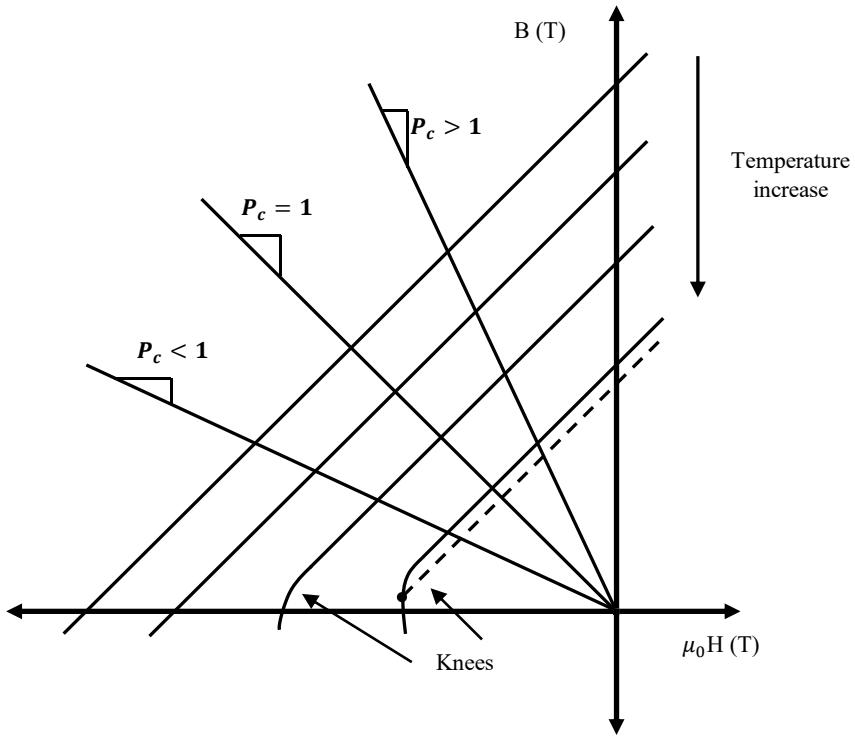

Source: Adaptation from Hanselman (2003)

Figure 17 shows that the decrease in the permeance coefficient causes the magnet to operate with a lower magnetic flux density, producing less magnetic flux. For PM operating at higher temperatures and having the knee, operating with a low permeance coefficient value (low flux density) may represent a risk of permanent demagnetisation. This is because, since the recoil permeability is unchanged, once the PM operates at the knee of the demagnetisation curve, it no longer returns to its original remanent induction but instead to a lower value, as shown in the dotted line in Figure 17 (HENDERSHOT; MILLER, 2010).

A complete understanding of the characteristic curve of PM is essential for the PMSG design. Because it is linked to the modelling of the machine's magnetic circuit, determining the permeance coefficient plays an essential role in the machine design, as it defines the magnetic flux density at which the magnets operate. Surrounding a PM with a ferromagnetic material and adding an air-gap, the magnetic circuit is represented in Figure 18.

Figure 18 – Magnetic circuit with a permanent magnet

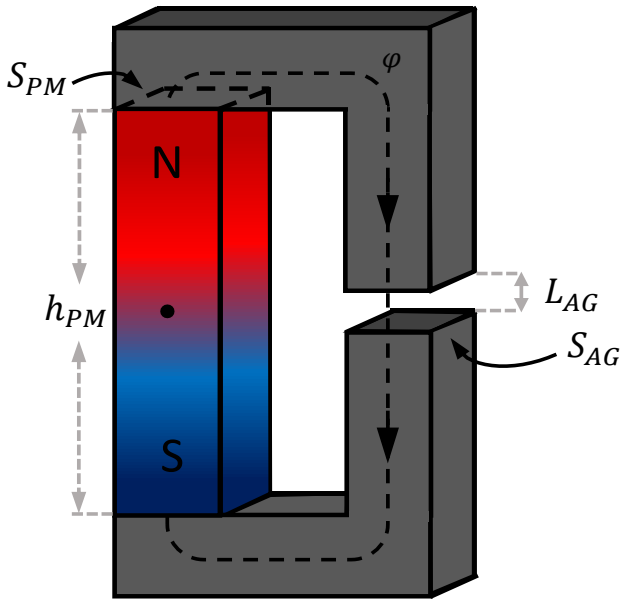

Source: Adaptation from Hanselman (2003)

Applying Ampère's law to this circuit (HANSELMAN, 2003):

$$\oint Hdl = H_{PM} \cdot h_{PM} + H_{ES} \cdot L_{ES} + H_{AG} \cdot L_{AG} = 0 \tag{19}$$

where H_{PM} and h_{PM} are the magnitude of the magnetic field in the magnet and its height, respectively, and similarly, H_{AG} and L_{AG} are the field and length of the air-gap. The relative magnetic permeability of electrical steel (μ_{rES}) used in electric machines is thousands of times greater than that of air (μ_0); therefore, the product of the field in the electrical steel and its length ($H_{ES} \cdot L_{ES}$) can be disregarded (MILLER, 2002). Thus, the magnetic flux in the magnet can be defined as:

$$H_{PM} = -\frac{H_{AG} \cdot L_{AG}}{h_{PM}} \tag{20}$$

According to the law of magnetic flux conservation, the flux densities in the magnet and the air-gap are related according to the following:

$$B_{PM} \cdot S_{PM} = B_{AG} \cdot S_{AG} \tag{21}$$

where S_{PM} and S_{AG} are the cross-sectional areas of the magnet and the air-gap, respectively. Therefore, as $B_{PM} = \mu_0 H_{PM}$ and $B_{AG} = \mu_0 H_{AG}$, we have:

$$\frac{B_{PM}}{H_{PM}} = -\mu_0 \frac{h_{PM} \cdot S_{AG}}{S_{PM} \cdot L_{AG}} = -\mu_0 \cdot PC \tag{22}$$

Although these equations are developed based on the circuit in Figure 18, they can be extended to more complex circuits, such as that of electrical machines. For permanent magnet machines, the air-gap and magnet areas (S_{AG} and S_{PM} respectively) have very close values and flux leakage is relatively low, which allows neglecting the division of the air-gap area by the magnet area. Thus, the permeance coefficient would be reduced to the relationship between the magnet height and the length of the air-gap in its magnetic circuit:

$$PC = \frac{h_{PM}}{L_{AG}} \tag{23}$$

As PC indicates the magnetic flux density produced by the magnet (operating point on the demagnetisation curve), it directly impacts the air-gap flux density, which

highly affects the no-load voltage. Also, this coefficient significantly affects the machine power density, as it determines the volume of magnets (by defining its height) necessary for the generator to produce a certain amount of power.

3 PERMANENT MAGNET GENERATOR DESIGN

The design of any rotating electrical machine starts with defining a few basic characteristics, such as the machine type (i.e., asynchronous, synchronous, DC reluctance machines, etc.) and type of construction (external rotor, internal rotor, axial flux, radial flux machine, etc.).Thereafter, the first step of the design consists of defining the specifications of the generator, such as apparent power, the desired power factor, rated angular speed, rated frequency, rated terminal voltage, and the number of phases of the machine (PYRHÖNEN; JOKINEN; HRABOVCOVÁ, 2008).

Considering that the designed machine is the pilot exciter of the excitation system of a wound-rotor synchronous generator, these specifications will be determined according to the automatic voltage regulator needs and the main generator characteristics. An intrinsic feature of the pilot exciter is that it is mounted on the main generator shaft, so its angular speed is obviously the same. Along with the rated input power frequency of the AVR, this angular speed will determine the number of poles of the PMSG. Thus, the remaining design specifications are strictly tied to the AVR needs. Additional information, such as efficiency and manufacturing details, should also be considered during the design process.

Using this information, it is possible to design the electrical machine, i.e., obtain its physical dimensions, define material properties, windings characteristics, and draw manufacturing instructions. Even though the specifications can be the same for different types of machines, a design procedure does not apply to all types of machines. Therefore, adaptations to well-established methodologies to better adapt to the particular needs of the designer become interesting (HENDERSHOT; MILLER, 2010). Thus, the proposed design methodology for surface-mounted PMSG is based on the design procedure developed by Bazzo, Moura, and Carlson (2021) for designing salient-pole WRSG. In this methodology, the design is divided into no-load and full-load designs. Figure 19 shows the flow chart from this methodology.

Figure 19 – Flow chart of the WRSG design methodology

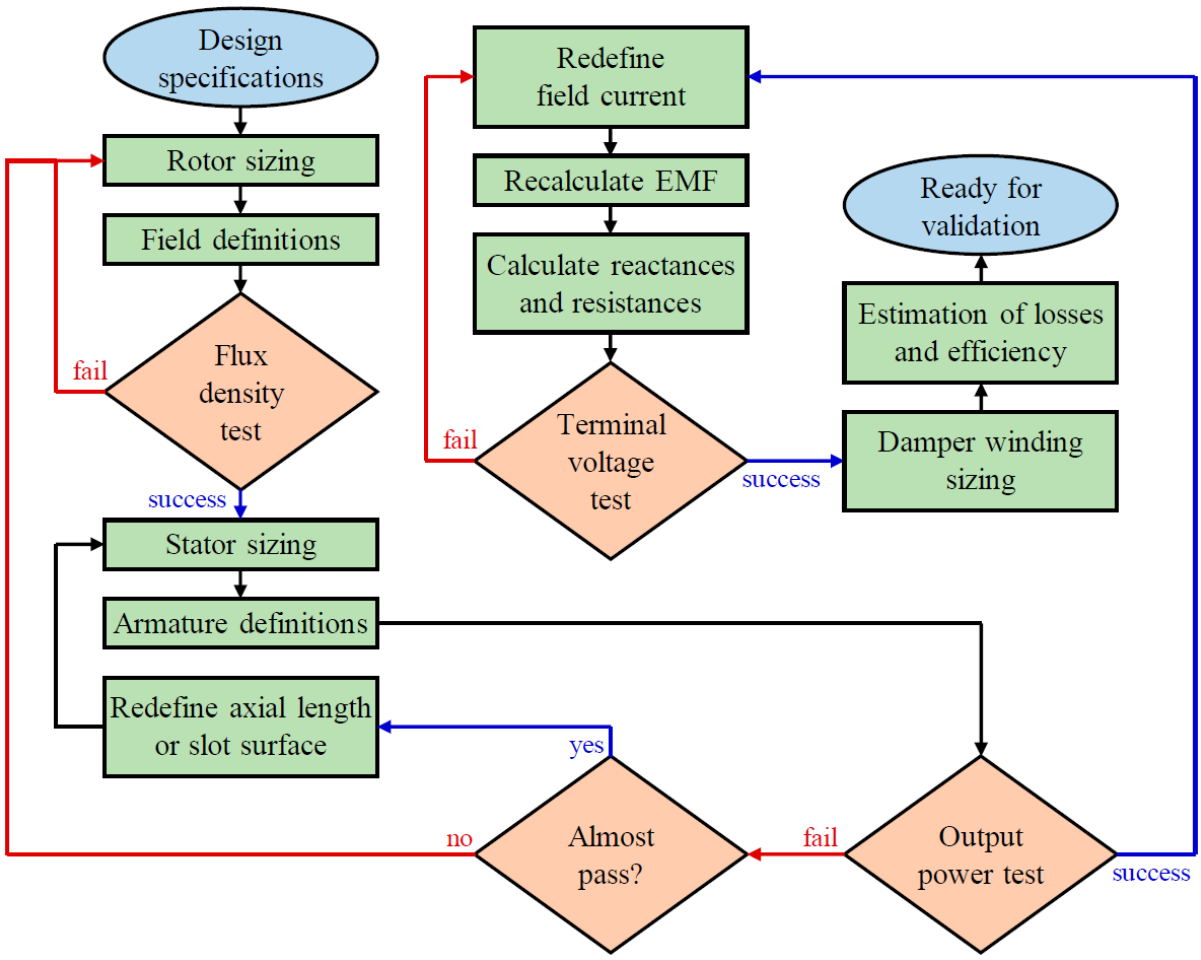

Source: Adaptation from Bazzo, Moura, and Carlson (2021)

Naturally, the no-load design is the first part, where rotor and stator dimensions are calculated from the design specifications. At the very beginning of this design methodology, the rotor outer diameter is defined since it is assumed to be an input parameter known by the designer, either from a previous calculation or by experience. With the rotor geometry completed, the field winding total surface can be found to obtain the number of turns of the field coils and ultimately calculate the field produced in the rotor. If the magnetic flux density in the rotor pole body is within the desired range, the design proceeds to stator sizing.

By dimensioning the stator slots, its total area will be used to estimate the armature current, considering a maximum conductor current density previously set. With the desired terminal voltage value, a number of turns per coil to meet this design requirement is chosen, and with the slot surface found, the conductor surface is calculated. With both conductor surface and current density, the armature current is obtained. Then, the output power can be obtained with both the desired terminal

voltage and armature current values as a final step of the no-load design. If this value does not correspond to the apparent power from the specifications, a few parameters can be adjusted, either from rotor or stator sizings.

Since the terminal voltage is a design specification, output power adjustments must be made in the armature current. For minor differences, this can be done by increasing the machine's stack length, or the slot geometry should be altered. Increasing its area allows more armature current by increasing the wire cross-section while keeping the same current density. If more significant changes are necessary, the rotor outer diameter should be adjusted since the rotor magnetic flux does not correspond to the desired output power. Alternatively, the armature current density could be altered, but this value is usually chosen to guarantee operation under maximum temperature or given by a thermal model.

After passing the output power test, the full-load design can be initiated. As explained in section 2.2.2, during load operation, the armature current creates a magnetic field that interacts with the rotor magnetic field, resulting in distorted net magnetic flux density and decreasing or increasing its value, depending on the load. This will correspond to a smaller or bigger terminal voltage (with inductive and capacitive loads, respectively). To accurately calculate the machine terminal voltage, the armature resistance and the axis reactances must be obtained. The first is easily calculated, depending only on the armature conductor’s characteristics. However, since salient-pole machines have a very complex air-gap geometry, analytically calculating the direct and quadrature axis reactances leads to inaccurate results (HENDERSHOT; MILLER, 2010).

Therefore, two other methods remain feasible: reluctance networks and finite element simulations. Reluctance networks are magnetic circuits that model the magnetic flux paths of electromagnetic devices. Thus, it can provide the flux linkage for a certain rotor position (aligned with the direct or quadrature axis), and, using equation (6), it could be used to find the axis inductance and, consequently, the reactance. Through finite element simulations, an inductance curve as a function of rotor position can be extracted, and the direct axis inductance will be half of the maximum inductance value and the quadrature axis inductance half of the minimum inductance value (JONES, 1967).

Since finite element simulation is a highly precise reactance-obtaining method, it is the one used in the design methodology developed by Bazzo, Moura, and Carlson

(2021). With the no-load induced voltage, axis reactances, and armature resistance, the terminal voltage can be found with equation (17). To precisely match the calculated terminal voltage with the specified one, the field current (which has been chosen underestimating the field conductor's capacity at the no-load design) can be adjusted. After this verification, all generator geometry has already been defined, leading to the sizing of the damper winding. As a final step, a loss estimation is made, calculating field and armature windings copper losses, and iron losses of the machine stator. Finally, to confirm that the design specifications are met, a final finite element simulation can be performed.

Naturally, WRSG and PMSG have not only different construction but also different field excitation methods. As a result, the proposed method differs from the one described for WRSG. Methodology-wise, the main difference is in the number of turns of the armature per phase calculation since now it requires an iterative process to be found, whereas, geometry-wise, the stator sizing remains basically the same, but the rotor sizing had to be developed from scratch.

The following subsections address surface-mounted PMSG. Section 3.1 shows the generator cross-section in detail, as well as all its parameters. Section 3.2 discusses the surface-mounted PMSG design procedure and explains its stages, steps, tests, and iterative processes. Finally, Section 3.3 describes the parameters imposed throughout the design procedure of the non-salient pole generator to find the complete geometry, armature winding characteristics, and losses, providing suggested ranges as a guideline for others to replicate and complete a PMSG design. Section 3.4 presents an alternative salient-pole PMSG topology that can also be designed with the proposed design method.

3.1 PMSG Topology and Geometry Parameters

The proposed procedure was developed for surface-mounted permanent magnet generators, which can be seen in Figure 20, which is considered a very conventional rotor topology in the literature (HANSELMAN, 2003). However, it can also be adapted to other PM machines. In order to do that, in the rotor sizing, equation (29) and the remaining of the rotor sizing would be slightly different for a straight PM rotor, and additional equations would have to be included eventually. Changes in the rotor geometry require a different phasor diagram than the one presented in Section 3.2.8 for the surface PM machines. They shall be similar to the one developed for salient-

pole PM machines in Section 2.2.2 (Figure 15). An example of a different PMSG geometry that can also be designed with the proposed method is presented in Section 3.4.

The main geometric parameters of the surface-mounted PM generator depicted in Figure 20 are organised as follows: Figure 20a shows the diameters and air-gap length; Figure 20b shows the full and effective pole pitches, the slot pitch, the slot angle at the top and the stator yoke height; the rotor dimensions are shown in Figure 20c; and the stator topology in Figure 20d.

Figure 20 – Main geometric parameters of the non-salient pole PMSG: a) diameters and the air-gap, b) main angles and stator yoke, c) PM pole dimensions, and d) slot dimensions

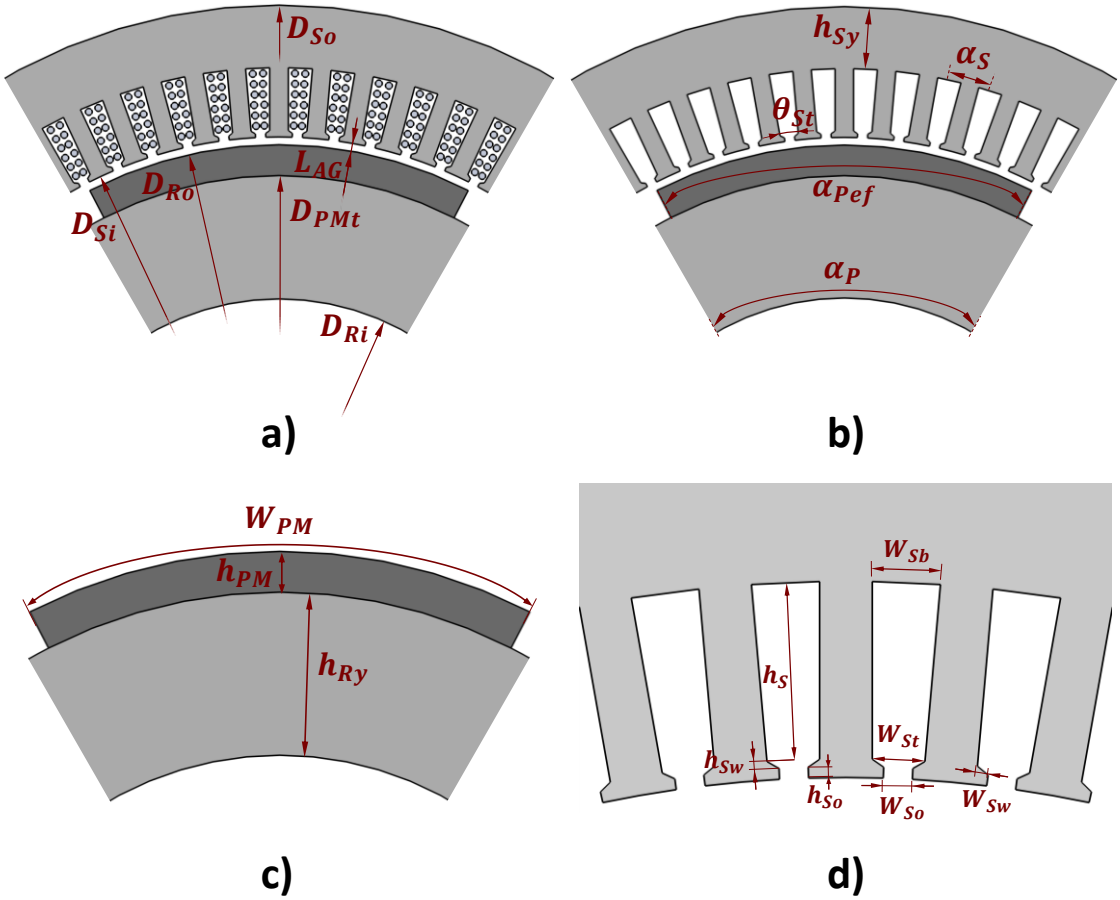

Source: Own authorship (2024)

3.2 Proposed Design Methodology

The proposed design methodology is composed of 66 analytical equations, and its general flowchart is shown in Figure 21. From the specifications, the majority of the generator dimensions are calculated with analytical equations, and the

remaining dimensions are found using parameters imposed by the designer. The proposed method is an iterative design procedure that allows adjustments on dimensions and parameters so that the calculated values match the design specifications in a very straightforward manner. The iterations within the procedure happen with the flux density, output power, and terminal voltage tests. Furthermore, the rectangular blocks in the flowchart of Figure 21 represent the design stages of the procedure, and each one has a subsection dedicated to explaining its steps. Every stage is composed of a set of equations (steps), and their numbers can be seen in the right corner of their stage in Figure 21.

Figure 21 – Flow chart of the PMSG design methodology

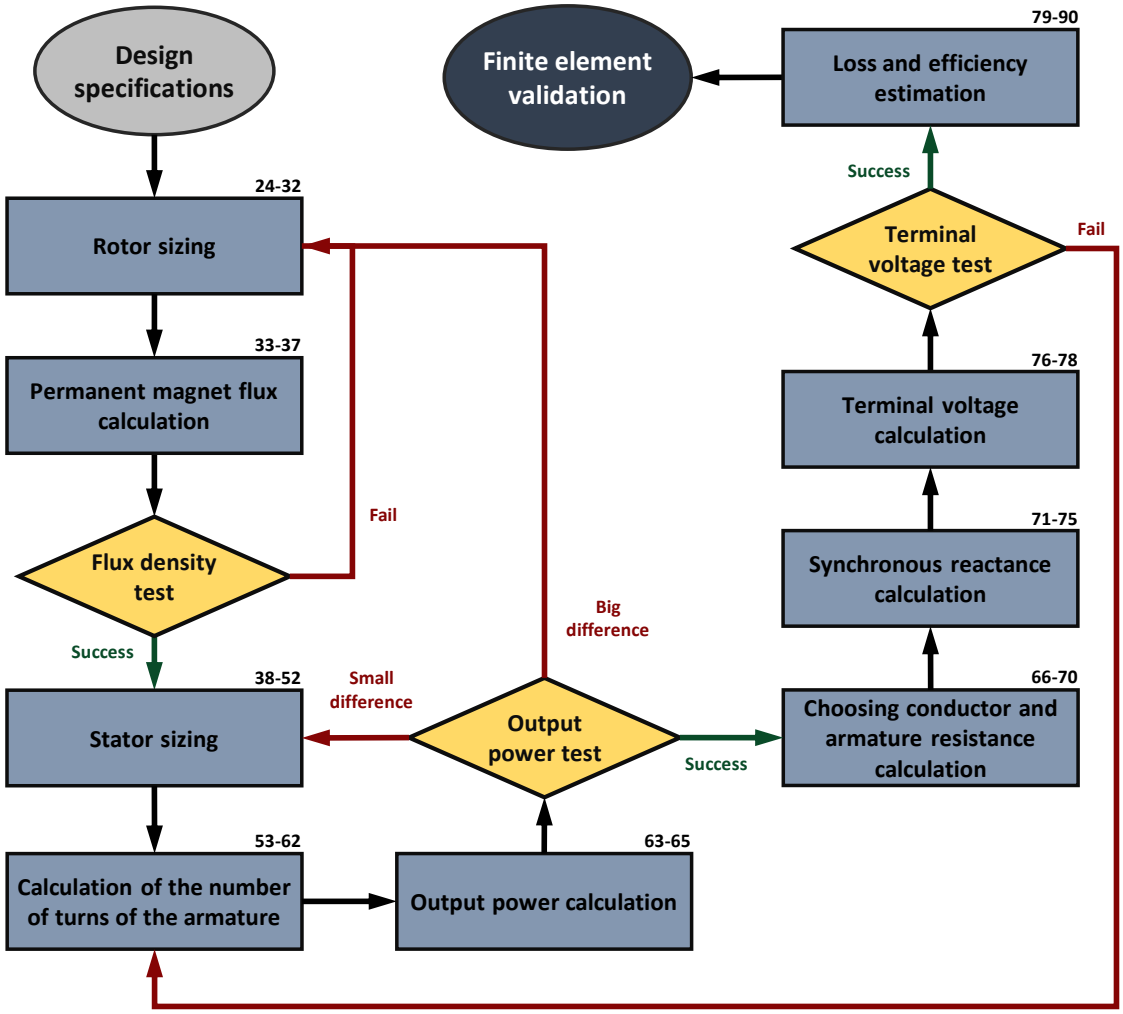

Source: Own authorship (2024)

As shown in Figure 21, the proposed design procedure begins with the specifications, followed by sizing the rotor and stator to find all their dimensions. In the

rotor sizing (Subsection 3.2.1), the first steps depend on defining the rotor external diameter. This design methodology considers it an input parameter known by the designer, either from a previous calculation (which can be guided by bibliography materials such as Pyrhönen, Jokinen, Hrabovcová (2008) and Hendershot, Miller (2010)) or by experience. The remaining rotor dimensions, such as PM dimensions and rotor internal diameter, are found using a few imposed parameters and with the desired magnetic flux density in the rotor core, respectively.

Knowing all PM dimensions and after defining the PM type, operative temperature, and permeance coefficient, the design proceeds to PM flux calculation (Subsection 3.2.2), as Figure 21 shows. Thus, with the air-gap length and the generator axial length, the magnetic flux in the air-gap is calculated and used to find the air-gap flux density. If this magnetic flux density is not within the desired range, the PM permeance coefficient can be increased or decreased to have more or less magnetic flux density in the air-gap, respectively. Another solution would be changing the PM grade, which is a specification that indicates its maximum energy product. However, higher grades also mean higher PM costs (HANSELMAN, 2003).

According to Figure 21, with an acceptable air-gap flux density, the design proceeds to stator sizing (Subsection 3.2.3), where a few imposed parameters are used once more, and stator teeth and slot dimensions are found. Then, the armature windings are defined (Subsection 3.2.4), with the armature conductor surface being the final obtained parameter. Based on the magnetic flux on the air-gap previously calculated, a number of turns per coil of the armature winding is found using an imposed no-load voltage value. With the slot surface and the number of turns, the armature conductor surface can be found. Considering a previously set maximum conductor current density, the conductor surface is then used to obtain the armature current.

As shown in Figure 21, the next step is the output power calculation. By using the desired terminal voltage value and the armature current from the previous step, the admissible output power can be calculated (Subsection 3.2.5). Even though the specified terminal voltage value is used, this is not an inconsistency of the proposed design methodology since the procedure is only completed after matching the calculated terminal voltage value with the specifications (explained further in this subsection). Calculating the admissible output power at this early stage of the

procedure allows the designer to assess if the machine's latest size and dimensions correspond to a solution not too far from the desired output power.

If this value does not correspond to the apparent power from the specifications, a few parameters can be adjusted, either from rotor or stator sizings, as depicted in Figure 21. Since the terminal voltage is a design specification (meaning its value is fixed), output power adjustments must be made targeting the armature current by changing the conductor cross-section, either by changing the slot dimensions or reducing the number of turns of the windings. Since in this design methodology the stator sizing defines an armature conductor that can be fitted in the slots, for minor differences, this can be done by adjusting the machine's stack length or the slot geometry.

For example, increasing the generator length would result in more flux linked by the armature coils; thus, fewer turns are required to match the terminal voltage, and consequently, a bigger conductor cross-section may be used. Ultimately, this results in a bigger value of admissible current while maintaining both the same slot area and specified current density. On the other hand, increasing the slot area directly allows a bigger conductor surface when maintaining the number of turns in the armature coils. Thus, more armature current is admissible while keeping the same current density. Evidently, this logic can be applied when adjustments must be made to decrease the admissible output power of the generator.

If the admissible power is too far from the specified value, more significant changes are necessary. In this case, parameters in the rotor sizing should be adjusted since the current PM volume does not produce the magnetic flux that, when linked by the armature coils, corresponds to the desired output power. Either the PM magnetic flux is less than needed, and more turns are required, which reduces the conductor surface, or too much magnetic flux is produced and needs fewer turns to match the imposed voltage value, which allows a bigger conductor. In this case, the rotor outer diameter or the effective pole pitch can be adjusted. The latter must be more carefully altered since it greatly impacts flux leakage. It is not recommended to alter the armature current density since this value is usually chosen to guarantee operation under maximum temperature or given by a thermal model.

The proposed method has a noteworthy differential from other design methodologies concerning the output power calculation and the iterative process discussed previously. As seen in Figure 21 and explained earlier in this subsection,

the proposed design comes from rotor sizing to stator sizing, where the slot area is defined; then, with the number of turns of the armature coils, the conductor cross-section that can be fitted within the slots is calculated, then the armature current is found and, consequently, the admissible output power is found. In other design methodologies (Hebala, Ghoneim, and Ashur (2019) and Yazdanpanah, Afroozeh, Eslami (2022), for example), this part is inverted, where, with the specified output power and terminal voltage, the armature current is calculated, which is then used to find the conductor cross-section after defining the armature current density. Thus, slot dimensions are found so that the slot area can accommodate the conductor previously found. With this approach, the design is susceptible to result in a too-large stator compared to the rotor and would only be noticed by the designer when the generator cross-section is drawn. On the other hand, with the proposed approach, the designer deals directly with the dimensions and quickly assesses their relation to the output power. Furthermore, performing the iterative process of the output power test, the relation between the generator rotor and stator dimensions becomes clearer and clearer.

At the end of the output power design stage, all generator dimensions are known, and now the loading effects have to be considered before proceeding with the design method, as Figure 21 shows. Firstly, a combination of copper conductors (or a single one) is chosen to match the calculated armature conductor surface. From its specifications, the armature resistance is found (Subsection 3.2.6). During load operation, the armature current creates a magnetic field that interacts with the rotor magnetic field, resulting in distorted net magnetic flux density with decreased or increased value, depending on the load. This will correspond to a smaller or bigger terminal voltage (with inductive and capacitive loads, respectively). A reactance can electrically represent this armature reaction field, so obtaining its value is an essential design step. For non-salient pole PM machines, the reluctance of the air-gap is constant as the magnetic permeability of the magnets is very close to that of air. Thus, the armature reaction reactance does not assume different values depending on the rotor position and can be analytically calculated since the rotor geometry is less complex than in other types of PM machines.

In addition to the armature reaction reactance, the armature coils also have a leakage inductance that becomes leakage reactance when multiplied by the synchronous speed of the machine. Adding these two reactance values results in the

synchronous reactance of the generator (Subsection 3.2.7). After calculating the voltage drops in the armature resistance and the synchronous reactance, the terminal voltage is estimated (Subsection 3.2.8) and should be compared with the desired voltage value from the specifications. As shown in Figure 21, in the case of a difference, the designer should adjust the imposed voltage used in the design step that calculates the number of turns of the armature coils per phase. A new value would result in more or less turns for the same rotor dimensions and air-gap magnetic flux. Since the design is taken back to the armature definitions, the output power assumes a new value in the next stage, and naturally, adjustments should be performed. How to perform these adjustments is already discussed earlier, where minor differences require less effort from the designer, and a big difference may take a few iterations more and take the design back to stator or rotor sizing (eventually).

When the terminal voltage matches its desired value, the next stage consists of a loss estimation (Subsection 3.2.9) to further compute the generator efficiency, as Figure 21 shows. The proposed design procedure considers copper losses in armature windings, iron losses in the stator core, and permanent magnet losses. Finally, after calculating the efficiency, the surface-mounted permanent magnet generator design is completed. If the designer is satisfied with the designed generator, then a finite element simulation should be carried out. This way, a thorough analysis can be realised, and the designed machine can be eventually verified.

3.2.1 Rotor Sizing

From the specified operative electrical frequency f (Hz) and rotational speed ω (rpm), the first step of the rotor sizing can be executed, which is the calculation of the number of poles of the machine P:

$$P = \frac{120 \cdot f}{\omega} \tag{24}$$

The number of poles determines the pole pitch α_P (rad), which is the angle available for each pole:

$$\alpha_P = \frac{2\pi}{P} \tag{25}$$

The pole pitch factor ($k_{\alpha P}$) is used to define the angle occupied by the permanent magnet, called effective pole pitch α_{Pef} (rad):

$$\alpha_{Pef} = \alpha_P \cdot k_{\alpha P} \tag{26}$$

The generator air-gap length L_{AG} (mm) is an extremely important parameter, usually imposed by the designer. In the proposed procedure it will be determined using the rotor outer diameter D_{Ro} (mm) and the air-gap factor (k_{AG}):

$$L_{AG} = D_{Ro} \cdot k_{AG} \tag{27}$$

As explained in Section 2.2.2.1, by imposing a permeance coefficient (PC) value, the permanent magnet height h_{PM} (mm) can be found with:

$$h_{PM} = L_{AG} \cdot PC \tag{28}$$

In the arc-shaped PM rotor of Figure 20, the outer surface is wider than the inner surface attached to the rotor yoke. Thus, to calculate the permanent magnet's width, the arc length at its centre is used:

$$W_{PM} = \left(\frac{D_{Ro}}{2} - \frac{h_{PM}}{2}\right) \cdot \alpha_{Pef} \tag{29}$$

The rotor yoke height h_{Ry} (mm) is found using the PM operative magnetic flux density B_{PM} (T) and after setting the desired magnetic flux density in the rotor yoke B_{Ry} (T) at no-load:

$$h_{Ry} = \frac{B_{PM}}{B_{Ry}} \cdot \frac{W_{PM}}{2} \tag{30}$$

As one of the last dimensions in rotor sizing, the diameter at the permanent magnets top D_{PMt} (mm) is calculated with:

$$D_{PMt} = D_{Ro} - 2 \cdot h_{PM} \tag{31}$$

With the last dimension, the rotor inner diameter D_{Ri} (mm) is found:

$$D_{Ri} = D_{PMt} - 2 \cdot h_{Ry} \tag{32}$$

3.2.2 Permanent Magnet Flux Calculation

Once the permanent magnet type (component material and its temperature ratings), its grade, and the desired permeance coefficient have been previously chosen, the operative permanent magnet flux density (B_{PM}) can be obtained with a curve similar to Figure 17. Thus, the permanent magnet flux φ_{PM} (Wb) is calculated with:

$$\varphi_{PM} = B_{PM} \cdot W_{PM} \cdot L_G \tag{33}$$

where L_G (mm) is the machine stack length, which is an imposed parameter by the designer. In this design methodology it will be found by determining the machine shape factor (k_{MS}):

$$L_G = D_{Ro} \cdot k_{MS} \tag{34}$$

The air-gap magnetic flux φ_{AG} (Wb) can then be calculated with:

$$\varphi_{AG} = \varphi_{PM} \cdot \Delta\varphi_{PMAG} \tag{35}$$

where $\Delta\varphi_{PMAG}$ is the permanent magnet to air-gap leakage flux factor. To assess if the designed PM corresponds to the desired air-gap magnetic flux density, the length of the arc at the middle of the air-gap L_{AGa} (mm) must be found:

$$L_{AGa} = \left(\frac{D_{Ro} + L_{AG}}{2}\right) \cdot \alpha_P \cdot k_{\alpha P} \tag{36}$$

Finally, the air-gap magnetic flux density B_{AG} (T) is calculated with:

$$B_{AG} = \frac{W_{PM}}{L_{AGa}} \cdot B_{PM} \cdot \Delta\varphi_{PMAG} \tag{37}$$

This last equation is the magnetic flux density test of Figure 21, detailed in Section 3.2.

3.2.3 Stator Sizing

With the rotor sizing completed and the air-gap magnetic flux density test being a success, the stator sizing begins with the stator inner diameter (D_{Si}):

$$D_{Si} = D_{Ro} + 2 \cdot L_{AG} \tag{38}$$

Then, the slot opening and tooth tips must be defined. Firstly, using the slot opening factor k_{Sow} and the number of slots of the stator N_S, the slot opening width W_{So} (mm) is found:

$$W_{So} = \frac{D_{Ro}}{N_S} \cdot k_{Sow} \tag{39}$$

Then, the heights of the slot opening h_{So} (mm) and wedge h_{Sw} are related to W_{So}, with the slot opening height factor k_{Soh} and the wedge height factor k_{Sw}:

$$h_{So} = W_{So} \cdot k_{Soh} \tag{40}$$

$$h_{Sw} = W_{So} \cdot k_{Sw} \tag{41}$$

With these two height values, the diameter at the top of the slot D_{St} (mm) can be calculated:

$$D_{St} = D_{Si} + 2 \cdot (h_{So} + h_{Sw}) \tag{42}$$

To continue the stator sizing, the slot pitch α_S (rad) must be determined:

$$\alpha_S = \frac{2\pi}{N_S} \tag{43}$$

Since the slot pitch corresponds to one slot and one stator tooth, the proportion of how much of this pitch is occupied by one or the other can be determined with the tooth-to-slot width factor (k_{TS}):

$$\theta_{St} = \frac{\alpha_S}{1 + k_{TS}} \tag{44}$$

With the angle of the slot on the top θ_{St} (°), the widths of the slot on the top W_{St} (mm) and of the tooth W_t (mm) are calculated:

$$W_{St} = D_{St} \cdot \tan\frac{\theta_{St}}{2} \tag{45}$$

$$W_t = D_{St} \cdot \tan\frac{\alpha_S - \theta_{St}}{2} \tag{46}$$

With slot width at the top, the slot wedge width W_{Sw} (mm) can be found:

$$W_{Sw} = \frac{(W_{St} - W_{So})}{2} \tag{47}$$

The next stator dimension to be determined is the height of the stator yoke h_{Sy} (mm), found after choosing a value for the permanent-magnet-width-to-stator-yoke factor k_{PMSy}:

$$h_{Sy} = W_{PM} \cdot k_{PMSy} \tag{48}$$

Another factor is used to ensure a proper proportionality between the stator yoke height and the slot height, called the stator-yoke-to-slot-height factor k_{SyS}:

$$h_S = h_{Sy} \cdot k_{SyS} \tag{49}$$

In low-voltage machines, the stator teeth usually have the same width at the top and bottom. This means that a constant magnetic flux density is maintained throughout their length (neglecting flux leakage crossing the slots), and the slots increase in width along their height. Thus, to keep the teeth parallel, the inclination angle of the slot edge θ_{Sei} (rad) must be:

$$\theta_{Sei} = \frac{\alpha_S}{2} \tag{50}$$

The last slot dimension to be found is its bottom width W_{Sb} (mm):

$$W_{Sb} = W_{St} + 2 \cdot h_s \cdot \tan \theta_{Sei} \tag{51}$$

To complete the stator sizing, the stator outer diameter D_{So} (mm) is calculated:

$$D_{So} = D_{St} + 2 \cdot \left(h_S + h_{Sy}\right) \tag{52}$$

3.2.4 Armature Winding Definitions

In this design stage, all the characteristics of the armature windings are defined and calculated. The armature windings are coils with a certain number of turns inserted in the stator slots. With the slot pitch and pole pitch, it is possible to determine how many slots correspond to one pole pitch and which slot a phase coil enters or exits. This distance is the armature coil pitch α_{AC} (rad), found after defining a value for the armature coil-shortening factor k_{Ac}:

$$\alpha_{AC} = \alpha_P \cdot k_{Ac} \cdot \frac{P}{2} \tag{53}$$

Multiplying it by the number of pole pairs, this angle goes from mechanical to electrical radians.

As the coil is shortened, the magnetic flux linked by the armature coil is decreased (PYRHÖNEN; JOKINEN; HRABOVCOVÁ, 2008). The reduction factor due to coil shortening $\Delta\varphi_{Cs}$ is:

$$\Delta\varphi_{Cs} = \sin\frac{\alpha_{Ac}}{2} \tag{54}$$

After defining the number of slots N_S and the number of phases of the generator N_{ph}, the number of slots per pole per phase q is found:

$$q = \frac{N_S}{N_{ph} \cdot P} \tag{55}$$

The fact that the armature coils are spatially distributed within the stator slots means that the sum of the voltages generated in each coil is not the same as if there were only one coil (concentrated winding) since the voltage of each coil has a lag in relation to the others. Therefore, a reduction factor due to winding distribution $\Delta\varphi_{Wd}$ must be considered in this step of the design:

$$\Delta\varphi_{Wd} = \frac{\sin\left(q \cdot \frac{\alpha_{Ac}}{2} \cdot \frac{P}{2}\right)}{q \cdot \sin\left(\frac{\alpha_{Ac}}{2} \cdot \frac{P}{2}\right)} \tag{56}$$

With these coil factors, the next step would be to calculate the number of turns in the armature winding per phase T_A. In the proposed design methodology, to find this winding parameter, the designer must impose a voltage value E_{Af} (V):

$$T_A = \frac{E_{Af}}{\sqrt{2} \cdot \pi \cdot f \cdot \Delta\varphi_{Cs} \cdot \Delta\varphi_{Wd} \cdot \varphi_{AG} \cdot \Delta\varphi_{AGA}} \tag{57}$$

A thorough discussion on how this voltage value should be determined can be seen in Section 3.3. The air-gap-to-armature flux leakage factor $\Delta\varphi_{AGA}$ is used to adjust the number of turns. By choosing a number of parallel paths of armature windings N_{Cp} and the consequent pole factor k_{Cop}, the number of coils in series per phase N_{Cs} is found:

$$N_{Cs} = \frac{P}{N_{Cp} \cdot k_{Cop}} \tag{58}$$

Then, by defining the number of slot layers N_{Sl}, the number of coils per pole per phase N_{Cpp} is found:

$$N_{Cpp} = q \cdot \frac{k_{Cop} \cdot N_{Sl}}{2} \tag{59}$$

Finally, the number of turns of the armature winding per coil T_{Ac} can be calculated with:

$$T_{Ac} = \frac{T_A}{N_{Cpp} \cdot N_{Cs}} \tag{60}$$

To complete the armature definition the conductor surface S_{Ac} (mm²) should be found. Firstly, since the stator slot is trapezoidal, its surface S_S (mm²) is:

$$S_S = \frac{(W_{Sb} + W_{St})}{2} \cdot h_S \tag{61}$$

The conductor surface is calculated after considering the slot fill factor k_{Sf}:

$$S_{Ac} = \frac{S_s \cdot K_{Sf}}{T_{Ac} \cdot N_{Sl}} \tag{62}$$

3.2.5 Output Power Calculation

By defining the armature current density J_A (A/mm²) and with the area of the armature conductor, the allowable armature current I_A (A) can be found:

$$I_A = S_{Ac} \cdot J_A \tag{63}$$

With the desired terminal voltage value V_{Td} (V) from the specifications, the apparent output power of the generator S_E (VA) is:

$$S_E = \sqrt{3} \cdot V_{Td} \cdot I_A \tag{64}$$

With this equation, the output power test of the procedure depicted in Figure 21 is performed. The iterative process involving this test is detailed in Section 3.2. Lastly, with the specified power factor PF, the output active power P_E (W) is found with:

$$P_E = S_E \cdot PF \tag{65}$$

3.2.6 Armature Resistance Calculation

To find the resistance of the armature windings, it is necessary to know their total length first. The distance between the entering slot and the exiting slot of a turn of the coil is an arc, so the arc length between two slots L_C (mm) of the same coil is:

$$L_C = (D_{St} + h_S) \cdot \frac{\alpha_{AC}}{P} \tag{66}$$

Similarly to Equation (53), the number of poles is used to convert the armature coil pitch back to mechanical radians.

Assuming that the coil end has the shape of a half-circle, L_C is its diameter and, thus, the coil end length L_{Ce} (mm) is:

$$L_{Ce} = \pi \cdot \frac{L_C}{2} \tag{67}$$

Then, the total length of the armature coils is L_{At} (mm):

$$L_{At} = 2 \cdot L_{Ce} + 2 \cdot L_G \tag{68}$$

The total length of the armature coils is necessary because copper conductors' resistance depends on their length. Thus, the armature resistance at the reference temperature R_{Aref} (Ω) can be obtained with:

$$R_{Aref} = R_{km} \cdot L_{At} \cdot T_A \tag{69}$$

after defining the resistance per kilometre of the selected conductor R_{km} (Ω/km), specified by its manufacturer. Considering that, due to the Joule effect, the conductor's temperature will be increased, the resistance value should be corrected (HENDERSHOT; MILLER, 2010):

$$R_A = R_{Aref} \cdot \frac{243.5\ °\text{C} + T_{op}}{243.5\ °\text{C} + T_{ref}} \tag{70}$$

where T_{op} (°C) is the operating temperature and T_{ref} (°C) is the reference temperature from the manufacturer. The value of 243.5 °C is the ratio of the copper resistance at 20 °C, which is usually the reference temperature at which the manufacturer measured the wire resistance.

3.2.7 Synchronous Reactance Calculation

Non-salient pole PM generators have a much simpler rotor geometry; thus, the armature reaction can be easily calculated with analytical equations. The synchronous inductance L_S (H) of surface PM generators is composed by the air-gap inductance L_{ag} (H), the air-gap mutual inductance M_{ag} (H), and the slot-leakage inductance L_{Sl} (H) (HENDERSHOT; MILLER, 2010). The armature winding coil end inductance is not considered in the proposed method since the verification finite element simulations are in 2D. Thus, it does not account for this end inductance, and providing the calculated value to the simulation model would not alter the results.

The air-gap inductance (L_{ag}) can be obtained with:

$$L_{ag} = \frac{\mu_0 \cdot \pi \cdot {T_A}^2 \cdot L_G \cdot D_{Si}}{4 \cdot \left(\frac{P}{2}\right)^2 \cdot (L_{AG} + h_{PM})} \tag{71}$$

in which μ_0 is the vacuum magnetic permeability. The air-gap mutual inductance (M_{ag}) can be calculated with (HENDERSHOT; MILLER, 2010):

$$M_{ag} = -\frac{L_{ag}}{3} \tag{72}$$

Lastly, the slot-leakage inductance (L_{Sl}) can be found with (PYRHÖNEN; JOKINEN; HRABOVCOVÁ, 2008):

$$L_{Sl} = 4 \cdot \frac{N_{ph}}{N_S} \cdot \mu_0 \cdot L_G \cdot {T_A}^2 \cdot \left(\frac{h_S}{3 \cdot W_{St}} + \frac{h_{So}}{W_{So}} + \frac{h_{Sw}}{W_{St} - W_{So}} \cdot \ln\left(\frac{W_{St}}{W_{So}}\right) \right) \quad (73)$$

With all its components, the generator's synchronous inductance can be found:

$$L_S = L_{ag} + L_{Sl} - M_{ag} \quad (74)$$

Finally, the synchronous reactance for the non-salient pole PM generator X_S (Ω) is calculated with:

$$X_S = 2 \cdot \pi \cdot f \cdot L_S \quad (75)$$

3.2.8 Terminal Voltage Calculation

The generator phasor diagram is presented in Figure 22. The analysis developed with this diagram that results in the following equations does not consider either the harmonic content or transients, only the fundamental component at steady state.

Figure 22 – Phasor diagram for non-salient pole PMSG

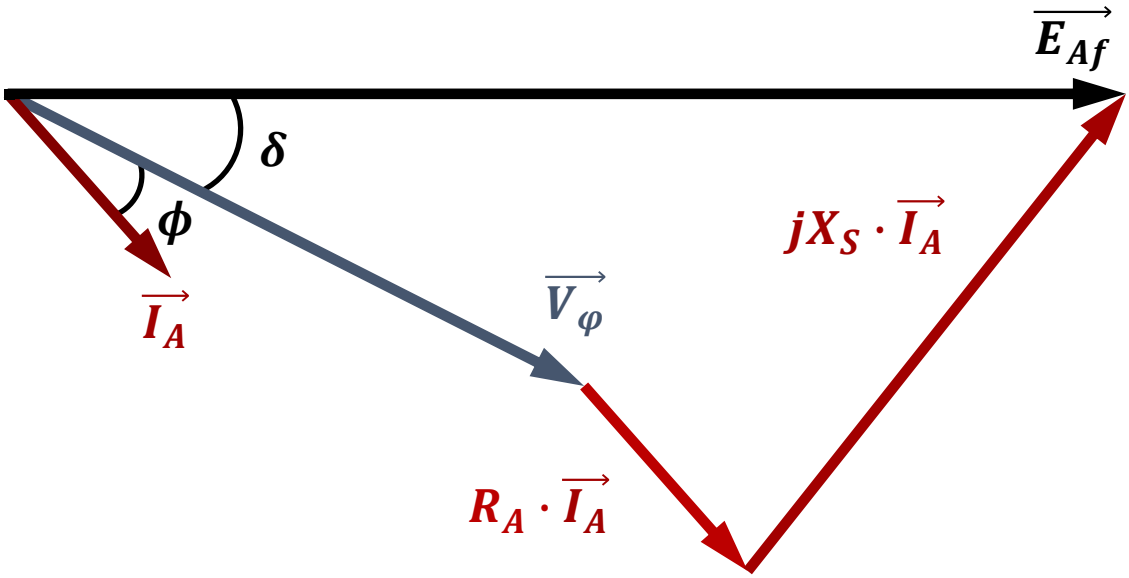

Source: Own authorship (2024)

In the phasor diagram of Figure 3, ϕ (°) is the displacement angle between the terminal voltage and the armature current, and δ (°) is the load angle. To find the phase value of the terminal voltage V_φ (V), the phasor diagram clarifies that the voltage drops in the armature resistance and the synchronous reactances must be known. To that end, both the amplitude value of the armature and its phase must be known. The first is found with Equation (63), and the latter is the sum of ϕ and δ. The displacement angle between the terminal voltage and the armature current is essentially a design specification, equal to the arc cosine of the machine power factor (PF). Thus, the last parameter needed is the load angle value:

$$\delta = \sin^{-1} \frac{I_A \cdot X_S \cdot \cos\phi - I_A \cdot R_A \cdot \sin\phi}{E_{Af}} \tag{76}$$

Then, knowing all the presented parameter values, the phase value of the terminal voltage is:

$$\overrightarrow{V_\varphi} = \overrightarrow{E_{Af}} - \overrightarrow{I_A} \cdot (R_A + jX_S) \tag{77}$$

Finally, the generator terminal voltage is:

$$V_T = \sqrt{3} \cdot \left|\dot{V}_\varphi\right| \tag{78}$$

This last equation is used to perform the terminal voltage test shown in Figure 21, and the related iterative process is explained in Section 3.2.

3.2.9 Estimation of Losses

A simplified loss estimation is made by calculating the losses on the armature windings, the stator core, and in the permanent magnets. The copper loss P_{Ac} (W) due to the Joule effect in the armature windings is the simplest to be found:

$$P_{Ac} = 3 \cdot R_A \cdot {I_A}^2 \tag{79}$$

In the proposed methodology the iron losses estimation is derived from (GRAUERS, 1996). As a first step, the volume of the stator yoke V_{Sy} (mm³) and the stator teeth V_{St} (mm³) are found:

$$V_{Sy} = \frac{\pi}{4} \cdot L_S \cdot \left[{D_{So}}^2 - \left(D_{So} - 2 \cdot h_{Sy}\right)^2\right] \tag{80}$$

$$V_{St} = N_S \cdot L_G \cdot [W_t \cdot h_S + (W_t + W_{Sw}) \cdot h_{Sw} + (W_t + W_{Sw}) \cdot h_{So}] \tag{81}$$

Next, the peak value of the magnetic flux density at the stator yoke and teeth needs to be estimated. As an approximation, these can be found based on the magnetic flux density of the PM:

$$B_{Sy} = B_{PM} \cdot \frac{{W_{PM}}/{2}}{h_{Sy}} \cdot \Delta\varphi_{AGA} \cdot \Delta\varphi_{PMAG} \tag{82}$$

$$B_{St} = B_{PM} \cdot \frac{W_{PM}}{N_S/_P \cdot W_t} \tag{83}$$

Using the losses per kilogram due to Foucault P_f (W/kg), hysteresis P_h (W/kg) and the mass density ρ_{ee} (g/cm³) of the selected electrical steel, the iron losses on the stator yoke can be calculated. The hysteresis P_{Syh} (W) and Foucault P_{Syf} (W) losses on the stator yoke are (GRAUERS, 1996):

$$P_{Syh} = k_{Syh} \cdot V_{Sy} \cdot \rho_{ee} \cdot P_h \cdot \frac{f}{50\ Hz} \cdot \left(\frac{B_{Sy}}{1.5\ T}\right)^2 \tag{84}$$

$$P_{Syf} = k_{Syf} \cdot V_{Sy} \cdot \rho_{ee} \cdot P_f \cdot \left(\frac{f}{50\ Hz}\right)^2 \cdot \left(\frac{B_{Sy}}{1.5\ T}\right)^2 \tag{85}$$

Similarly, stator teeth hysteresis P_{Sth} (W) and Foucault losses P_{Stf} (W) can be calculated with:

$$P_{Sth} = k_{Sth} \cdot V_{St} \cdot \rho_{ee} \cdot P_h \cdot \frac{f}{50\ Hz} \cdot \left(\frac{B_{St}}{1.5\ T}\right)^2 \tag{86}$$

$$P_{Stf} = k_{Stf} \cdot V_{St} \cdot \rho_{ee} \cdot P_f \cdot \left(\frac{f}{50\ Hz}\right)^2 \cdot \left(\frac{B_{St}}{1.5\ T}\right)^2 \tag{87}$$

At last, a rough estimate of the permanent magnet losses P_{PM} (W) of the generator are calculated (GRAUERS, 1996):

$$P_{PM} = P \cdot k_{PM} \cdot W_{PM} \cdot L_G \tag{88}$$

where k_{PM} (W/m²) is the PM specific losses. Ultimately, the total losses P_T (W) still should consider stray losses, thus the stray losses factor k_{Sl} is used (PYRHÖNEN; JOKINEN; HRABOVCOVÁ, 2008):

$$P_T = (1 + k_{Sl}) \cdot \left(P_{Ac} + P_{Syh} + P_{SyF} + P_{Sth} + P_{StF} + P_{PM}\right) \tag{89}$$

Finally, the efficiency (η) is calculated:

$$\eta = \frac{P_E}{P_E + P_T} \tag{90}$$

3.3 Imposed Parameters and Their Suggested Ranges

In the proposed design procedure, the designer has to determine a considerable number of imposed parameters. Thus, this section addresses these parameters seen throughout Section 3.2 since they significantly impact the generator results. To explain in the most straightforward manner possible, this section follows the same order as the previous section, going from rotor sizing all the way to losses and efficiency estimation. The suggested ranges are mostly based on the literature and papers that address the matter and can be seen in resume in Table 1.

Table 1 - Suggested ranges of the imposed parameters in PMSG design

Symbol	Unit	Description	Suggested Range
D_{Ro}	mm	Rotor outer diameter	[1]
$k_{\alpha P}$	-	Pole pitch factor	1/2 – 4/5
k_{AG}	-	Air-gap factor	0.01 – 0.015
PC	-	Permeance coefficient	3 – 8
B_{PM}	T	Operative permanent magnet flux density	[2]
B_{Ry}	T	Magnetic flux density in the rotor yoke	1.0 – 1.5
k_{MS}	-	Machine shape factor	[1]
$\Delta\varphi_{PMAG}$	-	PM to air-gap leakage factor	[3]
N_S	slots	Number of slots	[4]
k_{Sow}	-	Slot opening factor	0.25 – 1
k_{Soh}	-	Slot opening height factor	0.25 – 1
k_{Sw}	-	Wedge height factor	0.25 – 1
k_{TS}	-	Tooth-to-slot width factor	0.8 – 3
k_{PMSy}	-	PM width to stator yoke factor	0.25 – 1
k_{SyS}	-	Stator yoke to slot height factor	0.25 – 1
k_{Ac}	-	Coil-shortening factor	2/3 or 5/6[5]
k_{Cop}	-	Consequent pole factor	1 or 2
N_{Sl}	layers	Numbers of slot layers	1 or 2
$\Delta\varphi_{AGA}$	-	Air-gap to armature leakage factor	[3]
E_{Af}	V	Induced voltage value	[6]
N_{Cp}	paths	Number of parallel paths in the armature windings	1 or 2[7]
k_{Sf}	-	Slot fill factor	0.3 – 0.6
J_A	A/mm²	Armature current density	4 – 6.5
R_{km}	Ω/km	Conductor resistance per kilometre	[8]
T_{ref}	°C	Reference temperature	[9]
T_{op}	°C	Operating temperature	100 – 140
ρ_{ee}	g/cm³	Electrical steel mass density	[9]
P_F	W/kg	Foucault loss per kilogram	[9]
P_h	W/kg	Hysteresis loss per kilogram	[9]
k_{Syh}	-	Hysteresis losses factor (yoke)	2
k_{SyF}	-	Foucault losses factor (yoke)	1.8
k_{Sth}	-	Hysteresis losses factor (teeth)	1.2
k_{StF}	-	Foucault losses factor (teeth)	2.5
k_{PM}	W/m²	PM specific losses factor	100 – 300
k_{Sl}	-	Stray losses factor	0.01 – 0.02

[1]Not a straightforward range of values can be suggested since it depends on the intended generator output power. [2]Found with the PM demagnetisation curve after choosing its grade, temperature, and the permeance coefficient. [3]Obtained through magnetostatic FES. [4]Recommended to lead to an integer N_{Cpp}. [5]These are conventional suggestions, but other values can be chosen. [6]Determined to match the calculated terminal voltage with the specifications. [7]Or multiples of the number of poles. [8]Equivalent resistance at the reference temperature of a combination of wires in parallel or a single conductor with a cross-section close to S_{Ac}. [9]Found in the electrical steel manufacturer's spreadsheet.
Source: Own authorship (2024)

As explained in Section 3.2, after defining the design specifications, the rotor outer diameter (D_{Ro}) should be chosen. To simplify the design procedure, the equations that guide an external rotor diameter calculation were not included since they can be found in several works in the literature (such as Vaschetto et al. (2017) and Kim et al. (2017)). Thus, the proposed method treats it as an imposed parameter, allowing the designer to find it with one of the methods in the mentioned literature or freely choose it based on their experience.

Alternatively, it is possible to follow the "ABC" procedure presented by Hendershot and Miller (2010), where the torque per unit of rotor volume (and consequently the rotor external diameter) is obtained from the electric and magnetic loadings, assuring proper temperature rise. This procedure can be carried out by adopting the range values suggested by Pyrhönen, Jokinen, and Hrabovcová (2008). The imposed D_{Ro}, presented in Table 1 implies on values of electric loading (A/m) and magnetic flux densities (T) according to reference values from Pyrhönen, Jokinen, Hrabovcová (2008).

After analysing the electrical machine design equations, it will become clear that the machine's electrical power is proportional to its volume (considering the same rotational speed). This means that it is not possible to suggest a range for the rotor outer diameter since it will heavily depend on the desired output power of the generator. Even though stator dimensions will also affect the outer diameter of the machine (and consequently its volume), most of the stator dimensions are attached to PM dimensions, which in turn are proportional to the rotor outer diameter (as seen in subsection 3.2.1).

3.3.1 Rotor Parameters

Regarding rotor sizing, four parameters need to be imposed by the designer: pole pitch factor ($k_{\alpha P}$), air-gap factor (k_{AG}), permeance coefficient (PC), and the desired magnetic flux density in the rotor yoke (B_{Ry}). Firstly, the pole pitch factor will determine

the angle occupied by the PM, defining how much of the entire pole pitch (α_P) can be effectively used to produce flux (α_{Pef}). Permanent magnet machines, in general, should not utilise the entire pole pitch. Utilising the entire pole pitch in surface-mounted machines would mean that the permanent magnets of adjacent poles would be in contact with each other, resulting in significant leakage flux since the flux lines will feel a path of lesser reluctance when compared to the one to cross the air-gap. It is also not advised for the PM to occupy less than half of the pole, resulting in low rotor volume utilisation.

The generator air-gap length (L_{AG}) is an extremely important parameter, and it is recommended to keep it as small as possible to maximise the PM flux. However, in addition to torque ripple under load operation, other vibration sources can cause contact between the rotor and stator; thus, a safety margin should be considered. To ensure a reasonable proportion between air-gap length and rotor size, the air-gap factor (k_{AG}) should have its value considering manufacturing and mechanical aspects. A good reference would be to keep its value between 0.01 and 0.015 (meaning an air-gap length of 1% to 1.5% of the rotor outer diameter) (BAZZO; MOURA; CARLSON, 2021).

Since the permeance coefficient (PC) is better explained in the next section, the last imposed parameter of the rotor sizing is the magnetic flux density in the rotor yoke (B_{Ry}). At no-load operation, the magnetic flux density in the rotor yoke tends to be proportional to the PM width since the PM magnetic flux divides itself in the yoke on both sides. Thus, by dividing the PM operative magnetic flux density by the desired flux density in the yoke (at no-load) and multiplying by the PM width, the yoke height (h_{Ry}) is found. The magnetic flux density in the rotor yoke should be between 1.0 and 1.5T during full-load operation (PYRHÖNEN; JOKINEN; HRABOVCOVÁ, 2008). Therefore, since the B_{Ry} value is imposed in a no-load part of the design, the designer should consider a safety margin to ensure that this range is still respected during full-load.

3.3.2 Permanent Magnet Parameters

One of the most important values in the PM generator design is the operative permanent magnet flux density (B_{PM}), which is obtained from the PM demagnetisation curve (similar to the one in Figure 17). Even though it is first used in the rotor sizing

part, the permeance coefficient (PC) is a paramount parameter for the PM flux calculation stage since its intersection with the demagnetisation curve corresponds to the PM operating magnetic flux density (B_{PM}) at no-load. As seen in Section 2.2.2.1, it can be simplified as being the ratio between the air-gap length (L_{AG}) and the PM height (h_{PM}). Therefore, with the air-gap length, choosing the PC coefficient defines the PM height and its operative magnetic flux density at no-load.

Increasing its value moves the no-load operating flux density towards the PM remanent flux density, which is the maximum that the PM can generate (while maintaining the same temperature). On the other hand, smaller values correspond to a smaller operating magnetic flux density, bringing the PM operating point closer to the knee of the demagnetisation curve (as shown in Figure 17), which could cause permanent demagnetisation (HENDERSHOT; MILLER, 2010). There is no consensus concerning a correct range of the PC value. Some authors in the PM generator design literature use the range suggested by Hendershot, and Miller (2010) of a PC between 5 and 10, whereas others follow the range indicated by Hanselman (2003), which is between 4 and 6.

In the proposed design methodology, values between 3 and 8 could be used as long as the designer is conscious that a safety margin should ensure that during load operation (and even under overload transients) the PM is not under the possibility of having permanent demagnetisation. Additionally, even though the permeance coefficient may assume values more in the middle of the suggested range (or even towards the upper limit), too small PM heights are usually more complicated to manufacture (HANSELMAN, 2003). Values close to the top end of the suggested range would result in bigger PM height (and volume) and no-load operative flux density. Normally, this would also increase the machine cost; however, shortening the machine stack length could adjust the generator price and result in the same magnetic flux linked by the coils as a smaller PC.

At the very beginning of the design procedure, while choosing the permanent magnet and its permeance coefficient, the operating temperature of the PM (T_{op}) should also be considered since the demagnetisation curve tends to shrink towards the origin as the temperature is increased (see Figure 17). Therefore, since the armature windings tend to dissipate heat and increase the generator temperature when

feeding a load, the designer should consider a temperature rise roughly between 100 and 140°C when choosing the PM material, its grade, and the PC.

Another parameter necessary to calculate the PM magnetic flux is the generator stack length (L_G), found by imposing a value for the machine shape factor (k_{MS}), which usually assumes values between 0.5 and 2. For the lower half of this range, the axial length of the rotor is smaller than its diameter, resulting in more rotor inertia than upper values in the suggested range. Additionally, the efficiency of the machine tends to be lower, as there is relatively more copper in the coil ends. For values between one and two, the rotor has lower mechanical stress, but cooling the machine becomes costlier (KIM et al., 2017).

To find the magnetic flux in the air-gap of the machine, the permanent magnet to air-gap leakage factor ($\Delta\varphi_{PMAG}$) is used to consider leakage flux that tends to return to the adjacent pole (or even the opposite side of the same PM) and does not reach the air-gap. Its value can be obtained with reluctance networks or finite element simulations of the generator under no-load operation. With this factor value, the designer can more accurately assess if the designed PM corresponds to the desired air-gap magnetic flux density, which should be between 0.85 and 1.05T (PYRHÖNEN; JOKINEN; HRABOVCOVÁ, 2008).

Similarly to the permanent magnet to air-gap leakage factor that accounts for the leakage flux from the PM that does not reach the air-gap, the air-gap to armature leakage flux factor ($\Delta\varphi_{AGA}$) is used in the number of turns of armature winding (T_A) calculation to consider the magnetic flux that is not linked by the coils, returning to the air-gap through the stator teeth. This factor may also be adjusted after performing a magnetostatic no-load finite element simulation of the machine, which does not take more than a few seconds.

3.3.3 Stator Parameters

The stator sizing begins with choosing the number of slots (N_S), which is strictly linked to the number of poles since their ratio strongly affects the machine's winding scheme and the presence of harmonics of certain orders. Additionally, the ratio between the number of poles and slots, together with the slot opening width, influences the presence of cogging torque. Furthermore, this tends to become a constrained choice since the number of slots and their layers are limited by production feasibility

and winding manufacturability aspects (PYRHÖNEN; JOKINEN; HRABOVCOVÁ, 2008). Therefore, since synchronous machine winding is an extensive topic alone, the recommendation here is to choose the number of stator slots so that the number of coils per pole per phase is an integer, preferably between 1 and 4. As a reminder, this is a recommendation; other values (even non-integer ones) could be used as long as the designer knows the subject very well and its repercussions on the design.

Subsequently, the slot sizing requires definitions of the slot opening and the tooth dimensions. These dimensions have an impact on the cogging torque and Foucault losses, demanding special care and experience from the designer (HANSELMAN, 2003). Due to their significance in the overall result, in this design procedure they are linked in an attempt to maintain reasonable proportions and allow inexperienced designers to find an appropriate PM generator geometry.

Firstly, the slot opening width (W_{So}) is bounded to the rotor outer diameter and the number of stator slots, ensuring that a proportion with the overall size and number of slots of the machine is established. To adjust this proportion, aiming for the slot width to be feasible (in terms of manufacturability) and allowing the armature conductors to be inserted in the slots, the slot opening factor (k_{Sow}) is used. It is not elementary to suggest a range of values for this imposed parameter since it can vary substantially, but a range between 0.25 and 1 should cover most cases.

The remaining tooth tip dimensions being linked to the slot opening (seen in equations (40) and (41)) would avoid excessively thin or too long and fragile tooth tips. Both the slot opening height factor (k_{Soh}) and the wedge height factor (k_{Sw}) could assume values between 0.25 and 1. Ultimately, the tooth tip proportions could only be verified when the stator sizing is finished and the generator cross-section is drawn. However, with the slot wedge dimensions (imposed slot wedge height and slot wedge width calculated with equation (47)), the wedge inclination could be found and analysed:

$$\theta_{Sw} = \tan^{-1}\frac{h_{Sw}}{W_{Sw}} \tag{91}$$

An imbalance between wedge height and width could be easily noticed if this value becomes smaller than 20° or bigger than 40°.

Also during the stator sizing, a proportion of how much of the slot pitch corresponds to the slot or the stator teeth is defined by the tooth-to-slot width factor (k_{TS}). As the value of this imposed parameter increases, the slot begins to occupy a smaller portion of the slot pitch, reducing the total slot area, which reduces the armature conductor surface and, therefore, the power produced in this stator volume. On the other hand, decreasing the value of this imposed parameter will reduce the tooth width (W_t) and increase its magnetic flux density, which can lead to saturation. Therefore, this parameter could assume values within the 0.8 to 3 range. The designer can assess if the stator teeth are close to saturation at no-load operation by calculating the teeth average magnetic flux density:

$$B_{St} = B_{PM} \cdot \left(\frac{W_{PM}}{W_t}\right) \cdot \left(\frac{P}{N_S}\right) \tag{92}$$

The magnetic flux density in the stator teeth should be between 1.5 to 2.0T (PYRHÖNEN; JOKINEN; HRABOVCOVÁ, 2008) at full-load operation; thus, similarly to the imposed rotor yoke flux density, the k_{TS} should also consider a margin so that the stator teeth will not saturate when the generator feeds rated load. The magnetostatic simulation used to adjust the leakage flux factors can also be used to verify if this range is respected and if there is a reduced risk of saturation.

Seeking to establish a certain relationship with the magnetic flux density produced by the magnets with the maximum flux density in the stator yoke, its height (h_{Sy}) is chosen to be a portion of the width of the magnets (equation (48)). Keeping the permanent magnet width to stator yoke factor (k_{PMSy}) within 0.25 and 1, it is possible to avoid designing an unnecessarily large stator with a low air-gap magnetic flux density or an overly saturated one. The flux density in the stator yoke should be kept between 1.0 and 1.5T at full-load (PYRHÖNEN; JOKINEN; HRABOVCOVÁ, 2008). Thus, using:

$$B_{Sy} = B_{PM} \cdot \left(\frac{W_{PM}}{2 \cdot h_{Sy}}\right) \cdot \Delta\varphi_{AGA} \cdot \Delta\varphi_{PMAG} \tag{93}$$

the designer can assess if a margin is reasonable and ensure that this would not exceed the recommended flux density. Lastly, for PM generators with many poles,

defining the stator yoke height only by its desired flux density can lead to excessively thin yokes. In this case, a mechanical constraint could be incorporated.

Lastly, the slot height (h_S) is tied to the stator yoke height with the stator yoke to slot height factor (k_{SyS}). Even more than the width, the slot height influences the power density of the machine, as, with larger slots, it is possible to increase the conductor's surface, allowing more current. As discussed in Section 3.2, with this approach, in essence, the designer freely defines the generator output power by imposing the last two factors instead of choosing an armature conductor based on the output power and then finding the slot dimensions to fit the conductors. Additionally, a proportionality between the volume of magnets and the volume of copper in the stator is also ensured indirectly. The suggested range is also between 0.25 and 1.

3.3.4 Armature Windings Parameters

During the armature winding definitions, a coil-shortening factor (k_{Ac}) is defined to calculate the armature coil pitch (α_{AC}). Usually, the coil pitch is shortened so that the length of the coil end becomes shorter and the total copper mass is reduced (HENDERSHOT; MILLER, 2010). This results in a smaller armature resistance and fewer copper losses, which increases the efficiency of the generator since it is the most significant loss in synchronous generators. Furthermore, with the correct factor value, the shortened coil can attenuate the harmonic content of the air-gap magnetic flux density and result in a more sinusoidal linked flux compared to a full-pitch coil (PYRHÖNEN; JOKINEN; HRABOVCOVÁ, 2008).

The armature coil-shortening factor is a fraction of the original pole pitch, composed of values multiple of the original pitch, resulting in an integer shortened pitch. Since many combinations between the number of poles and stator slots are possible, this fraction can be composed of a large quantity of multiples. Shortening factors of 2/3 and 5/6 are more conventional, known to reduce significantly third and ninth-order components and fifth and seventh-order components, respectively (BAZZO; MOURA; CARLSON, 2021).

To find the other component of the winding factor (i.e. the winding distribution factor $\Delta\varphi_{Wd}$), the number of slots per pole per phase must be found, which depends on the number of phases of the generator (N_{ph}). This can be selected freely in principle,

but since most supply networks are three-phase, most electrical machines are three-phase (PYRHÖNEN; JOKINEN; HRABOVCOVÁ, 2008).

Further on the proposed design methodology, one of the most important parameters is defined, the number of armature winding turns per phase (T_A), calculated with equation (57). This equation is basically Faraday's law, i.e. the voltage induced in a coil depends on the time variation of the flux linked and its number of turns, with the addition of flux linkage reduction factors due to coil shortening ($\Delta\varphi_{Cs}$), winding distribution ($\Delta\varphi_{Wd}$), and flux leakage ($\Delta\varphi_{AGA}$). Thus, in essence, a number of turns is found based on the magnetic flux produced by the PM and the imposed voltage value (E_{Af}).

To more effectively elucidate how this voltage value can be chosen, WRSG design is used. In this case, the voltage value used to calculate the number of turns is the no-load voltage, given that for both no-load or full-load conditions it is possible to adjust the rotor windings excitation and maintain the specified terminal voltage (BAZZO; MOURA; CARLSON, 2021). This is not the case for permanent magnet generators since the PM magnetic flux cannot be adjusted dynamically according to the generator load. Therefore, for PMSG, the voltage value used to calculate the number of turns of the armature winding must be the induced voltage estimated to be generated when feeding a load, having to be big enough so that it is equal to the desired terminal voltage after the voltage drops across the armature resistance and due to the armature reaction.

This is an iterative stage of the design (depicted in Figure 21) since it is very unlikely that the first imposed voltage value will precisely correspond to the desired terminal voltage of the specifications. However, matching the calculated terminal voltage to the specified value usually takes only a few iterations. An adequate first guest could be a voltage 1.3 times bigger than the phase value of the specified terminal voltage. After calculating the terminal voltage with equation (78), this value is adjusted, but related parameters should eventually be adjusted concurrently.

For example, increasing E_{Af} would result in more turns per coil, thus, a smaller conductor cross-section can be fitted in the slots. Considering that the stator geometry (slot dimensions) and the stator current density are not altered, less armature current is admissible, corresponding to less admissible output power. To correct that, the generator stack length could be adjusted, meaning more linked flux, and the number

of turns would be restored to the previous value (this is the simpler way to deal with that since the cross-section of the generator remains the same). Another way would be to adjust the slot size, allowing the bigger conductor surface that resulted in the original output power. However, the designer should know that this changes the value of the air-gap to armature leakage factor ($\Delta\varphi_{AGA}$).

Instead of just imposing a generic number of turns, defining a voltage value (E_{Af}) is more palpable since it would be the equivalent of expecting a voltage regulation (of 30%, for example). Furthermore, if the proposed method were to be implemented in optimisation software, the algorithm itself would be capable of finding the exact value of E_{Af}, because the terminal voltage and output power are fixed variables.

The last imposed parameters that defines the armature windings are the consequent pole factor (k_{Cop}), the numbers of slot layers (N_{Sl}), and the number of parallel paths in the armature windings (N_{Cp}). Both k_{Cop} and N_{Sl} are either 1 or 2. For the consequent pole factor, a value of 2 would be chosen to have a consequent pole armature winding. The number of parallel paths in the armature windings is a multiple of the number of poles (BAZZO; MOURA; CARLSON, 2021). For example, for a six-pole generator, N_{Cp} could be 1, 2, 3 or even 6. However, in this work the suggestion is either 1 or 2. Again, this is a recommendation; other values can be used for specific cases or applications as long as the designer is aware that this will deeply impact the generator winding scheme. With these values, both the number of coils in series per phase (N_{Cs}) and the number of coils per pole per phase (N_{Cpp}) are found.

Lastly, before moving on to the armature current (I_A) calculation, the designer must impose values for the slot fill factor (k_{Sf}) and the admissible armature current density (J_A). Considering that it is not possible to fill the slot entirely with conductors due to the conductor's insulation and manufacturability aspects, a slot fill factor is considered. The main aspects include the techniques available during manufacturing (allowing perfectly nested conductors or not), square or round conductors, and single or double layers (BOLDEA, 2006). Usually, slot fill factors between 40 and 45% are a bit optimistic for random-wound coils, and for higher values, rectangular wires more precisely fitted are required (HENDERSHOT; MILLER, 2010). Thus, in this paper, a range between 30% and 60% is suggested.

Finally, the current density in the armature conductors must be carefully analysed, considering two major aspects. The first is the operation temperature of the

generator, which is intensely related to the thermal class of the conductors' insulation. High-thermal-class insulation materials can sustain higher operation temperatures, thus allowing more current density. The last is the cooling system chosen, with a high efficiency cooling method allowing more current density. In more complex design procedures that include a thermal model of the generator, the operating temperature of the armature winding can be an imposed parameter, so the conductor current density is a free parameter. To simplify the design procedure, the imposed current density in the armature conductors is suggested to be within 4 and 6.5 A/mm² (PYRHÖNEN; JOKINEN; HRABOVCOVÁ, 2008).

3.3.5 Armature Resistance Parameters

To find the resistance per kilometre of the conductor (R_{km}), firstly, the designer should choose the number of wires that correspond to a conductor. If a single wire is used, then its surface should be very close to the armature conductor surface (calculated with equation (62)), and the resistance per kilometre is found on the spreadsheet of the conductor's manufacturer. Suppose two or more wires of different sizes are chosen. In that case, a combination of these wires (each with a different size) is found to closely match the armature conductor surface (S_{Ac}), and the resistance per kilometre of this conductor is now the equivalent resistance considering all wires in parallel.

Finally, to find the armature winding resistance (R_A), the temperature must be corrected (HENDERSHOT; MILLER, 2010). From the spreadsheet, the reference temperature in which the manufacturer measured the resistance (T_{ref}) is found. The operating temperature (T_{op}) would be accurately calculated with a thermal model of the machine. However, for simplification purposes, it can be estimated to be between 100 and 140°C. These values should also be considered when choosing the PM, as they influence its grade and temperature class.

3.3.6 Losses Parameters

The proposed design methodology estimates the iron losses based on the method from Grauers (1996). This method considers the loss per kilogram value (P_f and P_h) provided by the electrical steel manufacturer and is divided into hysteresis (P_{Syh} and P_{Sth}) and eddy current losses (P_{Syf} and P_{Stf}). From this same spreadsheet,

the mass density (ρ_{ee}) of the selected material can also be found. Additionally, as the stator yoke and teeth may have different magnetic flux densities, these two elements must have their losses estimated separately. Furthermore, empirical factors are used to account for Foucault and hysteresis losses (k_{Syf} and k_{Stf}, and k_{Syh} and k_{Sth}, respectively), which, naturally, should have their values based on the recommendations of Grauers (1996).

Therefore, the hysteresis and Foucault empirical factors are 2 and 1.8 for the stator yoke and 1.3 and 2.5 for the stator teeth. Another empirical factor used in the loss estimation is PM specific losses factor (k_{PM}). This is roughly based on the current loading of the machine, being between 100 and 300W/m², with higher values for higher current loadings (GRAUERS, 1996). Finally, the total losses (P_T) still consider stray losses, which usually are between 0.1% and 0.2% of the total value (which means a stray losses factor (k_{Sl}) between 0.01 and 0.02) (PYRHÖNEN; JOKINEN; HRABOVCOVÁ, 2008).

3.4 Variant Design: Commercial Machine Topology

As mentioned in Section 3.1, this methodology is developed to design surface-mounted PMSG, but it can be applied to PM machines with different rotor geometries, even salient-pole ones. Thus, to verify that, adaptations to the design equations and methodology were developed to match a commercial machine geometry. This more complex PM generator geometry can be seen in Figure 23 and Figure 24.

Figure 23 – Main geometric parameters of the salient-pole PMSG: a) diameters and the air-gap, b) main angles and stator yoke

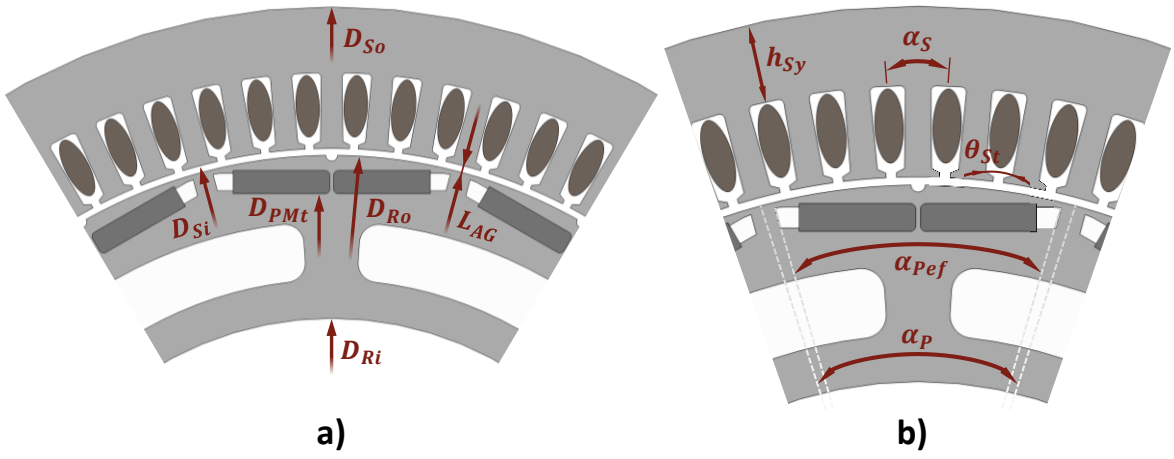

Source: Own authorship (2023)

Figure 23a) shows the correspondent diameters as seen for the surface-mounted PMSG (Figure 20a): rotor outer and inner diameters (D_{Ro} and D_{Ri}), stator inner and outer diameters (D_{Si} and D_{So}), the diameter at the permanent magnet top (D_{PMt}) and also the air-gap length (L_{AG}). Figure 23b) shows the same important angles as seen in Figure 20b, the pole pitch (α_P) and the effective pole pitch (α_{Pef}) on the rotor, as well as the slot pitch (α_S) and the angle of the slot on the top (θ_{St}).

The salient-pole rotor geometry can be seen in detail in Figure 24a). It inherits a few important dimensions from the non-salient pole geometry of Figure 20, such as the PM height (h_{PM}) and width (W_{PM}). The remaining dimensions were included to better model the commercial machine geometry. For example, the angle between permanent magnets (θ_{PM}) can have its value defined to enable wider PM in the rotor while maintaining the same effective pole pitch and allow flux concentration. The blank spaces at the outer side of the permanent magnets are flux barriers used to create a high reluctance flux path and reduce leakage flux that tends to go from the bottom surface to the top surface of the same magnet or to the bottom surface of the adjacent magnet. These barriers have different widths at the top (W_{fbt}) and at the bottom (W_{ftb}) and a height (h_{fb}). In the case of the flux barrier height being smaller than the PM height, a gap will appear, hence the barrier gap length (L_{fb}).

Figure 24 – Main geometric parameters of the salient-pole PMSG: a) PM pole dimensions, and b) slot dimensions diameters and rotor and stator pitches

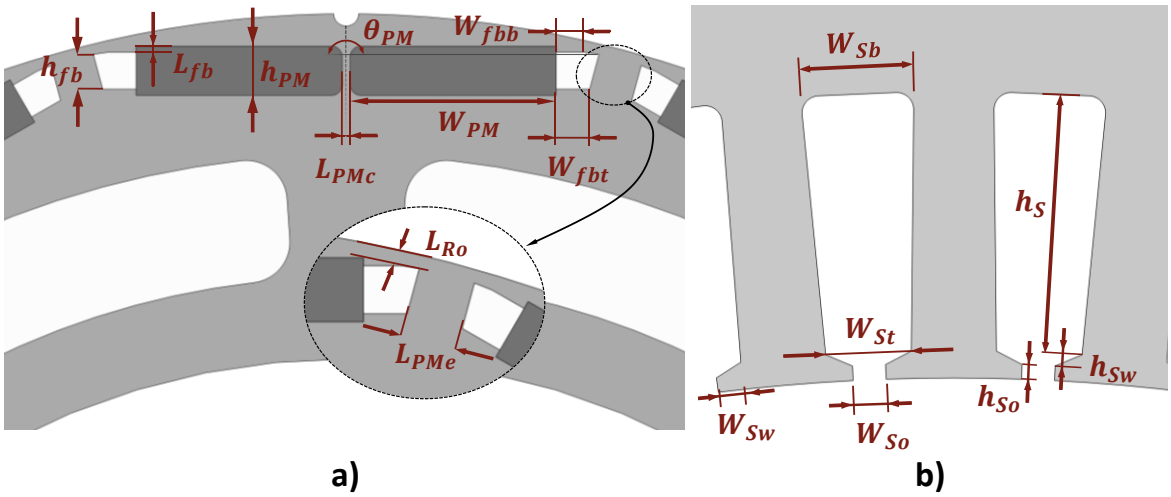

Source: Own authorship (2023)

Other dimensions shown in Figure 24a) are the lengths of the gaps between PM of the same pole (L_{PMc}), between the PM tip and the rotor outer diameter (L_{Ro}) and

between the PM edges (L_{PMe}). These gaps have a similar effect as the side flux barriers but are not made of air. Once these small sections of ferromagnetic material saturate, no additional leakage flux lines tend to make the shorter route to the adjacent PM surface. Finally, Figure 24b) shows the dimensions of the stator, which are the same as seen for the surface-mounted PMSG in Figure 20.

Since the rotor geometry differs from the non-salient pole PMSG, the rotor sizing has different equations. These equations for the commercial pilot exciter cross-section with a complex salient-pole geometry are shown in Appendix A. Nonetheless, the methodology remains the same, as well as its flowchart, design tests, and iterative processes. In addition to the rotor sizing equations, another stage that is affected by this difference in machine geometry is the reactance calculation. Since calculating these values analytically leads to imprecise results, a method for obtaining them is also explained in Appendix A.

4 PMSG OPTIMISATION

Using the proposed design method thoroughly described in Section 3, an optimisation for surface-mounted permanent magnet synchronous generators is developed in CADES (Component Architecture for Design of Engineering Systems). CADES is a software suite developed around an optimisation dedicated software. It contains several generation tools capable of creating components (models) from multiphysical algebraic equations, electromagnetic reluctance networks, and electromagnetic geometrical representations. These models can be further utilised by the services within CADES suite for computation or optimisation (DELINCHANT et al., 2007). The flowchart of Figure 25 illustrates how the PMSG optimisation is implemented in CADES.

Figure 25 – PMSG optimisation flow chart

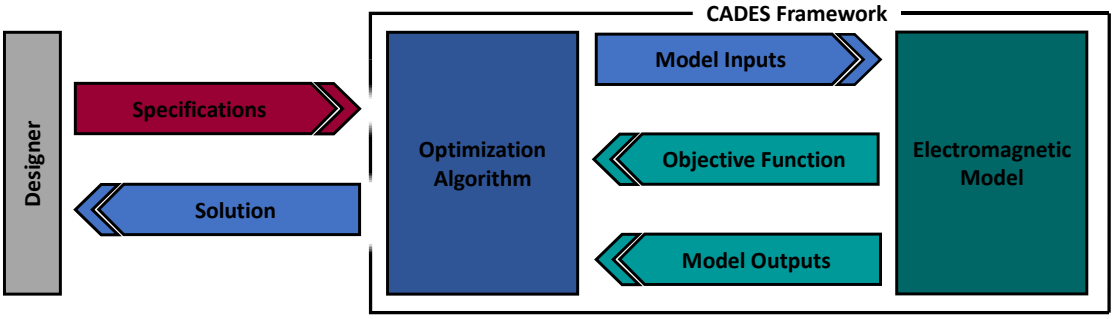

Source: Adaptation from Bazzo (2017)

Much like the design methodology, the optimisation process starts by providing the machine specifications, with the difference that, instead of the designer adjusting the parameters to find the output parameters of the machine, now is the optimisation algorithm that manipulates the values of the parameters towards an optimal solution. However, the designer's presence is still required to guide the optimisation, define the objective function and optimisation constraints, and evaluate the feasibility of the solution. During each iteration, the optimisation algorithm processes the model outputs and the objective function and supplies new inputs until all variables converge to an optimal solution and all constraints are respected. The optimisation process is completed when the objective function reaches the target value (either a maximum or minimum) determined by the designer (BAZZO, 2017).

CADES offers a variety of optimisation algorithms such as SQP (Sequential Quadratic Programming), genetic, hybrid, global, or mixed discrete-continuous

(DELINCHANT et al., 2007). Sequential (or successive) quadratic programming (SQP) represents one of the state-of-the-art, most effective, and robust methods for solving nonlinearly constrained optimisation. SQP is a deterministic algorithm that utilises the gradient (partial derivatives of the output as a function of the inputs) to find a solution. This means that it reaches the same result through the same search direction within the feasible region (if the initial conditions are maintained). Therefore, this kind of algorithm tends to be more efficient than Stochastic ones (like the genetic algorithm, for example), needing fewer iterations and not relying on probabilities to search the domain for optimal solutions (NOCEDAL; WRIGHT, 2006).

The fundamental idea of sequential quadratic programming is to solve a sequence of optimisation subproblems, which are less expensive to compute during every iteration since they are quadratic approximations of the Lagrange function (which is composed of the objective function and the constraints of the optimisation problem). At each iteration, the solution to these subproblems is used to determine the search direction and next trial solution. Another significant strength of SQP algorithms is their ability to solve problems with significant nonlinearities in the constraints by reducing them to a series of linear problems (YANG, 2017).

Engineering problems tend to be large, with numerous constraints of various natures. Thus, in a large nonlinearly constrained optimisation (such as the design optimisation of a PMSG), SQP is the better-fitted algorithm. Since it is a deterministic algorithm, CADES can use the signal of the partial derivative of the output as a function of the input to learn if the input should be increased or decreased in order to increase or decrease the output. Furthermore, the value of the partial derivatives of the output as a function of the inputs allows the software to know which input has more influence over the output value (objective function) (BAZZO, 2017).

Nonetheless, apart from requiring an initial condition relatively close to the final condition, this algorithm also requires a search direction in the solution space, which is obtained by calculating the gradient (partial derivatives). This could be a drawback if the optimisation problem outputs are not derivable, even as a function of one of the inputs. Additionally, given its characteristics, there is also the risk of the optimisation algorithm reaching a local minimum or maximum instead of a global minimum or maximum. However, this can be avoided by using more than one initial condition and reaching the solution by more than one direction.

The electromagnetic model is a direct and optimization-oriented model in which the performance parameters of the PMSG are obtained through its dimensions. Its basis comes from the PMSG design methodology presented in section 3. A few adaptations to the methodology were made, and improvements and submodels were also incorporated to improve the accuracy of the results and provide a few more degrees of freedom for the optimisation. Conveniently, the electromagnetic model is divided into sub-models that are strongly connected among themselves:

- Geometric Submodel: calculates all geometric parameters of the generator;
- No-Load Magnetic Submodel: provides the PM, air-gap, and armature linked flux values, as well as rotor yoke, air-gap, stator teeth (body and tips), and stator yoke magnetic flux densities;
- Armature Reaction Magnetic Submodel: provides the synchronous inductance and reactance values;
- Electric Submodel: calculates the main performance parameters of the PMSG (number of turns of the armature, armature current, terminal voltage, output power, torque density, efficiency, etc.).

The electromagnetic model is implemented in the CADES built-in programming environment, which has its own specific language, the System Modelling Language (SML). This programming language allows analytical and/or semi-analytical model equations. Analytical models are developed in SML with the basic arithmetic operators, basic mathematical functions, and user-defined functions. Semi-analytical models are an intermediary approach between analytical and numerical equations, coupling analytical equations to numerical approaches to calculate outputs (ENCIU et al., 2009). The developed electromagnetic model is composed by analytical equations, present in both the geometric and electric submodels, and semi-analytical equations from the no-load and armature reaction magnetic submodels (since they are RN).

As a result of SML only allowing analytical and semi-analytical model equations, the partial derivatives of these models can be exactly determined, either symbolically or by using derivation theorems. A drawback of this language is that it does not allow the direct use of conditional (if-else) and loops (for, do-while) programming structures. However, CADES has built-in implemented modules that enable the differentiation of C codes, so it is possible to obtain the Jacobian matrix associated to a function containing such programming structures (STAUDT, 2015).

4.1 Electromagnetic Model

To turn the design method presented in Section 3.2 into a PMSG optimization-oriented model and to implement it in CADES, a few adaptations had to be performed. Even though the design methodology is changed considerably, its general flow is maintained for the optimisation, as shown in Figure 26, meaning that it still starts with the rotor sizing and finishes with the loss and efficiency estimation. However, stages are placed in a slightly different order and with a few absences and different equations.

Figure 26 – Electromagnetic model flow chart

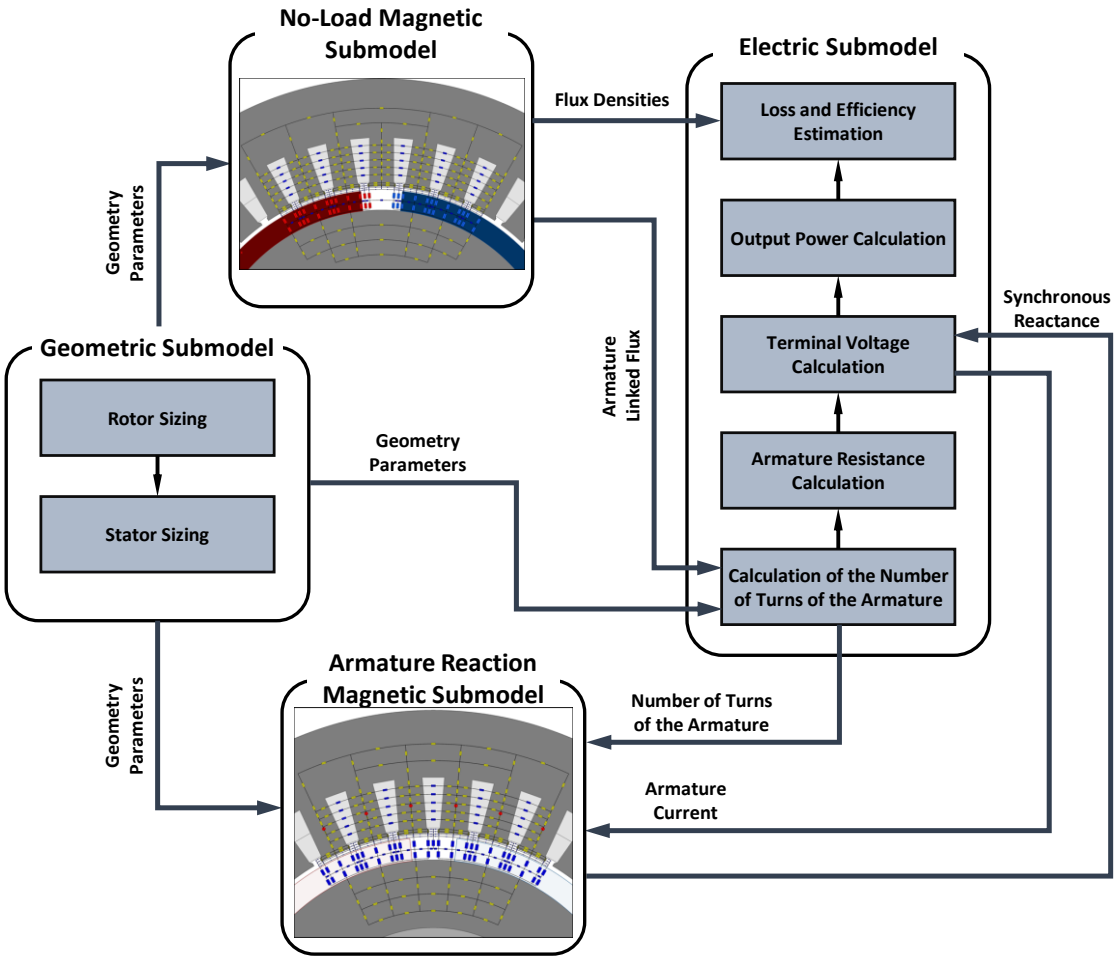

Source: Own authorship (2024)

From the PMSG design methodology described in Section 3.2, rotor and stator sizings now compose the Geometric Submodel depicted in Figure 26. In addition to calculating all geometric parameters of the generator, it now also provides the rotor, stator, and overall volume of the machine. The only modification on the correspondent equations from the PMSG procedure is a different way to calculate the rotor yoke

height (previously calculated with equation (30)). As discussed in Section 3.2 and 3.3.1, the rotor yoke height (h_{Ry}) is calculated by imposing a desired rotor yoke density (B_{Ry}) and it is based on the remanent magnetic flux density (B_{PM}) and width (W_{PM}) of the PM. In the geometric submodel, it is now calculated by imposing the rotor yoke height to PM width factor (k_{PMRy}):

$$h_{Ry} = k_{PMRy} \cdot \frac{W_{PM}}{2} \tag{94}$$

This enables the optimisation to find the rotor yoke based on the PM width and then obtain the rotor yoke magnetic flux density (at no-load) rather than the other way around.

Additionally, equations (34) and (36) (not originally in the rotor sizing of PMSG design in section 3.2.1), as well as a new equation, were included in the rotor sizing of this submodel. The first two were transferred from the permanent magnet flux calculation stage to the rotor sizing of the geometric submodel to calculate the stack length of the machine (L_G) and the length of the arc at the middle of the air-gap (L_{AGa}), respectively. The referred included equation calculates the rotor volume of the generator V_R (mm³):

$$V_R = \left[\pi \cdot \left(\frac{{D_{PMt}}^2 - {D_{Ri}}^2}{4}\right) + P \cdot (W_{PM} \cdot h_{PM})\right] \cdot L_G \tag{95}$$

Still in the geometric submodel, seven equations were included in its stator sizing stage. The first is used to calculate the angle occupied by a tooth at the top of the slot:

$$\theta_t = \frac{\alpha_S - \theta_{St}}{2} \tag{96}$$

Another two were included to calculate the angle occupied by the slot opening θ_{WSo} (rad) and slot wedge θ_{WSw} (rad) at the top of the slot, respectively:

$$\theta_{WSo} = 2 \cdot \tan^{-1} \frac{W_{So}}{D_{St}} \tag{97}$$

$$\theta_{WSw} = \frac{\theta_{St} - \theta_{WSo}}{2} \tag{98}$$

These two were included to provide the angles occupied by the slot opening and wedge widths to the no-load and armature reaction magnetic submodels shown in Figure 26. The following two are concerning the slot area. Equation (61) was taken from the armature winding definitions stage (Section 3.2.4) and included in the submodel with a different denomination, now called effective slot area S_{Sef} (mm²) since it represents the slot area available to accommodate the armature windings:

$$S_{Sef} = \frac{(W_{Sb} + W_{St})}{2} \cdot h_S \tag{99}$$

whereas, the slot area S_S (mm²) is calculated with:

$$S_S = \frac{(W_{Sb} + W_{St})}{2} \cdot h_S + (W_{So} \cdot h_{So}) + \frac{(W_{St} + W_{So})}{2} \cdot h_{Sw} \tag{100}$$

These last two are used to calculate the stator volume V_S (mm³):

$$V_S = \left[\pi \cdot \left(\frac{{D_{So}}^2 - {D_{Si}}^2}{4}\right) - N_S \cdot \left(S_S - S_{Sef}\right)\right] \cdot L_G \tag{101}$$

Lastly, the last included equation is used to find the generator volume V_G (mm³):

$$V_G = V_R + V_S \tag{102}$$

These changes were implemented to concentrate the generator dimensions in a single submodel. Furthermore, calculating the magnetic flux and the synchronous inductance of the generator analytically was found to be an imprecision source in the proposed design method. Thus, a new method was developed for obtaining these electromagnetic quantities, which requires all the geometry parameters to be found previously.

A major modification when adapting the design methodology of Figure 21 into the electromagnetic model optimisation oriented is the substitution of the permanent magnet flux calculation stage with the No-Load Magnetic Submodel (section 4.1.1.1), as Figure 26 shows. This submodel consists of a reluctance network that magnetically models the PM generator in a no-load condition. In the design procedure (Section 3), the PM magnetic flux was analytically calculated (equation (33)), and, using flux leakage factors ($\Delta\varphi_{PMAG}$ and $\Delta\varphi_{AGA}$), the flux linked by the armature coils was found. These factors were obtained by performing 2D magnetostatic FES after the machine cross-section was defined. To eliminate the need for a magnetostatic FES and still obtain the PM and air-gap magnetic fluxes and the armature linked flux accurately, this no-load RN was developed.

Hence, this RN takes the geometric submodel outputs (the machine geometry parameters) as inputs to provide the magnetic flux values and magnetic flux densities at various regions. The air-gap magnetic flux is found by extracting the flux of the reluctances used to model the correspondent region, and it is used to ensure that the air-gap magnetic flux density (B_{AG}) is within the desired range (as discussed in 3.3.2), using the length of the arc at the middle of the air-gap (L_{AGa}). CADES also automatically calculates the magnetic flux density of every reluctance in the RN. Thus, the rotor yoke density (B_{Ry}) is found directly from its reluctances and have their value constrained during the optimisation to respect the range discussed in section 3.3.1. Similarly, the stator yoke and teeth densities are also constrained within a value range (discussed in section 3.3.3), and they are used in the last stage of the Electric Submodel, as shown in Figure 26. The losses estimation uses the peak magnetic flux density value at the yoke and teeth, which eliminates the need for equations (82) and (83).

Another RN was developed to substitute the synchronous reactance calculation stage (from Figure 21) and constitutes the Armature Reaction Submodel (4.1.1.2). This new submodel magnetically models the armature reaction of the PM generator to accurately provide the synchronous inductance (consequently the PM are

removed from the magnetic circuit). For this, its inputs are the geometry parameters provided by the geometric submodel, the number of turns of the armature winding per coil (T_{Ac}) and the armature current value (I_A).The last two are from the two different stages of the electric submodel, as depicted in Figure 26. Magnetomotive sources are used to represent the armature windings and they are placed in the middle of the stator teeth according to the armature winding diagram. A detailed explanation of how the two mentioned RN were developed is provided in sections 4.1.1.1 and 4.1.1.2 for the no-load magnetic and armature reaction submodels, respectively.

During the process of adapting the PMSG design methodology into the electromagnetic model, the permanent magnet flux and synchronous reactance calculations were substituted for more complex and robust methods (reluctance networks). On the other hand, the flux density, output power, and terminal voltage tests were naturally removed from the optimization-oriented model. If, during the generator design, the designer was responsible for iteratively evaluating if the magnetic flux density, output power, and terminal voltage tests were satisfied, now he is responsible for checking if the optimisation respects its constraints, which, obviously, are (among others) the air-gap magnetic flux density, the generator output power and terminal voltage.

Thus, now there is no need to assess if the machine's current size corresponds to the desired output power, resulting in the output power calculation being moved further on the optimisation model in relation to the design procedure (when comparing Figure 21 and Figure 26) since now its value is directly calculated with the terminal voltage value rather than with the desired value. The output power calculation stage now also calculates the torque density of the machine ρ_τ (Nm/m³):

$$\rho_\tau = \left(\frac{P_E}{\frac{2 \cdot \pi \cdot n}{60}} \right) \Big/ V_G \tag{103}$$

The Electric Submodel concentrates the calculation of the electric quantities and performance parameters of the machine. It is constituted by the armature winding definitions, armature resistance, terminal voltage and output power calculations, and the losses and efficiency estimation (sections 3.2.4, 3.2.6, 3.2.8, 3.2.5, and 3.2.9, respectively). Apart from the previously mentioned retrieved equations, these former

stages of the design procedure of Section 3.2 do not have adaptations to their equations, as seen in the rotor and stator sizings of the geometric submodel. The complete SML code of the electromagnetic model is presented in Appendix B, where all the submodels and their stages are shown.

4.1.1 Reluctance Networks

An RN is an electromagnetic circuit that models the magnetic flux paths of an electromagnetic device. RN for electrical machines includes the stator, rotor, air-gap, permanent magnets, and its electrical components (stator and rotor windings) (PERHO, 2002). If the magnetic characteristics of the material of the machine are provided, the RN can deliver precise results under different saturation conditions. This circuit consists of passive and active elements, namely, reluctances and magnetomotive sources.

Reluctance represents the opposition that a magnetic flux encounters when it tries to flow through the material, and its value depends on the length, relative permeability, and cross-sectional area of the modelled element, as seen in equation (7). On the other hand, magnetomotive force (MMF) sources represent stator windings and other flux sources of the machine. The MMF value of a source F_{mm} $(A \cdot turns)$ is calculated with:

$$F_{mm} = N \cdot I \tag{104}$$

where N is the number of turns of the winding and I is the current that circulates in it. A special type of MMF source in CADES is the PM source, consisting of a MMF source in series with a reluctance. The software determines the MMF and flux values of the source according to the remanent magnetic flux density of PM, whereas the reluctance is determined by the PM dimensions (length and area).

The RN construction consists mainly of two steps: the definition of the MMF sources and the modelling of the flux paths by defining and arranging the reluctances. The arrangement of these RN elements is based on the flux paths of the machine cross-section and the configuration of the windings. Thus, prior to developing an RN, magnetostatic simulations of the machine in the right positions are necessary so that the flux lines can be observed and used to guide the modelling.

The modelling of magnetomotive force sources consists of defining their position and value. The MMF sources of the RN must be placed where they better represent the modelled source, PM or armature winding. For the PMSG, the better place to model the PM is their correspondent region, i.e., between rotor yoke and air-gap. On the other hand, the armature MMF sources must be placed in every tooth under the influence of the MMF of an armature winding coil.

In the reluctance modelling, they are placed in significant flux paths (according to the FES analysis) to model this part of the machine. RN construction is iterative, meaning that in order to obtain precise results, the magnetic flux values in specific regions of the RN are constantly compared with the ones from FES. As long as the results are not satisfactory, the RN is modified by adding new reluctances in an attempt to model significant flux paths not considered before, or new connections should be made when it is understood that it will improve the modelling of a flux line.

As mentioned in the previous section, two RN were developed to model the PMSG, in a no-load condition and its armature reaction. These RN are semi-analytical models since they solve nonlinear equations by considering magnetic material nonlinearities and, at the same time, have the reluctances parametrically calculated with analytical equations. Their main advantage (as of every semi-analytical model) is their good trade-off between precision and computation time (ENCIU et al., 2009).

Both developed RN are described in detail in the upcoming sections. The iron reluctances follow a provided BH curve from a known electrical steel, thus considering saturation and flux leakage. The RN were based on the machine of De Menezes et al. (2024), which is a 6-pole, 36-slots machine. The armature windings are double-layer lap windings, with an armature coil shortening of 5/6, resulting in 2 coils per pole per phase, as the diagram of Figure 27 shows.

Figure 27 – Surface-mounted PMSG winding diagram

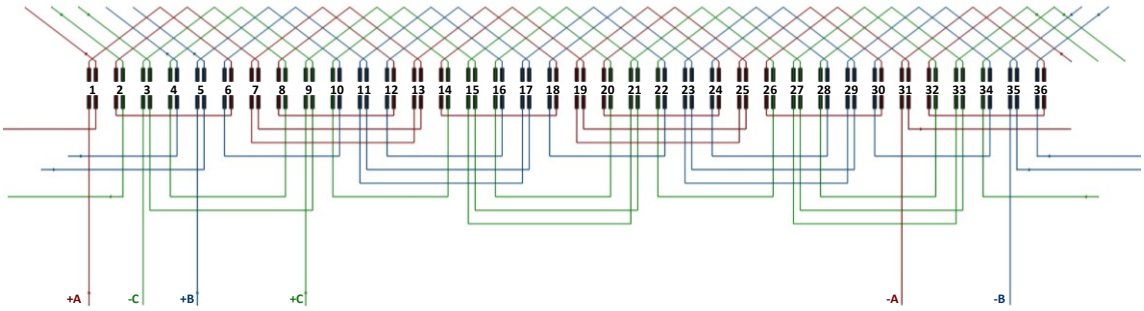

Source: Own authorship (2024)

4.1.1.1 No-Load Magnetic Submodel

The no-load RN was developed by observing the flux paths from Figure 28, which is a magnetostatic FES of the generator designed by De Menezes et al. (2024) in a no-load condition. The red PM has its flux lines leaving its bottom surface in the radial direction towards the stator, whereas the blue PM has flux lines reaching its bottom surface and going towards the rotor yoke. As this generator has six poles, it has six symmetrical flux linkages on the entire geometry, and only a sixth of the generator needs to be constructed on the RN to represent its behaviour. This means that the RN models the flux linkage within the dotted lines in Figure 28, going from half of the teeth in front of the red PM to half of the teeth in front of the blue PM.

Figure 28 – No-load magnetic flux lines for the RN construction

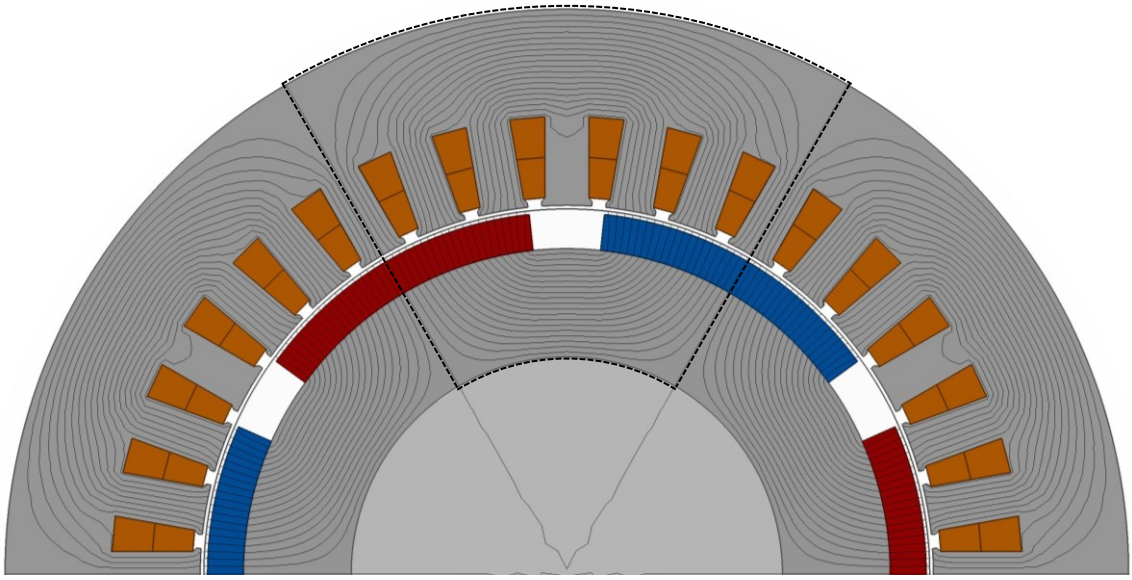

Source: Own authorship (2024)

In this RN, the armature windings are not modelled, and the MMF only comes from the PM. As mentioned earlier, CADES receives the dimensions of the PM generator (length and cross-section) and the remanent magnetic flux density and calculates the magnetic flux and MMF produced. Iteratively comparing the flux per pole and the flux values in several regions of the machine between FES and the RN, a final version was found, and its representation over the PMSG cross-section is shown in Figure 29.

The yellow rectangles represent the iron reluctances, in which the saturation curve of the electrical steel is inserted. On the other hand, the dark blue rectangles are the air reluctances. The red rectangles are magnetic flux sources that represent the red PM (whose flux direction is towards the stator), and light blue rectangles represent the blue PM (whose flux direction is towards the rotor). This reluctance network is relatively large (with over 400 elements), and the length and area values of every reluctance and source are presented in Appendix C. Figure 29 still shows four flux sources on the right side of the red PM and another four sources on the left side of the blue PM that exceed the PM width. An analytical expression is used in each PM source to determine their remanent magnetic flux density value based on whether the PM reaches the region that they represent. These eight sources in particular do not contribute to flux generation, behaving as air reluctances.

Figure 29 – Developed no-load RN over the PMSG cross-section

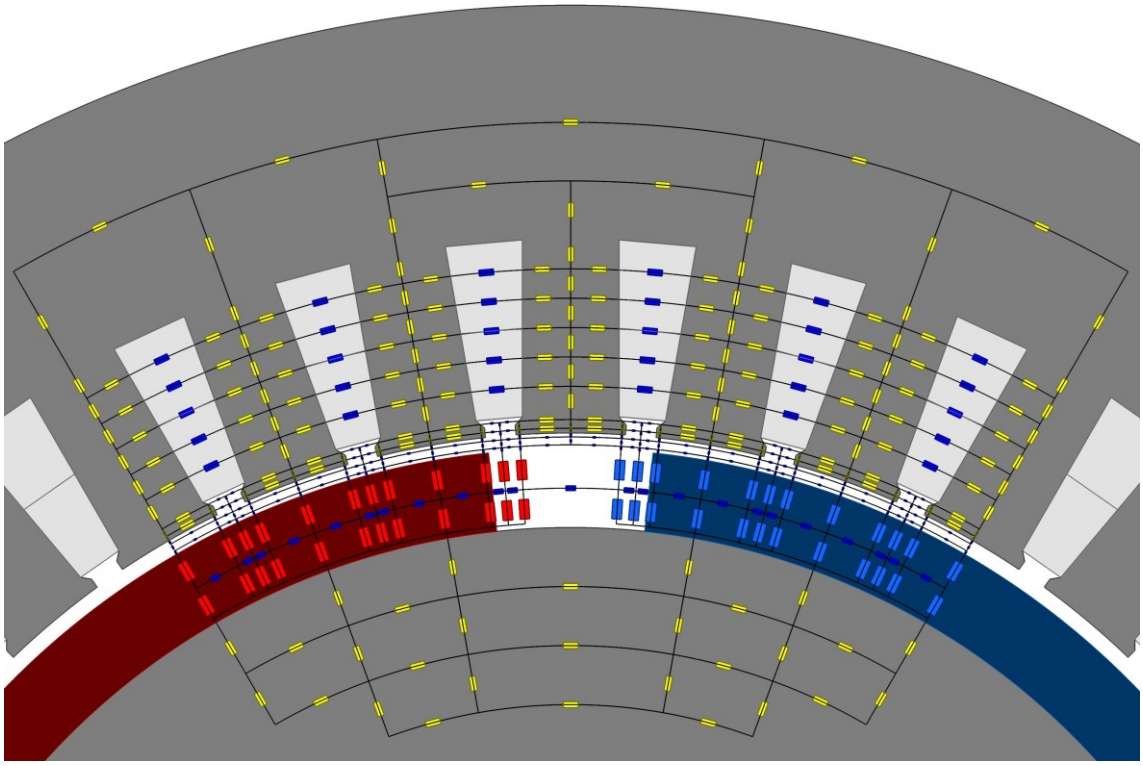

Source: Own authorship (2024)

To determine the magnetic flux density value of each PM source, a small C/C++ external code is coupled to the RN, and it verifies the position of each PM source in relation to the effective pole pitch value. If a PM source position remains within the PM width (and consequently within the effective pole pitch), its flux density value corresponds to the remanent magnetic flux density of the selected PM. However, in case of a PM source position exceeding the effective pole pitch, its flux density is either nullified or adjusted to a percentage of the PM remanent magnetic flux density. For instance, in Figure 28 and Figure 29, the red PM width extends up to the right tip of a stator tooth. If it actually extended over half of the adjacent slot opening, the flux density for the sources representing that PM region would be set to half (50%) of the PM remanent magnetic flux density. Since this is not the case, these sources are assigned a null flux density (0% of the PM remanent flux density). Consequently, they are turned into air reluctances, given that air and PM have almost the same relative permeability and that they do not contribute with magnetic flux anymore.

In essence, this RN is capable of precise modelling of PM machines with different PM arc lengths and effective pole pitches (KASPER et al., 2022). Furthermore, this approach allows the optimisation to accurately find the no-load

magnetic flux for different combinations of stator tooth widths (body and tips), slot opening widths, and PM widths. The developed C/C++ code can be seen in Appendix D. Since the air-gap and stator teeth tip reluctances in Figure 29 are relatively small size in comparison to the overall size of the machine, they are shown in detail in Figure 30.

Figure 30 – Air-gap and teeth tips reluctances of the no-load RN in detail

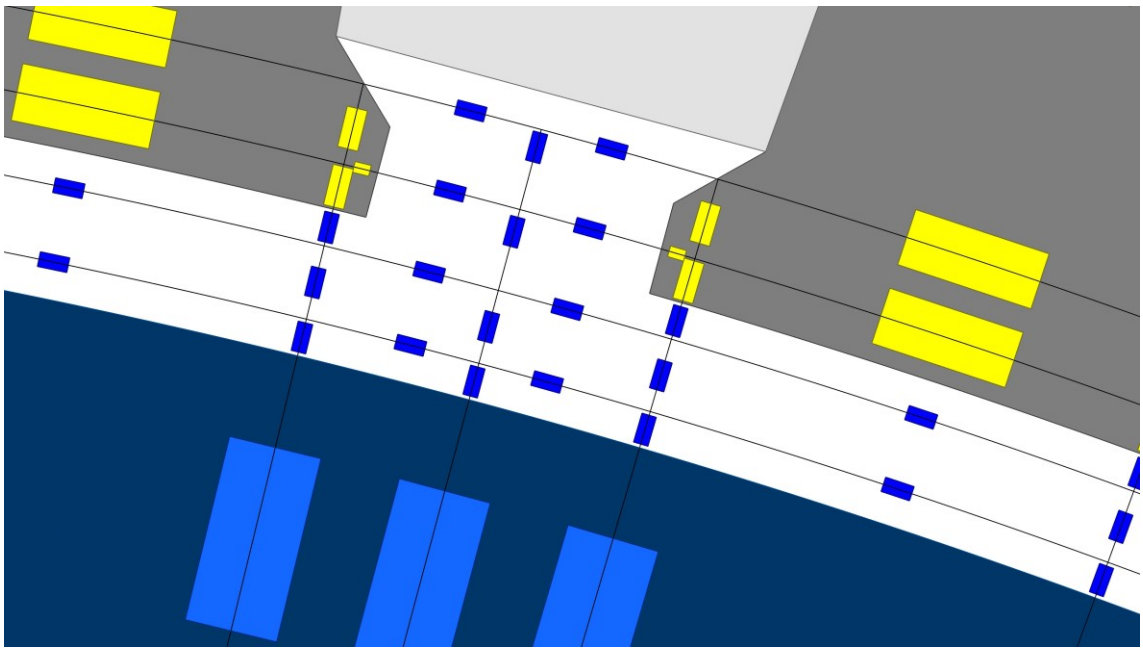

Source: Own authorship (2024)

Extracting the flux values of the reluctances that model the PM, air-gap and the middle of the stator teeth (representing the flux linked by the coils), the RN presents a 1.48% difference in the PM magnetic flux, 0.29% in the air-gap and 0.52% in the armature linked magnetic flux when comparing with the magnetostatic simulation of the machine, thus, verifying the developed RN. Even though this RN was developed over a single machine cross-section and parameters, it can represent other six pole 36 slots machines (or six slots per pole machines). This RN was also used to model other six slots per pole machines but with different effective pole pitches, showing similar differences when compared to FES.

4.1.1.2 Armature Reaction Submodel

As mentioned in section 4.1.1, to develop the RN, a magnetostatic simulation of the machine in the right position is required to observe the flux lines and guide the modelling. In order to represent the armature reaction of synchronous machines with

a FES, the MMF sources that are not the armature windings should be retrieved from the simulation (like rotor windings or PM), not producing magnetic flux that would alter the windings magnetic field and affecting the linked flux. Then, two of the three phase windings must be connected in series, and a direct current of nominal value should be applied while leaving the third phase winding de-energized. This should create a similar saturation condition as when the machine is operating at full load.

This method was developed for WRSG, where, as the rotor assumes different positions over time, the magnetic flux produced varies in value due to the variation in the reluctance path from the direct to the quadrature axis. By dividing the magnetic flux by the current, the inductance values are obtained depending on the position of the rotor. This way, the self-inductance of the two phases in series has only the second-order harmonic and a DC component different from zero (JONES, 1967).

In surface-mounted PMSG, the magnetic flux produced does not vary its value as the rotor assumes different positions over time since there is no variation of reluctance when going from the direct to the quadrature axis. Therefore, only one position of the machine needs to be modelled through the RN to obtain the linkage flux of the armature windings and, consequently, find the synchronous inductance (as shown by Equation (6)).

Starting the armature reaction RN by the MMF sources, as explained in section 4.1.1, they should be placed in every tooth under the influence of the MMF of a coil. Connecting phases A and B of the winding diagram of Figure 27 in series would create a new winding where the coil directions are not the same as before. By superimposing each coil and its direction over the machine cross-section, Figure 31 can be obtained, and it guides the understanding of how the MMF sources were modelled. Every coil starts with the colour black, indicating where each originates, and ends on white to indicate where they end.

The colour and arrows in Figure 31 also indicate the current direction. For example, considering the same reference of Figure 27, slot number one would be between teeth two and three of Figure 31 (in the white numbers). Thus, the current leaves the figure plane in the external layer of slot one and enters the figure plane in the internal layer of slot number five (which is between teeth 33 and 34). With the adopted current directions, by using the right-hand rule, it is possible to determine the direction of the MMF produced by each coil. The value of each MMF source will be the sum of the contributions of each coil on a particular tooth. If the MMF of the coils over

a tooth have the same direction, their values are added up, otherwise, they subtract each other (MOURA et al., 2020).

Figure 31 – Magnetomotive sources analysis and modelling

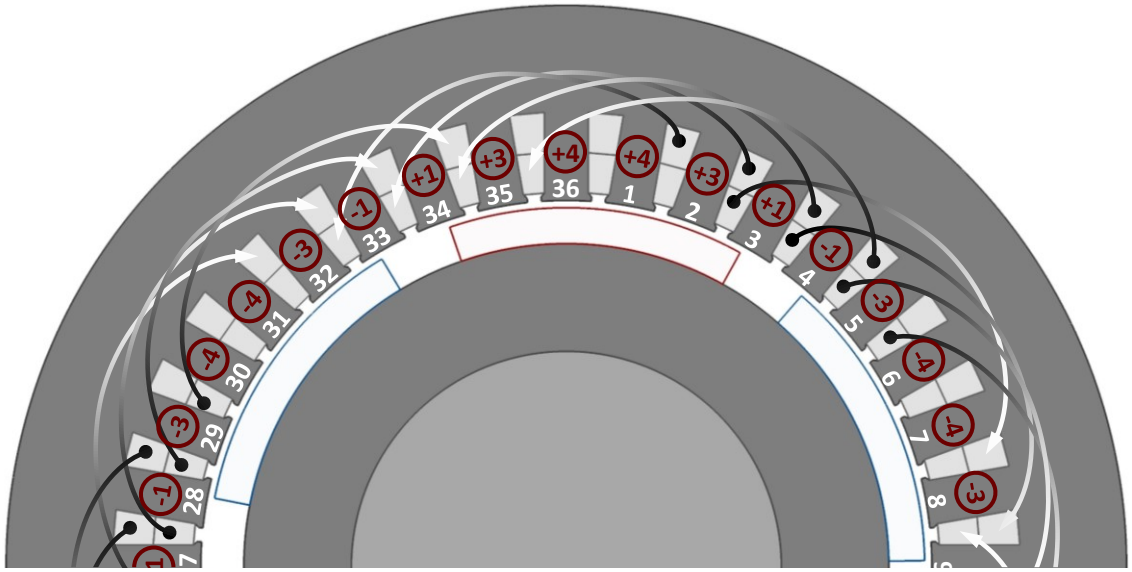

Source: Own authorship (2024)

In Figure 31, every tooth has a signal followed by a number, indicating the MMF direction (going in or out of the machine) and their resultant value. For example, tooth number one has a +4 on it since there are four coils over it, and they produce MMF in the same direction, which is conventional as going towards the inside of the machine. Meanwhile, tooth number four has -1 on it since there are three coils over it, two of which produce MMF adopted as going out of the machine and one MMF towards the inside.

Similarly as in section 4.1.1.1, due to machine symmetry, only a sixth of the machine has to be modelled. Thus, MMF sources and reluctance modelling of the armature reaction RN can be restrained within the linkage flux that goes from the right half of the slot between teeth one and thirty-six to the left half of the slot between teeth six and seven. For this RN, reluctance modelling is performed by analysing the flux lines of Figure 32.

Figure 32 – Armature reaction magnetic flux lines for the RN construction

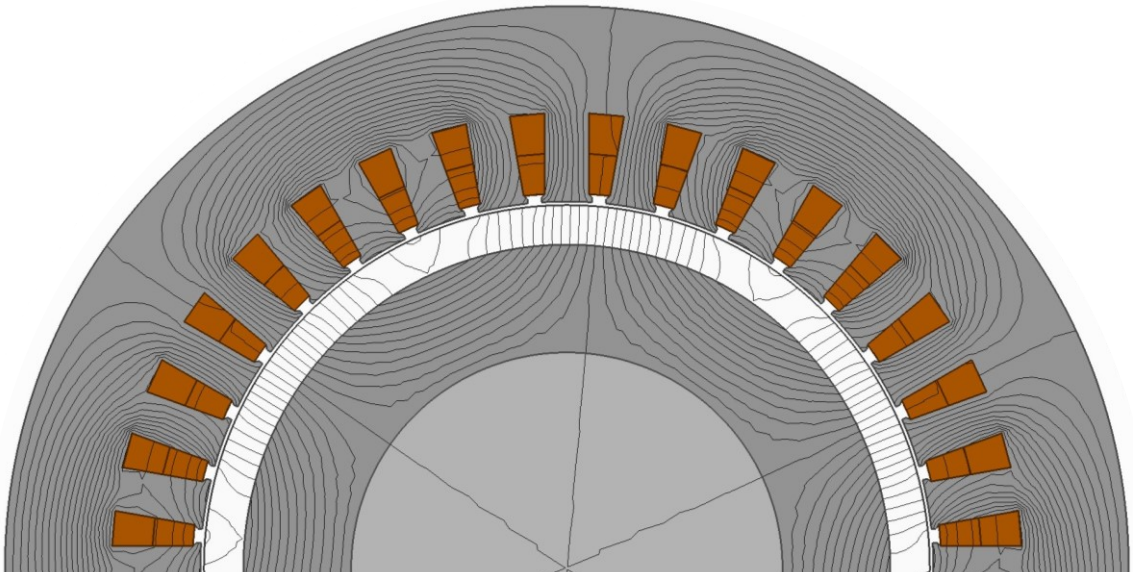

Source: Own authorship (2024)

Analysing the flux paths of Figure 32, reluctances are added to the network until the flux values in several regions of the machine present acceptable differences when compared to FES. Since the flux lines of the ferromagnetic material have a simpler behaviour, they are relatively easier to model. In contrast, those that represent the air-gap are more complex since the flux path is not well defined there. The armature reaction RN is represented over the PMSG cross-section in Figure 33.

Just as in the representation of the no-load RN (Figure 29), the yellow rectangles represent the iron reluctances that accounts for saturation (which has the same BH-curve of the electrical steel on the no-load RN), and the blue rectangles represent the air reluctances. However, now the magnetomotive force sources are represented by the red circles, and their values were explained earlier. This reluctance network is also large (with over 400 elements). Thus, the length, area, and MMF values of every reluctance and source are presented in Appendix E. Once again, the air-gap and stator teeth tip reluctances are shown in detail in Figure 34 due to their relatively small size in comparison to the overall size of the machine.

Figure 33 – Developed armature reaction RN over the PMSG cross-section

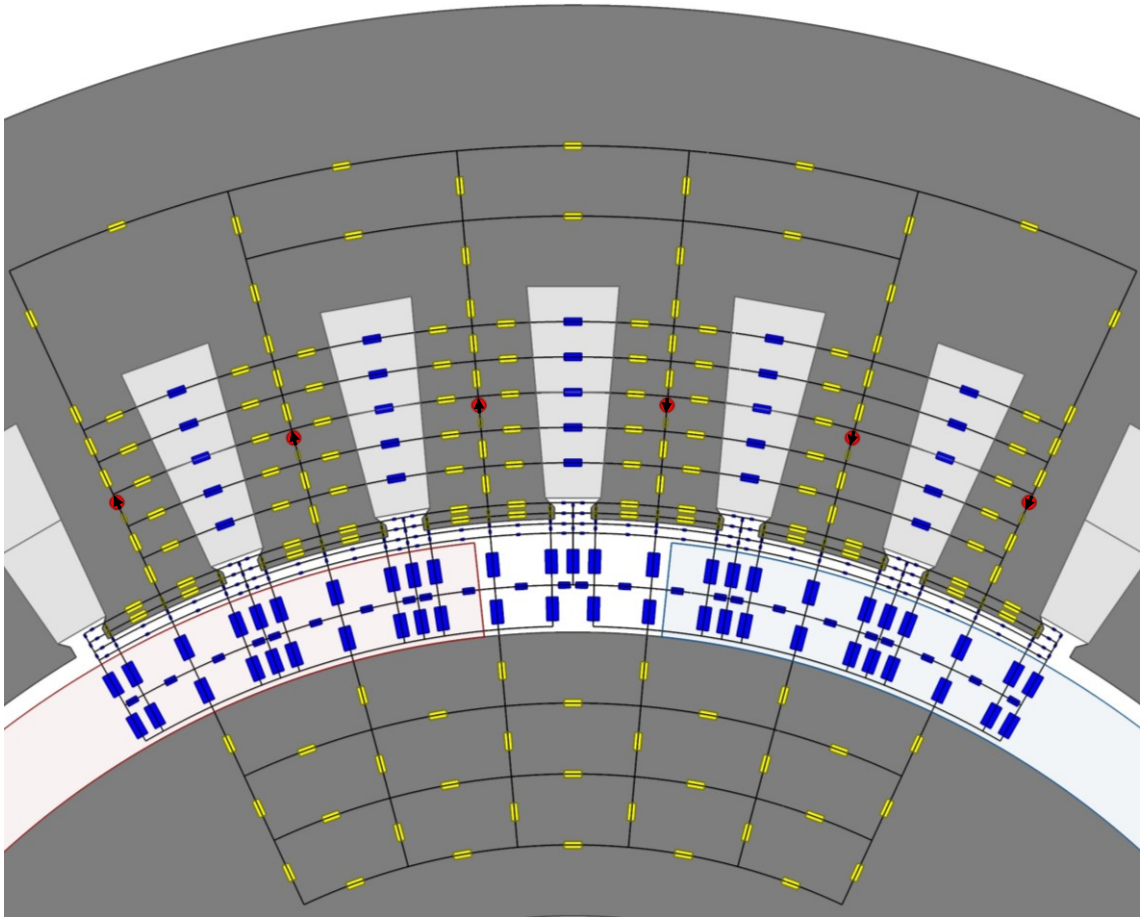

Source: Own authorship (2024)

Adding the extracted magnetic flux values of the reluctances that model the middle of the stator teeth would provide the linkage flux. Then, dividing this value by the armature current results in the synchronous inductance of the machine. This last version of the RN presents a 0.72% difference in the synchronous inductance value when compared with the magnetostatic simulation of the machine. This acceptable difference verifies the second developed RN. Similarly as the no-load RN, this RN was developed over a single machine cross-section and parameters, but can also represent other six pole, 36 slots machines (or six slots per pole machines).

Figure 34 – Air-gap and teeth tips reluctances of the armature reaction RN in detail

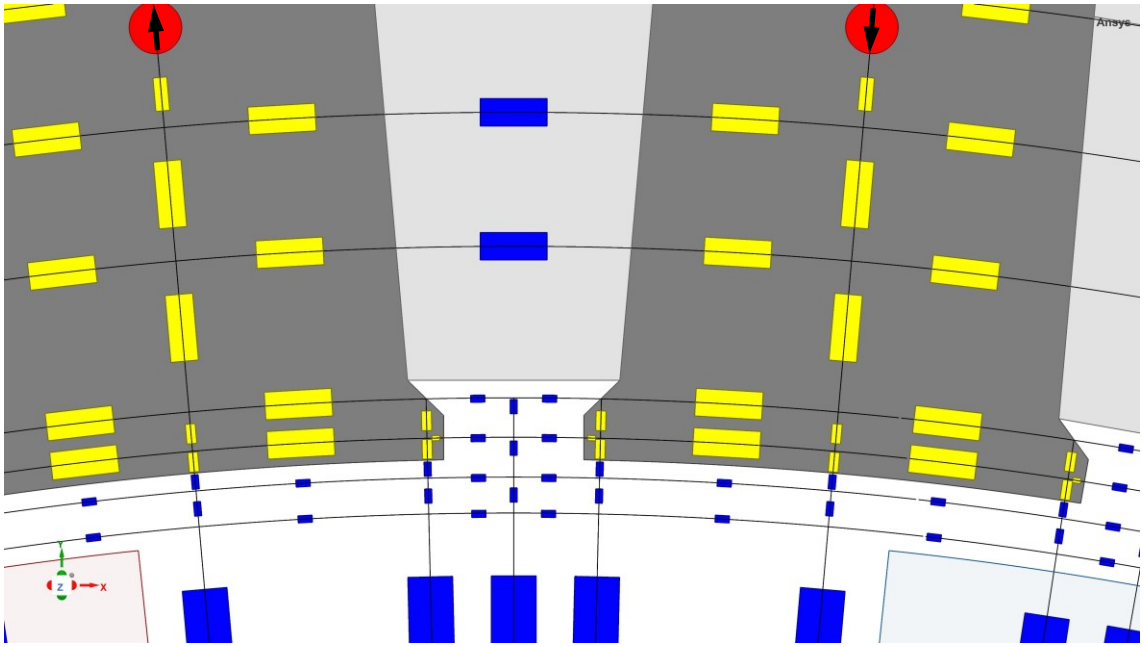

Source: Own authorship (2024)

5 RESULTS AND DISCUSSIONS

This Section concentrates the results of the design methodology, applied to design both surface-mounted and salient-pole PMSG, and the design optimisation of surface-mounted PMSG.

To show the proposed design methodology's (presented in Section 3) effectiveness, it is applied to design a PMSG with the non-salient pole geometry of Figure 20. To complete the design of the generator and find its geometry, a handful of parameters must be imposed. The specifications of the generator are presented in Table 2, and all values of these design choices are shown in Table 3, Table 4, Table 5, Table 6 and Table 9. These were found following the suggested ranges discussed in section 3.3 and resumed in Table 1. The design results are compared with finite element simulations to allow discussions on their accuracy (section 5.1).

A second design is developed with the salient-pole PMSG topology of Figure 23 and Figure 24. The imposed parameters now have their values chosen so that the designed generator precisely matches the commercial machine geometry and has the same output characteristics as the commercial machine. FES are used to aid the design of this more complex machine and, ultimately, to verify the accuracy of the method when applied to a commercial machine (section 5.2).

Finally, the optimization-oriented model is used to find an optimum machine design according to the chosen objective functions. A Pareto front is brought to compare the results of these confronting optimisation objectives and provide insights that help in selecting a final machine. Once again, finite element simulations are used to verify the accuracy of the electromagnetic model and the optimisation procedure (section 5.3).

5.1 Surface-Mounted PMSG Design

As seen in the flowchart of the proposed design method (Figure 21), the PMSG design starts with the generator specifications shown in Table 2.

Table 2 – Surface-mounted PMSG design specifications

Symbol	Unit	Description	Value
S_{Ed}	VA	Desired Output Power	100,000
V_{Td}	V	Desired Terminal Voltage	380
f	Hz	Electrical Frequency	60
PF	–	Power Factor	0.9
n	rpm	Rotation	1200

Source: Own authorship (2024)

The values of the imposed parameters used to complete the design of the generator and find its complete geometry are shown in Table 3.

Table 3 – Surface-mounted PMSG geometry-imposed parameters

Symbol	Unit	Description	Value
D_{Ro}	mm	Rotor outer diameter	410
$k_{\alpha P}$	-	Pole pitch factor	0.800
k_{AG}	-	Air-gap factor	0.010
PC	-	Permeance coefficient	5.00
B_{Ry}	T	Magnetic flux density in the rotor yoke	1.30
N_S	slots	Number of slots	36.0
k_{Sow}	-	Slot opening factor	0.702
k_{Soh}	-	Slot opening height factor	0.313
k_{Sw}	-	Slot wedge height factor	0.250
k_{TS}	-	Tooth-to-slot width factor	2.08
k_{PMSy}	-	PM width to stator yoke factor	0.374
k_{SyS}	-	Stator yoke to slot height factor	0.752

Source: Own authorship (2024)

With the values from Table 2 and Table 3 and employing the design procedure detailed in Section 3, all the dimensions of the PM generator are obtained and shown in Table 4.

Table 4 – Surface-mounted PMSG main dimensions

Symbol	Unit	Description	Value
P	–	Number of poles	6.00
α_P	°	Pole pitch	60.0
L_{AG}	mm	Air-gap length	4.10
h_{PM}	mm	PM height	20.5
W_{PM}	mm	PM width	163
L_G	mm	Generator stack length	86.4
D_{PMt}	mm	Diameter at the PM top	369
D_{Ri}	mm	Rotor inner diameter	246
α_S	°	Slot pitch	5.00
D_{Si}	mm	Stator inner diameter	418
W_{So}	mm	Slot opening width	8.00
h_{So}	mm	Slot opening height	2.50
h_{Sw}	mm	Slot wedge height	2.00
D_{St}	mm	Diameter at the slot top	427
θ_{St}	°	Angle at the slot top	3.25
W_{St}	mm	Slot width at the top	12.1
W_t	mm	Teeth width at the top	25.2
W_{Sw}	mm	Slot wedge width	2.06
h_{Sy}	mm	Stator yoke height	61.0
h_S	mm	Slot height	45.9
θ_{Sei}	°	Inclination angle of the slot edge	5.00
W_{Sb}	mm	Slot width at the bottom	20.2
D_{So}	mm	Stator outer diameter	641

Source: Own authorship (2024)

To provide a graphical representation of these generator dimensions presented in Table 4, Figure 35 shows the generator cross-section when constructed in the Ansys Maxwell software.

Figure 35 – Designed surface-mounted PMSG

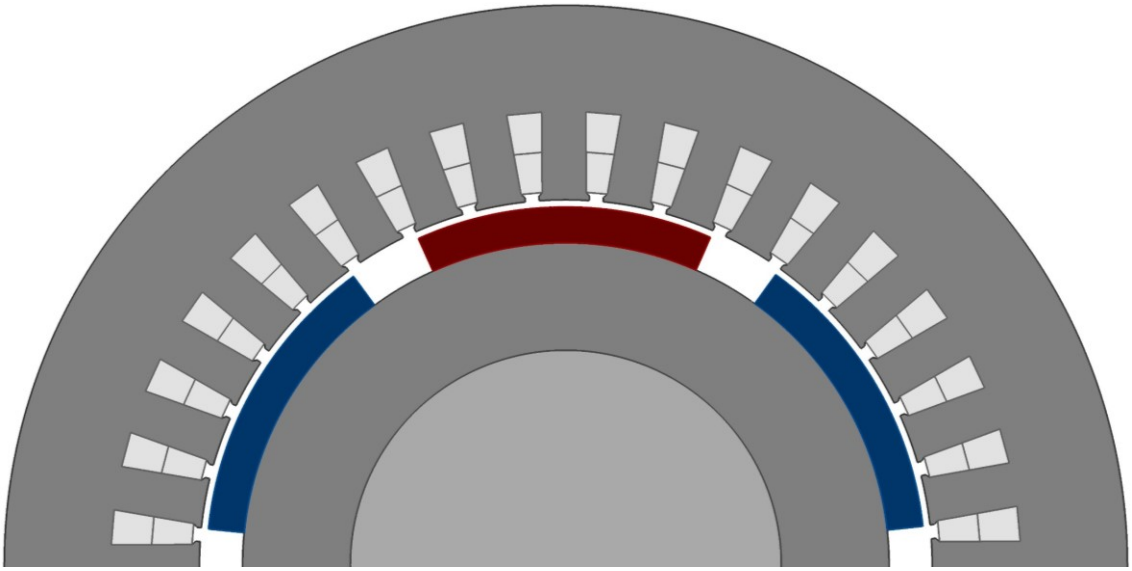

Source: Own authorship (2024)

At the very beginning of the design procedure, a permanent magnet and its permeance coefficient are chosen. In this design, the Neodymium-Iron-Boron of grade 42 and thermal class SH was selected. Moreover, as the demagnetisation curve depends on the operating temperature of the PM, a maximum temperature rise of 100°C was considered, resulting in an operative temperature (T_{op}) of 120°C if the ambient temperature (T_{ref}) is considered to be around 20°C. Therefore, the demagnetisation curve of the N42SH from the spreadsheet of its manufacturer (K&J MAGNETICS, 2024) is shown in Figure 36.

Figure 36 – Demagnetization curve of the N42SH at 120 °C.

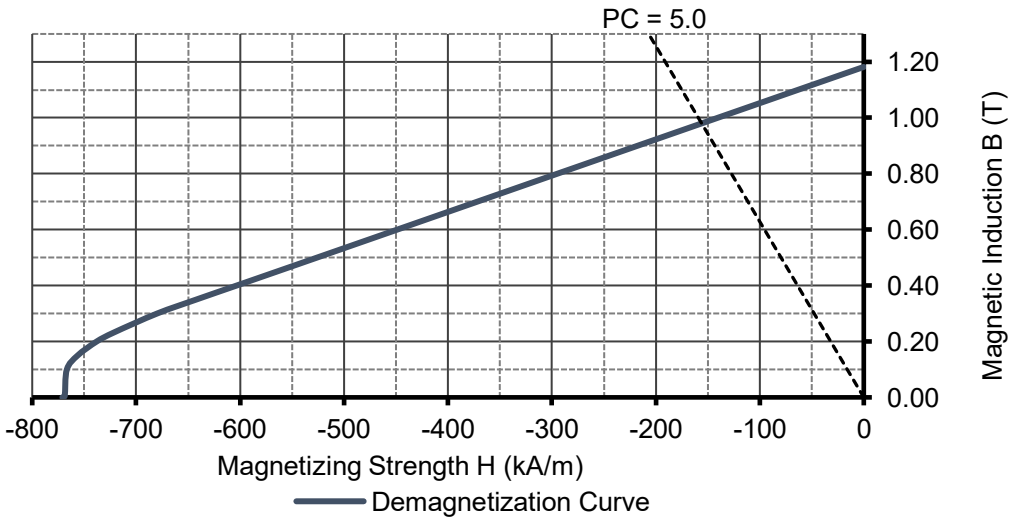

Source: Own authorship (2024)

The PM magnetic flux calculation parameters, including the operative magnetic flux density of the N42SH from Figure 36, are summarised in Table 5.

Table 5 – Surface-mounted PMSG flux-related imposed parameters

Symbol	Unit	Description	Value
B_{PM}	T	Operative permanent magnet flux density	0.980
k_{MS}	-	Machine shape factor	0.224
$\Delta\varphi_{PMAG}$	-	PM to air-gap leakage factor	0.973[1]
$\Delta\varphi_{AGA}$	-	Air-gap to armature leakage factor	1.00[1]
T_{ref}	°C	Reference temperature	20.0
T_{op}	°C	Operating temperature	120

[1]Obtained through magnetostatic FES.
Source: Own authorship (2024)

The remaining design information concerns the machine's winding. A distributed double-layer winding was chosen, resulting in two coils per pole per phase. The parameters imposed throughout the armature winding definition are presented in Table 6.

Table 6 – Surface-mounted PMSG imposed winding parameters

Symbol	Unit	Description	Value
J_A	A/mm²	Armature current density	5.75
E_{Af}	V	Estimated induced voltage	281
N_{ph}	-	Number of phases	3.00
k_{Ac}	-	Coil-shortening factor	0.833
k_{Sf}	-	Slot fill factor	0.500
N_{Cp}	paths	Number of parallel paths in the armature windings	1.00
N_{Sl}	layers	Numbers of slot layers	2.00
k_{Cop}	-	Consequent pole factor	1.00

Source: Own authorship (2024)

The resulting winding parameters are found with the imposed parameters of Table 6 and can be seen in Table 7.

Table 7 – Surface-mounted PMSG calculated winding parameters

Symbol	Unit	Description	Value
α_{Ac}	°	Armature coil pitch	150
$\Delta\emptyset_{Cs}$	–	Coil shortening factor	0.966
q	slots	Number of slots per pole per phase	2.00
$\Delta\emptyset_{Wd}$	–	Winding distribution factor	0.966
T_A	–	Number of turns of the armature per phase	84.0
N_{Cs}	–	Number of coils in series per phase	6.00
N_{Cpp}	–	Number of coils per group per phase	2.00
T_{Ac}	–	Number of turns of the armature per coil	7.00
S_S	mm²	Slot surface	740
S_{Ac}	mm²	Armature conductor surface	26.4

Source: Own authorship (2024)

Trying to match the armature conductor surface of Table 7, a combination of cooper conductors was chosen to find the resistance per kilometre of the armature conductor (R_{km}). By combining seven wires AWG 14 in parallel with nine AWG 16, which results in a total conductor surface of 26.35mm², an equivalent resistance is 0.643 Ω/km (at 20 °C). After completing the armature resistance, synchronous reactance, and terminal voltage calculations (developed in Sections 3.2.6, 3.2.7, and 3.2.8, respectively), the terminal voltage-related parameters are found, composing Table 8.

Table 8 – Surface-mounted PMSG terminal voltage and related parameters

Symbol	Unit	Description	Value
R_A	Ω	Armature single-phase resistance	0.063
L_{ag}	H	Air gap inductance	0.001
M_{ag}	H	Air gap mutual inductance	-0.000
L_{Sl}	H	Slot-leakage inductance	0.001
L_S	H	Synchronous inductance	0.002
X_S	Ω	Synchronous reactance	0.792
ϕ	°	Displacement angle between terminal voltage and armature current	25.8
δ	°	Load angle	20.4
I_A	A	Armature current	152
V_φ	V	Phase value of the terminal voltage	220
V_T	V	Terminal voltage	380

Source: Own authorship (2024)

To estimate the loss and efficiency of the generator, the parameters of Table 9 were imposed.

Table 9 – Surface-mounted PMSG loss-imposed parameters

Symbol	Unit	Description	Value
ρ_{ee}	g/cm³	Electrical steel mass density	7.75[1]
P_F	W/kg	Foucault loss per kilogram	3.68[1]
P_h	W/kg	Hysteresis loss per kilogram	3.68[1]
k_{Syh}	-	Hysteresis losses factor (yoke)	2.00
k_{SyF}	-	Foucault losses factor (yoke)	1.80
k_{Sth}	-	Hysteresis losses factor (teeth)	1.20
k_{StF}	-	Foucault losses factor (teeth)	2.50
k_{PM}	W/m²	PM specific losses factor	200
k_{Sl}	-	Stray losses factor	0.020

[1]Mass density and losses per kilogram of the electrical steel M400-50A E170.
Source: Own authorship (2024)

Finally, the losses and the efficiency of the designed PMSG are presented in Table 10.

Table 10 – Surface-mounted PMSG losses and efficiency

Symbol	Unit	Description	Value
P_{Ac}	kW	Armature copper losses	4.35
P_{Syh}	kW	Stator yoke hysteresis losses	0.534
P_{SyF}	kW	Stator yoke Foucault losses	0.577
P_{Sth}	kW	Stator teeth hysteresis losses	0.087
P_{StF}	kW	Stator teeth Foucault losses	0.217
P_{PMs}	kW	Permanent magnet losses	0.02
P_T	kW	Total losses	5.79
η	%	Estimated efficiency	94.0

Source: Own authorship (2024)

The validation of the designed PM synchronous generator is performed with finite element simulations, which were all carried out at the Ansys Maxwell in 2D. These time-stepping simulations consider the ferromagnetic saturation, naturally. The no-load and full-load magnetic flux lines and densities are presented in Figure 37 and Figure 38, respectively.

Figure 37 – Surface-mounted PMSG finite-element solution of the magnetic field and magnetic flux density distribution under no-load operation

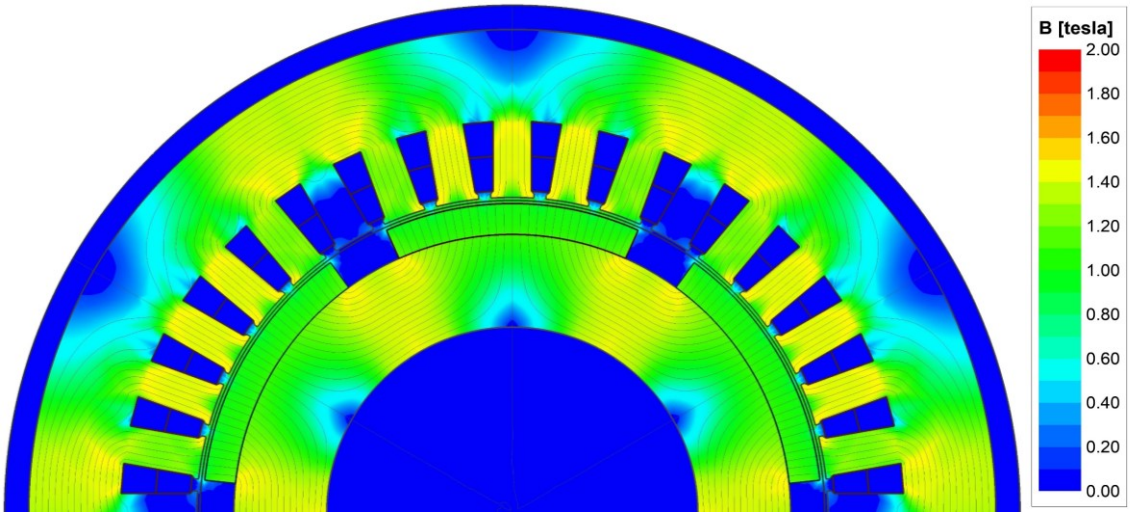

Source: Own authorship (2024)

Figure 38 – Surface-mounted PMSG finite-element solution of the magnetic field and magnetic flux density distribution under full-load operation

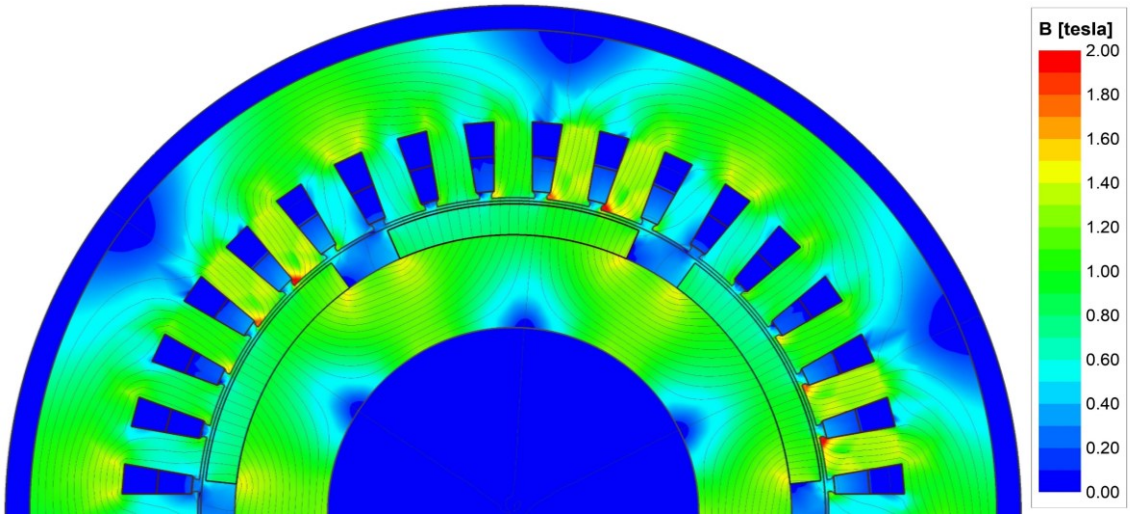

Source: Own authorship (2024)

Other important results extracted from the performed FES are the phase-to-phase voltages, shown in Figure 39, and the phase armature currents, presented in Figure 40, both under full-load operation. Moreover, Ansys Maxwell also allows a harmonic content calculation for both curves through a Fast Fourier Transformation (FFT).

Figure 39 – Surface-mounted PMSG full-load phase-to-phase voltages

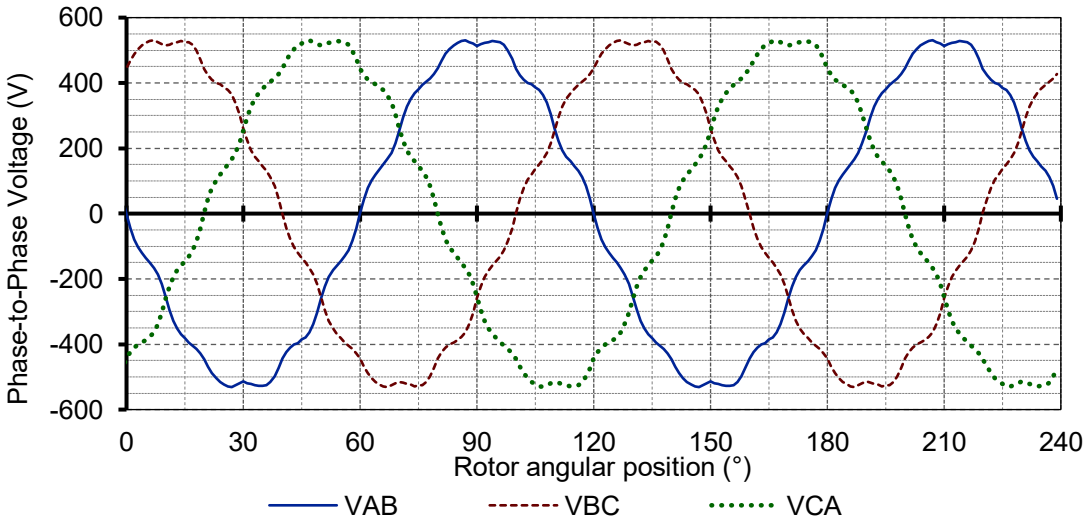

Source: Own authorship (2024)

The Total Harmonic Content (THD) of the phase-to-phase voltages of Figure 39 is 4.934%, whereby the eleventh and the thirteenth order components are the most significant (with 3.908% and 1.282%, respectively). The FFT of the armature currents of Figure 40 resulted in a THD of 7.493%, where the third-order component is the most significant, contributing 6.879%, followed by the ninth with 1.016%.

Figure 40 – Surface-mounted PMSG full-load armature currents

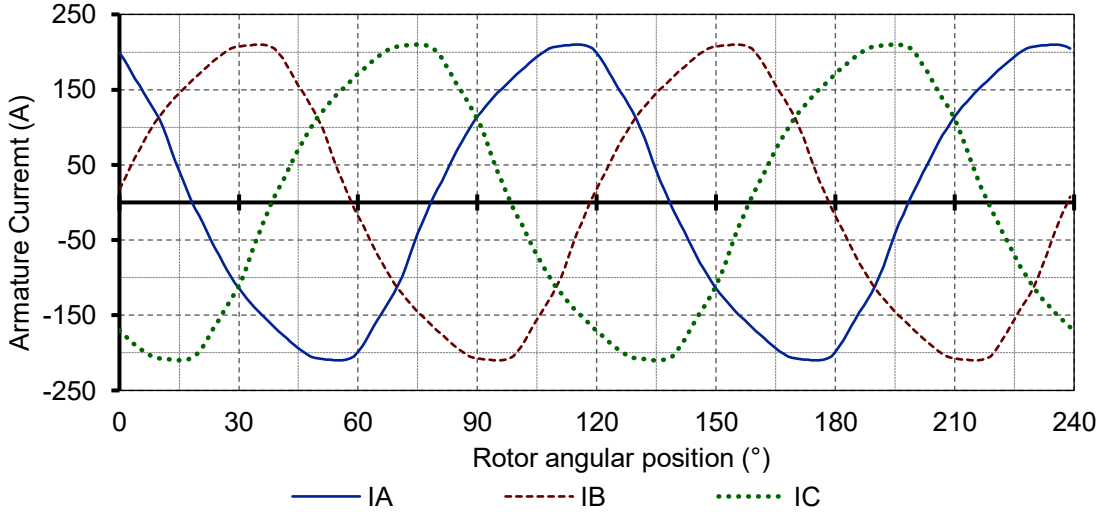

Source: Own authorship (2024)

The main electromagnetic results are shown in Table 11, and a percentual difference with the finite element simulation (in Maxwell 2D) is also presented. From the difference values, it is clear that the proposed design methodology presents good accuracy, with the differences between the design model and finite element simulation

being around 2% in terminal voltage and 3% armature current. The four to five per cent difference in the output power is a consequence of the terminal voltage and armature current differences and is within an acceptable range, thus not affecting the overall merit of the method.

Table 11 – Surface-mounted PMSG main electromagnetic results

Symbol	Unit	Design	FES	Difference (%)
B_{AG}[1]	T	0.897	0.899	0.285
I_A	A	152.0	148.0	-2.710
V_T	V	382.3	375.4	-1.831
S_E[2]	kVA	100.6	96.23	-4.590
P_E[3]	kW	90.58	87.02	-4.093

[1]Flux density during no-load operation with the magnetic flux measured at the middle of the air-gap. [2]FES result is the product of rms values of V_T, I_A and $\sqrt{3}$. [3]FES result obtained by the mean value of the instantaneous power.
Source: Own authorship (2024)

5.2 Salient-Pole Commercial PMSG Design

Applying the proposed design method, developed for surface-mounted PMSG, to find the commercial PMSG also starts by defining the generator specifications, which are shown in Table 12.

Table 12 – Commercial PMSG design specifications

Symbol	Unit	Description	Value
S_{Ed}	VA	Desired Output Power	30,000
V_{Td}	V	Desired Terminal Voltage	220
f	Hz	Electrical Frequency	180
PF	–	Power Factor	1
n	rpm	Rotation	1800

Source: Own authorship (2024)

As seen throughout Section 3, a handful of imposed parameters had to be imposed to find the complete geometry of the generator. In order to match the exact geometry and output characteristics of the commercial machine, the parameters of rotor and stator sizings are the ones in Table 13.

Table 13 – Commercial PMSG geometry-imposed parameters

Symbol	Unit	Description	Value
D_{ro}	mm	Rotor outer diameter	519
$k_{\alpha P}$	–	Pole pitch factor	0.921
PC	–	Permeance coefficient	3.43
k_M	–	PM form factor	4.17
θ_{PM}	°	Angle between PMs at the centre	180
k_{Ro}	–	PM tip to rotor outer diameter factor	0.208
k_{fbt}	–	Barrier top width to PM height factor	0.675
k_{fbb}	–	Barrier bottom width to PM height factor	0.575
k_{fbh}	–	Barrier height to PM height factor	0.708
k_{fb}	–	Barrier gap to PM height factor	0.125
θ_{fb}	°	Inclination angle of the flux barrier	15.0
k_{Ry}	–	Rotor yoke factor	2.79
k_{AG}	–	Air-gap length factor	0.007
N_S	–	Number of slots	72.0
k_{Sow}	–	Slot opening factor	0.486
k_{Soh}	–	Slot opening height factor	0.286
k_{Sw}	–	Slot wedge height factor	0.197
k_{TS}	–	Tooth-to-slot width factor	3.06
k_{PMSy}	–	PM width to stator yoke height factor	2.03
k_{SyS}	–	Stator yoke to slot height factor	0.185

Source: Own authorship (2024)

With the design specifications and the imposed parameters, the permanent magnet synchronous generator's main dimensions obtained with the procedure detailed in Section 3 are in Table 14.

Table 14 – Commercial PMSG main dimensions

Symbol	Unit	Description	Value
P	–	Number of poles	12.0
α_P	°	Pole pitch	5.00
L_{AG}	mm	Air-gap length	3.50
h_{PM}	mm	PM height	12.0
W_{PM}	mm	PM width	50.0
L_{Ro}	mm	Length of the gap between the PM tip and the rotor outer diameter	2.50
h_{fb}	mm	Flux barrier height	8.50
L_{fb}	mm	Length of the gap between PM and flux barrier	1.50
W_{fbt}	mm	Flux barrier top width	8.10
W_{fbb}	mm	Flux barrier bottom width	6.90
L_{PMc}	mm	Length of the gap between PMs at the centre	1.00
D_{PMt}	mm	Diameter at the PM top	479
D_{Ri}	mm	Rotor inner diameter	201
L_G	mm	Machine stack length	60.3
α_S	°	Slot pitch	5.00
D_{Si}	mm	Stator inner diameter	526
W_{So}	mm	Slot opening width	3.50
h_{So}	mm	Slot opening height	1.00
h_{Sw}	mm	Slot wedge height	0.690
D_{St}	mm	Diameter at the slot top	529
θ_{St}	°	Angle at the slot top	1.23
W_t	mm	Teeth width at the top	17.4
W_{St}	mm	Slot width at the top	5.69
W_{Sw}	mm	Slot wedge width	1.09
h_{Sy}	mm	Stator yoke height	102
h_S	mm	Slot height	18.8
θ_{Sei}	°	Inclination angle of the slot edge	2.50
W_{Sb}	mm	Slot width at the bottom	7.33
D_{So}	mm	Stator outer diameter	770

Source: Own authorship (2024)

These dimensions result in the generator geometry of Figure 41, which is the exact geometry of the known commercial permanent magnet generator.

Figure 41 – Commercial PMSG cross-section

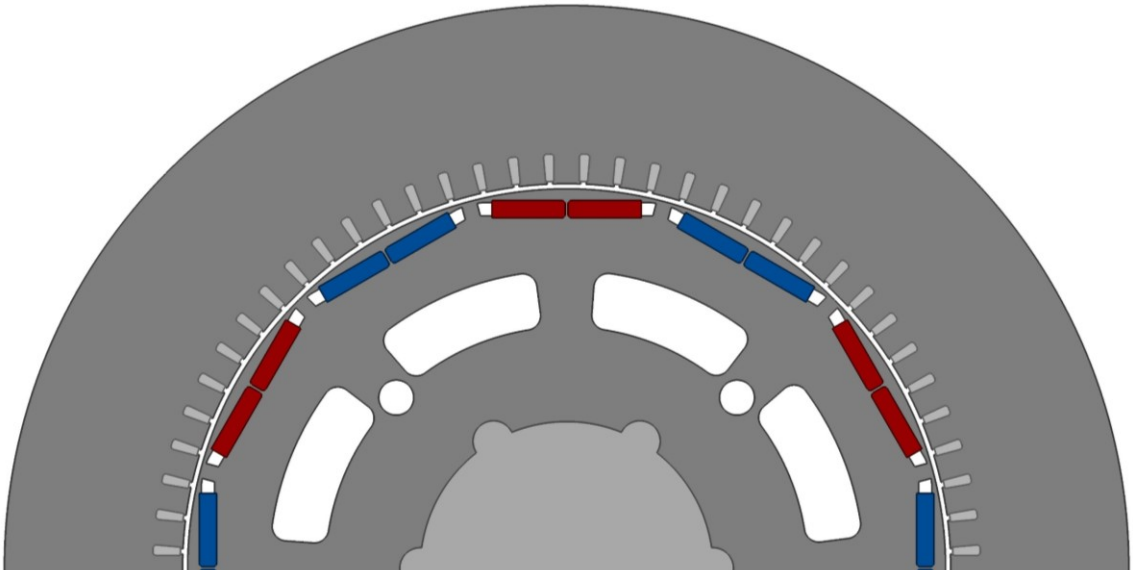

Source: Own authorship (2024)

The permanent magnet used in this commercial generator is Neodymium-Iron-Boron of grade 28 and thermal class UH. From the spreadsheet and graphics of the permanent magnet (provided by the manufacturer), the demagnetisation curves for different temperatures, going from 20°C to 180°C, are extracted and shown in Figure 42.

Figure 42 – Demagnetization curves of the N28UH

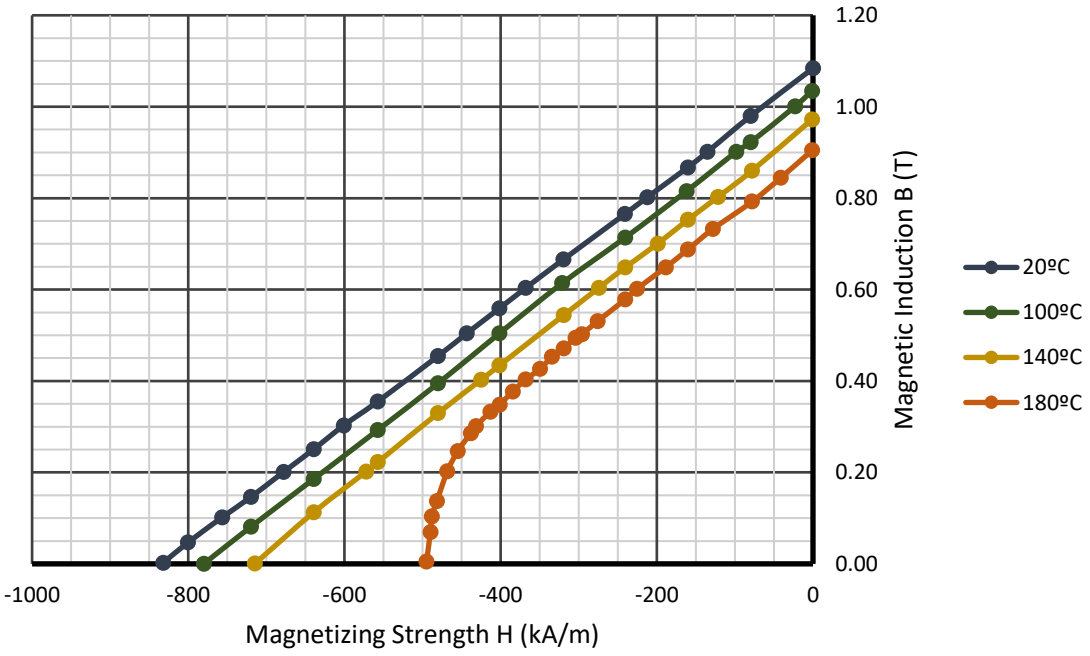

Source: Own authorship (2024)

In this first version, the considered permanent magnet operative temperature is 20°C. From the permeance coefficient (shown in Table 13) and the demagnetisation curve of this temperature, the operative magnetic flux density of the PM is found, and the flux per pole can be calculated (with equation (33)). The flux-related parameters imposed in the PM magnetic flux calculation stage are resumed in Table 15.

Table 15 – Commercial PMSG flux-related imposed parameters

Symbol	Unit	Description	Value
B_{PM}	T	Operative permanent magnet flux density	0.825
k_{MS}	-	Machine shape factor	0.116
$\Delta\varphi_{PMAG}$	-	PM to air-gap leakage factor	0.788[1]
$\Delta\varphi_{AGA}$	-	Air-gap to armature leakage factor	0.982[1]
T_{ref}	°C	Reference temperature	20.0
T_{op}	°C	Operating temperature	20.0

[1]Obtained through magnetostatic FES.
Source: Own authorship (2024)

The remaining design information concerns the machine's winding, which the generator manufacturer also provided. This machine uses consequent pole concentric windings. Thus, the consequent pole factor is set to two, as can be seen in the imposed winding parameters of Table 16.

Table 16 – Commercial PMSG imposed winding parameters

Symbol	Unit	Description	Value
J_A	A/mm²	Armature current density	5.00
E_{Af}	V	Estimated induced voltage	152
N_{ph}	–	Number of phases	3.00
k_{Ac}	–	Coil shortening factor	1.00
k_{Sf}	–	Slot fill factor	0.50
N_{Cp}	–	Number of coils in parallel per phase	1.00
N_{Sl}	–	Number of slot layers	1.00
k_{Cop}	–	Consequent pole factor	2.00

Source: Own authorship (2024)

As a result, this machine's winding has two coils per group per phase, as shown in the resulting winding parameters of Table 17.

Table 17 – Commercial PMSG winding calculated parameters

Symbol	Unit	Description	Value
α_{Ac}	°	Armature coil pitch	180
$\Delta\emptyset_{Cs}$	–	Coil shortening factor	1.00
q	–	Number of slots per pole per phase	2.00
$\Delta\emptyset_{Wd}$	–	Winding distribution factor	0.999
T_A	–	Number of turns of the armature per phase	48.0
N_{Cs}	–	Number of coils in series per phase	6.00
N_{Cpp}	–	Number of coils per group per phase	2.00
T_{Ac}	–	Number of turns of the armature per coil	4.00
S_S	mm²	Slot surface	122
S_{Ac}	mm²	Armature conductor surface	15.3

Source: Own authorship (2024)

Each turn of the armature coil is made of one AWG14 in parallel with ten AWG16 to match the calculated conductor surface. With this combination, the armature resistance is calculated since the total length of the coil and the conductor resistance are known.

Following the armature resistance, the armature reaction should be calculated since, as explained in Section 2.2.2, the terminal voltage is also affected by the armature reaction. In salient-pole machines, it is composed by the direct and quadrature axis reactances. The procedure to obtain these electromagnetic quantities is explained along with the complementary design equation of the commercial machine design in Appendix A. Following the described method, an inductance curve as a function of rotor position can be extracted, as shown in Figure 43.

Figure 43 – Commercial PMSG inductance as a function of rotor position

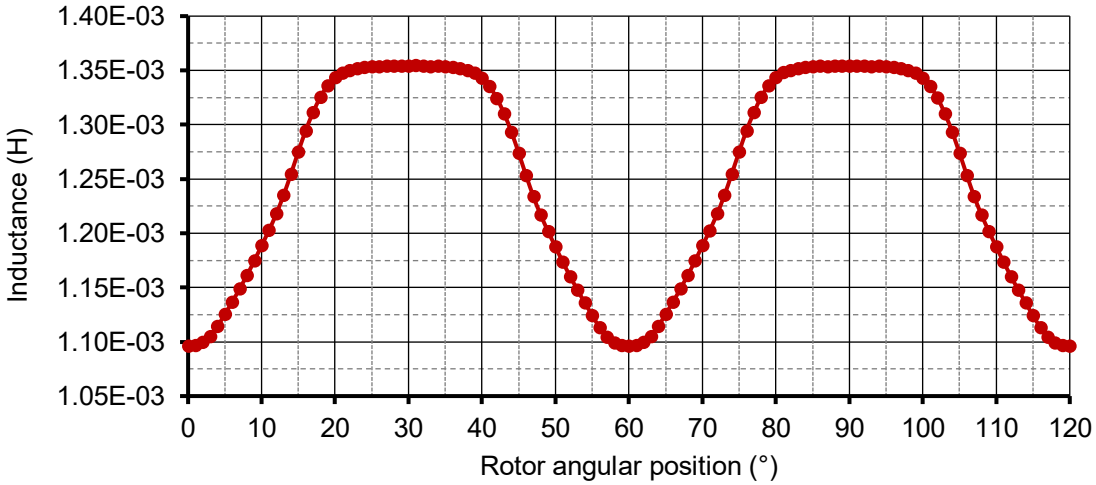

Source: Own authorship (2024)

From Figure 43, the maximum and minimum inductance values are 1.35 mH and 1.10 mH, and with equation (119), the d-q axis reactances are calculated. With the three last-mentioned quantities (armature resistance and axis reactances), the terminal voltage of the generator can be found from equation (63) to (120) and is presented in Table 18.

Table 18 – Commercial PMSG terminal voltage and related parameters

Symbol	Unit	Description	Value
R_A	Ω	Armature single-phase resistance	0.031
L_d	mH	Direct axis synchronous inductance	0.548
L_q	mH	Quadrature axis synchronous inductance	0.677
X_d	Ω	Direct axis synchronous reactance	0.619
X_q	Ω	Quadrature axis synchronous reactance	0.766
ϕ	°	Displacement angle between terminal voltage and armature current	0.000
δ	°	Load angle	24.4
I_d	A	Direct axis component of the armature current	31.6
I_q	A	Quadrature axis component of the armature current	69.7
V_d	V	Direct axis component of the terminal voltage	52.4
V_q	V	Quadrature axis component of the terminal voltage	130
V_T	V	Terminal voltage	242

Source: Own authorship (2024)

The losses and the efficiency were also estimated for this commercial PMSG. To estimate the loss and efficiency of the generator, the parameters of Table 19 were imposed.

Table 19 – Commercial PMSG loss-imposed parameters

Symbol	Unit	Description	Value
ρ_{ee}	g/cm³	Electrical steel mass density	7.75[1]
P_F	W/kg	Foucault loss per kilogram	3.68[1]
P_h	W/kg	Hysteresis loss per kilogram	3.68[1]
k_{Syh}	-	Hysteresis losses factor (yoke)	2.00
k_{SyF}	-	Foucault losses factor (yoke)	1.80
k_{Sth}	-	Hysteresis losses factor (teeth)	1.20
k_{StF}	-	Foucault losses factor (teeth)	2.50
k_{PM}	W/m²	PM specific losses factor	200
k_{Sl}	-	Stray losses factor	0.020

[1]Mass density and losses per kilogram of the electrical steel M400-50A E170.
Source: Own authorship (2024)

The losses and the efficiency values and their related results are presented in Table 20.

Table 20 – Commercial PMSG losses and efficiency

Symbol	Unit	Description	Value
P_{Ac}	kW	Armature copper losses	0.536
P_{Syh}	kW	Stator yoke hysteresis losses	0.224
P_{SyF}	kW	Stator yoke Foucault losses	0.725
P_{Sth}	kW	Stator teeth hysteresis losses	0.048
P_{StF}	kW	Stator teeth Foucault losses	0.362
P_{PMs}	kW	Permanent magnet losses	0.007
P_T	kW	Total losses	1.91
η	%	Estimated efficiency	94.4

Source: Own authorship (2024)

Again, the validation of the commercial PM synchronous generator is performed with finite element simulations in the Ansys Maxwell, which also considers the ferromagnetic saturation. The first results are once more the no-load and full-load flux lines and magnetic flux densities, presented in Figure 44 and Figure 45, respectively.

Figure 44 – Commercial PMSG finite-element solution of the magnetic field and magnetic flux density distribution under no-load operation

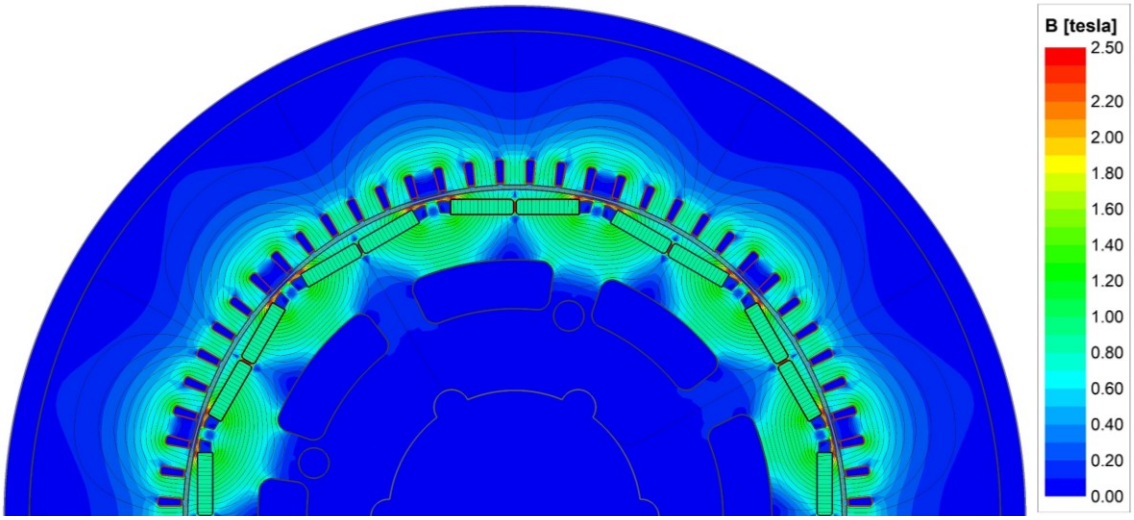

Source: Own authorship (2024)

Figure 45 – Commercial PMSG finite-element solution of the magnetic field and magnetic flux density distribution under full-load operation

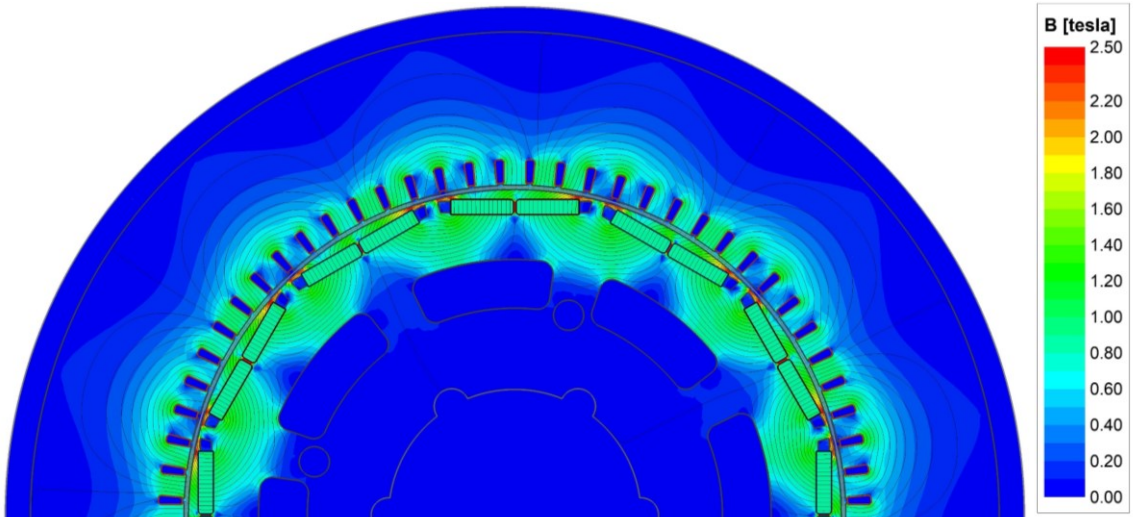

Source: Own authorship (2024)

The remaining important results obtained with the FES are the phase-to-phase voltages under full-load operation, shown in Figure 46, and the phase armature currents under full-load operation, presented in Figure 47.

Figure 46 – Commercial PMSG full-load phase-to-phase voltages

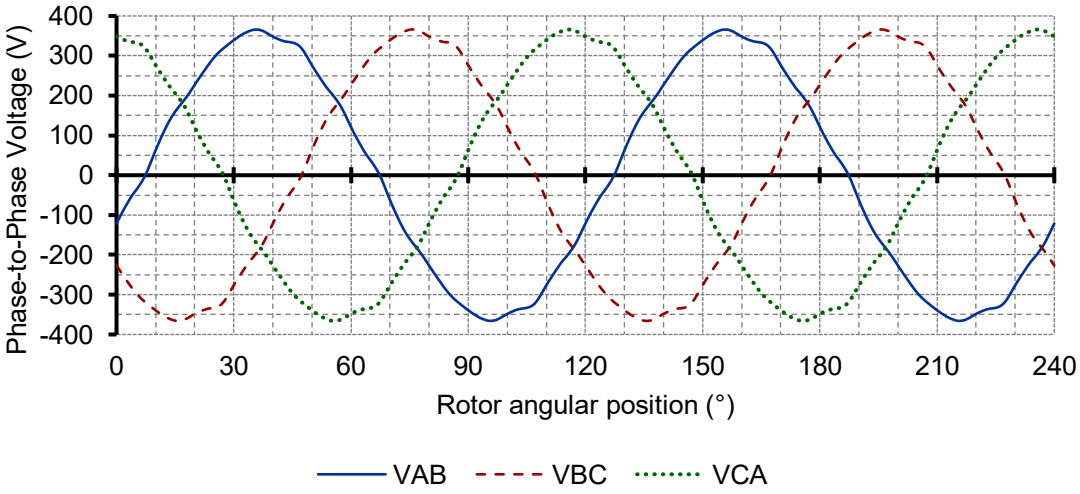

Source: Own authorship (2024)

The Total Harmonic Content (THD) of the phase-to-phase voltages of Figure 46 is 4.462%, whereby the seventh and the eleventh order components are the most significant (with 1.226% and 1.497%, respectively). The FFT of the armature currents of Figure 47 resulted in a THD of 14.79%, where the third-order component is the most significant, contributing 13.63%, followed by the ninth with 3.691%.

Figure 47 – Commercial PMSG full-load armature currents

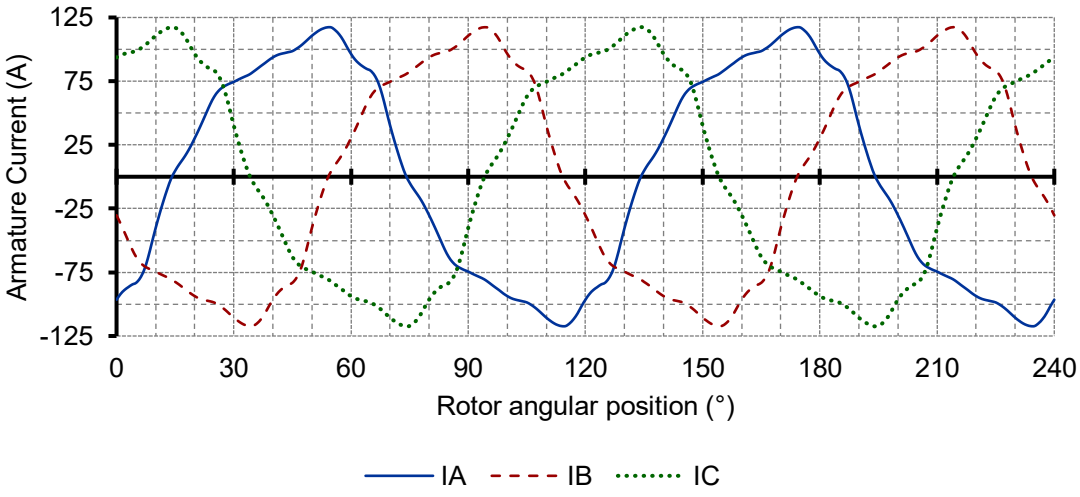

Source: Own authorship (2024)

The main electromagnetic result can be summarised in Table 21.

Table 21 – Commercial PMSG main electromagnetic results

Symbol	Unit	Design	FES	Difference (%)
I_A	A	76.49	81.05	5.630
V_T	V	242.7	254.7	4.696
S_E[1]	kVA	32.15	35.75	10.06
P_E[2]	kW	32.15	36.07	10.86

[1]FES result is the product of rms values of V_T, I_A and $\sqrt{3}$. [2]FES result obtained by the mean value of the instantaneous power.
Source: Own authorship (2024)

It is evident that there are greater differences between FES and the design values in the commercial PMSG than in the surface-mounted PMSG when comparing Table 11 and Table 21. One of the reasons for this is, firstly, the fact that this commercial machine has a much more complex geometry, resulting in a more complex magnetic flux distribution and significantly more flux leakage from the rotor to the stator. This tends to difficult the calculation of number of turns of the armature coils, and, consequently the terminal voltage.

Secondly, the method for obtaining the armature reaction components L_d and L_q (explained in Appendix A), based on FES, does not result in flux density distribution and saturation conditions similar to the one when the machine is under full-load operation. Since this is one of the premises of this direct and quadrature axis inductances obtaining method, it ends up affecting the terminal voltage and, consequently, the output power calculations (JONES, 1967). Moreover, since the stator utilisation (how much of the stator is occupied by the slots) is relatively small, the armature reaction is also relatively weak. Therefore, even though the FES method is not accurate for this machine, it still results in a difference of around 10% in the output power.

However, as the slots are increased to house a larger armature conductor (and have more admissible output power), the armature current and the armature reaction field would increase in magnitude (according to Figure 14), and these discrepancies would become more pronounced and lead to an even more significant deviation in the final results.

5.3 Surface-Mounted PMSG Optimization

As discussed in Section 2.1.3.1.3, the method of using a PMG to power supply the AVR of a WRSG excitation system provides superior performance when compared to the self-excited systems (outlined in 2.1.3). However, it also comes with the counterpart of adding length, weight, and complexity to the generating system. Thus, to remain a competitive generating solution, the PE of the excitation system should have minimised cost while delivering high efficiency.

In order to minimise the cost of the machine, the price per kilogram of the materials used in the PMG (electrical steel, copper and permanent magnets) is required. However, obtaining reliable values of these material prices can be challenging. They can vary significantly across manufacturers, each often working with its own pricing models, making it difficult to establish a standardised cost framework.

Alternatively to minimising the cost of the machine, maximising power or torque densities could be the focus of the optimisation. This approach enables the delivery of higher output power for a given size and weight, a crucial aspect for maintaining competitiveness. Between the two, power density may initially seem more appropriate for comparing generators, as the torque value is often an overlooked parameter. However, since torque density allows for a comparison of the generator power output independent of its synchronous rotational speed, it is the preferred metric for optimisation in this case.

Beyond achieving a generator with high torque density and efficiency, the optimisation must also adhere to several constraints, as discussed in Section 4. These constraints are essential for avoiding undesirable or impractical solutions. In the PMSG optimisation, they encompass geometric, operational, and magnetic considerations. The primary constraints applied in the optimisation process are outlined in Table 22, in which the magnetic flux densities follow the ranges explained in sections 3.3.1 and 3.3.3.

Table 22 – Surface-mounted PMSG optimisation constraints

Symbol	Unit	Description	Constraint Range
S_{Ed}	kVA	Output Power	100.0
V_{Td}	V	Terminal Voltage	380.0
B_{Ry}	T	Rotor Yoke Magnetic Flux Density	1.00 – 1.50[1]
B_{AG}	T	Air-gap Magnetic Flux Density	0.85 – 1.05
B_{St}	T	Stator Teeth Magnetic Flux Density	1.00 – 1.50[1]
B_t	T	Stator Teeth Tips Magnetic Flux Density	1.00 – 1.85[1]
B_{Ry}	T	Stator Yoke Magnetic Flux Density	1.00 – 1.50[1]
θ_{Sw}	°	Stator Teeth Wedge Inclination	20.00 – 40.00

[1]Peak values of magnetic flux density.
Source: Own authorship (2024)

In addition to the output constraints, the optimisation inputs are also constrained within a range, again to ensure a practical solution. Table 23 presents the applied ranges, which were discussed in Section 3.3 and presented in Table 1, with the exception of the rotor outer diameter (D_{Ro}) and the induced voltage (E_{Af}) values. CADES requires that the inputs are constrained to be either fixed, interval, parametric, database, discrete, uncertain, or not yet defined. Therefore, a wide range is chosen for D_{Ro} and E_{Af} since they could be freely chosen in theory.

Table 23 – Surface-mounted PMSG optimisation input constraints

Symbol	Unit	Description	Constraint Range
D_{Ro}	mm	Rotor outer diameter	100.0 – 600.0
$k_{\alpha P}$	-	Pole pitch factor	0.50 – 0.80
k_{AG}	-	Air-gap factor	0.01 – 0.02
k_{MS}	-	Machine shape factor	0.20 – 2.00
k_{PMRy}	-	Rotor yoke height to PM width factor	0.25 – 0.80
PC	-	Permeance coefficient	3.00 – 10.0
k_{PMSy}	-	PM width to stator yoke factor	0.25 – 1.00
k_{Sow}	-	Slot opening factor	0.25 – 1.00
k_{Soh}	-	Slot opening height factor	0.25 – 1.00
k_{Sw}	-	Wedge height factor	0.25 – 1.00
k_{TS}	-	Tooth-to-slot width factor	0.80 – 3.00
k_{PMSy}	-	PM width to stator yoke factor	0.25 – 1.00
k_{SyS}	-	Stator yoke to slot height factor	0.25 – 1.00
E_{Af}	V	Induced voltage value	220.0 – 441.0

Source: Own authorship (2024)

The remaining design optimisation variables were treated as fixed parameters, reducing the number of variables the optimisation algorithm must process. This approach simplifies the problem and can result in faster convergence of the optimisation. These are listed in Table 24.

Table 24 - Surface-mounted PMSG optimisation parameters

Symbol	Unit	Description	Value
B_R	T	Permanent magnet remanent flux density	1.18[1]
f	Hz	Electrical Frequency	60.0
n	rpm	Rotation	1200
N_S	slots	Number of slots	36.0
k_{Ac}	-	Coil-shortening factor	5/6
k_{Cop}	-	Consequent pole factor	1.00
N_{Sl}	layers	Numbers of slot layers	2.00
N_{Cp}	paths	Number of parallel paths in the armature windings	1.00
k_{Sf}	-	Slot fill factor	0.50
PF	–	Power Factor	0.90
J_A	A/mm²	Armature current density	5.75
R_{km}	Ω/km	Conductor resistance per kilometre	0.64
T_{ref}	°C	Reference temperature	20.0
T_{op}	°C	Operating temperature	120
ρ_{ee}	g/cm³	Electrical steel mass density	7.75
P_F	W/kg	Foucault loss per kilogram	3.68
P_h	W/kg	Hysteresis loss per kilogram	3.68
k_{Syh}	-	Hysteresis losses factor (yoke)	2.00
k_{SyF}	-	Foucault losses factor (yoke)	1.80
k_{Sth}	-	Hysteresis losses factor (teeth)	1.20
k_{StF}	-	Foucault losses factor (teeth)	2.50
k_{PM}	W/m²	PM specific losses factor	200
k_{Sl}	-	Stray losses factor	0.02

[1]Remanent magnetic flux density of the N42SH of Figure 36.
Source: Own authorship (2024)

All of these parameters have the same values as those presented in the surface-mounted PMSG design in Section 5.1, with the exception of the PM remanent magnetic flux density. In the PMSG design procedure, the designer must obtain the operative magnetic flux density of the PM using its demagnetisation curve after defining the permeance coefficient. In the PMSG optimisation, however, the remanent

magnetic flux density of the PM is provided directly, as the no-load magnetic submodel can assess both its operational magnetic flux density and magnetic flux values. Thus, the permeance coefficient is only used to define the PM height as a function of the air-gap length.

With all the constraints presented, the optimisation objectives remain to be addressed. Maximising torque density and efficiency are conflicting objectives. Higher torque density often requires the machine to operate at increased current density and saturation levels, both of which lead to greater losses and, consequently, less efficiency. Conversely, maximising efficiency demands a reduction in losses due to Joule effect, hysteresis and Foucault currents, which in turn requires a reduction in the current density and lower values of magnetic flux density distribution in the machine cross-section. Instead of prioritising one objective and accepting compromises in the other, a Pareto front is proposed. This approach allows for the identification of optimal trade-offs between torque density and efficiency, offering a range of solutions where improvements in one objective do not excessively sacrifice the other (LOBATO, 2008).

In order to obtain the Pareto front to guide the selection of an optimal generator, the optimisation-oriented model described in Section 4 was employed with the two conflicting objective functions. Firstly, the optimisation was performed with efficiency as the objective, leaving torque density unconstrained. Then, the optimisation was repeated with maximum torque density as the objective, leaving efficiency unconstrained. These two solutions represent the boundaries of the trade-offs between torque density and efficiency and define the range within which the optimal solution resides.

To map out the Pareto front between these extremes, forty-nine intermediate solutions were generated in a stepped manner. The efficiency range between the extreme cases was divided into fifty equal increments of 0.05% in efficiency. For each increment, the optimisation algorithm was tasked with finding the maximum torque density for a specified efficiency. Thus, a consistent increase in efficiency across the fifty-one solutions and how the torque density is affected can be analysed. Figure 48 shows the resulting Pareto front from the described method. It is pertinent to state that all Pareto solutions respected the optimisation constraints of Table 22 and Table 23.

In addition to the Pareto front, Figure 48 also shows four infeasible solutions, four dominated solutions, and the dominant solutions. Infeasible solutions do not satisfy at least one of the optimisation problem's constraints, rendering them non-

viable. In contrast, dominated solutions are those outperformed in both objectives simultaneously by at least one other solution. The Pareto front delineates the boundary that separates feasible solutions from infeasible ones based on the two conflicting objectives. This boundary is composed of dominant solutions, defined as such because no other feasible solution exceeds them in both objectives (BAZZO, 2017).

Figure 48 – Pareto front between torque density and efficiency with dominant, dominated and infeasible solutions

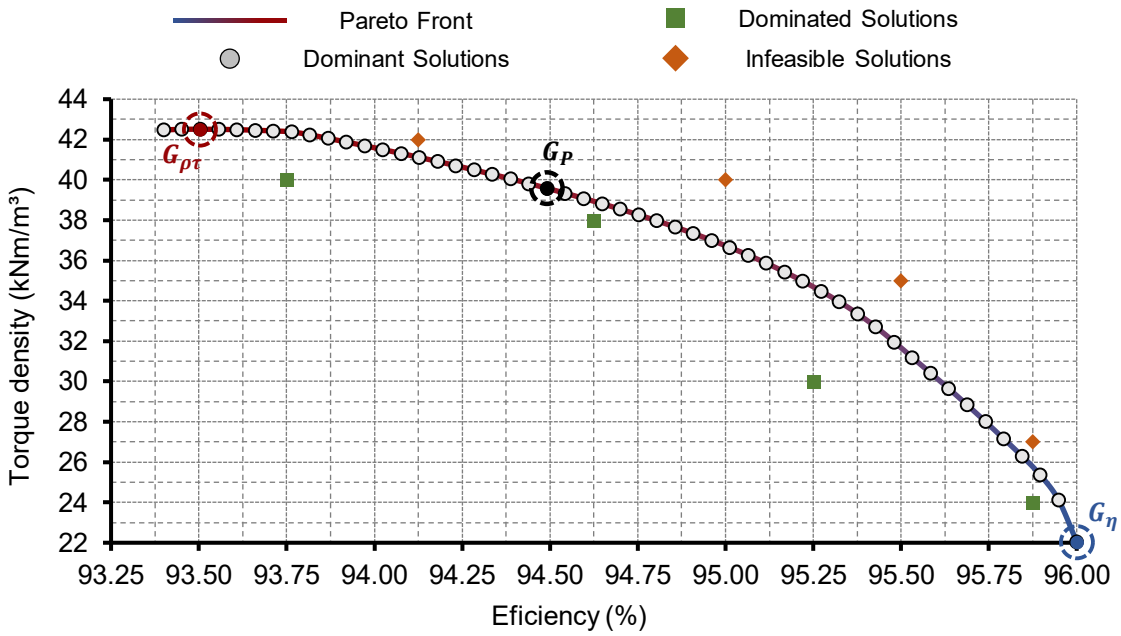

Source: Own authorship (2024)

Figure 48 provides a visual summary of the range of potential optimal solutions. A first analysis of the Pareto front allows for the immediate exclusion of the first and second machines (from the left to the right in the curve) as potential candidates for the optimal solution. This is due to the fact that the first machine offers a 0.06% reduction in efficiency (from 93.40% to 93.45%) compared to the second while achieving 0.08% less torque density (from 42.47 to 42.51 kNm/m³). The same can be observed between the second and third machines, with the same consistent decrease in efficiency and providing less torque density. This suggests that these first two solutions are not ideal candidates, as there is no trade-off.

Consequently, the remaining dominant solutions between $G_{\rho\tau}$ and G_η, which are the generators with the highest torque density and most efficiency, respectively, are all possible candidates for the optimal solution. In practice, there are no bad choices between any solution of the referred range since each one has both an

advantage and a disadvantage when compared to the others. The designer can select the solution that best meets its specific application requirements, balancing torque density and efficiency according to the design objectives. Therefore, an arbitrary machine G_P is highlighted in Figure 48, which is a third solution between $G_{\rho\tau}$ and G_η. The characteristics of these three machines are listed in Table 25.

Table 25 – Three Pareto front optimal solutions comparison

Parameter	PMSG G_η	PMSG G_P	PMSG $G_{\rho\tau}$
Rotor outer diameter, D_{Ro} (mm)	269.1	341.8	381.3
Permeance coefficient, PC	10.00	10.00	5.483
Permanent magnet height, h_{PM} (mm)	30.41	36.45	36.82
Machine stack length, L_G (mm)	252.0	96.24	76.27
Tooth width on the top, W_t (mm)	14.24	18.85	19.93
Slot height, h_S (mm)	26.66	44.57	46.65
Stator outer diameter, D_{So} (mm)	437.8	533.6	588.5
Torque density, ρ_τ (kNm/m³)	22.04	39.58	42.51
Efficiency, η (%)	96.00	94.49	93.50
Mass (kg)	279.4	183.4	181.2

Source: Own authorship (2024)

Table 25 shows a 92.8% increase in the torque density with a 2.60% reduction in the efficiency between G_η and $G_{\rho\tau}$. This is primarily attributed to a significant increase in stator utilisation, with slot height increased by 42.9% to house more armature conductors. Given the fixed armature current (as output power and terminal voltage are constrained), the armature conductor surface remains unchanged, allowing only the number of coils to be adjusted. This is further reflected in a 45.2% reduction in the permeance coefficient, indicating less reliance on permanent magnet height adjustments and more compromise in copper volume reduction (the main contributor to total losses) to respect the terminal voltage and output power to the constrained values of Table 22.

The arbitrary G_P solution represents a machine closer to the high torque density solutions while still achieving high efficiency, positioned near the midpoint of the Pareto front's efficiency range. Compared to G_η it has 1.57% less efficiency while producing 79.55% more torque density. Conversely, in comparison with $G_{\rho\tau}$, it achieves 1.06% higher efficiency, with a trade-off of 6.89% lower torque density. To provide a visual representation of their differences, their cross-sections are shown in Figure 49.

Figure 49 – Cross section of the three optimal PMSG of the Pareto Front

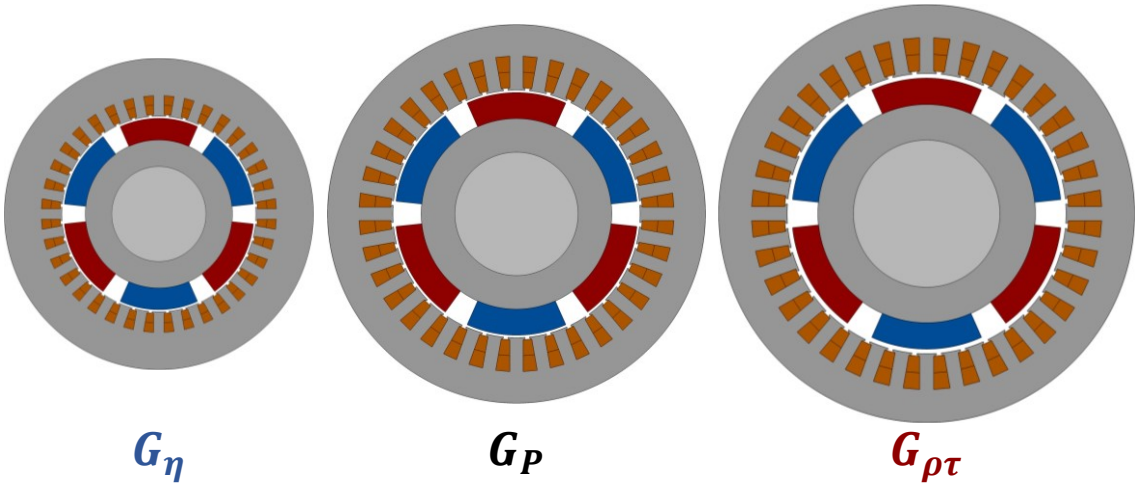

Source: Own authorship (2024)

Figure 49 highlights the significant difference in cross-sectional size between the machines, with the most efficient one notably having a smaller diameter. However, this does not translate to being the smallest; rather, it is the largest in terms of total volume compared G_P and $G_{\rho\tau}$. To respect the optimisation constraints, the optimisation algorithm balanced the reduced number of turns in the armature coils by extending the stack length of the machine. This resulted in a stack length greater than the combined values of G_P and $G_{\rho\tau}$. Consequently, this machine is 52% heavier than G_P and 54% heavier then $G_{\rho\tau}$, which can be confirmed by analysing the total mass values of Table 25.

5.3.1 Optimised Pareto PMSG validation

In order to verify the accuracy of the developed optimisation, the optimal solution G_P from the Pareto front needs to be validated. The validation of the designed PM synchronous generator is performed with finite element simulations, once more carried out at Ansys Maxwell in 2D. The no-load and full-load flux lines and densities are presented in Figure 50 and Figure 51, respectively.

Figure 50 – Optimized surface-mounted PMSG finite-element solution of the magnetic field and magnetic flux density distribution under no-load operation

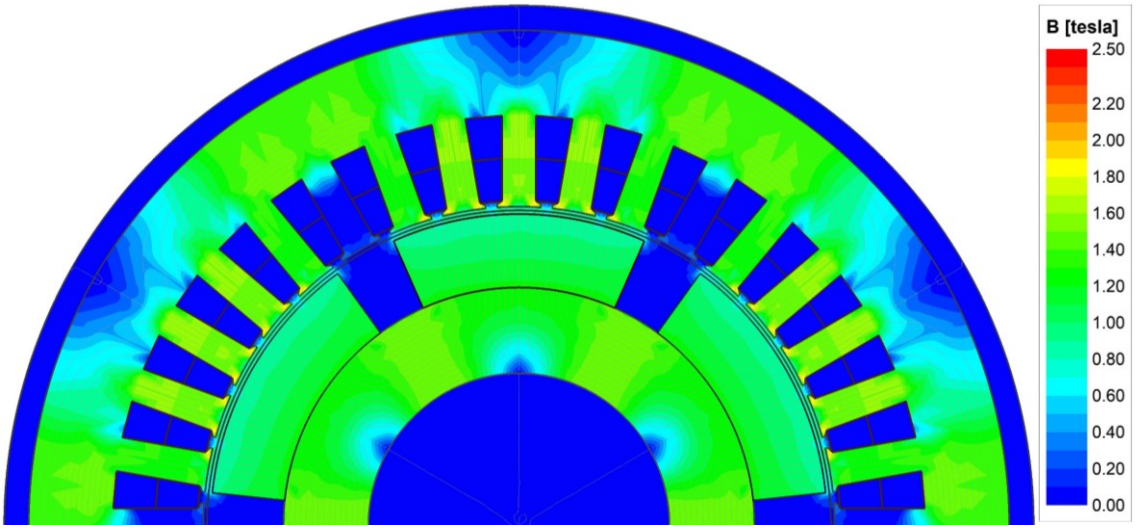

Source: Own authorship (2024)

Figure 51 – Optimized surface-mounted PMSG finite-element solution of the magnetic field and magnetic flux density distribution under full-load operation

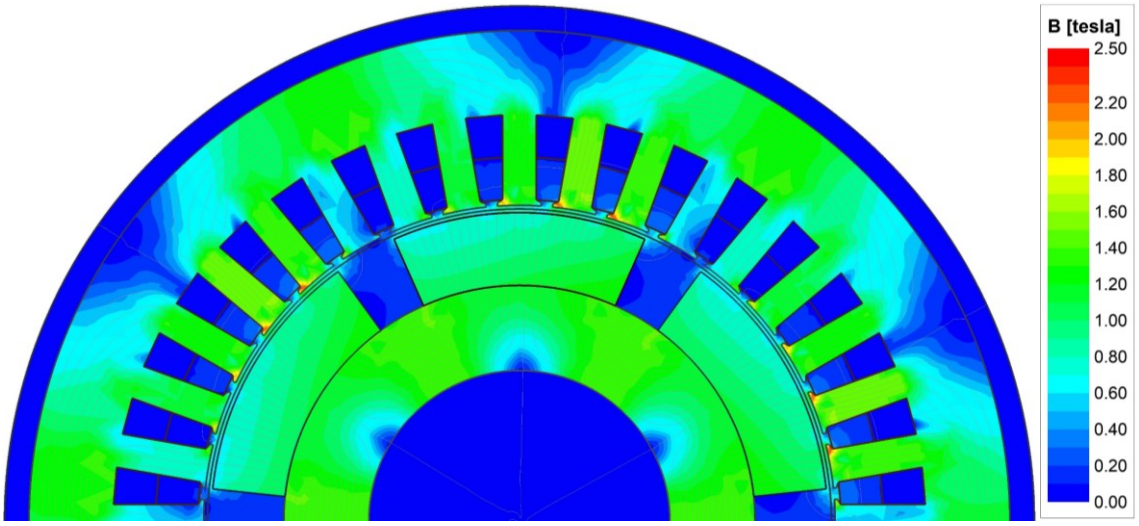

Source: Own authorship (2024)

Other important results obtained with the FES are the phase-to-phase voltages under full-load operation, shown in Figure 52, and the phase armature currents under full-load operation, presented in Figure 53.

Figure 52 – Optimized surface-mounted PMSG full-load phase-to-phase voltages

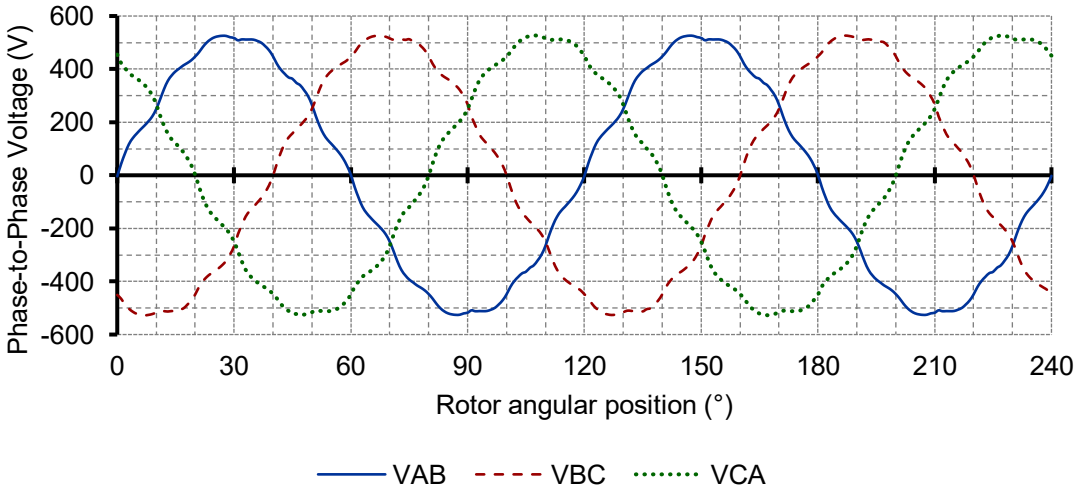

Source: Own authorship (2024)

The Total Harmonic Content (THD) of the phase-to-phase voltages of Figure 52 is 4.484%, whereby the eleventh and the thirteenth order components are the most significant (with 3.908% and 1.282%, respectively). The FFT of the armature currents of Figure 53 resulted in a THD of 6.417%, where the third-order component is the most significant, contributing 6.879%, followed by the ninth with 0.851%.

Figure 53 – Optimized surface-mounted PMSG full-load armature currents

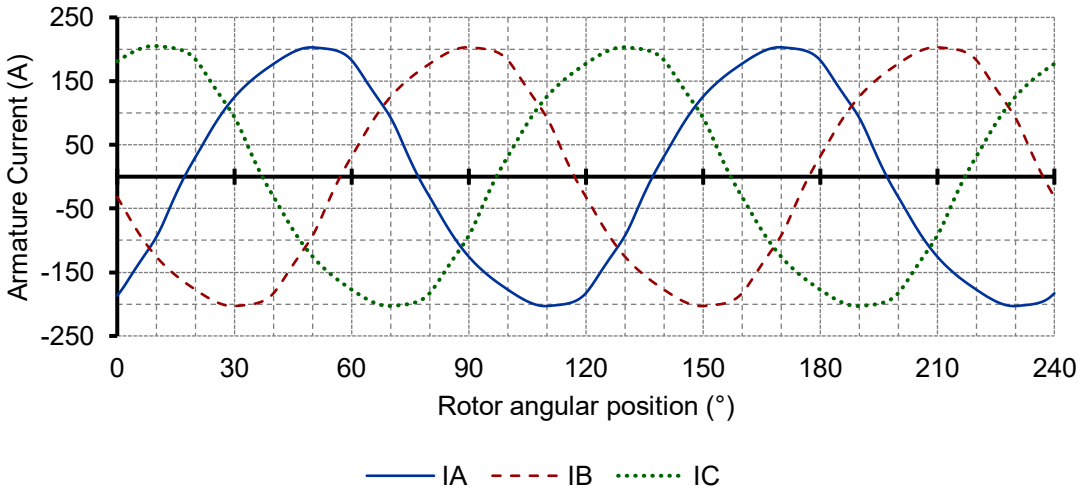

Source: Own authorship (2024)

The output power is the last important result from the FES, as shown in Figure 55.

Figure 54 – Optimised surface-mounted PMSG output power

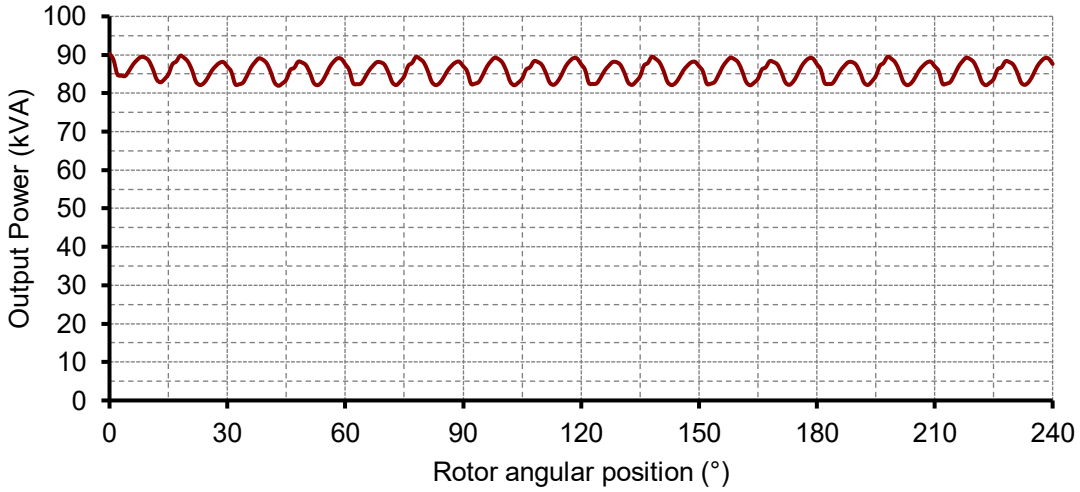

Source: Own authorship (2024)

The main electromagnetic results for the design optimisation are shown in Table 26, along with the percentage differences compared to finite element simulations performed in Maxwell 2D. These differences indicate that the optimisation achieves high accuracy, with terminal voltage and armature current differing by approximately 2% and 3%, respectively, from simulation results. The five per cent variance in output power is consistent with the differences in terminal voltage and armature current. It remains within an acceptable range, which confirms the overall validity of the optimisation-oriented electromagnetic model.

Table 26 – Optimized surface-mounted PMSG main electromagnetic results

Symbol	Unit	Optimisation	FES	Difference (%)
B_{AG}[1]	T	0.914	0.908	-0.684
I_A	A	151.9	147.3	-3.176
V_T	V	380.0	371.7	-2.242
S_E[2]	kVA	100.0	94.80	-5.489
P_E[3]	kW	90.00	85.66	-5.068

[1]Flux density during no-load operation with the magnetic flux measured at the middle of the air-gap. [2]FES result is the product of rms values of V_T, I_A and $\sqrt{3}$. [3]FES result obtained by the mean value of the instantaneous power.
Source: Own authorship (2024)

6 CONCLUSIONS

In this work, the design of surface-mounted permanent magnet synchronous generators was developed as an early stage of the design optimisation of permanent magnet synchronous generators applied to a pilot exciter. With the constant growth of electrical energy consumption over recent years, the generator market has become ever more competitive. Therefore, optimised machines that deliver high efficiency and performance at a smaller size are more likely to succeed.

By adapting a design methodology for wound-rotor synchronous generators, a design procedure for surface-mounted permanent magnet synchronous generators was developed. This procedure was validated against finite element simulations, showing strong agreement and thus contributing to the literature on synchronous machine design. The first part of this dissertation was subsequently published in a journal (DE MENEZES et al., 2024). This procedure was also tested with a variant PM generator geometry of a commercial machine. Although the accuracy compared to finite element simulations was lower than for the surface-mounted topology, the results were still reasonable, given the significant topological differences.

Furthermore, a reluctance network was developed to precisely find the no-load linkage flux and eliminate the need for leakage flux factors in determining the number of turns of the armature coils. A second reluctance network was developed to model the armature reaction of the generator, enabling an accurate calculation of armature reactance and, consequently, the terminal voltage (without time-consuming finite element simulations). These RN are essential for optimisation since analytically calculating the no-load magnetic flux and armature reactance leads to inaccuracy, and finite element methods would substantially increase the optimisation computational time.

An optimisation-oriented magnetic model was then developed based on the design equations presented in Section 3 and the magnetic circuits described in Sections 4.1.1.1 and 4.1.1.2. Since maximising torque density and efficiency are conflicting objectives, a Pareto front was proposed to provide a balanced range of solutions and avoid prioritising one objective and accepting compromises in the other. When obtaining the extremes of the Pareto front, the optimisation took only 6.3 seconds to identify the highest torque density solution and 50 seconds for the highest

efficiency machine, with a precision of 10^{-13} in both cases, while satisfying all established constraints.

The Pareto front presents fifty-one optimal solutions ranging from 20.0 to 42.5 kNm/m³ in torque density and 93.4 to 96.0% in efficiency, with the presented constraints. Each solution has both advantages and disadvantages when compared to the others, and could all be considered viable candidates for an optimal pilot exciter. Consequently, each solution could be well-suited to a generator-set specification. Thus, for validation purposes, an arbitrary solution was chosen and analysed via finite element simulations. The simulations confirmed the accuracy of the proposed optimisation methodology, with terminal voltage and armature current differing by approximately 2% and 3%, respectively, from simulation results. Although the output power showed a difference of around five per cent (compared to FES), this is still within an acceptable range. Ultimately, the accuracy of the optimisation-oriented electromagnetic model and the overall optimisation procedure are confirmed.

6.1 Future Developments

Even though this work presents the development and validation of a comprehensive design optimisation method for surface-mounted permanent magnet synchronous generators, there still are avenues for further research to enhance its modelling capabilities and reduce the gap between theoretical predictions and real-world performance. Firstly, this optimisation method could be adapted to other PM machine topologies, such as interior permanent magnets that are more complex. These offer advantages in terms of field weakening capabilities and possibly mechanical robustness, which are beneficial in high-speed and high-torque applications.

A major development would be integrating thermal and mechanical models into the optimisation process since they could provide a more precise assessment of temperature rise and mechanical stress, key factors in machine performance and longevity. Incorporating a thermal model would allow the optimisation to evaluate heat distribution and cooling requirements, whereas a mechanical model would enable a structural integrity evaluation. In this context, exploring the sizing and model inclusion of a retaining sleeve could be explored to manage the mechanical stresses in surface-mounted PM rotors. This multiphysics approach would create a more balanced

optimisation framework by addressing electromagnetic, thermal, and mechanical aspects.

Another significant development would be to improve the loss estimation approach that currently relies on empirical factors, which, while practical, introduce uncertainties that do not reflect on real-world behaviour. A physics-based loss model would eliminate the need for empirical coefficients in iron losses (Foucault and eddy current), PM losses, and stray losses, ultimately improving efficiency estimates.

Finally, 3D modelling could significantly advance both the optimisation framework and finite element validation. In the optimisation model, a 3D representation would allow an accurate calculation of end-winding inductance, which can have a significant impact on machine performance, particularly as machine diameter is increased, like in high-torque-density designs. It would also require the development of a 3D finite element model, which is far more complex than 2D models but would allow a representation of the armature windings in its entirety. Once more, this improvement would bring the current method closer to real-world representation.

REFERENCES

BAZZO, T. de P. M. **Projeto Ótimo Multidisciplinar de Geradores Síncronos de Ímãs Permanentes para Aerogeradores Considerando a Curva de Ocorrência do Vento**. Advisors: Prof. Dr. Renato Carlson(UFSC), Prof. Dr. Frédéric Wurtz (UGA). Co-Advisors: Prof. Dr. Nelson Sadowski (UFSC), Prof. Dr. Laurent Gerbaud (UGA). 2017. 321 p. Thesis (Doctorate in Electrical Engineering), 2017.

FRATILA, R. **Modélisation numérique de la perte d'aimantation d'aimants permanents sous les contraintes magnétique et thermique rencontrées dans les dispositifs électriques**. Advisors: Abdelmounaïm Tounzi, Abdelkader Benabou. 2014. Thesis (Doctorate in Electrical Engineering) - Doctoral School of Engineering Sciences (Lille), 2014.

BAZZO, T. DE P. M.; KÖLZER, J. F.; CARLSON, R.; WURTZ, Fr.; GERBAUD, L. Multiphysics Design Optimization of a Permanent Magnet Synchronous Generator. **IEEE Transactions on Industrial Electronics**, v. 64, n. 12, 2017.

BAZZO, T. DE P. M.; MOURA, V. DE O.; CARLSON, R. A Step-by-Step Procedure to Perform Preliminary Designs of Salient-Pole Synchronous Generators. **Energies**, v. 14, n. 16, p. 4989, 14 aug. 2021.

BOLDEA, I; NASAR, S. **The Electric Generators Handbook**: Synchronous Generators. Taylor & Francis Group, LLC, 2006. ISBN 0-8493-5725-X.

BORISAVLJEVIC, A.; POLINDER, H.; FERREIRA, J. A. On the Speed Limits of Permanent-Magnet Machines. **IEEE Transactions on Industrial Electronics**, v. 57, pp. 220-227, 2010.

CARLSON, R.; WURTZ, F. Optimal design of a set of permanent magnet generators with the same cross section. **Journal of Microwaves, Optoelectronics and Electromagnetic Applications**, v. 12, n. 2, 2013.

CHAPMAN, S. J. **Electric machinery fundamentals**. 5. ed. Porto Alegre: AMGH Editora Ltda, 2013. 698 p. ISBN 0073529540/9780073529547.

CHEN, A. L.; MARTINEZ, D. H. A heuristic method based on genetic algorithm for the baseline-product design. **Expert Systems with Applications**, v. 39, ed. 5, p. 5829 - 5837, 2012.

DELINCHANT, B.; DURET, D.; ESTRABAUT, L.; GERBAUD, L.; HUU, H. NGUYEN; DU PELOUX, B.; RAKOTOARISON, H.L.; VERDIERE, F.; WURTZ, F. An optimizer using the software component paradigm for the optimization of engineering systems. **COMPEL - The International Journal for Computation and Mathematics in Electrical and Electronic Engineering**, v. 26, n. 2, p. 368 - 379, 2007.

DEL TORO, V. **Fundamentos de máquinas elétricas**. Rio de Janeiro, RJ: LTC - Livros Técnicos e Científicos, 1999. 568 p. ISBN 85-216-1184-6.

De MENEZES, G.G.; MACIEJEWSKI, N.A.R.; DE CARVALHO, E.S.; BAZZO T.de P.M. A Thorough Procedure to Design Surface-Mounted Permanent Magnet Synchronous Generators. **Machines**, v.12, n.6, p. 384, 4 June 2024

EMPRESA DE PESQUISA ENERGÉTICA. **Balanço Energético Nacional (ano-base 2016)**. 2017. Available in: <https://www.epe.gov.br/sites-pt/publicacoes-dados-abertos/publicacoes/PublicacoesArquivos/publicacao-46/topico-82/Relatorio_Final_BEN_2017.pdf>.

EMPRESA DE PESQUISA ENERGÉTICA. **Balanço Energético Nacional (ano-base 2017)**. 2018. Available in: < https://www.epe.gov.br/sites-pt/publicacoes-dados-abertos/publicacoes/PublicacoesArquivos/publicacao-303/topico-419/BEN2018__Int.pdf>.

EMPRESA DE PESQUISA ENERGÉTICA. **Balanço Energético Nacional (ano-base 2018)**. 2019. Available in: < https://www.epe.gov.br/sites-pt/publicacoes-dados-abertos/publicacoes/PublicacoesArquivos/publicacao-377/topico-494/BEN%202019%20Completo%20WEB.pdf>.

EMPRESA DE PESQUISA ENERGÉTICA. **Balanço Energético Nacional (ano-base 2019)**. 2020. Available in: < https://www.epe.gov.br/sites-pt/publicacoes-dados-abertos/publicacoes/PublicacoesArquivos/publicacao-479/topico-528/BEN2020_sp.pdf>.

EMPRESA DE PESQUISA ENERGÉTICA. **Balanço Energético Nacional (ano-base 2020)**. 2021. Available in: < https://www.epe.gov.br/sites-pt/publicacoes-dados-abertos/publicacoes/PublicacoesArquivos/publicacao-601/topico-596/BEN2021.pdf>.

ENCIU, P.; WURTZ, F.; GERBAUD, L.; DELINCHANT , B. Automatic differentiation for electromagnetic models used in optimization. **COMPEL - The international journal for computation and mathematics in electrical and electronic engineering**, v. 28, n. 5, p. 1313-1326, 11 Sep. 2009.

FANG, H.; QU, R.; LI, J.; ZHENG, P.; FAN, X. Rotor Design for High-Speed High-Power Permanent-Magnet Synchronous Machines. **IEEE Transactions on Industrial Applications**, v. 53, pp. 3411-3419, 2017.

FITZGERALD, A. E.; KINGSLEY, C. JR.; UMANS, S. D. **Electric machinery**. 6. ed. New York, NY: McGraw-Hill Higher Education, 2003. 703 p. ISBN 0-07-112193-5.

GERADA, D.; MEBARKI, A.; BROWN, N. L.; CAVAGNINO, A.; BOGLIETTI, A. A. High-Speed Electrical Machines: Technologies, Trends, and Developments. **IEEE Transactions on Industrial Electronics**, v. 61, pp. 2946-2959, 2014.

GIERAS, J. F.; WILL, M. **Permanent magnet motors technology: Design and Applications**. 2. ed. New York, NY: Marcel Dekker, Inc, 2002. 611 p. ISBN 0-8247-0739-7.

HANSELMAN, D. **Brushless permanent magnet motor design**. 2. ed.: Magna Physics Publishing, 2003. 411 p. ISBN 1-881855-15-5.

HEBALA, A.; GHONEIM, W. A. M.; ASHOUR, H. A. Detailed Design Procedures for PMSG Direct-Driven by Wind Turbines. **Journal of Electrical Engineering & Technology**, 2019.

HENDERSHOT, J.R.; MILLER, T.J.E. **Design of brushless permanent-magnet machines**. Motor Design Books LLC, 2010. 824 p. ISBN 978-0-9840687-0-8.

HENDERSHOT, J.R.; MILLER, T.J.E. **Design of brushless permanent-magnet motors**. Magna Physics Publishing, 1994. 582 p. ISBN 0-19-859389-9.

JONES, C.V. **The Unified Theory of Electrical Machines**, Plenum Press: 1967.

K&J MAGNETICS. Demagnetization (BH) Curves for Neodymium Magnets. **K&J Magnetics**, 2024. Available on: <https://www.kjmagnetics.com/bhcurves.asp>. Accessed in: 2024.

KASPER, J. V. G.; MOURA, V. DE O.; DE MENEZES, G. G.; BAZZO, T. DE P. M.; MALAGOLI, J. A. Projeto Ótimo de um Gerador Síncrono de Polos Salientes utilizando Redes de Relutâncias. **14th IEEE International Conference on Industry Applications**, 2021.

KASPER, J. V. G.; KUO-PENG, Patrick; BAZZO, T. DE P. M.; DE MENEZES, G. G. Methodology to Generate a Reluctance Network Applied to Permanent Magnet Synchronous Generators. **Journal of Microwaves, Optoelectronics and Electromagnetic Applications**, v. 21, n. 4, p. 549 - 569, Oct-Dec 2022.

KIM, H.; JEONG, J.; YOON, M.; MOON, J.; HONG, J. Simple Size Determination of Permanent-Magnet Synchronous Machines. **IEEE Transactions on Industrial Electronics**, v. 64, pp. 7972–7983, 2017.

KLEMPNER, G.; KERSZENBAUM, I. **Operation and Maintenance of Large Turbo-Generators**. John Wiley & Sons, INC., 2004. ISBN 0-471-61447-5.

KRAUSE, P. C.; WASYNCZUK, O.; SUDHOFF, S. D. **Analysis of Electric Machinery and Drive Systems**. 2. ed. United States of America: John Wiley & Sons, 2002. ISBN 0-471-14326-X.

KRISHNAN, R. **Permanent magnet synchronous and brushless DC motor drives**. Taylor and Francis Group, LLC, 2010. 588 p. ISBN 978-0-8247-5384-9.

STAUDT, T. **Brushless Doubly-Fed Reluctance Machine Modeling, Design and Optimization**. Advisors: Frédéric Wurtz and Nelson Jhoe Batistela. 2015. 418 p. Thesis (Doctor in Electrical Engineering), 2015.

LALIBERTE, G. “A Comparison of Generator Excitation Systems”. Technical information from Cummins Power Generation White paper, 2023.

LASI, H.; FETTKE, P.; FELD, T.; HOFFMANN, Michael. **Industry 4.0. Business & Information Systems Engineering**, v. 6, n. 4, p. 239-242, 19 jun. 2014.

LOBATO, F. S. **Otimização multi-objetivo para o projeto de sistemas de engenharia**. Advisor: Valder Steffen Júnior. 2008. 402 f. Thesis (Doctorate in Engineering) - Universidade Federal de Uberlândia, 2008.

MAHON, L. L. J. **Diesel Generator Handbook**. Elsevier Butterworth-Heinemann, 1992. ISBN 0750611472.

MILLER, T. J. E. **SPEED's electric motors**: an outline of some of the theory in the SPEED software for electric machine design with problems and solutions. University of Glasgow: 2002. 307 p.

MOURA, V. O. **Metodologia de Desenvolvimento de Redes de Relutâncias Estáticas para Geradores Síncronos**. 2022. Dissertation – Post-graduate Program in Energy Systems (PPGSE), Federal Technological University of Paraná (UTFPR), 2022.

NOCEDAL, J.; WRIGHT, S. J. **Numerical Optimization**. 2. ed. Spring Street, New York, NY 10013, USA: Springer Science+Business Media, 2006. 683 p. ISBN 78-0387-30303-1.

NØLAND, J. K.; NUZZO, S.; TESSAROLO, A.; ALVES, E. F. Excitation System Technologies for Wound-Field Synchronous Machines: Survey of Solutions and Evolving Trends. **IEEE Access**, v. 64, pp. 109699-109718, 2019.

NUZZO, S.; GALEA, M.; GERADA, C.; BROWN, N. Analysis, Modeling, and Design Considerations for the Excitation Systems of Synchronous Generators. **IEEE Transactions on Industrial Electronics**, v. 65, n. 4, 2018.

PERHO, J. Reluctance network for analysing induction machines. **Acta Polytechnica Scandinavica**: Electrical Engineering Series, n. 110, p. 1 - 147, 12 dez. 2002.

PYRHÖNEN, J.; JOKINEN, T.; HRABOVCOVÁ, V. **Design of rotating electrical machines**. 1. ed. atual. Wiltshire, Great Britain: John Wiley & Sons, Ltd, 2008. 541 p. ISBN 978-0-470-69516-6.

SAY, M G. **Alternating current machines**. 4. ed. Pitman Publishing Limited, 1976. ISBN 0-273-36197-X.

SIMPSON, T. W.; MAIER, J. R. A.; MISTREE, F. Product Platform Design: Method and Application. **Research in Engineering Design - Theory, Applications, and Concurrent Engineering**, v. 13, n. 1, p. 2-22, 2001.

SIMPSON, T. W.; MARION, T.; DE WECK, O.; HÖLTTÄ-OTTO, K.; KOKKOLARAS, M.; SHOOTER, S. B. Platform-based design and development: Current trends and needs in industry. **Proceedings of the ASME Design Engineering Technical Conference**, v. 2006, 2006.

TARTIBI, M.; DOMIJAN, A. Optimizing AC-exciter design. **IEEE Transactions on Energy Conversion**, vol. 11, pp. 16-24, March 1996.

UMANS, S. **Máquinas Elétricas** de Fitzgerald e Kingsley. 7ª. ed. Porto Alegre: AMGH Editora Ltda, v. Único, 2014.

VASCHETTO , S.; TENCONI, A.; BRAMERDORFER, G. Sizing procedure of surface mounted PM machines for fast analytical evaluations. **2017 IEEE International Electric Machines and Drives Conference (IEMDC)**, Miami, FL, USA, 2017.

YANG, Xin-She. **Engineering Mathematics**: with Examples and Applications. 1. ed. 125 London Wall, London EC2Y 5AS, United Kingdom: Elsevier, 2017. 400 p. ISBN 978-0-12-809730-4.

YAZDANPANAH, R.; AFROOZEH, A.; ESLAMI, M. Analytical design of a radial-flux PM generator for direct-drive wind turbine renewable energy application. **Energy Reports**, v. 8, pp. 3011-3017, 2022.

APPENDIX A – Salient-pole PM Generator Design Equations

As mentioned in Section 3.1, this methodology is developed to design surface-mounted PMSG, but it is also applied to match the commercial pilot exciter topology presented in Section 3.4., a complex salient-pole geometry. The equations needed to be included in the rotor sizing stage of the proposed design method to find all rotor geometry parameters of the machine described in Figure 23 and Figure 24 are described in this Appendix.

The first equation for this new geometry would be included after equation (28). Thus, the previous equations remain in the rotor sizing, and equations (29), (30), (31), and (32) are substituted with the ones described below. Differently from the surface-mounted machine where the permanent magnet's width is calculated with the effective pole pitch (α_{Pef}), for this salient-pole geometry, they can be either calculated or imposed. From the effective pole pitch, the pole width is kwon and, after defining the remaining gaps (L_{PMc}, L_{Ro} and L_{PMe}) and flux barrier dimensions, the PM width would be found. On the other hand, the designer can set its value and (after also setting a few parameters) find the remaining dimensions. From the PM height and choosing a value for the PM form factor (k_M) its length can be obtained with:

$$W_{PM} = h_{PM} \cdot k_M \tag{105}$$

Another imposed parameter in the rotor sizing part of the design is the PM angle (θ_{PM}) shown in Figure 24. To ensure that the flux barrier dimensions are always proportional to the PM dimensions, imposed factors k_{fbt}, k_{fbb} and k_{fbh} were used:

$$W_{fbt} = h_{PM} \cdot k_{fbt} \tag{106}$$

$$W_{fbb} = h_{PM} \cdot k_{fbb} \tag{107}$$

$$h_{fb} = h_{PM} \cdot k_{fbh} \tag{108}$$

The gap between the magnet and the flux barrier heights L_{fb} (mm) can be found by imposing the flux barrier gap to PM height factor (k_{fb}):

$$L_{fb} = h_{PM} \cdot k_{fb} \tag{109}$$

Instead of choosing a value for the gap between the PM tip and the rotor outer diameter (L_{RO}), once again, a factor was used to ensure that proportions are kept:

$$L_{Ro} = h_{PM} \cdot k_{Ro} \tag{110}$$

After defining these parameters, the angle between PMs at the center θ_{PM} (°), and the inclination angle of the flux barrier θ_{fb} (°), the gap between PM of the same pole (L_{PMc}) can be calculated with:

$$\begin{aligned} L_{PMc} = \left(\frac{D_{Ro}}{2} - L_{Ro}\right) \cdot \sin\frac{\alpha_{Pef}}{2} \\ - \left(h_{fb} \cdot \tan\theta_{fb} + W_{fbt} + W_{PM}\right) \cdot \sin\theta_{PM} \\ + \left(h_{fb} + L_{fb} - h_{PM}\right) \cdot \cos\theta_{PM} \end{aligned} \tag{111}$$

This last parameter should have the smallest value possible so that it saturates with very few flux lines but enough for the PM not to touch.

To verify if the effective pole pitch results in an adequate margin between permanent magnets of adjacent poles, the coordinates on the top end of the flux barriers ($x_{fbe}; y_{fbe}$) must be known. These values are calculated with:

$$\begin{aligned} x_{fbe} = \left(\frac{D_{Ro}}{2} - L_{Ro}\right) \cdot \sin\frac{\alpha_{Pef}}{2} - \left(h_{fb} \cdot \tan\theta_{fb}\right) \cdot \sin\theta_{PM} + h_{fb} \\ \cdot \cos\theta_{PM} \end{aligned} \tag{112}$$

$$y_{fbe} = \left(\frac{D_{Ro}}{2} - L_{Ro}\right) \cdot \cos\frac{\alpha_{Pef}}{2} - \left(h_{fb} \cdot \tan\theta_{fb}\right) \cdot \cos\theta_{PM} - h_{fb} \cdot \sin\theta_{PM} \quad (113)$$

Then, both radius and angle at this point can also be obtained:

$$R_{fbe} = \sqrt{{x_{fbe}}^2 + {y_{fbe}}^2} \quad (114)$$

$$\theta_{fbe} = \tan^{-1}\frac{x_{fbe}}{y_{fbe}} \quad (115)$$

Finally, the length of the gap between the PM edges (L_{PMe}) is:

$$L_{fbe} = R_{fbe} \cdot \left(\alpha_P - 2 \cdot \theta_{fbe}\right) \quad (116)$$

In the case of this value not being deemed sufficient, because it might compromise the rotor structure, the permanent magnet and barrier widths (W_{PM} and W_{fbb} and W_{fbt} respectively should be adjusted, or the pole pitch factor ($k_{\alpha P}$) should be reduced, which will result in a smaller effective pole pitch (α_{Pef}).

As one of the last dimensions in rotor sizing, the diameter at the permanent magnets top is calculated with:

$$D_{PMt} = 2 \cdot \left[\left(\frac{D_{Ro}}{2} - L_{Ro}\right) \cdot \cos\frac{\alpha_{Pef}}{2} - \left(h_{fb} + L_{fb}\right) \cdot \sin\theta_{PM} + \left(h_{fb} \cdot \tan\theta_{fb} + W_{fbt} + W_{PM}\right) \cdot \cos\theta_{PM}\right] \quad (117)$$

The last dimension of the rotor sizing to be calculated is its inner diameter (D_{Ri}). Considering that the magnetic flux density of the rotor yoke should be between $1{,}0$ and $1{,}5\ T$ (PYRHÖNEN; JOKINEN; HRABOVCOVÁ, 2008), the permanent magnet area (its width times the machine length) should be proportional to the rotor yoke area

(its height times the machine length) according to magnetic flux conservation's law. Therefore, to guarantee this proportionality, another factor is used in the inner rotor diameter:

$$D_{Ri} = D_{PMt} - 2 \cdot k_{Ry} \cdot W_{PM} \tag{118}$$

in which k_{Ry} is the rotor yoke factor.

In addition to the rotor sizing equations, another stage that is affected by this difference in machine geometry is the reactance calculation. Since salient-pole machines have a more complex air-gap geometry, analytically calculating the direct and quadrature axis reactances leads to inaccurate results (HENDERSHOT; MILLER, 1994). As explained in section 2.2.2, the armature reaction in salient-pole synchronous machines is modelled through the direct and quadrature axis reactances. Since the reactances are the product of the rated operating frequency and inductance, finding the direct and quadrature inductance values is an important step of the permanent magnet synchronous generator design.

There are three ways to obtain direct and quadrature axis inductances: through analytical calculations, magnetic circuits (reluctance networks), or finite element simulations (HENDERSHOT; MILLER, 2010). Analytical calculations provide values quickly but do not present good precision for machines with complex geometry. Reluctance networks have better accuracy when compared to the previous method and do not require as much computational time as finite element simulations, but they do require significant development time. Finally, finite element simulations deliver the best accuracy among the three methods (MOURA et al., 2020).

To obtain the direct and quadrature axis inductances of a synchronous machine with finite element simulations, two-phase windings must be connected in series, and a direct current of nominal value to have a similar saturation as at full-load is applied while leaving the third phase winding de-energized. Also, the permanent magnets must be removed from the simulation, leaving their rotor space unfilled (or selected to air) so that it does not affect the linked flux. As the rotor assumes different positions over time, the magnetic flux produced varies in value due to the variation in the reluctance path from the direct to the quadrature axis. By dividing the magnetic flux by the current, the inductance values are obtained depending on the position of the

rotor. This way, the self-inductance of the two phases in series has only the second-order harmonic and a DC component different from zero (JONES, 1967).

For a WRSG, in the inductance curve as a function of rotor position, the direct axis inductance will be half of the maximum value and the quadrature axis inductance half of the minimum value. However, for this PMSG, the direct axis has a greater reluctance than the quadrature axis due to the rotor geometry. Thus, when the linked flux is aligned with the d-axis, the inductance value is minimum, and, consequently, when aligned with the q-axis, it reaches the maximum. Therefore, contrary to WRSG, in the inductance curve (as a function of rotor position) the direct axis inductance will be half of the minimum value and the quadrature axis inductance half of the maximum value. With the inductance values, the reactances are found with:

$$X_{d,q} = L_{d.q} \cdot 2 \cdot \pi \cdot f \tag{119}$$

where $L_{d,q}$ and $X_{d,q}$ are the axis synchronous inductance and reactance, respectively, either of the direct or the quadrature axis.

With these reactance values, the design would proceed to the terminal voltage calculation. However, the generator phasor diagram is now the one in Figure 15 for salient-pole PMSG. Having the armature current (I_A), power factor (PF), armature resistance (R_A) and direct and quadrature synchronous reactance values (X_d and X_q respectively), the load angle (δ) can be obtained with equation (18). Thereafter, all values necessary to calculate the generator terminal voltage are known. Equations (13) to (17) can be used to finally calculate the phase-to-phase value of the terminal voltage:

$$V_T = \sqrt{3} \cdot V_\varphi = \sqrt{3} \cdot \sqrt{{V_d}^2 + {V_q}^2} \tag{120}$$

If this value does not match the desired voltage from the design specifications (V_{Td}), then the estimated induced voltage (E_{Af}) must be adjusted. The methodology remains the same; thus, the iterative process necessary to match the terminal voltage to the specified value is the same as described in Section 3.2 (and further explained in Section 3.3.5), with the only difference being that now the inductances are found

through FES instead of being calculated analytically. In the case where only E_{Af} is adjusted, the machine geometry stays the same, and there is no need for a new finite element simulation to obtain the axis synchronous inductances. However, this may need adjustment of the machine stack length to have an integer value of T_{Ac}, which might affect the output power value calculated in Section 3.2.5.

APPENDIX B – SML Optimization Code

```
//Electromagnetic Model
//Surface-Mounted Permanent Magnet Synchronous Generators (PMSG) Optimization



//*****************************************************************************
//Geometric Submodel

parameter f; label f = "Electrical Frequency"; unit f = "Hz";
parameter n; label n = "Rotation"; unit n = "rpm";
parameter BR; label BR = "PM remanent flux density"; unit BR = "T";

group Par0_Spec = [f, n, BR];



//Rotor Sizing
//Number of poles
P=120*f/n;
label P = "Number of poles";

//Pole pitch
AlphaP=2*pi/P;
label AlphaP = "Pole pitch"; unit AlphaP = "rad";

//Effective Pole pitch
AlphaPef=kAlphaP*AlphaP;
label AlphaPef = "Effective Pole pitch"; unit AlphaPef = "rad";

//Air-gap length
LAG=DRo*kAG;
label LAG = "Air-gap length"; unit LAG = "mm";
label DRo = "Rotor outer diameter"; unit DRo = "mm";
label kAG = "Air-gap factor";

//Air-gap arc length
LAGa=((DRo/2)+(LAG/2))*AlphaPef;
label LAGa = "Air-gap arc length"; unit LAGa = "mm";

//PM height
hPM=PC*LAG;
label hPM = "PM height"; unit hPM = "mm";
label PC = "Permeance coefficient";

//PM width
WPM=(DRo/2-hPM/2)*AlphaPef;
```

```
label WPM = "PM width"; unit WPM = "mm";
label kAlphaP = "Pole pitch factor";

//Diameter at the PM top
DPMt=DRo-2*hPM;
label DPMt = "Diameter at the PM top"; unit DPMt = "mm";

//Rotor yoke height
hRy=kPMRy*(WPM/2);
label hRy = "Rotor yoke height"; unit hRy = "mm";
label kPMRy = "Rotor yoke height to PM width factor";

//Rotor inner diameter
DRi=DPMt-2*hRy;
label DRi = "Rotor inner diameter"; unit DRi = "mm";

//Generator stack length
LG=DRo*kMS;
label LG = "Generator stack length"; unit LG = "mm";
label kMS = "Machine shape factor";

//Rotor volume
VR=(((pi/4)*((pow(DPMt,2))-(pow(DRi,2))))+P*(WPM*hPM))*(LG/1000000000);
label VR = "Rotor volume"; unit VR = "m^3";

group In0_Rotor = [DRo, kAG, PC, kAlphaP, kPMRy, kMS];
group Out0_Rotor = [P, AlphaP, AlphaPef, LAGa, LAG, hPM, WPM,
DPMt, hRy, DRi, LG, VR];



//Stator Sizing
//Stator inner diameter
DSi=DRo+2*LAG;
label DSi = "Stator inner diameter"; unit DSi = "mm";

//Slot opening width
WSo=(DRo/NS)*kSow;
label WSo = "Slot opening width"; unit WSo = "mm";
label kSow = "Slot opening factor";

//Slot opening height
hSo=WSo*kSoh;
label hSo = "Slot opening height"; unit hSo = "mm";
label kSoh = "Slot opening height factor";

//Slot wedge height
hSw=WSo*kSw;
label hSw = "Slot wedge height"; unit hSw = "mm";
label kSw = "Slot wedge height factor";
```

```
//Diameter at the slot top
DSt=DSi+2*(hSo+hSw);
label DSt = "Diameter at the slot top"; unit DSt = "mm";

//Slot pitch
AlphaS=2*pi/NS;
label AlphaS = "Slot pitch"; unit AlphaS = "rad";
parameter NS; label NS = "Number of slots";

//Angle at the slot top
ThetaSt=AlphaS/(1+KTS);
label ThetaSt = "Angle at the slot top"; unit ThetaSt = "rad";
label KTS = "Tooth-to-slot width factor ";

//Teeth angle at the top
Thetat=AlphaS-ThetaSt;
label Thetat = "Teeth angle at the top"; unit Thetat = "rad";

//Slot opening angle at the top of the slot
ThetaWSo=2*atan(WSo/DSt);
label ThetaWSo = "Slot opening angle at the top of the slot";
unit ThetaWSo = "rad";

//Slot wedge angle at the top of the slot
ThetaWSw=(ThetaSt-ThetaWSo)/2;
label ThetaWSw = "Slot wedge angle at the top of the slot";
unit ThetaWSw = "rad";

//Slot width at the top
WSt=DSt*tan(ThetaSt/2);
label WSt = "Slot width at the top"; unit WSt = "mm";

//Teeth width at the top
Wt=DSt*tan(Thetat/2);
label Wt = "Teeth width at the top"; unit Wt = "mm";

//Slot wedge width
WSw=(WSt-WSo)/2;
label WSw = "Slot wedge width"; unit WSw = "mm";

//Slot wedge angle
ThetaSw=atan(hSw/WSw);
label ThetaSw = "Slot wedge angle"; unit ThetaSw = "rad";

//Stator yoke height
hSy=WPM*kPMSy;
label hSy = "Stator yoke height"; unit hSy = "mm";
label kPMSy = "PM width to stator yoke factor";
```

```
//Slot height
hS=hSy*kSyS;
label hS = "Slot height"; unit hS = "mm";
label kSyS = "Stator yoke to slot height factor";

//Inclination angle of the slot edge
ThetaSei=AlphaS/2;
label ThetaSei = "Inclination angle of the slot edge"; unit ThetaSei = "rad";

//Slot width at the bottom
WSb=WSt+2*hS*tan(ThetaSei);
label WSb = "Slot width at the bottom"; unit WSb = "mm";

//Slot area
SS=(((WSt+WSb)/2)*hS)+(hSo*WSo)+(((WSt+WSo)/2)*hSw);
label SS = "Slot area"; unit SS = "mm^2";

//Effective slot area
SSef=((WSt+WSb)/2)*hS;
label SSef = "Effective slot area"; unit SSef = "mm^2";

//Stator outer diameter
DSo=DSt+2*hS+2*hSy;
label DSo = "Stator outer diameter"; unit DSo = "mm";

//Stator volume
VS=(((pi/4)*((pow(DSo,2))-(pow(DSi,2))))-NS*(SS-SSef))*(LG/1000000000);
label VS = "Stator volume"; unit VS = "m^3";

//Generator volume
VG=VR+VS;
label VG = "Generator volume"; unit VG = "m^3";

group Par1_Stator = [NS];
group In1_Stator = [kSow, kSoh, kSw, KTS, kPMSy, kSyS];
group Out1_Stator = [DSi, WSo, hSo, hSw, DSt, AlphaS, ThetaSt, Thetat,
 ThetaWSo, ThetaWSw, WSt, Wt, WSw, ThetaSw,  hSy, hS, ThetaSei, WSb, SS,
 SSef, DSo, VS, VG];



//*************************************************************************



//*************************************************************************
//No-Load Magnetic Submodel
```

```
//Postion of the PM source:
thetaPMcT = 0.5*Thetat+0.0*ThetaWSo+0.0*ThetaWSw;
label thetaPMcT = "Central tooth source position";
unit thetaPMcT = "rad";

thetaPMcTrt = 0.5*Thetat+0.0*ThetaWSo+1.0*ThetaWSw;
label thetaPMcTrt = "Central tooth right tip source position";
unit thetaPMcTrt = "rad";

thetaPMcTfTWSo = 0.5*Thetat+1.0*ThetaWSo+1.0*ThetaWSw;
label thetaPMcTfTWSo = "Between central and first teeth source position";
unit thetaPMcTfTWSo = "rad";

thetaPMfTlt = 0.5*Thetat+1.0*ThetaWSo+2.0*ThetaWSw;
label thetaPMfTlt = "First tooth left tip source position";
unit thetaPMfTlt = "rad";

thetaPMfT = 1.5*Thetat+1.0*ThetaWSo+2.0*ThetaWSw;
label thetaPMfT = "First tooth source position";
unit thetaPMfT = "rad";

thetaPMfTrt = 1.5*Thetat+1.0*ThetaWSo+3.0*ThetaWSw;
label thetaPMfTrt = "First tooth right tip source position";
unit thetaPMfTrt = "rad";

thetaPMfTsTWSo = 1.5*Thetat+2.0*ThetaWSo+3.0*ThetaWSw;
label thetaPMfTsTWSo = "Between first and second teeth source position";
unit thetaPMfTsTWSo = "rad";

thetaPMsTlt = 1.5*Thetat+2.0*ThetaWSo+4.0*ThetaWSw;
label thetaPMsTlt = "Second tooth left tip source position";
unit thetaPMsTlt = "rad";

thetaPMsT = 2.5*Thetat+2.0*ThetaWSo+4.0*ThetaWSw;
label thetaPMsT = "Second tooth source position";
unit thetaPMsT = "rad";

thetaPMsTrt = 2.5*Thetat+2.0*ThetaWSo+5.0*ThetaWSw;
label thetaPMsTrt = "Second tooth right tip source position";
unit thetaPMsTrt = "rad";

thetaPMsTtTWSo = 2.5*Thetat+3.0*ThetaWSo+5.0*ThetaWSw;
label thetaPMsTtTWSo = "Between second and third teeth source position";
unit thetaPMsTtTWSo = "rad";

thetaPMtTlt = 2.5*Thetat+3.0*ThetaWSo+6.0*ThetaWSw;
label thetaPMtTlt = "Third tooth left tip source position";
unit thetaPMtTlt = "rad";
```

```
group Var1_0_thetaPMs = [thetaPMcT, thetaPMcTrt, thetaPMcTfTWSo,
thetaPMfTlt,
thetaPMfT, thetaPMfTrt, thetaPMfTsTWSo, thetaPMsTlt, thetaPMsT, thetaPMsTrt,
thetaPMsTtTWSo, thetaPMtTlt];



//External function calling: thetaPM - Which PM sources should contribute
import my.company:pmsg_1.fun_thetaPM:1.0;
//New model instance:
my_fun_thetaPM = new fun_thetaPM;

//Strength of the PM source:
deltaPMcT = fun_thetaPM(thetaPMcT,AlphaPef,Thetat/2.0);
deltaPMcTrt = fun_thetaPM(thetaPMcTrt,AlphaPef,ThetaWSw);
deltaPMcTfTWSo = fun_thetaPM(thetaPMcTfTWSo,AlphaPef,ThetaWSo);
deltaPMfTlt = fun_thetaPM(thetaPMfTlt,AlphaPef,ThetaWSw);
deltaPMfT = fun_thetaPM(thetaPMfT,AlphaPef,Thetat);
deltaPMfTrt = fun_thetaPM(thetaPMfTrt,AlphaPef,ThetaWSw);
deltaPMfTsTWSo = fun_thetaPM(thetaPMfTsTWSo,AlphaPef,ThetaWSo);
deltaPMsTlt = fun_thetaPM(thetaPMsTlt,AlphaPef,ThetaWSw);
deltaPMsT = fun_thetaPM(thetaPMsT,AlphaPef,Thetat);
deltaPMsTrt = fun_thetaPM(thetaPMsTrt,AlphaPef,ThetaWSw);
deltaPMsTtTWSo = fun_thetaPM(thetaPMsTtTWSo,AlphaPef,ThetaWSo);
deltaPMtTlt = fun_thetaPM(thetaPMtTlt,AlphaPef,ThetaWSw);

group Var1_1_deltaPMs = [deltaPMcT, deltaPMcTrt, deltaPMcTfTWSo,
deltaPMfTlt,
deltaPMfT, deltaPMfTrt, deltaPMfTsTWSo, deltaPMsTlt, deltaPMsT, deltaPMsTrt,
deltaPMsTtTWSo, deltaPMtTlt];

//Updating RN for fluxes and densities
import my.company:pmsg_1.Mag_Model:1.0;
//New model instance:
my_Mag_Model = new Mag_Model;

///Affect scalar inputs:
my_Mag_Model.DRo = DRo;
my_Mag_Model.hPM = hPM;
my_Mag_Model.AlphaP = AlphaP;
my_Mag_Model.AlphaPef = AlphaPef;
my_Mag_Model.LG = LG;
my_Mag_Model.DRi = DRi;
my_Mag_Model.hRy = hRy;
my_Mag_Model.WPM = WPM;
my_Mag_Model.kAlphaP = kAlphaP;
my_Mag_Model.AlphaS = AlphaS;
my_Mag_Model.DSo = DSo;
my_Mag_Model.hSy = hSy;
my_Mag_Model.hSw = hSw;
```

```
my_Mag_Model.hSo = hSo;
my_Mag_Model.WSo = WSo;
my_Mag_Model.WSw = WSw;
my_Mag_Model.LAG = LAG;
my_Mag_Model.BR = BR;
my_Mag_Model.deltaPMcTfTWSo = deltaPMcTfTWSo;
my_Mag_Model.ThetaWSo = ThetaWSo;
my_Mag_Model.Wt = Wt;
my_Mag_Model.deltaPMcT = deltaPMcT;
my_Mag_Model.Thetat = Thetat;
my_Mag_Model.ThetaWSw = ThetaWSw;
my_Mag_Model.deltaPMcTrt = deltaPMcTrt;
my_Mag_Model.hS = hS;
my_Mag_Model.WSb = WSb;
my_Mag_Model.deltaPMfTsTWSo = deltaPMfTsTWSo;
my_Mag_Model.deltaPMfT = deltaPMfT;
my_Mag_Model.deltaPMfTlt = deltaPMfTlt;
my_Mag_Model.deltaPMfTrt = deltaPMfTrt;
my_Mag_Model.deltaPMsTtTWSo = deltaPMsTtTWSo;
my_Mag_Model.deltaPMsT = deltaPMsT;
my_Mag_Model.deltaPMsTlt = deltaPMsTlt;
my_Mag_Model.deltaPMsTrt = deltaPMsTrt;
my_Mag_Model.deltaPMtTlt = deltaPMtTlt;
my_Mag_Model.ThetaSt = ThetaSt;
my_Mag_Model.DSt = DSt;

//Get scalar outputs:
//Flux at the PM sources
//Central PM tooth
Phi1PMLh = my_Mag_Model._1PM_Lh.flux;
Phi1PMUh = my_Mag_Model._1PM_Uh.flux;
//Central PM right tip
Phi1PMrtLh = my_Mag_Model._1PM_rt_Lh.flux;
Phi1PMrtUh = my_Mag_Model._1PM_rt_Uh.flux;

//Between central PM and first PM
Phi12PMWSoLh = my_Mag_Model._12PM_WSo_Lh.flux;
Phi12PMWSoUh = my_Mag_Model._12PM_WSo_Uh.flux;

//First PM left tip
Phi2PMltLh = my_Mag_Model._2PM_lt_Lh.flux;
Phi2PMltUh = my_Mag_Model._2PM_lt_Uh.flux;
//First PM tooth
Phi2PMLh = my_Mag_Model._2PM_Lh.flux;
Phi2PMUh = my_Mag_Model._2PM_Uh.flux;
//First PM right tip
Phi2PMrtLh = my_Mag_Model._2PM_rt_Lh.flux;
Phi2PMrtUh = my_Mag_Model._2PM_rt_Uh.flux;

//Between first PM and second PM
```

```
Phi23PMWSoLh = my_Mag_Model._23PM_WSo_Lh.flux;
Phi23PMWSoUh = my_Mag_Model._23PM_WSo_Uh.flux;

//Second PM left tip
Phi3PMltLh = my_Mag_Model._3PM_lt_Lh.flux;
Phi3PMltUh = my_Mag_Model._3PM_lt_Uh.flux;
//Second PM tooth
Phi3PMLh = my_Mag_Model._3PM_Lh.flux;
Phi3PMUh = my_Mag_Model._3PM_Uh.flux;
//Second PM right tip
Phi3PMrtLh = my_Mag_Model._3PM_rt_Lh.flux;
Phi3PMrtUh = my_Mag_Model._3PM_rt_Uh.flux;

//Between second PM and third PM
Phi34PMWSoLh = my_Mag_Model._34PM_WSo_Lh.flux;
Phi34PMWSoUh = my_Mag_Model._34PM_WSo_Uh.flux;

//Third PM left tip
Phi4PMltLh = my_Mag_Model._4PM_lt_Lh.flux;
Phi4PMltUh = my_Mag_Model._4PM_lt_Uh.flux;


//Flux at the Air-gap
//Central tooth
Phi1AG = my_Mag_Model._1AG.flux;
//Central tooth right tip
Phi1AGrt = my_Mag_Model._1AG_rt.flux;

//Between central tooth and first tooth
Phi12AGWSo = my_Mag_Model._12AG_WSo.flux;

//First tooth left tip
Phi2AGlt = my_Mag_Model._2AG_lt.flux;
//First tooth
Phi2AG = my_Mag_Model._2AG.flux;
//First tooth right tip
Phi2AGrt = my_Mag_Model._2AG_rt.flux;

//Between first tooth and second tooth
Phi23AGWSo = my_Mag_Model._23AG_WSo.flux;

//Second tooth left tip
Phi3AGlt = my_Mag_Model._3AG_lt.flux;
//Second tooth
Phi3AG = my_Mag_Model._3AG.flux;
//Second tooth right tip
Phi3AGrt = my_Mag_Model._3AG_rt.flux;

//Between second tooth and third tooth
Phi34AGWSo = my_Mag_Model._34AG_WSo.flux;
```

```
//Third tooth left tip
Phi4AGlt = my_Mag_Model._4AG_lt.flux;


//Flux at the Armature
//Central tooth
Phi1T3s = my_Mag_Model._1T_3s.flux;
Phi1T4s = my_Mag_Model._1T_4s.flux;
//First tooth
Phi2T3s = my_Mag_Model._2T_3s.flux;
Phi2T4s = my_Mag_Model._2T_4s.flux;
//Second tooth
Phi3T3s = my_Mag_Model._3T_3s.flux;
Phi3T4s = my_Mag_Model._3T_4s.flux;

group Var2_0_Fluxes = [Phi1PMLh, Phi1PMUh, Phi1PMrtLh, Phi1PMrtUh,
 Phi12PMWSoLh, Phi12PMWSoUh, Phi2PMltLh, Phi2PMltUh, Phi2PMLh,
Phi2PMUh,
 Phi2PMrtLh, Phi2PMrtUh, Phi23PMWSoLh, Phi23PMWSoUh, Phi3PMltLh,
Phi3PMltUh,
 Phi3PMLh, Phi3PMUh, Phi3PMrtLh, Phi3PMrtUh, Phi34PMWSoLh,
Phi34PMWSoUh,
 Phi4PMltLh, Phi4PMltUh, Phi1AG, Phi1AGrt, Phi12AGWSo, Phi2AGlt, Phi2AG,
 Phi2AGrt, Phi23AGWSo, Phi3AGlt, Phi3AG, Phi3AGrt, Phi34AGWSo, Phi4AGlt,
 Phi1T3s, Phi1T4s, Phi2T3s, Phi2T4s, Phi3T3s, Phi3T4s];

//Flux and Flux Densities
//PM flux
PhiPM = 2*(deltaPMcT*((Phi1PMLh+Phi1PMUh)/2)
+deltaPMcTrt*((Phi1PMrtLh+Phi1PMrtUh)/2)
+deltaPMcTfTWSo*((Phi12PMWSoLh+Phi12PMWSoUh)/2)
+deltaPMfTlt*((Phi2PMltLh+Phi2PMltUh)/2)
+deltaPMfT*((Phi2PMLh+Phi2PMUh)/2)
+deltaPMfTrt*((Phi2PMrtLh+Phi2PMrtUh)/2)
+deltaPMfTsTWSo*((Phi23PMWSoLh+Phi23PMWSoUh)/2)
+deltaPMsTlt*((Phi3PMltLh+Phi3PMltUh)/2)
+deltaPMsT*((Phi3PMLh+Phi3PMUh)/2)
+deltaPMsTrt*((Phi3PMrtLh+Phi3PMrtUh)/2)
+deltaPMsTtTWSo*((Phi34PMWSoLh+Phi34PMWSoUh)/2)
+deltaPMtTlt*((Phi4PMltLh+Phi4PMltUh)/2));
label PhiPM = "PM flux"; unit PhiPM = "Wb";

//Air-gap flux
PhiAG = 2*(deltaPMcT*(Phi1AG)
+deltaPMcTrt*(Phi1AGrt)
+deltaPMcTfTWSo*(Phi12AGWSo)
+deltaPMfTlt*(Phi2AGlt)
+deltaPMfT*(Phi2AG)
+deltaPMfTrt*(Phi2AGrt)
```

```
+deltaPMfTsTWSo*(Phi23AGWSo)
+deltaPMsTlt*(Phi3AGlt)
+deltaPMsT*(Phi3AG)
+deltaPMsTrt*(Phi3AGrt)
+deltaPMsTtTWSo*(Phi34AGWSo)
+deltaPMtTlt*(Phi4AGlt));
label PhiAG = "Air-gap flux"; unit PhiAG= "Wb";

//Armature flux
PhiAM=2*(((Phi1T3s+Phi1T4s)/2)+((Phi2T3s+Phi2T4s)/2)+((Phi3T3s+Phi3T4s)/2));
label PhiAM = "Armature flux"; unit PhiAM = "Wb";

group Out2_Flux = [PhiPM, PhiAG, PhiAM];



//Rotor yoke flux densities
//Between central(1) and first(2) teeth: Lower quarter
BRy12Lq = my_Mag_Model.Ry_12_Lq.B;
//Between central(1) and first(2) teeth: Upper quarter
BRy12Uq = my_Mag_Model.Ry_12_Uq.B;
//Central(1) tooth: Lower quarter
BRy1Lq = my_Mag_Model.Ry_1_Lq.B;
//Central(1) tooth: Upper quarter
BRy1Uq = my_Mag_Model.Ry_1_Uq.B;
//Between first(2) and second(3) teeth: Lower half
BRy23Lh = my_Mag_Model.Ry_23_Lh.B;
//Step 34.4 - Between first(2) and second(3) teeth: Lower quarter
BRy23Lq = my_Mag_Model.Ry_23_Lq.B;
//Between first(2) and second(3) teeth: Upper quarter
BRy23Uq = my_Mag_Model.Ry_23_Uq.B;
//First(2) tooth: Lower half
BRy2Lh = my_Mag_Model.Ry_2_Lh.B;
//First(2) tooth: Lower quarter
BRy2Lq = my_Mag_Model.Ry_2_Lq.B;
//First(2) tooth: Upper quarter
BRy2Uq = my_Mag_Model.Ry_2_Uq.B;
//Between second(3) and fourth(5) teeth: Lower half
BRy35Lh = my_Mag_Model.Ry_35_Lh.B;
//Between second(3) and fourth(5) teeth: Lower quarter
BRy35Lq = my_Mag_Model.Ry_35_Lq.B;
//Between second(3) and fourth(5) teeth: Upper quarter
BRy35Uq = my_Mag_Model.Ry_35_Uq.B;
//Second(3) tooth: Lower half
BRy3Lh = my_Mag_Model.Ry_3_Lh.B;
//Second(3) tooth: Lower quarter
BRy3Lq = my_Mag_Model.Ry_3_Lq.B;
//Second(3) tooth: Upper quarter
BRy3Uq = my_Mag_Model.Ry_3_Uq.B;
```

```
group Var2_1_BRy = [BRy12Lq, BRy12Uq, BRy1Lq, BRy1Uq, BRy23Lh, BRy23Lq,
BRy23Uq,
BRy2Lh, BRy2Lq, BRy2Uq, BRy35Lh, BRy35Lq, BRy35Uq, BRy3Lh,
BRy3Lq,BRy3Uq];



//Air-gap flux density
BAG=(PhiAG/(LAGa*LG))*1000000;
label BAG = "Air-gap flux density"; unit BAG = "T";


//Stator teeth flux densities
//Central(1) tooth
B1T3s = my_Mag_Model._1T_3s.B;
B1T4s = my_Mag_Model._1T_4s.B;

//First(2) tooth
B2T3s = my_Mag_Model._2T_3s.B;
B2T4s = my_Mag_Model._2T_4s.B;

//Second(3) tooth
B3T3s = my_Mag_Model._3T_3s.B;
B3T4s = my_Mag_Model._3T_4s.B;

group Var2_2_BSt = [B1T3s, B1T4s, B1T, B2T3s, B2T4s, B2T, B3T3s, B3T4s,
B3T];



BSt=(B1T3s+B1T4s)/2;
label BSt = "Peak stator teeth flux density"; unit BSt = "T";


//Stator teeth tips flux densities
//Central(1) tooth: right tip hSo right half
B1ThSor = my_Mag_Model._1T_hSo_r.B;
//Central(1) tooth: right tip hSo
B1ThSort = my_Mag_Model._1T_hSo_rt.B;
//Central(1) tooth: right tip
B1Trt = my_Mag_Model._1T_rt.B;
//Central(1) tooth: right tip hSw right half
B1ThSwr = my_Mag_Model._1T_hSw_r.B;
//Central(1) tooth: right tip hSw
B1ThSwrt = my_Mag_Model._1T_hSw_rt.B;
//First(2) tooth: left tip hSo left half
B2ThSol = my_Mag_Model._2T_hSo_l.B;
//First(2) tooth: left tip hSo
B2ThSolt = my_Mag_Model._2T_hSo_lt.B;
//First(2) tooth: left tip
```

```
B2Tlt = my_Mag_Model._2T_lt.B;
//First(2) tooth: right tip hSo right half
B2ThSor = my_Mag_Model._2T_hSo_r.B;
//First(2) tooth: right tip hSo
B2ThSort = my_Mag_Model._2T_hSo_rt.B;
//First(2) tooth: right tip
B2Trt = my_Mag_Model._2T_rt.B;
//First(2) tooth: left tip hSw left half
B2ThSwl = my_Mag_Model._2T_hSw_l.B;
//First(2) tooth: left tip hSw
B2ThSwlt = my_Mag_Model._2T_hSw_lt.B;
//First(2) tooth: right tip hSw right half
B2ThSwr = my_Mag_Model._2T_hSw_r.B;
//First(2) tooth: right tip hSw
B2ThSwrt = my_Mag_Model._2T_hSw_rt.B;
//Second(3) tooth: left tip hSo left half
B3ThSol = my_Mag_Model._3T_hSo_l.B;
//Second(3) tooth: left tip hSo
B3ThSolt = my_Mag_Model._3T_hSo_lt.B;
//Second(3) tooth: left tip
B3Tlt = my_Mag_Model._3T_lt.B;
//Second(3) tooth: right tip hSo right half
B3ThSor = my_Mag_Model._3T_hSo_r.B;
//Second(3) tooth: right tip hSo
B3ThSort = my_Mag_Model._3T_hSo_rt.B;
//Second(3) tooth: left tip hSw left half
B3Trt = my_Mag_Model._3T_rt.B;
//Second(3) tooth: left tip hSw left half
B3ThSwl = my_Mag_Model._3T_hSw_l.B;
//Second(3) tooth: left tip hSw
B3ThSwlt = my_Mag_Model._3T_hSw_lt.B;
//Second(3) tooth: right tip hSw right half
B3ThSwr = my_Mag_Model._3T_hSw_r.B;
//Second(3) tooth: right tip hSw
B3ThSwrt = my_Mag_Model._3T_hSw_rt.B;

group Var2_3_Bt = [B1ThSor, B1ThSort, B1Trt, B1ThSwr, B1ThSwrt, B2ThSol,
B2ThSolt, B2Tlt, B2ThSor, B2ThSort, B2Trt, B2ThSwl, B2ThSwlt, B2ThSwr,
B2ThSwrt, B3ThSol, B3ThSolt, B3Tlt, B3ThSor, B3ThSort, B3Trt, B3ThSwl,
B3ThSwlt, B3ThSwr, B3ThSwrt];



//Stator yoke flux densities
//Central(1) tooth to stator yoke
B1TSy = my_Mag_Model._1T_Sy.B;
//First(2) tooth to stator yoke
B2TSy = my_Mag_Model._2T_Sy.B;
//Second(3) tooth to stator yoke: lower half
B3TSyLh = my_Mag_Model._3T_Sy_Lh.B;
```

```
//Second(3) tooth to stator yoke: upper half
B3TSyUh = my_Mag_Model._3T_Sy_Uh.B;
//Between central(1) and first(2) teeth
BSy12 = my_Mag_Model.Sy_12.B;
//Between first(2) and second(3) teeth
BSy23 = my_Mag_Model.Sy_23.B;
//Between second(3) and fourth(5) teeth
BSy35 = my_Mag_Model.Sy_35.B;
//Between second(3) and third(4) teeth
BT34Sy = my_Mag_Model.T34_Sy.B;

group Var2_4_BSy = [B1TSy, B2TSy, B3TSyLh, B3TSyUh, BSy12, BSy23, BSy35,
BT34Sy];


BSy=BT34Sy;
label BSy = "Peak stator yoke flux density"; unit BSy = "T";

group Out3_Densities = [BAG, BSt, BSy];



//*************************************************************************



//*************************************************************************
//Armature Reaction Submodel


//Number of turns of each tooth on the armature sources
//N on the first tooth
N_1T = 4*TAc;
label N_1T = "N of the first tooth";

//N on the second tooth
N_2T = 3*TAc;
label N_2T = "N of the second tooth";

//N on the third tooth
N_3T = 1*TAc;
label N_3T = "N of the third tooth";

//N on the fourth tooth
N_4T = 1*TAc;
label N_4T = "N of the fourth tooth";

//N on the fifth tooth
N_5T = 3*TAc;
```

```
label N_5T = "N of the fifth tooth";

//N on the sixth tooth
N_6T = 4*TAc;
label N_6T = "N of the sixth tooth";

group Var3_0_NsA = [N_1T, N_2T, N_3T, N_4T, N_5T, N_6T];



//Updating RN for inductance
import my.company:pmsg_1.Ind_Model:1.0;
//New model instance:
my_Ind_Model = new Ind_Model;

///Affect scalar inputs:
my_Ind_Model.AlphaS = AlphaS;
my_Ind_Model.DRi = DRi;
my_Ind_Model.hRy = hRy;
my_Ind_Model.LG = LG;
my_Ind_Model.DSo = DSo;
my_Ind_Model.hSy = hSy;
my_Ind_Model.hSw = hSw;
my_Ind_Model.hSo = hSo;
my_Ind_Model.WSo = WSo;
my_Ind_Model.WSw = WSw;
my_Ind_Model.LAG = LAG;
my_Ind_Model.hPM = hPM;
my_Ind_Model.DRo = DRo;
my_Ind_Model.ThetaWSo = ThetaWSo;
my_Ind_Model.Wt = Wt;
my_Ind_Model.Thetat = Thetat;
my_Ind_Model.ThetaWSw = ThetaWSw;
my_Ind_Model.hS = hS;
my_Ind_Model.WSb = WSb;
my_Ind_Model.ThetaSt = ThetaSt;
my_Ind_Model.DSt = DSt;
my_Ind_Model.IA = IA;
my_Ind_Model.N_1T = N_1T;
my_Ind_Model.N_2T = N_2T;
my_Ind_Model.N_3T = N_3T;
my_Ind_Model.N_4T = N_4T;
my_Ind_Model.N_5T = N_5T;
my_Ind_Model.N_6T = N_6T;



//FMMs values
//Get scalar outputs:
_1T_NI = my_Ind_Model._1T.NI;
label _1T_NI = "FMM of the first tooth";
```

```
_2T_NI = my_Ind_Model._2T.NI;
label _2T_NI = "FMM of the second tooth";
_3T_NI = my_Ind_Model._3T.NI;
label _3T_NI = "FMM of the third tooth";
_4T_NI = my_Ind_Model._4T.NI;
label _4T_NI = "FMM of the fourth tooth";
_5T_NI = my_Ind_Model._5T.NI;
label _5T_NI = "FMM of the fifth tooth";
_6T_NI = my_Ind_Model._6T.NI;
label _6T_NI = "FMM of the sixth tooth";

group Var3_1_FMMs = [_1T_NI, _2T_NI, _3T_NI, _4T_NI, _5T_NI, _6T_NI];



_1T3s = my_Ind_Model._1T_3s.flux;
_1T4s = my_Ind_Model._1T_4s.flux;
_1T = (_1T3s + _1T4s)/2;
label _1T = "Flux in central(1) tooth"; unit _1T = "Wb";

_2T3s = my_Ind_Model._2T_3s.flux;
_2T4s = my_Ind_Model._2T_4s.flux;
_2T = (_2T3s + _2T4s)/2;
label _2T = "Flux in first(2) tooth"; unit _2T = "Wb";

_3T3s = my_Ind_Model._3T_3s.flux;
_3T4s = my_Ind_Model._3T_4s.flux;
_3T = (_3T3s + _3T4s)/2;
label _3T = "Flux in second(3) tooth"; unit _3T = "Wb";

_4T3s = my_Ind_Model._4T_3s.flux;
_4T4s = my_Ind_Model._4T_4s.flux;
_4T = (_4T3s + _4T4s)/2;
label _4T = "Flux in third(4) tooth"; unit _4T = "Wb";

_5T3s = my_Ind_Model._5T_3s.flux;
_5T4s = my_Ind_Model._5T_4s.flux;
_5T = (_5T3s + _5T4s)/2;
label _5T = "Flux in fourth(5) tooth"; unit _5T = "Wb";

_6T3s = my_Ind_Model._6T_3s.flux;
_6T4s = my_Ind_Model._6T_4s.flux;
_6T = (_6T3s + _6T4s)/2;
label _6T = "Flux in fifth(6) tooth"; unit _6T = "Wb";

group Var3_2_IndModel = [_1T3s, _1T4s, _1T, _2T3s, _2T4s, _2T, _3T3s, _3T4s,
_3T,
 _4T3s, _4T4s, _4T, _5T3s, _5T4s, _5T, _6T3s, _6T4s, _6T];

//Flux linkage
```

```
Lambda = TAc*P*((4*_1T)+(3*_2T)+(1*_3T)+(1*_4T)+(3*_5T)+(4*_6T));
label Lambda = "Flux linkage"; unit Lambda = "Wb";

//Synchronous inductance
LS=(Lambda/IA)/2;
label LS = "Synchronous inductance"; unit LS = "H";

//Synchronous reactance
XS=2*pi*f*LS;
label XS = "Synchronous reactance"; unit XS = "ohm";

group Out6_SynReac = [Lambda, LS, XS];



//*************************************************************************



//*************************************************************************
//Electric Submodel


//Armature Definitions
//Armature coil pitch
AlphaAc=AlphaP*kAc*(P/2);
label AlphaAc = "Armature coil pitch"; unit AlphaAc = "rad";
parameter kAc; label kAc = "Armature coil-shortening factor";

//Coil shortening factor
DeltaPhiAc=sin(AlphaAc/2);
label DeltaPhiAc = "Coil shortening factor";

//Slots per pole per phase
q=NS/(Nph*P);
label q = "Slots per pole per phase";
parameter Nph; label Nph = "Number of phases of the generator";

//Windings distribution factor
DeltaPhiWd=(sin(((q*AlphaS)/2)*(P/2)))/(q*sin((AlphaS/2)*(P/2)));
label DeltaPhiWd = "Windings distribution factor";

//Number of turns of the armature winding per phase
TA=EAf/(sqrt(2)*pi*f*DeltaPhiAc*DeltaPhiWd*PhiAM);
label TA = "Number of turns of the armature winding per phase";
label EAf = "Induced voltage estimated to be generated when feeding a load";
unit EAf= "V";

//Number of coils in series per phase
```

```
NCs=P/(NCp*kCop);
label NCs = "Number of coils in series per phase";
parameter NCp; label NCp = "Number of coils in parallel per phase";
parameter kCop; label kCop = "Consequent pole factor";

//Coils per pole per phase
NCpp=(q*NSl*kCop)/2;
label NCpp = "Coils per pole per phase";
parameter NSl; label NSl = "Number of slot layers";

//Number of turns of the armature winding per coil
TAc=TA/(NCpp*NCs);
label TAc = "Number of turns of the armature winding per coil";

//Armature conductor surface
SAc=(SSef*kSf)/(TAc*NSl);
label SAc = "Armature conductor surface"; unit SAc = "mm^2";
parameter kSf; label kSf = "Slot fill factor";

group Par2_ArmWin = [kAc, NSl, kCop, Nph, NCp, kSf];
group In2_ArmWin = [EAf];
group Out4_ArmWin = [AlphaAc, DeltaPhiAc, q, DeltaPhiWd, TA, NCs, NCpp, TAc,
 SAc];



//Armature Resistance Calculation
//Arc length between two slots of the same coil
LC=(DSt+hS)*(AlphaAc/P);
label LC = "Arc length between two slots of the same coil"; unit LC = "m";

//Coil end length
LCe=(LC/2)*pi;
label LCe = "Coil end length"; unit LCe = "m";

//Coil end resistance
RCe=2*LCe*TA*RAkm*(1/1000000);
label RCe = "Coil end resistance"; unit RCe = "ohm";
parameter RAkm; label RAkm = "Resistance per kilometer of the conductor";
unit RAkm = "ohm/km";

//Total length of the armature coil
LAt=2*LG+2*LCe;
label LAt = "Total length of the armature coil"; unit LAt = "m";

//Armature single phase resistance
RAref=LAt*TA*RAkm*(1/1000000);
label RAref = "Armature single phase resistance"; unit RAref = "ohm";

//Armature single phase resistance corrected
```

```
RA=RAref*((234.5+Top)/(234.5+Tref));
label RA = "Armature single phase resistance corrected"; unit RA = "ohm";
parameter Top; label Top = "Operative temperature"; unit Top = "ºC";
parameter Tref; label Tref = "Reference temperature"; unit Tref = "ºC";

group Par3_ArmRes = [RAkm, Top, Tref];
group Out5_ArmRes = [LC, LCe, RCe, LAt, RAref, RA];



//Terminal Voltage Calculation
//Current capacity of the armature
IA=SAc*JA;
label IA = "Current capacity of the armature"; unit IA = "A";
parameter JA; label JA = "Maximum current density of the armature";
unit JA = "A/mm^2";

//Angle between terminal voltage and armature current
Phi=acos(PF);
label Phi = "Angle between terminal voltage and armature current";
unit Phi = "rad";
parameter PF; label PF = "Power Factor";

//Load angle
Delta=asin((IA*XS*cos(Phi)-IA*RA*sin(Phi))/EAf);
label Delta = "Load angle"; unit Delta = "rad";

//Real component of the complex armature current
IAr=IA*cos(Phi+Delta);
label IAr = "Real component of the complex armature current"; unit IAr = "A";

//Imaginary component of the complex armature current
IAi=IA*sin(Phi+Delta);
label IAi = "Imaginary component of the complex armature current";
unit IAi = "A";

//Real component of the complex phase terminal voltage
VPhir=EAf-RA*IAr-XS*IAi;
label VPhir = "Real component of the complex phase terminal voltage";
unit VPhir = "V";

//Imaginary component of the complex phase terminal voltage
VPhii=-RA*IAi+XS*IAr;
label VPhii = "Imaginary component of the complex phase terminal voltage";
unit VPhii = "V";

//Phase value of the terminal voltage
VPhi=sqrt((pow(VPhir,2))+(pow(VPhii,2)));
label VPhi = "Phase value of the terminal voltage"; unit VPhi = "V";
```

```
//Phase-to-phase value of the terminal voltage
VT=sqrt(3)*VPhi;
label VT = "Phase-to-phase value of the terminal voltage"; unit VT = "V";

group Par4_TermVolt = [JA, PF];
group Out7_TermVolt = [IA, Phi, Delta, IAr, IAi, VPhir, VPhii, VPhi, VT];



//Output power
//Admissible apparent power
SE=3*IA*(VT/sqrt(3));
label SE = "Admissible apparent power"; unit SE = "VA";

//Admissible active power
PE=SE*PF;
label PE = "Admissible active power"; unit PE = "W";

//Generator torque density
rohtau=((PE/((n*2*pi)/60))/VG)/1000;
label rohtau = "Generator torque density"; unit rohtau = "kNm/m^3";

group Out8_Power = [SE, PE, rohtau];



//Losses and Efficiency estimation
//Copper losses
PAc=3*RA*pow(IA,2);
label PAc = "Copper losses"; unit PAc = "W";

//Stator yoke volume
VSy=(pi/4)*(LG/1000000000)*((pow(DSo,2))-(pow((DSo-(2*hSy)),2)));
label VSy = "Stator yoke volume"; unit VSy = "m^3";

//Stator teeth volume
VSt=NS*(LG/1000000000)*((Wt*hS)+(Wt+WSw)*hSw+(Wt+WSw)*hSo);
label VSt = "Stator teeth volume"; unit VSt = "m^3";

//Stator yoke hysteresis losses
PSyh=kSyh*VSy*Roee*Ph*(f/50)*pow(BSy/1.5,2);
label PSyh = "Stator yoke hysteresis losses"; unit PSyh = "W";
parameter kSyh; label kSyh = "Hysteresis losses factor (Yoke)";
parameter Roee;label Roee = "Manufacturer density electrical steel";
unit Roee = "kg/m^3";
parameter Ph; label Ph = "Hysteresis loss density at 1,5T and 50Hz";
unit Ph = "W/kg";

//Stator yoke Foucault losses
PSyf=kSyf*VSy*Roee*Pf*pow(f/50,2)*pow(BSy/1.5,2);
```

```
label PSyf = "Stator yoke Foucault losses"; unit PSyf = "W";
parameter kSyf; label kSyf = "Foucault losses factor (Yoke)";
parameter Pf; label Pf = "Foucault loss density at 1,5T and 50Hz";
unit Pf = "W/kg";

//Stator teeth hysteresis losses
PSth=kSth*VSt*Roee*Ph*(f/50)*pow(BSt/1.5,2);
label PSth = "Stator teeth hysteresis losses"; unit PSth = "W";
parameter kSth; label kSth = "Hysteresis losses factor (Teeth)";

//Stator teeth Foucault losses
PStf=kStf*VSt*Roee*Pf*pow(f/50,2)*pow(BSt/1.5,2);
label PStf = "Stator teeth Foucault losses"; unit PStf = "W";
parameter kStf; label kStf = "Foucault losses factor (Teeth)";

//PM losses
PPMs=(P*kPM*WPM*LG)/1000000;
label PPMs = "PM losses"; unit PPMs = "W";
parameter kPM; label kPM = "PM specific loss"; unit kPM = "W/m^2";

//Total losses
PT=(1+kSl)*(PAc+PSyh+PSyf+PSth+PStf+PPMs);
label PT = "Total losses"; unit PT = "W";
parameter kSl; label kSl = "Stray losses factor";

//Efficiency
Eta=((PE)/(PE+PT))*100;
label Eta = "Efficiency"; unit Eta = "%";

group Par5_Loss = [Pf, Ph, kSyh, Roee, kSyf, kSth, kStf, kPM, kSl];
group Var10_Loss = [PAc, VSy, VSt, PSyh, PSyf, PSth, PStf, PPMs, PT, Eta];



//*************************************************************************
```

APPENDIX C – Parameterised No-Load Magnetic Submodel Equations

This appendix presents the equations that define areas and lengths of the reluctances and sources in the network used for calculating the PMSG linkage flux. Figure 55 shows the parameterised no-load reluctance network implemented in CADES.

Figure 55 – No-load flux magnetic submodel implemented in CADES

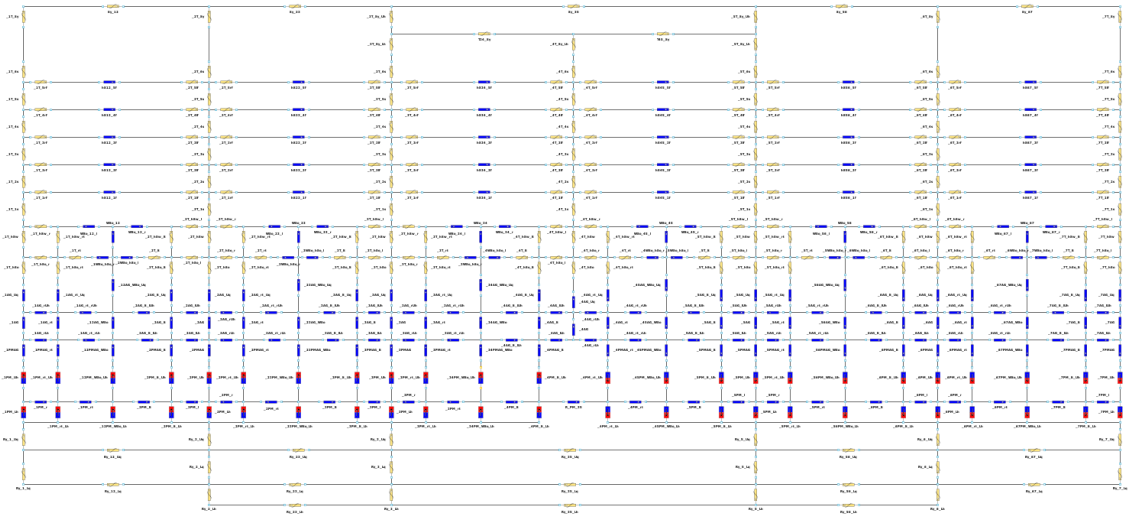

Source: Own authorship (2024)

Table 27 shows the length and area equations of each air and iron reluctances.

Table 27 – Length and area of the air and iron reluctances of the no-load flux reluctance network

Reluctance	Length	Area
_12AG_WSo	LAG/2	(WSo)*LG
_12AG_WSo_Uq	(LAG/4)+(hSo/2)	(WSo)*LG
_12PMAG_WSo	LAG/4	(WSo)*LG
_1AG	LAG/2	(Wt/2)*LG
_1AG_rLh	(Wt/2)+(WSw/2)	(LAG/2)*LG
_1AG_rt	LAG/2	(WSw)*LG
_1AG_rt_rLh	(WSw/2)+(WSo/2)	(LAG/2)*LG
_1AG_rt_rUh	(WSw/2)+(WSo/2)	(LAG/2)*LG
_1AG_rt_Uq	LAG/4	(WSw)*LG
_1AG_rUh	(Wt/2)+(WSw/2)	(LAG/2)*LG
_1AG_Uq	LAG/4	(Wt/2)*LG
_1PM_r	((DRo/2)-(hPM/2))*((Thetat/2)+(ThetaWSw/2))	hPM*LG

_1PM_rt	((DRo/2)-(hPM/2))*((ThetaWSw/2)+(ThetaWSo/2))	hPM*LG
_1PMAG	LAG/4	(Wt/2)*LG
_1PMAG_rt	LAG/4	(WSw)*LG
_1T_1rf	Wt/2	(hS/5)*LG
_1T_1s	(hSw/2)+(hS/6)	(Wt/2)*LG
_1T_2rf	Wt/2	(hS/5)*LG
_1T_2s	hS/6	(Wt/2)*LG
_1T_3rf	Wt/2	(hS/5)*LG
_1T_3s	hS/6	(Wt/2)*LG
_1T_4rf	Wt/2	(hS/5)*LG
_1T_4s	hS/6	(Wt/2)*LG
_1T_5rf	Wt/2	(hS/5)*LG
_1T_5s	hS/6	(Wt/2)*LG
_1T_6s	hS/6	(Wt/2)*LG
_1T_hSo	hSo/2	(Wt/2)*LG
_1T_hSo_r	(Wt/4)+(WSw/2)	((hSo/2)+(hSw/2))*LG
_1T_hSo_rt	hSo/2	(WSw)*LG
_1T_hSw	(hSo/2)+(hSw/2)	(Wt/2)*LG
_1T_hSw_r	(Wt/4)+(WSw/2)	hSw*LG
_1T_hSw_rt	(hSo/2)+(hSw/2)	(WSw)*LG
_1T_rt	(WSw/2)	(hSo)*LG
_1T_Sy	hSy/2	((Wt/2)+(WSb/2))*LG
_1WSo_hSo_r	(WSo/2)	(hSo)*LG
_23AG_WSo	LAG/2	(WSo)*LG
_23AG_WSo_Uq	(LAG/4)+(hSo/2)	(WSo)*LG
_23PMAG_WSo	LAG/4	(WSo)*LG
_2AG	LAG/2	(Wt)*LG
_2AG_lLh	(Wt/2)+(WSw/2)	(LAG/2)*LG
_2AG_lt	LAG/2	(WSw)*LG
_2AG_lt_lLh	(WSw/2)+(WSo/2)	(LAG/2)*LG
_2AG_lt_lUh	(WSw/2)+(WSo/2)	(LAG/2)*LG
_2AG_lt_Uq	LAG/4	(WSw)*LG
_2AG_lUh	(Wt/2)+(WSw/2)	(LAG/2)*LG
_2AG_rLh	(Wt/2)+(WSw/2)	(LAG/2)*LG
_2AG_rt	LAG/2	(WSw)*LG
_2AG_rt_rLh	(WSw/2)+(WSo/2)	(LAG/2)*LG
_2AG_rt_rUh	(WSw/2)+(WSo/2)	(LAG/2)*LG
_2AG_rt_Uq	LAG/4	(WSw)*LG
_2AG_rUh	(Wt/2)+(WSw/2)	(LAG/2)*LG
_2AG_Uq	LAG/4	(Wt)*LG

_2PM_l	((DRo/2)-(hPM/2))*((ThetaWSw/2)+(Thetat/2))	hPM*LG
_2PM_lt	((DRo/2)-(hPM/2))*((ThetaWSo/2)+(ThetaWSw/2))	hPM*LG
_2PM_r	((DRo/2)-(hPM/2))*((Thetat/2)+(ThetaWSw/2))	hPM*LG
_2PM_rt	((DRo/2)-(hPM/2))*((ThetaWSw/2)+(ThetaWSo/2))	hPM*LG
_2PMAG	LAG/4	(Wt)*LG
_2PMAG_lt	LAG/4	(WSw)*LG
_2PMAG_rt	LAG/4	(WSw)*LG
_2T_1lf	Wt/2	(hS/5)*LG
_2T_1rf	Wt/2	(hS/5)*LG
_2T_1s	(hSw/2)+(hS/6)	(Wt)*LG
_2T_2lf	Wt/2	(hS/5)*LG
_2T_2rf	Wt/2	(hS/5)*LG
_2T_2s	hS/6	(Wt)*LG
_2T_3lf	Wt/2	(hS/5)*LG
_2T_3rf	Wt/2	(hS/5)*LG
_2T_3s	hS/6	(Wt)*LG
_2T_4lf	Wt/2	(hS/5)*LG
_2T_4rf	Wt/2	(hS/5)*LG
_2T_4s	hS/6	(Wt)*LG
_2T_5lf	Wt/2	(hS/5)*LG
_2T_5rf	Wt/2	(hS/5)*LG
_2T_5s	hS/6	(Wt)*LG
_2T_6s	hS/6	(Wt)*LG
_2T_hSo	hSo/2	(Wt)*LG
_2T_hSo_l	(Wt/2)+(WSw/2)	((hSo/2)+(hSw/2))*LG
_2T_hSo_lt	hSo/2	(WSw)*LG
_2T_hSo_r	(Wt/2)+(WSw/2)	((hSo/2)+(hSw/2))*LG
_2T_hSo_rt	hSo/2	(WSw)*LG
_2T_hSw	(hSo/2)+(hSw/2)	(Wt)*LG
_2T_hSw_l	(Wt/2)+(WSw/2)	hSw*LG
_2T_hSw_lt	(hSo/2)+(hSw/2)	(WSw)*LG
_2T_hSw_r	(Wt/2)+(WSw/2)	hSw*LG
_2T_hSw_rt	(hSo/2)+(hSw/2)	(WSw)*LG
_2T_lt	(WSw/2)	(hSo)*LG
_2T_rt	(WSw/2)	(hSo)*LG
_2T_Sy	hSy/2	(Wt+WSb)*LG
_2WSo_hSo_l	(WSo/2)	(hSo)*LG
_2WSo_hSo_r	(WSo/2)	(hSo)*LG

_34AG_WSo	LAG/2	(WSo)*LG
_34AG_WSo_Uq	(LAG/4)+(hSo/2)	(WSo)*LG
_34PMAG_WSo	LAG/4	(WSo)*LG
_3AG	LAG/2	(Wt)*LG
_3AG_lLh	(Wt/2)+(WSw/2)	(LAG/2)*LG
_3AG_lt	LAG/2	(WSw)*LG
_3AG_lt_lLh	(WSw/2)+(WSo/2)	(LAG/2)*LG
_3AG_lt_lUh	(WSw/2)+(WSo/2)	(LAG/2)*LG
_3AG_lt_Uq	LAG/4	(WSw)*LG
_3AG_lUh	(Wt/2)+(WSw/2)	(LAG/2)*LG
_3AG_rLh	(Wt/2)+(WSw/2)	(LAG/2)*LG
_3AG_rt	LAG/2	(WSw)*LG
_3AG_rt_rLh	(WSw/2)+(WSo/2)	(LAG/2)*LG
_3AG_rt_rUh	(WSw/2)+(WSo/2)	(LAG/2)*LG
_3AG_rt_Uq	LAG/4	(WSw)*LG
_3AG_rUh	(Wt/2)+(WSw/2)	(LAG/2)*LG
_3AG_Uq	LAG/4	(Wt)*LG
_3PM_l	((DRo/2)-(hPM/2))*((ThetaWSw/2)+(Thetat/2))	hPM*LG
_3PM_lt	((DRo/2)-(hPM/2))*((ThetaWSo/2)+(ThetaWSw/2))	hPM*LG
_3PM_r	((DRo/2)-(hPM/2))*((Thetat/2)+(ThetaWSw/2))	hPM*LG
_3PM_rt	((DRo/2)-(hPM/2))*((ThetaWSw/2)+(ThetaWSo/2))	hPM*LG
_3PMAG	LAG/4	(Wt)*LG
_3PMAG_lt	LAG/4	(WSw)*LG
_3PMAG_rt	LAG/4	(WSw)*LG
_3T_1lf	Wt/2	(hS/5)*LG
_3T_1rf	Wt/2	(hS/5)*LG
_3T_1s	(hSw/2)+(hS/6)	(Wt)*LG
_3T_2lf	Wt/2	(hS/5)*LG
_3T_2rf	Wt/2	(hS/5)*LG
_3T_2s	hS/6	(Wt)*LG
_3T_3lf	Wt/2	(hS/5)*LG
_3T_3rf	Wt/2	(hS/5)*LG
_3T_3s	hS/6	(Wt)*LG
_3T_4lf	Wt/2	(hS/5)*LG
_3T_4rf	Wt/2	(hS/5)*LG
_3T_4s	hS/6	(Wt)*LG
_3T_5lf	Wt/2	(hS/5)*LG
_3T_5rf	Wt/2	(hS/5)*LG

_3T_5s	hS/6	(Wt)*LG
_3T_6s	(hS/6)	(Wt)*LG
_3T_hSo	hSo/2	(Wt)*LG
_3T_hSo_l	(Wt/2)+(WSw/2)	((hSo/2)+(hSw/2))*LG
_3T_hSo_lt	hSo/2	(WSw)*LG
_3T_hSo_r	(Wt/2)+(WSw/2)	((hSo/2)+(hSw/2))*LG
_3T_hSo_rt	hSo/2	(WSw)*LG
_3T_hSw	(hSo/2)+(hSw/2)	(Wt)*LG
_3T_hSw_l	(Wt/2)+(WSw/2)	hSw*LG
_3T_hSw_lt	(hSo/2)+(hSw/2)	(WSw)*LG
_3T_hSw_r	(Wt/2)+(WSw/2)	hSw*LG
_3T_hSw_rt	(hSo/2)+(hSw/2)	(WSw)*LG
_3T_lt	(WSw/2)	(hSo)*LG
_3T_rt	(WSw/2)	(hSo)*LG
_3T_Sy_Lh	hSy/4	(Wt+WSb)*LG
_3T_Sy_Uh	hSy/2	(Wt+WSb)*LG
_3WSo_hSo_l	(WSo/2)	(hSo)*LG
_3WSo_hSo_r	(WSo/2)	(hSo)*LG
_45AG_WSo	LAG/2	(WSo)*LG
_45AG_WSo_Uq	(LAG/4)+(hSo/2)	(WSo)*LG
_45PMAG_WSo	LAG/4	(WSo)*LG
_4AG	LAG/2	(Wt)*LG
_4AG_lLh	(WSw/2)+(Wt/2)	(LAG/2)*LG
_4AG_lt	LAG/2	(WSw)*LG
_4AG_lt_lLh	(WSw/2)+(WSo/2)	(LAG/2)*LG
_4AG_lt_lUh	(WSw/2)+(WSo/2)	(LAG/2)*LG
_4AG_lt_Uq	LAG/4	(WSw)*LG
_4AG_lUh	(WSw/2)+(Wt/2)	(LAG/2)*LG
_4AG_rLh	(WSw/2)+(Wt/2)	(LAG/2)*LG
_4AG_rt	LAG/2	(WSw)*LG
_4AG_rt_rLh	(WSw/2)+(WSo/2)	(LAG/2)*LG
_4AG_rt_rUh	(WSw/2)+(WSo/2)	(LAG/2)*LG
_4AG_rt_Uq	LAG/4	(WSw)*LG
_4AG_rUh	(WSw/2)+(Wt/2)	(LAG/2)*LG
_4AG_Uq	LAG/4	(Wt)*LG
_4PM_lt	((DRo/2)-(hPM/2))*((ThetaWSo/2)+(ThetaWSw/2))	hPM*LG
_4PM_rt	((DRo/2)-(hPM/2))*((ThetaWSo/2)+(ThetaWSw/2))	hPM*LG
_4PMAG_lt	LAG/4	(WSw)*LG
_4PMAG_rt	LAG/4	(WSw)*LG
_4T_1lf	Wt/2	(hS/5)*LG

_4T_1rf	Wt/2	(hS/5)*LG
_4T_1s	(hSw/2)+(hS/6)	(Wt)*LG
_4T_2lf	Wt/2	(hS/5)*LG
_4T_2rf	Wt/2	(hS/5)*LG
_4T_2s	hS/6	(Wt)*LG
_4T_3lf	Wt/2	(hS/5)*LG
_4T_3rf	Wt/2	(hS/5)*LG
_4T_3s	hS/6	(Wt)*LG
_4T_4lf	Wt/2	(hS/5)*LG
_4T_4rf	Wt/2	(hS/5)*LG
_4T_4s	hS/6	(Wt)*LG
_4T_5lf	Wt/2	(hS/5)*LG
_4T_5rf	Wt/2	(hS/5)*LG
_4T_5s	hS/6	(Wt)*LG
_4T_6s	(hS/6)	(Wt)*LG
_4T_hSo	hSo/2	(Wt)*LG
_4T_hSo_l	(Wt/2)+(WSw/2)	((hSo/2)+(hSw/2))*LG
_4T_hSo_lt	hSo/2	(WSw)*LG
_4T_hSo_r	(Wt/2)+(WSw/2)	((hSo/2)+(hSw/2))*LG
_4T_hSo_rt	hSo/2	(WSw)*LG
_4T_hSw	(hSo/2)+(hSw/2)	(Wt)*LG
_4T_hSw_l	(Wt/2)+(WSw/2)	hSw*LG
_4T_hSw_lt	(hSo/2)+(hSw/2)	(WSw)*LG
_4T_hSw_r	(Wt/2)+(WSw/2)	hSw*LG
_4T_hSw_rt	(hSo/2)+(hSw/2)	(WSw)*LG
_4T_lt	(WSw/2)	(hSo)*LG
_4T_rt	(WSw/2)	(hSo)*LG
_4T_Sy_Lh	hSy/4	(Wt+WSb)*LG
_4WSo_hSo_l	(WSo/2)	(hSo)*LG
_4WSo_hSo_r	(WSo/2)	(hSo)*LG
_56AG_WSo	LAG/2	(WSo)*LG
_56AG_WSo_Uq	(LAG/4)+(hSo/2)	(WSo)*LG
_56PMAG_WSo	LAG/4	(WSo)*LG
_5AG	LAG/2	(Wt)*LG
_5AG_lLh	(Wt/2)+(WSw/2)	(LAG/2)*LG
_5AG_lt	LAG/2	(WSw)*LG
_5AG_lt_lLh	(WSw/2)+(WSo/2)	(LAG/2)*LG
_5AG_lt_lUh	(WSw/2)+(WSo/2)	(LAG/2)*LG
_5AG_lt_Uq	LAG/4	(WSw)*LG
_5AG_lUh	(Wt/2)+(WSw/2)	(LAG/2)*LG
_5AG_rLh	(Wt/2)+(WSw/2)	(LAG/2)*LG

_5AG_rt	LAG/2	(WSw)*LG
_5AG_rt_rLh	(WSw/2)+(WSo/2)	(LAG/2)*LG
_5AG_rt_rUh	(WSw/2)+(WSo/2)	(LAG/2)*LG
_5AG_rt_Uq	LAG/4	(WSw)*LG
_5AG_rUh	(Wt/2)+(WSw/2)	(LAG/2)*LG
_5AG_Uq	LAG/4	(Wt)*LG
_5PM_l	((DRo/2)-(hPM/2))*((Thetat/2)+(ThetaWSw/2))	hPM*LG
_5PM_lt	((DRo/2)-(hPM/2))*((ThetaWSw/2)+(ThetaWSo/2))	hPM*LG
_5PM_r	((DRo/2)-(hPM/2))*((ThetaWSw/2)+(Thetat/2))	hPM*LG
_5PM_rt	((DRo/2)-(hPM/2))*((ThetaWSo/2)+(ThetaWSw/2))	hPM*LG
_5PMAG	LAG/4	(Wt)*LG
_5PMAG_lt	LAG/4	(WSw)*LG
_5PMAG_rt	LAG/4	(WSw)*LG
_5T_1lf	Wt/2	(hS/5)*LG
_5T_1rf	Wt/2	(hS/5)*LG
_5T_1s	(hSw/2)+(hS/6)	(Wt)*LG
_5T_2lf	Wt/2	(hS/5)*LG
_5T_2rf	Wt/2	(hS/5)*LG
_5T_2s	hS/6	(Wt)*LG
_5T_3lf	Wt/2	(hS/5)*LG
_5T_3rf	Wt/2	(hS/5)*LG
_5T_3s	hS/6	(Wt)*LG
_5T_4lf	Wt/2	(hS/5)*LG
_5T_4rf	Wt/2	(hS/5)*LG
_5T_4s	hS/6	(Wt)*LG
_5T_5lf	Wt/2	(hS/5)*LG
_5T_5rf	Wt/2	(hS/5)*LG
_5T_5s	hS/6	(Wt)*LG
_5T_6s	(hS/6)	(Wt)*LG
_5T_hSo	hSo/2	(Wt)*LG
_5T_hSo_l	(Wt/2)+(WSw/2)	((hSo/2)+(hSw/2))*LG
_5T_hSo_lt	hSo/2	(WSw)*LG
_5T_hSo_r	(Wt/2)+(WSw/2)	((hSo/2)+(hSw/2))*LG
_5T_hSo_rt	hSo/2	(WSw)*LG
_5T_hSw	(hSo/2)+(hSw/2)	(Wt)*LG
_5T_hSw_l	(Wt/2)+(WSw/2)	hSw*LG
_5T_hSw_lt	(hSo/2)+(hSw/2)	(WSw)*LG
_5T_hSw_r	(Wt/2)+(WSw/2)	hSw*LG

_5T_hSw_rt	(hSo/2)+(hSw/2)	(WSw)*LG
_5T_lt	(WSw/2)	(hSo)*LG
_5T_rt	(WSw/2)	(hSo)*LG
_5T_Sy_Lh	hSy/4	(Wt+WSb)*LG
_5T_Sy_Uh	hSy/2	(Wt+WSb)*LG
_5WSo_hSo_l	(WSo/2)	(hSo)*LG
_5WSo_hSo_r	(WSo/2)	(hSo)*LG
_67AG_WSo	LAG/2	(WSo)*LG
_67AG_WSo_Uq	(LAG/4)+(hSo/2)	(WSo)*LG
_67PMAG_WSo	LAG/4	(WSo)*LG
_6AG	LAG/2	(Wt)*LG
_6AG_lLh	(Wt/2)+(WSw/2)	(LAG/2)*LG
_6AG_lt	LAG/2	(WSw)*LG
_6AG_lt_lLh	(WSw/2)+(WSo/2)	(LAG/2)*LG
_6AG_lt_lUh	(WSw/2)+(WSo/2)	(LAG/2)*LG
_6AG_lt_Uq	LAG/4	(WSw)*LG
_6AG_lUh	(Wt/2)+(WSw/2)	(LAG/2)*LG
_6AG_rLh	(Wt/2)+(WSw/2)	(LAG/2)*LG
_6AG_rt	LAG/2	(WSw)*LG
_6AG_rt_rLh	(WSw/2)+(WSo/2)	(LAG/2)*LG
_6AG_rt_rUh	(WSw/2)+(WSo/2)	(LAG/2)*LG
_6AG_rt_Uq	LAG/4	(WSw)*LG
_6AG_rUh	(Wt/2)+(WSw/2)	(LAG/2)*LG
_6AG_Uq	LAG/4	(Wt)*LG
_6PM_l	((DRo/2)-(hPM/2))*((Thetat/2)+(ThetaWSw/2))	hPM*LG
_6PM_lt	((DRo/2)-(hPM/2))*((ThetaWSw/2)+(ThetaWSo/2))	hPM*LG
_6PM_r	((DRo/2)-(hPM/2))*((ThetaWSw/2)+(Thetat/2))	hPM*LG
_6PM_rt	((DRo/2)-(hPM/2))*((ThetaWSo/2)+(ThetaWSw/2))	hPM*LG
_6PMAG	LAG/4	(Wt)*LG
_6PMAG_lt	LAG/4	(WSw)*LG
_6PMAG_rt	LAG/4	(WSw)*LG
_6T_1lf	Wt/2	(hS/5)*LG
_6T_1rf	Wt/2	(hS/5)*LG
_6T_1s	(hSw/2)+(hS/6)	(Wt)*LG
_6T_2lf	Wt/2	(hS/5)*LG
_6T_2rf	Wt/2	(hS/5)*LG
_6T_2s	hS/6	(Wt)*LG
_6T_3lf	Wt/2	(hS/5)*LG

_6T_3rf	Wt/2	(hS/5)*LG
_6T_3s	hS/6	(Wt)*LG
_6T_4lf	Wt/2	(hS/5)*LG
_6T_4rf	Wt/2	(hS/5)*LG
_6T_4s	hS/6	(Wt)*LG
_6T_5lf	Wt/2	(hS/5)*LG
_6T_5rf	Wt/2	(hS/5)*LG
_6T_5s	hS/6	(Wt)*LG
_6T_6s	hS/6	(Wt)*LG
_6T_hSo	hSo/2	(Wt)*LG
_6T_hSo_l	(Wt/2)+(WSw/2)	((hSo/2)+(hSw/2))*LG
_6T_hSo_lt	hSo/2	(WSw)*LG
_6T_hSo_r	(Wt/2)+(WSw/2)	((hSo/2)+(hSw/2))*LG
_6T_hSo_rt	hSo/2	(WSw)*LG
_6T_hSw	(hSo/2)+(hSw/2)	(Wt)*LG
_6T_hSw_l	(Wt/2)+(WSw/2)	hSw*LG
_6T_hSw_lt	(hSo/2)+(hSw/2)	(WSw)*LG
_6T_hSw_r	(Wt/2)+(WSw/2)	hSw*LG
_6T_hSw_rt	(hSo/2)+(hSw/2)	(WSw)*LG
_6T_lt	(WSw/2)	(hSo)*LG
_6T_rt	(WSw/2)	(hSo)*LG
_6T_Sy	hSy/2	(Wt+WSb)*LG
_6WSo_hSo_l	(WSo/2)	(hSo)*LG
_6WSo_hSo_r	(WSo/2)	(hSo)*LG
_7AG	LAG/2	(Wt/2)*LG
_7AG_lLh	(Wt/2)+(WSw/2)	(LAG/2)*LG
_7AG_lt	LAG/2	(WSw)*LG
_7AG_lt_lLh	(WSw/2)+(WSo/2)	(LAG/2)*LG
_7AG_lt_lUh	(WSw/2)+(WSo/2)	(LAG/2)*LG
_7AG_lt_Uq	LAG/4	(WSw)*LG
_7AG_lUh	(Wt/2)+(WSw/2)	(LAG/2)*LG
_7AG_Uq	LAG/4	(Wt/2)*LG
_7PM_l	((DRo/2)-(hPM/2))*((Thetat/2)+(ThetaWSw/2))	hPM*LG
_7PM_lt	((DRo/2)-(hPM/2))*((ThetaWSw/2)+(ThetaWSo/2))	hPM*LG
_7PMAG	LAG/4	(Wt/2)*LG
_7PMAG_lt	LAG/4	(WSw)*LG
_7T_1lf	Wt/2	(hS/5)*LG
_7T_1s	(hSw/2)+(hS/6)	(Wt/2)*LG
_7T_2lf	Wt/2	(hS/5)*LG
_7T_2s	hS/6	(Wt/2)*LG

_7T_3lf	Wt/2	(hS/5)*LG
_7T_3s	hS/6	(Wt/2)*LG
_7T_4lf	Wt/2	(hS/5)*LG
_7T_4s	hS/6	(Wt/2)*LG
_7T_5lf	Wt/2	(hS/5)*LG
_7T_5s	hS/6	(Wt/2)*LG
_7T_6s	hS/6	(Wt/2)*LG
_7T_hSo	hSo/2	(Wt/2)*LG
_7T_hSo_l	(Wt/4)+(WSw/2)	((hSo/2)+(hSw/2))*LG
_7T_hSo_lt	hSo/2	(WSw)*LG
_7T_hSw	(hSo/2)+(hSw/2)	(Wt/2)*LG
_7T_hSw_l	(Wt/4)+(WSw/2)	hSw*LG
_7T_hSw_lt	(hSo/2)+(hSw/2)	(WSw)*LG
_7T_lt	(WSw/2)	(hSo)*LG
_7T_Sy	hSy/2	((Wt/2)+(WSb/2))*LG
_7WSo_hSo_l	(WSo/2)	(hSo)*LG
hS12_1f	((DSt/2)+(hS/5))*(ThetaSt)	(hS/5)*LG
hS12_2f	((DSt/2)+(2*hS/5))*(ThetaSt)	(hS/5)*LG
hS12_3f	((DSt/2)+(3*hS/5))*(ThetaSt)	(hS/5)*LG
hS12_4f	((DSt/2)+(4*hS/5))*(ThetaSt)	(hS/5)*LG
hS12_5f	((DSt/2)+(5*hS/6))*(ThetaSt)	(hS/5)*LG
hS23_1f	((DSt/2)+(hS/5))*(ThetaSt)	(hS/5)*LG
hS23_2f	((DSt/2)+(2*hS/5))*(ThetaSt)	(hS/5)*LG
hS23_3f	((DSt/2)+(3*hS/5))*(ThetaSt)	(hS/5)*LG
hS23_4f	((DSt/2)+(4*hS/5))*(ThetaSt)	(hS/5)*LG
hS23_5f	((DSt/2)+(5*hS/6))*(ThetaSt)	(hS/5)*LG
hS34_1f	((DSt/2)+(hS/5))*(ThetaSt)	(hS/5)*LG
hS34_2f	((DSt/2)+(2*hS/5))*(ThetaSt)	(hS/5)*LG
hS34_3f	((DSt/2)+(3*hS/5))*(ThetaSt)	(hS/5)*LG
hS34_4f	((DSt/2)+(4*hS/5))*(ThetaSt)	(hS/5)*LG
hS34_5f	((DSt/2)+(5*hS/6))*(ThetaSt)	(hS/5)*LG
hS45_1f	((DSt/2)+(hS/5))*(ThetaSt)	(hS/5)*LG
hS45_2f	((DSt/2)+(2*hS/5))*(ThetaSt)	(hS/5)*LG
hS45_3f	((DSt/2)+(3*hS/5))*(ThetaSt)	(hS/5)*LG
hS45_4f	((DSt/2)+(4*hS/5))*(ThetaSt)	(hS/5)*LG
hS45_5f	((DSt/2)+(5*hS/6))*(ThetaSt)	(hS/5)*LG
hS56_1f	((DSt/2)+(hS/5))*(ThetaSt)	(hS/5)*LG
hS56_2f	((DSt/2)+(2*hS/5))*(ThetaSt)	(hS/5)*LG
hS56_3f	((DSt/2)+(3*hS/5))*(ThetaSt)	(hS/5)*LG
hS56_4f	((DSt/2)+(4*hS/5))*(ThetaSt)	(hS/5)*LG
hS56_5f	((DSt/2)+(5*hS/6))*(ThetaSt)	(hS/5)*LG

hS67_1f	((DSt/2)+(hS/5))*(ThetaSt)	(hS/5)*LG
hS67_2f	((DSt/2)+(2*hS/5))*(ThetaSt)	(hS/5)*LG
hS67_3f	((DSt/2)+(3*hS/5))*(ThetaSt)	(hS/5)*LG
hS67_4f	((DSt/2)+(4*hS/5))*(ThetaSt)	(hS/5)*LG
hS67_5f	((DSt/2)+(5*hS/6))*(ThetaSt)	(hS/5)*LG
R_PM_35	((DRo/2)-(hPM/2))*(AlphaP-AlphaPef)	hPM*LG
Ry_12_Lq	((DRi/2)+((5*hRy)/8))*AlphaPef*(1/4)	(hRy/4)*LG
Ry_12_Uq	((DRi/2)+((7*hRy)/8))*AlphaPef*(1/4)	(hRy/4)*LG
Ry_1_Lq	hRy/4	(WPM/6)*LG
Ry_1_Uq	hRy/4	(WPM/6)*LG
Ry_23_Lh	((DRi/2)+(hRy/4))*AlphaPef*(1/4)	(hRy/2)*LG
Ry_23_Lq	((DRi/2)+((5*hRy)/8))*AlphaPef*(1/4)	(hRy/4)*LG
Ry_23_Uq	((DRi/2)+((7*hRy)/8))*AlphaPef*(1/4)	(hRy/4)*LG
Ry_2_Lh	hRy/2	(WPM/3)*LG
Ry_2_Lq	hRy/4	(WPM/6)*LG
Ry_2_Uq	hRy/4	(WPM/6)*LG
Ry_35_Lh	((DRi/2)+(hRy/4))*AlphaP*(1-kAlphaP)	(hRy/2)*LG
Ry_35_Lq	((DRi/2)+((5*hRy)/8))*AlphaP*(1-kAlphaP)	(hRy/4)*LG
Ry_35_Uq	((DRi/2)+((7*hRy)/8))*AlphaP*(1-kAlphaP)	(hRy/4)*LG
Ry_3_Lh	hRy/2	(WPM/6)*LG
Ry_3_Lq	hRy/4	(WPM/6)*LG
Ry_3_Uq	hRy/4	(WPM/6)*LG
Ry_56_Lh	((DRi/2)+(hRy/4))*AlphaPef*(1/4)	(hRy/2)*LG
Ry_56_Lq	((DRi/2)+((5*hRy)/8))*AlphaPef*(1/4)	(hRy/4)*LG
Ry_56_Uq	((DRi/2)+((7*hRy)/8))*AlphaPef*(1/4)	(hRy/4)*LG
Ry_5_Lh	hRy/2	(WPM/6)*LG
Ry_5_Lq	hRy/4	(WPM/6)*LG
Ry_5_Uq	hRy/4	(WPM/6)*LG
Ry_67_Lq	((DRi/2)+((5*hRy)/8))*AlphaPef*(1/4)	(hRy/4)*LG
Ry_67_Uq	((DRi/2)+((7*hRy)/8))*AlphaPef*(1/4)	(hRy/4)*LG
Ry_6_Lh	hRy/2	(WPM/3)*LG
Ry_6_Lq	hRy/4	(WPM/6)*LG
Ry_6_Uq	hRy/4	(WPM/6)*LG
Ry_7_Lq	hRy/4	(WPM/6)*LG
Ry_7_Uq	hRy/4	(WPM/6)*LG
Sy_12	((DSo/2)-(hSy/2))*AlphaS	hSy*LG
Sy_23	((DSo/2)-(hSy/2))*AlphaS	hSy*LG
Sy_35	((DSo/2)-(hSy/4))*2*AlphaS	(hSy/2)*LG
Sy_56	((DSo/2)-(hSy/2))*AlphaS	hSy*LG
Sy_67	((DSo/2)-(hSy/2))*AlphaS	hSy*LG

T34_Sy	((DSo/2)-(3*hSy/4))*AlphaS	(hSy/2)*LG
T45_Sy	((DSo/2)-(3*hSy/4))*AlphaS	(hSy/2)*LG
WSo_12	(hSw/2)+(hSo/2)	(WSo+(WSw/2))*LG
WSo_12_l	(WSo+WSw)/2	(hSw)*LG
WSo_12_r	(WSo+WSw)/2	(hSw)*LG
WSo_23	(hSw/2)+(hSo/2)	(WSo+(WSw/2))*LG
WSo_23_l	(WSo+WSw)/2	(hSw)*LG
WSo_23_r	(WSo+WSw)/2	(hSw)*LG
WSo_34	(hSw/2)+(hSo/2)	(WSo+(WSw/2))*LG
WSo_34_l	(WSo+WSw)/2	(hSw)*LG
WSo_34_r	(WSo+WSw)/2	(hSw)*LG
WSo_45	(hSw/2)+(hSo/2)	(WSo+(WSw/2))*LG
WSo_45_l	(WSo+WSw)/2	(hSw)*LG
WSo_45_r	(WSo+WSw)/2	(hSw)*LG
WSo_56	(hSw/2)+(hSo/2)	(WSo+(WSw/2))*LG
WSo_56_l	(WSo+WSw)/2	(hSw)*LG
WSo_56_r	(WSo+WSw)/2	(hSw)*LG
WSo_67	(hSw/2)+(hSo/2)	(WSo+(WSw/2))*LG
WSo_67_l	(WSo+WSw)/2	(hSw)*LG
WSo_67_r	(WSo+WSw)/2	(hSw)*LG

Source: Own authorship (2024)

Table 28 shows the length and area equations of the permanent magnet sources.

Table 28 – Length and area of the permanent magnet sources of the no-load flux reluctance network

Source	Length	Area
_12PM_WSo_Lh	hPM/2	(WPM/2)*((ThetaWSo)/(AlphaPef/2))*LG
_12PM_WSo_Uh	hPM/2	(WPM/2)*((ThetaWSo)/(AlphaPef/2))*LG
_1PM_Lh	hPM/2	(WPM/2)*((Thetat/2)/(AlphaPef/2))*LG
_1PM_rt_Lh	hPM/2	(WPM/2)*((ThetaWSw)/(AlphaPef/2))*LG
_1PM_rt_Uh	hPM/2	(WPM/2)*((ThetaWSw)/(AlphaPef/2))*LG
_1PM_Uh	hPM/2	(WPM/2)*((Thetat/2)/(AlphaPef/2))*LG
_23PM_WSo_Lh	hPM/2	(WPM/2)*((ThetaWSo)/(AlphaPef/2))*LG
_23PM_WSo_Uh	hPM/2	(WPM/2)*((ThetaWSo)/(AlphaPef/2))*LG
_2PM_Lh	hPM/2	(WPM/2)*((Thetat)/(AlphaPef/2))*LG
_2PM_lt_Lh	hPM/2	(WPM/2)*((ThetaWSw)/(AlphaPef/2))*LG
_2PM_lt_Uh	hPM/2	(WPM/2)*((ThetaWSw)/(AlphaPef/2))*LG

_2PM_rt_Lh	hPM/2	(WPM/2)*((ThetaWSw)/(AlphaPef/2))*LG
_2PM_rt_Uh	hPM/2	(WPM/2)*((ThetaWSw)/(AlphaPef/2))*LG
_2PM_Uh	hPM/2	(WPM/2)*((Thetat)/(AlphaPef/2))*LG
_34PM_WSo_Lh	hPM/2	(WPM/2)*((ThetaWSo)/(AlphaPef/2))*LG
_34PM_WSo_Uh	hPM/2	(WPM/2)*((ThetaWSo)/(AlphaPef/2))*LG
_3PM_Lh	hPM/2	(WPM/2)*((Thetat)/(AlphaPef/2))*LG
_3PM_lt_Lh	hPM/2	(WPM/2)*((ThetaWSw)/(AlphaPef/2))*LG
_3PM_lt_Uh	hPM/2	(WPM/2)*((ThetaWSw)/(AlphaPef/2))*LG
_3PM_rt_Lh	hPM/2	(WPM/2)*((ThetaWSw)/(AlphaPef/2))*LG
_3PM_rt_Uh	hPM/2	(WPM/2)*((ThetaWSw)/(AlphaPef/2))*LG
_3PM_Uh	hPM/2	(WPM/2)*((Thetat)/(AlphaPef/2))*LG
_45PM_WSo_Lh	hPM/2	(WPM/2)*((ThetaWSo)/(AlphaPef/2))*LG
_45PM_WSo_Uh	hPM/2	(WPM/2)*((ThetaWSo)/(AlphaPef/2))*LG
_4PM_lt_Lh	hPM/2	(WPM/2)*((ThetaWSw)/(AlphaPef/2))*LG
_4PM_lt_Uh	hPM/2	(WPM/2)*((ThetaWSw)/(AlphaPef/2))*LG
_4PM_rt_Lh	hPM/2	(WPM/2)*((ThetaWSw)/(AlphaPef/2))*LG
_4PM_rt_Uh	hPM/2	(WPM/2)*((ThetaWSw)/(AlphaPef/2))*LG
_56PM_WSo_Lh	hPM/2	(WPM/2)*((ThetaWSo)/(AlphaPef/2))*LG
_56PM_WSo_Uh	hPM/2	(WPM/2)*((ThetaWSo)/(AlphaPef/2))*LG
_5PM_Lh	hPM/2	(WPM/2)*((Thetat)/(AlphaPef/2))*LG
_5PM_lt_Lh	hPM/2	(WPM/2)*((ThetaWSw)/(AlphaPef/2))*LG
_5PM_lt_Uh	hPM/2	(WPM/2)*((ThetaWSw)/(AlphaPef/2))*LG
_5PM_rt_Lh	hPM/2	(WPM/2)*((ThetaWSw)/(AlphaPef/2))*LG
_5PM_rt_Uh	hPM/2	(WPM/2)*((ThetaWSw)/(AlphaPef/2))*LG
_5PM_Uh	hPM/2	(WPM/2)*((Thetat)/(AlphaPef/2))*LG
_67PM_WSo_Lh	hPM/2	(WPM/2)*((ThetaWSo)/(AlphaPef/2))*LG
_67PM_WSo_Uh	hPM/2	(WPM/2)*((ThetaWSo)/(AlphaPef/2))*LG
_6PM_Lh	hPM/2	(WPM/2)*((Thetat)/(AlphaPef/2))*LG
_6PM_lt_Lh	hPM/2	(WPM/2)*((ThetaWSw)/(AlphaPef/2))*LG
_6PM_lt_Uh	hPM/2	(WPM/2)*((ThetaWSw)/(AlphaPef/2))*LG
_6PM_rt_Lh	hPM/2	(WPM/2)*((ThetaWSw)/(AlphaPef/2))*LG
_6PM_rt_Uh	hPM/2	(WPM/2)*((ThetaWSw)/(AlphaPef/2))*LG
_6PM_Uh	hPM/2	(WPM/2)*((Thetat)/(AlphaPef/2))*LG
_7PM_Lh	hPM/2	(WPM/2)*((Thetat/2)/(AlphaPef/2))*LG
_7PM_lt_Lh	hPM/2	(WPM/2)*((ThetaWSw)/(AlphaPef/2))*LG
_7PM_lt_Uh	hPM/2	(WPM/2)*((ThetaWSw)/(AlphaPef/2))*LG
_7PM_Uh	hPM/2	(WPM/2)*((Thetat/2)/(AlphaPef/2))*LG

Source: Own authorship (2024)

Table 29 shows the remanent flux density equations of the permanent magnet sources.

Table 29 – Remanent flux densities of the permanent magnet sources of the no-load flux reluctance network

Source	Remanent Flux Density
_12PM_WSo_Lh	BR*(deltaPMcTfTWSo)
_12PM_WSo_Uh	BR*(deltaPMcTfTWSo)
_1PM_Lh	BR*(deltaPMcT)
_1PM_rt_Lh	BR*(deltaPMcTrt)
_1PM_rt_Uh	BR*(deltaPMcTrt)
_1PM_Uh	BR*(deltaPMcT)
_23PM_WSo_Lh	BR*(deltaPMfTsTWSo)
_23PM_WSo_Uh	BR*(deltaPMfTsTWSo)
_2PM_Lh	BR*(deltaPMfT)
_2PM_lt_Lh	BR*(deltaPMfTlt)
_2PM_lt_Uh	BR*(deltaPMfTlt)
_2PM_rt_Lh	BR*(deltaPMfTrt)
_2PM_rt_Uh	BR*(deltaPMfTrt)
_2PM_Uh	BR*(deltaPMfT)
_34PM_WSo_Lh	BR*(deltaPMsTtTWSo)
_34PM_WSo_Uh	BR*(deltaPMsTtTWSo)
_3PM_Lh	BR*(deltaPMsT)
_3PM_lt_Lh	BR*(deltaPMsTlt)
_3PM_lt_Uh	BR*(deltaPMsTlt)
_3PM_rt_Lh	BR*(deltaPMsTrt)
_3PM_rt_Uh	BR*(deltaPMsTrt)
_3PM_Uh	BR*(deltaPMsT)
_45PM_WSo_Lh	BR*(deltaPMsTtTWSo)
_45PM_WSo_Uh	BR*(deltaPMsTtTWSo)
_4PM_lt_Lh	BR*(deltaPMtTlt)
_4PM_lt_Uh	BR*(deltaPMtTlt)
_4PM_rt_Lh	BR*(deltaPMtTlt)
_4PM_rt_Uh	BR*(deltaPMtTlt)
_56PM_WSo_Lh	BR*(deltaPMfTsTWSo)
_56PM_WSo_Uh	BR*(deltaPMfTsTWSo)
_5PM_Lh	BR*(deltaPMsT)
_5PM_lt_Lh	BR*(deltaPMsTrt)
_5PM_lt_Uh	BR*(deltaPMsTrt)
_5PM_rt_Lh	BR*(deltaPMsTlt)
_5PM_rt_Uh	BR*(deltaPMsTlt)
_5PM_Uh	BR*(deltaPMsT)
_67PM_WSo_Lh	BR*(deltaPMcTfTWSo)

_67PM_WSo_Uh	BR*(deltaPMcTfTWSo)
_6PM_Lh	BR*(deltaPMfT)
_6PM_lt_Lh	BR*(deltaPMfTrt)
_6PM_lt_Uh	BR*(deltaPMfTrt)
_6PM_rt_Lh	BR*(deltaPMfTlt)
_6PM_rt_Uh	BR*(deltaPMfTlt)
_6PM_Uh	BR*(deltaPMfT)
_7PM_Lh	BR*(deltaPMcT)
_7PM_lt_Lh	BR*(deltaPMcTrt)
_7PM_lt_Uh	BR*(deltaPMcTrt)
_7PM_Uh	BR*(deltaPMcT)

Source: Own authorship (2024)

APPENDIX D – C/C++ External Code of the No-Load Magnetic Submodel

```
//External C function for calculating the strength of each PM source

#include <muse.h>
MUSE_MODEL(name = "fun_thetaPM")

adouble fun_thetaPM(adouble theta, adouble AlphaPef, adouble thetaref) {

adouble thetaPM=(theta-(AlphaPef/2.0))/(thetaref);
if (thetaPM < 0.0){
    thetaPM=1.0;
}
if (thetaPM > 1.0){
    thetaPM=0.0;
}
if (thetaPM > 0.0 && thetaPM < 1.0){
    thetaPM=1.0-thetaPM;
}

return thetaPM;
}
```

APPENDIX E – Parameterised Armature Reaction Submodel Equations

This appendix presents the equations that define areas and lengths of the reluctances in the network used for calculating the PMSG armature reaction. Figure 56 shows the parameterised no-load reluctance network implemented in CADES.

Figure 56 – Armature reaction magnetic submodel implemented in CADES

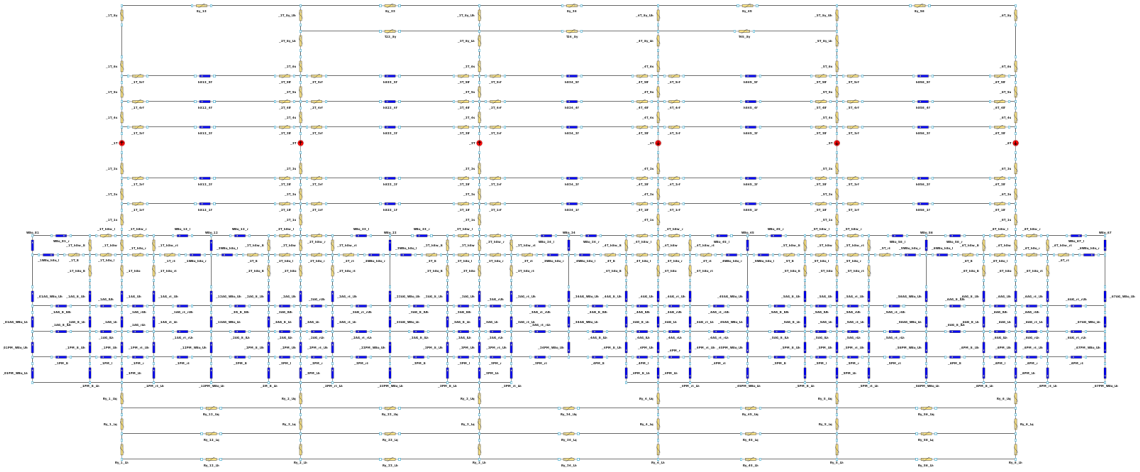

Source: Own authorship (2024)

Table 30 shows the length and area equations of each air and iron reluctances.

Table 30 – Length and area of the air and iron reluctances of the armature reaction reluctance network

Reluctance	Length	Area
_01AG_WSo_Lh	LAG/2	(WSo/2)*LG
_01AG_WSo_Uh	(LAG/2)+(hSo/2)	(WSo/2)*LG
_01PM_WSo_Lh	hPM/2	((DRo/2)-((3*hPM)/4))*(ThetaWSo/2)*LG
_01PM_WSo_Uh	hPM/2	((DRo/2)-(hPM/4))*(ThetaWSo/2)*LG
_12AG_WSo_Lh	LAG/2	(WSo)*LG
_12AG_WSo_Uh	(LAG/2)+(hSo/2)	(WSo)*LG
_12PM_WSo_Lh	hPM/2	((DRo/2)-((3*hPM)/4))*(ThetaWSo)*LG
_12PM_WSo_Uh	hPM/2	((DRo/2)-(hPM/4))*(ThetaWSo)*LG
_1AG_Lh	LAG/2	(Wt)*LG
_1AG_lLh	(Wt/2)+(WSw/2)	(LAG/2)*LG
_1AG_lt_Lh	LAG/2	(WSw)*LG
_1AG_lt_lLh	(WSw/2)+(WSo/2)	(LAG/2)*LG
_1AG_lt_lUh	(WSw/2)+(WSo/2)	(LAG/2)*LG

_1AG_lt_Uh	LAG/2	(WSw)*LG
_1AG_lUh	(Wt/2)+(WSw/2)	(LAG/2)*LG
_1AG_rLh	(Wt/2)+(WSw/2)	(LAG/2)*LG
_1AG_rt_Lh	LAG/2	(WSw)*LG
_1AG_rt_rLh	(WSw/2)+(WSo/2)	(LAG/2)*LG
_1AG_rt_rLh001	(WSw/2)+(WSo/2)	(LAG/2)*LG
_1AG_rt_rUh	(WSw/2)+(WSo/2)	(WSw)*LG
_1AG_rt_Uh	LAG/2	(LAG/2)*LG
_1AG_rUh	(Wt/2)+(WSw/2)	(Wt)*LG
_1AG_Uh	LAG/2	hPM*LG
_1PM_l	((DRo/2)-(hPM/2))*((ThetaWSw/2)+(Thetat/2))	((DRo/2)-((3*hPM)/4))*(Thetat)*LG
_1PM_Lh	hPM/2	hPM*LG
_1PM_lt	((DRo/2)-(hPM/2))*((ThetaWSo/2)+(ThetaWSw/2))	((DRo/2)-((3*hPM)/4))*(ThetaWSw)*LG
_1PM_lt_Lh	hPM/2	((DRo/2)-(hPM/4))*(ThetaWSw)*LG
_1PM_lt_Uh	hPM/2	hPM*LG
_1PM_r	((DRo/2)-(hPM/2))*((Thetat/2)+(ThetaWSw/2))	hPM*LG
_1PM_rt	((DRo/2)-(hPM/2))*((ThetaWSw/2)+(ThetaWSo/2))	((DRo/2)-((3*hPM)/4))*(ThetaWSw)*LG
_1PM_rt_Lh	hPM/2	((DRo/2)-(hPM/4))*(ThetaWSw)*LG
_1PM_rt_Uh	hPM/2	((DRo/2)-(hPM/4))*(Thetat)*LG
_1PM_Uh	hPM/2	(hS/5)*LG
_1T_1rf	Wt/2	(Wt)*LG
_1T_1s	(hSw/2)+(hS/6)	(hS/5)*LG
_1T_2rf	Wt/2	(Wt)*LG
_1T_2s	hS/6	(hS/5)*LG
_1T_3rf	Wt/2	(Wt)*LG
_1T_3s	hS/6	(hS/5)*LG
_1T_4rf	Wt/2	(Wt)*LG
_1T_4s	hS/6	(hS/5)*LG
_1T_5rf	Wt/2	(Wt)*LG
_1T_5s	hS/6	(Wt)*LG
_1T_6s	hS/6	(Wt)*LG
_1T_hSo	hSo/2	((hSo/2)+(hSw/2))*LG
_1T_hSo_l	(Wt/2)+(WSw/2)	(WSw)*LG
_1T_hSo_lt	hSo/2	((hSo/2)+(hSw/2))*LG
_1T_hSo_r	(Wt/2)+(WSw/2)	(WSw)*LG
_1T_hSo_rt	hSo/2	(Wt)*LG
_1T_hSw	(hSo/2)+(hSw/2)	hSw*LG

_1T_hSw_l	(Wt/2)+(WSw/2)	(WSw)*LG
_1T_hSw_lt	(hSo/2)+(hSw/2)	hSw*LG
_1T_hSw_r	(Wt/2)+(WSw/2)	(WSw)*LG
_1T_hSw_rt	(hSo/2)+(hSw/2)	(hSo)*LG
_1T_lt	(WSw/2)	(hSo)*LG
_1T_rt	(WSw/2)	(Wt+WSb)*LG
_1T_Sy	hSy/2	(hSo)*LG
_1WSo_hSo_l	(WSo/2)	(hSo)*LG
_1WSo_hSo_r	(WSo/2)	(WSo)*LG
_23AG_WSo_Lh	LAG/2	(WSo)*LG
_23AG_WSo_Uh	(LAG/2)+(hSo/2)	((DRo/2)-((3*hPM)/4))*(ThetaWSo)*LG
_23PM_WSo_Lh	hPM/2	((DRo/2)-(hPM/4))*(ThetaWSo)*LG
_23PM_WSo_Uh	hPM/2	(Wt)*LG
_2AG_Lh	LAG/2	(LAG/2)*LG
_2AG_lLh	(Wt/2)+(WSw/2)	(WSw)*LG
_2AG_lt_Lh	LAG/2	(LAG/2)*LG
_2AG_lt_lLh	(WSw/2)+(WSo/2)	(WSw)*LG
_2AG_lt_Uh	LAG/2	(LAG/2)*LG
_2AG_lUh	(Wt/2)+(WSw/2)	(LAG/2)*LG
_2AG_rLh	(Wt/2)+(WSw/2)	(WSw)*LG
_2AG_rt_Lh	LAG/2	(LAG/2)*LG
_2AG_rt_rLh	(WSw/2)+(WSo/2)	(LAG/2)*LG
_2AG_rt_rUh	(WSw/2)+(WSo/2)	(WSw)*LG
_2AG_rt_Uh	LAG/2	(LAG/2)*LG
_2AG_rUh	(Wt/2)+(WSw/2)	(Wt)*LG
_2AG_Uh	LAG/2	(LAG/2)*LG
_2G_lt_lUh	(WSw/2)+(WSo/2)	((DRo/2)-((3*hPM)/4))*(ThetaWSw)*LG
_2M_lt_Lh	hPM/2	hPM*LG
_2PM_l	((DRo/2)-(hPM/2))*((ThetaWSw/2)+(Thetat/2))	((DRo/2)-((3*hPM)/4))*(Thetat)*LG
_2PM_Lh	hPM/2	hPM*LG
_2PM_lt	((DRo/2)-(hPM/2))*((ThetaWSw/2)+(ThetaWSo/2))	((DRo/2)-(hPM/4))*(ThetaWSw)*LG
_2PM_lt_Uh	hPM/2	hPM*LG
_2PM_r	((DRo/2)-(hPM/2))*((Thetat/2)+(ThetaWSw/2))	hPM*LG
_2PM_rt	((DRo/2)-(hPM/2))*((ThetaWSw/2)+(ThetaWSo/2))	((DRo/2)-((3*hPM)/4))*(ThetaWSw)*LG
_2PM_rt_Lh	hPM/2	((DRo/2)-(hPM/4))*(ThetaWSw)*LG
_2PM_rt_Uh	hPM/2	((DRo/2)-(hPM/4))*(Thetat)*LG
_2PM_Uh	hPM/2	(hS/5)*LG

_2T_1lf	Wt/2	(hS/5)*LG
_2T_1rf	Wt/2	(Wt)*LG
_2T_1s	(hSw/2)+(hS/6)	(hS/5)*LG
_2T_2lf	Wt/2	(hS/5)*LG
_2T_2rf	Wt/2	(Wt)*LG
_2T_2s	hS/6	(hS/5)*LG
_2T_3lf	Wt/2	(hS/5)*LG
_2T_3rf	Wt/2	(Wt)*LG
_2T_3s	hS/6	(hS/5)*LG
_2T_4lf	Wt/2	(hS/5)*LG
_2T_4rf	Wt/2	(Wt)*LG
_2T_4s	hS/6	(hS/5)*LG
_2T_5lf	Wt/2	(hS/5)*LG
_2T_5rf	Wt/2	(Wt)*LG
_2T_5s	hS/6	(Wt)*LG
_2T_6s	hS/6	(Wt)*LG
_2T_hSo	hSo/2	((hSo/2)+(hSw/2))*LG
_2T_hSo_l	(Wt/2)+(WSw/2)	(WSw)*LG
_2T_hSo_lt	hSo/2	((hSo/2)+(hSw/2))*LG
_2T_hSo_r	(Wt/2)+(WSw/2)	(WSw)*LG
_2T_hSo_rt	hSo/2	(Wt)*LG
_2T_hSw	(hSo/2)+(hSw/2)	hSw*LG
_2T_hSw_l	(Wt/2)+(WSw/2)	(WSw)*LG
_2T_hSw_lt	(hSo/2)+(hSw/2)	hSw*LG
_2T_hSw_r	(Wt/2)+(WSw/2)	(WSw)*LG
_2T_hSw_rt	(hSo/2)+(hSw/2)	(hSo)*LG
_2T_lt	(WSw/2)	(hSo)*LG
_2T_rt	(WSw/2)	(Wt+WSb)*LG
_2T_Sy_Lh	hSy/4	(Wt+WSb)*LG
_2T_Sy_Uh	hSy/2	(hSo)*LG
_2WSo_hSo_l	(WSo/2)	(hSo)*LG
_2WSo_hSo_r	(WSo/2)	(WSo)*LG
_34AG_WSo_Lh	LAG/2	(WSo)*LG
_34AG_WSo_Uh	(LAG/2)+(hSo/2)	((DRo/2)-(hPM/4))*(ThetaWSo)*LG
_34PM_WSo_Uh	hPM/2	(Wt)*LG
_3AG_Lh	LAG/2	(LAG/2)*LG
_3AG_lLh	(Wt/2)+(WSw/2)	(WSw)*LG
_3AG_lt_Lh	LAG/2	(LAG/2)*LG
_3AG_lt_lLh	(WSw/2)+(WSo/2)	(LAG/2)*LG
_3AG_lt_lUh	(WSw/2)+(WSo/2)	(WSw)*LG
_3AG_lt_Uh	LAG/2	(LAG/2)*LG

_3AG_lUh	(Wt/2)+(WSw/2)	(LAG/2)*LG
_3AG_rLh	(Wt/2)+(WSw/2)	(WSw)*LG
_3AG_rt_Lh	LAG/2	(LAG/2)*LG
_3AG_rt_rLh	(WSw/2)+(WSo/2)	(LAG/2)*LG
_3AG_rt_rUh	(WSw/2)+(WSo/2)	(WSw)*LG
_3AG_rt_Uh	LAG/2	(LAG/2)*LG
_3AG_rUh	(Wt/2)+(WSw/2)	(Wt)*LG
_3AG_Uh	LAG/2	hPM*LG
_3PM_l	((DRo/2)-(hPM/2))*((ThetaWSw/2)+(Thetat/2))	((DRo/2)-((3*hPM)/4))*(Thetat)*LG
_3PM_Lh	hPM/2	hPM*LG
_3PM_lt	((DRo/2)-(hPM/2))*((ThetaWSo/2)+(ThetaWSw/2))	((DRo/2)-((3*hPM)/4))*(ThetaWSw)*LG
_3PM_lt_Lh	hPM/2	((DRo/2)-(hPM/4))*(ThetaWSw)*LG
_3PM_lt_Uh	hPM/2	hPM*LG
_3PM_r	((DRo/2)-(hPM/2))*((Thetat/2)+(ThetaWSw/2))	hPM*LG
_3PM_rt	((DRo/2)-(hPM/2))*((ThetaWSw/2)+(ThetaWSo/2))	((DRo/2)-((3*hPM)/4))*(ThetaWSw)*LG
_3PM_rt_Lh	hPM/2	((DRo/2)-(hPM/4))*(ThetaWSw)*LG
_3PM_rt_Uh	hPM/2	((DRo/2)-(hPM/4))*(Thetat)*LG
_3PM_Uh	hPM/2	(hS/5)*LG
_3T_1lf	Wt/2	(hS/5)*LG
_3T_1rf	Wt/2	(Wt)*LG
_3T_1s	(hSw/2)+(hS/6)	(hS/5)*LG
_3T_2lf	Wt/2	(hS/5)*LG
_3T_2rf	Wt/2	(Wt)*LG
_3T_2s	hS/6	(hS/5)*LG
_3T_3lf	Wt/2	(hS/5)*LG
_3T_3rf	Wt/2	(Wt)*LG
_3T_3s	hS/6	(hS/5)*LG
_3T_4lf	Wt/2	(hS/5)*LG
_3T_4rf	Wt/2	(Wt)*LG
_3T_4s	hS/6	(hS/5)*LG
_3T_5lf	Wt/2	(hS/5)*LG
_3T_5rf	Wt/2	(Wt)*LG
_3T_5s	hS/6	(Wt)*LG
_3T_6s	hS/6	(Wt)*LG
_3T_hSo	hSo/2	((hSo/2)+(hSw/2))*LG
_3T_hSo_l	(Wt/2)+(WSw/2)	(WSw)*LG
_3T_hSo_lt	hSo/2	((hSo/2)+(hSw/2))*LG

_3T_hSo_r	(Wt/2)+(WSw/2)	(WSw)*LG
_3T_hSo_rt	hSo/2	(Wt)*LG
_3T_hSw	(hSo/2)+(hSw/2)	hSw*LG
_3T_hSw_l	(Wt/2)+(WSw/2)	(WSw)*LG
_3T_hSw_lt	(hSo/2)+(hSw/2)	hSw*LG
_3T_hSw_r	(Wt/2)+(WSw/2)	(WSw)*LG
_3T_hSw_rt	(hSo/2)+(hSw/2)	(hSo)*LG
_3T_lt	(WSw/2)	(hSo)*LG
_3T_rt	(WSw/2)	(Wt+WSb)*LG
_3T_Sy_Lh	hSy/4	(Wt+WSb)*LG
_3T_Sy_Uh	hSy/2	(hSo)*LG
_3WSo_hSo_l	(WSo/2)	(hSo)*LG
_3WSo_hSo_r	(WSo/2)	(WSo)*LG
_45AG_WSo_Lh	LAG/2	(WSo)*LG
_45AG_WSo_Uh	(LAG/2)+(hSo/2)	((DRo/2)-((3*hPM)/4))*(ThetaWSo)*LG
_45PM_WSo_Lh	hPM/2	((DRo/2)-(hPM/4))*(ThetaWSo)*LG
_45PM_WSo_Uh	hPM/2	(Wt)*LG
_4AG_Lh	LAG/2	(LAG/2)*LG
_4AG_lLh	(Wt/2)+(WSw/2)	(WSw)*LG
_4AG_lt_Lh	LAG/2	(LAG/2)*LG
_4AG_lt_lLh	(WSw/2)+(WSo/2)	(LAG/2)*LG
_4AG_lt_lUh	(WSw/2)+(WSo/2)	(WSw)*LG
_4AG_lt_Uh	LAG/2	(LAG/2)*LG
_4AG_lUh	(WSw/2)+(Wt/2)	(LAG/2)*LG
_4AG_rLh	(Wt/2)+(WSw/2)	(WSw)*LG
_4AG_rt_Lh	LAG/2	(LAG/2)*LG
_4AG_rt_rLh	(WSw/2)+(WSo/2)	(LAG/2)*LG
_4AG_rt_rUh	(WSw/2)+(WSo/2)	(WSw)*LG
_4AG_rt_Uh	LAG/2	(LAG/2)*LG
_4AG_rUh	(Wt/2)+(WSw/2)	(Wt)*LG
_4AG_Uh	LAG/2	hPM*LG
_4PM_l	((DRo/2)-(hPM/2))*((Thetat/2)+(ThetaWSw/2))	((DRo/2)-((3*hPM)/4))*(Thetat)*LG
_4PM_Lh	hPM/2	hPM*LG
_4PM_lt	((DRo/2)-(hPM/2))*((ThetaWSw/2)+(ThetaWSo/2))	((DRo/2)-((3*hPM)/4))*(ThetaWSw)*LG
_4PM_lt_Lh	hPM/2	((DRo/2)-(hPM/4))*(ThetaWSw)*LG
_4PM_lt_Uh	hPM/2	hPM*LG
_4PM_r	((DRo/2)-(hPM/2))*((ThetaWSw/2)+(Thetat/2))	hPM*LG

_4PM_rt	((DRo/2)-(hPM/2))*((ThetaWSo/2)+(ThetaWSw/2))	((DRo/2)-((3*hPM)/4))*(ThetaWSw)*LG
_4PM_rt_Lh	hPM/2	((DRo/2)-(hPM/4))*(ThetaWSw)*LG
_4PM_rt_Uh	hPM/2	((DRo/2)-(hPM/4))*(Thetat)*LG
_4PM_Uh	hPM/2	(hS/5)*LG
_4T_1lf	Wt/2	(hS/5)*LG
_4T_1rf	Wt/2	(Wt)*LG
_4T_1s	(hSw/2)+(hS/6)	(hS/5)*LG
_4T_2lf	Wt/2	(hS/5)*LG
_4T_2rf	Wt/2	(Wt)*LG
_4T_2s	hS/6	(hS/5)*LG
_4T_3lf	Wt/2	(hS/5)*LG
_4T_3rf	Wt/2	(Wt)*LG
_4T_3s	hS/6	(hS/5)*LG
_4T_4lf	Wt/2	(hS/5)*LG
_4T_4rf	Wt/2	(Wt)*LG
_4T_4s	hS/6	(hS/5)*LG
_4T_5lf	Wt/2	(hS/5)*LG
_4T_5rf	Wt/2	(Wt)*LG
_4T_5s	hS/6	(Wt)*LG
_4T_6s	hS/6	(Wt)*LG
_4T_hSo	hSo/2	((hSo/2)+(hSw/2))*LG
_4T_hSo_l	(Wt/2)+(WSw/2)	(WSw)*LG
_4T_hSo_lt	hSo/2	((hSo/2)+(hSw/2))*LG
_4T_hSo_r	(Wt/2)+(WSw/2)	(WSw)*LG
_4T_hSo_rt	hSo/2	(Wt)*LG
_4T_hSw	(hSo/2)+(hSw/2)	hSw*LG
_4T_hSw_l	(Wt/2)+(WSw/2)	(WSw)*LG
_4T_hSw_lt	(hSo/2)+(hSw/2)	hSw*LG
_4T_hSw_r	(Wt/2)+(WSw/2)	(WSw)*LG
_4T_hSw_rt	(hSo/2)+(hSw/2)	(hSo)*LG
_4T_lt	(WSw/2)	(hSo)*LG
_4T_rt	(WSw/2)	(Wt+WSb)*LG
_4T_Sy_Lh	hSy/4	(Wt+WSb)*LG
_4T_Sy_Uh	hSy/2	(hSo)*LG
_4WSo_hSo_l	(WSo/2)	(hSo)*LG
_4WSo_hSo_r	(WSo/2)	(WSo)*LG
_56AG_WSo_Lh	LAG/2	(WSo)*LG
_56AG_WSo_Uh	(LAG/2)+(hSo/2)	((DRo/2)-((3*hPM)/4))*(ThetaWSo)*LG
_56PM_WSo_Lh	hPM/2	((DRo/2)-(hPM/4))*(ThetaWSo)*LG

_56PM_WSo_Uh	hPM/2	(Wt)*LG
_5AG_Lh	LAG/2	(LAG/2)*LG
_5AG_lLh	(Wt/2)+(WSw/2)	(WSw)*LG
_5AG_lt_Lh	LAG/2	(LAG/2)*LG
_5AG_lt_lLh	(WSw/2)+(WSo/2)	(LAG/2)*LG
_5AG_lt_lUh	(WSw/2)+(WSo/2)	(WSw)*LG
_5AG_lt_Uh	LAG/2	(LAG/2)*LG
_5AG_lUh	(Wt/2)+(WSw/2)	(LAG/2)*LG
_5AG_rLh	(Wt/2)+(WSw/2)	(WSw)*LG
_5AG_rt_Lh	LAG/2	(LAG/2)*LG
_5AG_rt_rLh	(WSw/2)+(WSo/2)	(LAG/2)*LG
_5AG_rt_rUh	(WSw/2)+(WSo/2)	(WSw)*LG
_5AG_rt_Uh	LAG/2	(LAG/2)*LG
_5AG_rUh	(Wt/2)+(WSw/2)	(Wt)*LG
_5AG_Uh	LAG/2	hPM*LG
_5PM_l	((DRo/2)-(hPM/2))*((Thetat/2)+(ThetaWSw/2))	((DRo/2)-((3*hPM)/4))*(Thetat)*LG
_5PM_Lh	hPM/2	hPM*LG
_5PM_lt	((DRo/2)-(hPM/2))*((ThetaWSw/2)+(ThetaWSo/2))	((DRo/2)-((3*hPM)/4))*(ThetaWSw)*LG
_5PM_lt_Lh	hPM/2	((DRo/2)-(hPM/4))*(ThetaWSw)*LG
_5PM_lt_Uh	hPM/2	hPM*LG
_5PM_r	((DRo/2)-(hPM/2))*((ThetaWSw/2)+(Thetat/2))	hPM*LG
_5PM_rt	((DRo/2)-(hPM/2))*((ThetaWSw/2)+(ThetaWSo/2))	((DRo/2)-((3*hPM)/4))*(ThetaWSw)*LG
_5PM_rt_Lh	hPM/2	((DRo/2)-(hPM/4))*(ThetaWSw)*LG
_5PM_rt_Uh	hPM/2	((DRo/2)-(hPM/4))*(Thetat)*LG
_5PM_Uh	hPM/2	(hS/5)*LG
_5T_1lf	Wt/2	(hS/5)*LG
_5T_1rf	Wt/2	(Wt)*LG
_5T_1s	(hSw/2)+(hS/6)	(hS/5)*LG
_5T_2lf	Wt/2	(hS/5)*LG
_5T_2rf	Wt/2	(Wt)*LG
_5T_2s	hS/6	(hS/5)*LG
_5T_3lf	Wt/2	(hS/5)*LG
_5T_3rf	Wt/2	(Wt)*LG
_5T_3s	hS/6	(hS/5)*LG
_5T_4lf	Wt/2	(hS/5)*LG
_5T_4rf	Wt/2	(Wt)*LG
_5T_4s	hS/6	(hS/5)*LG

_5T_5lf	Wt/2	(hS/5)*LG
_5T_5rf	Wt/2	(Wt)*LG
_5T_5s	hS/6	(Wt)*LG
_5T_6s	hS/6	(Wt)*LG
_5T_hSo	hSo/2	((hSo/2)+(hSw/2))*LG
_5T_hSo_l	(Wt/2)+(WSw/2)	(WSw)*LG
_5T_hSo_lt	hSo/2	((hSo/2)+(hSw/2))*LG
_5T_hSo_r	(Wt/2)+(WSw/2)	(WSw)*LG
_5T_hSo_rt	hSo/2	(Wt)*LG
_5T_hSw	(hSo/2)+(hSw/2)	hSw*LG
_5T_hSw_l	(Wt/2)+(WSw/2)	(WSw)*LG
_5T_hSw_lt	(hSo/2)+(hSw/2)	hSw*LG
_5T_hSw_r	(Wt/2)+(WSw/2)	(WSw)*LG
_5T_hSw_rt	(hSo/2)+(hSw/2)	(hSo)*LG
_5T_lt	(WSw/2)	(hSo)*LG
_5T_rt	(WSw/2)	(Wt+WSb)*LG
_5T_Sy_Lh	hSy/4	(Wt+WSb)*LG
_5T_Sy_Uh	hSy/2	(hSo)*LG
_5WSo_hSo_l	(WSo/2)	(hSo)*LG
_5WSo_hSo_r	(WSo/2)	(WSo/2)*LG
_67AG_WSo_Lh	LAG/2	(WSo/2)*LG
_67AG_WSo_Uh	(LAG/2)+(hSo/2)	((DRo/2)-((3*hPM)/4))*(ThetaWSo/2)*LG
_67PM_WSo_Lh	hPM/2	((DRo/2)-(hPM/4))*(ThetaWSo/2)*LG
_67PM_WSo_Uh	hPM/2	(Wt)*LG
_6AG_Lh	LAG/2	(LAG/2)*LG
_6AG_lLh	(Wt/2)+(WSw/2)	(WSw)*LG
_6AG_lt_Lh	LAG/2	(LAG/2)*LG
_6AG_lt_lLh	(WSw/2)+(WSo/2)	(LAG/2)*LG
_6AG_lt_lUh	(WSw/2)+(WSo/2)	(WSw)*LG
_6AG_lt_Uh	LAG/2	(LAG/2)*LG
_6AG_lUh	(Wt/2)+(WSw/2)	(LAG/2)*LG
_6AG_rLh	(Wt/2)+(WSw/2)	(WSw)*LG
_6AG_rt_Lh	LAG/2	(LAG/2)*LG
_6AG_rt_rLh	(WSw/2)+(WSo/2)	(LAG/2)*LG
_6AG_rt_rUh	(WSw/2)+(WSo/2)	(WSw)*LG
_6AG_rt_Uh	LAG/2	(LAG/2)*LG
_6AG_rUh	(Wt/2)+(WSw/2)	(Wt)*LG
_6AG_Uh	LAG/2	hPM*LG
_6PM_l	((DRo/2)-(hPM/2))*((Thetat/2)+(ThetaWSw/2))	((DRo/2)-((3*hPM)/4))*(Thetat)*LG

_6PM_Lh	hPM/2	hPM*LG
_6PM_lt	((DRo/2)-(hPM/2))*((ThetaWSw/2)+(ThetaWSo/2))	((DRo/2)-((3*hPM)/4))*(ThetaWSw)*LG
_6PM_lt_Lh	hPM/2	((DRo/2)-(hPM/4))*(ThetaWSw)*LG
_6PM_lt_Uh	hPM/2	hPM*LG
_6PM_r	((DRo/2)-(hPM/2))*((ThetaWSw/2)+(Thetat/2))	hPM*LG
_6PM_rt	((DRo/2)-(hPM/2))*((ThetaWSo/2)+(ThetaWSw/2))	((DRo/2)-((3*hPM)/4))*(ThetaWSw)*LG
_6PM_rt_Lh	hPM/2	((DRo/2)-(hPM/4))*(ThetaWSw)*LG
_6PM_rt_Uh	hPM/2	((DRo/2)-(hPM/4))*(Thetat)*LG
_6PM_Uh	hPM/2	(hS/5)*LG
_6T_1lf	Wt/2	(Wt)*LG
_6T_1s	(hSw/2)+(hS/6)	(hS/5)*LG
_6T_2lf	Wt/2	(Wt)*LG
_6T_2s	hS/6	(hS/5)*LG
_6T_3lf	Wt/2	(Wt)*LG
_6T_3s	hS/6	(hS/5)*LG
_6T_4lf	Wt/2	(Wt)*LG
_6T_4s	hS/6	(hS/5)*LG
_6T_5lf	Wt/2	(Wt)*LG
_6T_5s	hS/6	(Wt)*LG
_6T_6s	hS/6	(Wt)*LG
_6T_hSo	hSo/2	((hSo/2)+(hSw/2))*LG
_6T_hSo_l	(Wt/2)+(WSw/2)	(WSw)*LG
_6T_hSo_lt	hSo/2	((hSo/2)+(hSw/2))*LG
_6T_hSo_r	(Wt/2)+(WSw/2)	(WSw)*LG
_6T_hSo_rt	hSo/2	(Wt)*LG
_6T_hSw	(hSo/2)+(hSw/2)	hSw*LG
_6T_hSw_l	(Wt/2)+(WSw/2)	(WSw)*LG
_6T_hSw_lt	(hSo/2)+(hSw/2)	hSw*LG
_6T_hSw_r	(Wt/2)+(WSw/2)	(WSw)*LG
_6T_hSw_rt	(hSo/2)+(hSw/2)	(hSo)*LG
_6T_lt	(WSw/2)	(hSo)*LG
_6T_rt	(WSw/2)	(Wt+WSb)*LG
_6T_Sy	hSy/2	(hSo)*LG
_6WSo_hSo_l	(WSo/2)	(hSo)*LG
_6WSo_hSo_r	(WSo/2)	(hS/5)*LG
hS12_1f	((DSt/2)+(hS/5))*(ThetaSt)	(hS/5)*LG
hS12_2f	((DSt/2)+(2*hS/5))*(ThetaSt)	(hS/5)*LG
hS12_3f	((DSt/2)+(3*hS/5))*(ThetaSt)	(hS/5)*LG

hS12_4f	((DSt/2)+(4*hS/5))*(ThetaSt)	(hS/5)*LG
hS12_5f	((DSt/2)+(5*hS/6))*(ThetaSt)	(hS/5)*LG
hS23_1f	((DSt/2)+(hS/5))*(ThetaSt)	(hS/5)*LG
hS23_2f	((DSt/2)+(2*hS/5))*(ThetaSt)	(hS/5)*LG
hS23_3f	((DSt/2)+(3*hS/5))*(ThetaSt)	(hS/5)*LG
hS23_4f	((DSt/2)+(4*hS/5))*(ThetaSt)	(hS/5)*LG
hS23_5f	((DSt/2)+(5*hS/6))*(ThetaSt)	(hS/5)*LG
hS34_1f	((DSt/2)+(hS/5))*(ThetaSt)	(hS/5)*LG
hS34_2f	((DSt/2)+(2*hS/5))*(ThetaSt)	(hS/5)*LG
hS34_3f	((DSt/2)+(3*hS/5))*(ThetaSt)	(hS/5)*LG
hS34_4f	((DSt/2)+(4*hS/5))*(ThetaSt)	(hS/5)*LG
hS34_5f	((DSt/2)+(5*hS/6))*(ThetaSt)	(hS/5)*LG
hS45_1f	((DSt/2)+(hS/5))*(ThetaSt)	(hS/5)*LG
hS45_2f	((DSt/2)+(2*hS/5))*(ThetaSt)	(hS/5)*LG
hS45_3f	((DSt/2)+(3*hS/5))*(ThetaSt)	(hS/5)*LG
hS45_4f	((DSt/2)+(4*hS/5))*(ThetaSt)	(hS/5)*LG
hS45_5f	((DSt/2)+(5*hS/6))*(ThetaSt)	(hS/5)*LG
hS56_1f	((DSt/2)+(hS/5))*(ThetaSt)	(hS/5)*LG
hS56_2f	((DSt/2)+(2*hS/5))*(ThetaSt)	(hS/5)*LG
hS56_3f	((DSt/2)+(3*hS/5))*(ThetaSt)	(hS/5)*LG
hS56_4f	((DSt/2)+(4*hS/5))*(ThetaSt)	(hS/5)*LG
hS56_5f	((DSt/2)+(5*hS/6))*(ThetaSt)	(hRy/2)*LG
Ry_12_Lh	((DRi/2)+(hRy/4))*AlphaS	(hRy/4)*LG
Ry_12_Lq	((DRi/2)+((5*hRy)/8))*AlphaS	(hRy/4)*LG
Ry_12_Uq	((DRi/2)+((7*hRy)/8))*AlphaS	((DRi/2)+(hRy/4))*(AlphaS)*LG
Ry_1_Lh	hRy/2	((DRi/2)+((5*hRy)/8))*(AlphaS)*LG
Ry_1_Lq	hRy/4	((DRi/2)+((7*hRy)/8))*(AlphaS)*LG
Ry_1_Uq	hRy/4	(hRy/2)*LG
Ry_23_Lh	((DRi/2)+(hRy/4))*AlphaS	(hRy/4)*LG
Ry_23_Lq	((DRi/2)+((5*hRy)/8))*AlphaS	(hRy/4)*LG
Ry_23_Uq	((DRi/2)+((7*hRy)/8))*AlphaS	((DRi/2)+(hRy/4))*(AlphaS)*LG
Ry_2_Lh	hRy/2	((DRi/2)+((5*hRy)/8))*(AlphaS)*LG
Ry_2_Lq	hRy/4	((DRi/2)+((7*hRy)/8))*(AlphaS)*LG
Ry_2_Uq	hRy/4	(hRy/2)*LG
Ry_34_Lh	((DRi/2)+(hRy/4))*AlphaS	(hRy/4)*LG
Ry_34_Lq	((DRi/2)+((5*hRy)/8))*AlphaS	(hRy/4)*LG
Ry_34_Uq	((DRi/2)+((7*hRy)/8))*AlphaS	((DRi/2)+(hRy/4))*(AlphaS)*LG
Ry_3_Lh	hRy/2	((DRi/2)+((5*hRy)/8))*(AlphaS)*LG
Ry_3_Lq	hRy/4	((DRi/2)+((7*hRy)/8))*(AlphaS)*LG
Ry_3_Uq	hRy/4	(hRy/2)*LG
Ry_45_Lh	((DRi/2)+(hRy/4))*AlphaS	(hRy/4)*LG

Ry_45_Lq	((DRi/2)+((5*hRy)/8))*AlphaS	(hRy/4)*LG
Ry_45_Uq	((DRi/2)+((7*hRy)/8))*AlphaS	((DRi/2)+(hRy/4))*(AlphaS)*LG
Ry_4_Lh	hRy/2	((DRi/2)+((5*hRy)/8))*(AlphaS)*LG
Ry_4_Lq	hRy/4	((DRi/2)+((7*hRy)/8))*(AlphaS)*LG
Ry_4_Uq	hRy/4	(hRy/2)*LG
Ry_56_Lh	((DRi/2)+(hRy/4))*AlphaS	(hRy/4)*LG
Ry_56_Lq	((DRi/2)+((5*hRy)/8))*AlphaS	(hRy/4)*LG
Ry_56_Uq	((DRi/2)+((7*hRy)/8))*AlphaS	((DRi/2)+(hRy/4))*(AlphaS)*LG
Ry_5_Lh	hRy/2	((DRi/2)+((5*hRy)/8))*(AlphaS)*LG
Ry_5_Lq	hRy/4	((DRi/2)+((7*hRy)/8))*(AlphaS)*LG
Ry_5_Uq	hRy/4	((DRi/2)+(hRy/4))*(AlphaS)*LG
Ry_6_Lh	hRy/2	((DRi/2)+((5*hRy)/8))*(AlphaS)*LG
Ry_6_Lq	hRy/4	((DRi/2)+((7*hRy)/8))*(AlphaS)*LG
Ry_6_Uq	hRy/4	hSy*LG
Sy_12	((DSo/2)-(hSy/2))*AlphaS	(hSy/2)*LG
Sy_23	((DSo/2)-(hSy/4))*AlphaS	(hSy/2)*LG
Sy_34	((DSo/2)-(hSy/4))*AlphaS	(hSy/2)*LG
Sy_45	((DSo/2)-(hSy/4))*AlphaS	hSy*LG
Sy_56	((DSo/2)-(hSy/2))*AlphaS	(hSy/2)*LG
T23_Sy	((DSo/2)-(3*hSy/4))*AlphaS	(hSy/2)*LG
T34_Sy	((DSo/2)-(3*hSy/4))*AlphaS	(hSy/2)*LG
T45_Sy	((DSo/2)-(3*hSy/4))*AlphaS	((WSo+(WSw/2))/2)*LG
WSo_01	(hSw/2)+(hSo/2)	(hSw)*LG
WSo_01_r	(WSo+WSw)/2	(WSo+(WSw/2))*LG
WSo_12	(hSw/2)+(hSo/2)	(hSw)*LG
WSo_12_l	(WSo+WSw)/2	(hSw)*LG
WSo_12_r	(WSo+WSw)/2	(WSo+(WSw/2))*LG
WSo_23	(hSw/2)+(hSo/2)	(hSw)*LG
WSo_23_l	(WSo+WSw)/2	(hSw)*LG
WSo_23_r	(WSo+WSw)/2	(WSo+(WSw/2))*LG
WSo_34	(hSw/2)+(hSo/2)	(hSw)*LG
WSo_34_l	(WSo+WSw)/2	(hSw)*LG
WSo_34_r	(WSo+WSw)/2	(WSo+(WSw/2))*LG
WSo_45	(hSw/2)+(hSo/2)	(hSw)*LG
WSo_45_l	(WSo+WSw)/2	(hSw)*LG
WSo_45_r	(WSo+WSw)/2	(WSo+(WSw/2))*LG
WSo_56	(hSw/2)+(hSo/2)	(hSw)*LG
WSo_56_l	(WSo+WSw)/2	(hSw)*LG
WSo_56_r	(WSo+WSw)/2	((WSo+(WSw/2))/2)*LG
WSo_67	(hSw/2)+(hSo/2)	(hSw)*LG
WSo_67_l	(WSo+WSw)/2	(WSo/2)*LG

Source: Own authorship (2024)

Table 31 shows the equations of the magnetomotive force sources.

Table 31 – Magnetomotive force sources number of turns and current

Source	Number of turns	Current
_1T	N_1T	IA
_2T	N_2T	IA
_3T	N_3T	IA
_4T	N_4T	IA
_5T	N_5T	IA
_6T	N_6T	IA

Source: Own authorship (2024)